DEPARTMENT OF TRANSPORTATION

Understanding and Mitigating the Dynamic Behavior of RICWS and DMS Under Wind Loading

Lauren Linderman, Principal Investigator
Department of Civil, Environmental, and Geo- Engineering
University of Minnesota

June 2020

Research Project
Final Report 2020-18

To request this document in an alternative format, such as braille or large print, call 651-366-4718 or 1-800-657-3774 (Greater Minnesota) or email your request to ADArequest.dot@state.mn.us. Please request at least one week in advance.

Technical Report Documentation Page

1. Report No.	2.	3. Recipients Accession No.	
MN 2020-18			
4. Title and Subtitle Understanding and Mitigating the Dynamic Behavior of RICWS and DMS Under Wind Loading		5. Report Date June 2020 6.	
7. Author(s) L. Linderman, M. Guala, C. French, D. Schillinger, N. Finley, M. Heisel, L. Nguyen, S. Stoter, J. Vievering, Q. Zhu		8. Performing Organization Report No.	
9. Performing Organization Name and Address Department of Civil, Environmental, and Geo- Engineering University of Minnesota 500 Pillsbury Dr. SE Minneapolis, MN 55455		10. Project/Task/Work Unit No. CTS#2018005 11. Contract (C) or Grant (G) No. (C) 1003325 (WO) 28	
12. Sponsoring Organization Name and Address Minnesota Department of Transportation Office of Research & Innovation 395 John Ireland Boulevard, MS 330 St. Paul, Minnesota 55155-1899		13. Type of Report and Period Covered Final Report 14. Sponsoring Agency Code	
15. Supplementary Notes http://mndot.gov/research/reports/2020/202018.pdf			

16. Abstract (Limit: 250 words)

Dynamic Messaging Signs (DMS) and Rural Intersection Conflict Warning Signs (RICWS) are roadside signs that feature much larger and heavier signs than are typically placed on their respective support systems. The excess weight and size of these signs, in conjunction with their breakaway support systems, introduces vibration problems not seen in the past. The AASHTO 2015 LRFD Specification for Structural Supports for Highway Signs, Luminaires, and Traffic Signals (SLTS) does not yet address vibration design for these nontraditional roadside signs. DMS and RICWS were instrumented in the field and numerically modeled to explore their wind-induced behavior. A dynamic numerical model was validated with experimental field data and used to evaluate the fatigue life of the DMS support system instrumented in the field. The resulting fatigue life differed significantly from the equivalent static pressure analysis prescribed in the AASHTO specification. The fatigue life of the DMS instrumented in the field was conservatively estimated to be 23.8 years. Based on data collected from a RICWS instrumented in the field and experiments done on a scaled model of the RICWS at the St. Anthony Falls Laboratory, vortex shedding was identified as the predominant wind phenomena acting on the RICWS structure. Three modifications were proposed to reduce the impacts of vortex shedding. The investigation of these newer sign types highlights the importance of considering the impact of dynamic behavior and vortex shedding on the structural design.

17. Document Analysis/Descriptors	18. Availability Statement		
Traffic signs, Fatigue strength, Service life, Wind	No restrictions. Document available from: National Technical Information Services, Alexandria, Virginia 22312		
19. Security Class (this report) Unclassified	20. Security Class (this page) Unclassified	21. No. of Pages 204	22. Price

UNDERSTANDING AND MITIGATING THE DYNAMIC BEHAVIOR OF RICWS AND DMS UNDER WIND LOADING

FINAL REPORT

Prepared by:

Lauren Linderman
Michele Guala
Catherine French
Dominik Schillinger
Nicole Finley
Michael Heisel
Lam Nguyen
Stein Stoter
Josh Vievering
Qiming Zhu
Department of Civil, Environmental, and Geo- Engineering
University of Minnesota

JUNE 2020

Published by:

Minnesota Department of Transportation
Office of Research & Innovation
395 John Ireland Boulevard, MS 330
St. Paul, Minnesota 55155-1899

ACKNOWLEDGMENTS

Numerical computations were performed using resources provided by the University of Minnesota Supercomputing Institute.

TABLE OF CONTENTS

LIST OF FIGURES

LIST OF TABLES

EXECUTIVE SUMMARY

Dynamic Messaging Signs (DMS) and Rural Intersection Conflict Warning Signs (RICWS) are roadside signs that feature much larger and heavier signs than are typically placed on their respective support systems. There is a concern that the excess weight and size of the DMS and RICWS, in conjunction with their breakaway support systems, may introduce wind-induced vibration problems not seen in the past. The AASHTO 2015 LRFD Specification for Structural Supports for Highway Signs, Luminaires, and Traffic Signals (SLTS) does not yet address vibration design for these nontraditional roadside signs. This research explores the wind-induced vibrations in the DMS and RICWS.

The DMS support system, specifically the friction fuse connection, is susceptible to the formation of stress concentrations and potential fatigue issues. A dynamic numerical model was validated with experimental field data and used to evaluate the fatigue life of the DMS support system instrumented in the field. The results of the dynamic analysis performed with the experimentally validated finite element model (FEM) differed significantly from the analysis with the equivalent static pressure equation for natural wind gusts prescribed in the AASHTO LRFD Specification for SLTS, which highlights the importance of considering the dynamic behavior of these heavier sign panels. The fatigue life of the DMS instrumented in the field was conservatively found to be approximately 23.8 years. Extension of the method to models of other large DMS in service showed a greater fatigue stress and a corresponding shorter conservative estimate of the fatigue life. Other DMS in service may also be subject to fatigue stresses beyond the CAFT depending on the size of the sign panel, height of the posts, sign location, and the relative location of the friction fuse connection. Results of the analysis should be expanded beyond the behavior of the specific DMS system instrumented in the field to encompass other varieties of the DMS in service. In addition, reasons for the disagreement between the dynamic analysis and AASHTO equivalent static pressure methods should continue to be explored.

Large amplitude oscillations under wind loading have already been observed in the RICWS. Based on data collected from a RICWS instrumented in the field and experiments done on a scaled model of the RICWS at the St. Anthony Falls Laboratory, vortex shedding was identified as the predominant wind phenomena acting on the RICWS structure. The field data and validated FEM and computational fluid dynamics (CFD) models were used to identify and evaluate possible modifications to reduce the amplitude of the wind-induced oscillations. Three modifications were proposed to reduce the impacts of vortex shedding: altering the dynamic characteristics of the sign by addressing base fixity or structural height; reducing the form drag by removing the background shields on the lights; and adding a pendulum-type tuned mass damper. One simple modification to adjust the stiffness while maintaining the breakaway status of the connection was explored in the field and found to be insufficient at significantly adjusting the stiffness. A different breakaway base connection design was recommended to improve the fixity and increase the stiffness. In addition, a broader investigation of these newer sign types should consider the impact of vortex shedding on the structural design.

CHAPTER 1: INTRODUCTION

1.1 MOTIVATION OF RESEARCH

Wind loading is a key concern for the design of structural support systems for roadway signs and signals. Vibrations due to wind loading can cause the structure to oscillate, which may lead to problems with fatigue and potentially result in premature failure of the structure. The AASHTO 2015 LRFD Specification for Structural Supports for Highway Signs, Luminaires, and Traffic Signals (SLTS) addresses fatigue design for overhead sign and signal structures and high mast light towers. Fatigue design for roadside signs is not addressed because these structures are traditionally smaller and have not observed fatigue problems in the past (AASHTO, 2015). In recent years, however, the advancement of roadside signs with larger mass and size than typically supported on their support systems has sparked concern that these structures may also be susceptible to fatigue under wind loading.

Dynamic Message Signs (DMS) and Rural Intersection Conflict Warning Signs (RICWS) are roadside signs that feature much larger and heavier signs than typically supported by traditional roadside sign support systems. Structures within a specified distance of the roadway, which include most roadside signs, must feature breakaway supports to reduce injury to vehicle operators in the case of impact (AASHTO, 2015). The breakaway supports are designed with weakened connections, intended to break away when struck by a vehicle. There is a concern that the excess weight and size of the DMS and RICWS, in conjunction with their breakaway support systems, may introduce vibration problems not seen in the past. Research was done to explore the wind-induced vibrations in the DMS and RICWS.

The DMS breakaway connection features a friction fuse connection composed of two plates. One of the plates, the fuse plate, is weakened by reducing the net area of the plate with empty holes. This plate is thought to be especially susceptible to stress concentrations and fatigue. This research evaluates the design loads and fatigue lifetime of the DMS, specifically within the components of the friction fuse connection, to ensure the adequate fatigue life of the DMS support structure. Large amplitude oscillations have previously been observed in the RICWS. The wind-induced dynamic behavior of the RICWS support structure is also explored to propose modifications for reducing the amplitudes of the vibrations.

1.2 OVERVIEW OF RESEARCH

Research was done to assess the fatigue life of the DMS support system and to explore the wind-induced dynamic behavior of the RICWS. Field monitoring was used to validate numerical models of both structures to explore their response under wind loading conditions that could potentially occur in the region but were not readily observed during the field instrumentation. The information gathered from the numerical simulations was used to evaluate the fatigue life of the DMS support system and identify potential modifications to the RICWS support system for reducing the amplitude of the oscillations experienced by the sign structure.

The presentation of the research is organized as follows.

- Chapter 2 provides a brief background of the purpose of the DMS and RICWS signs, as well as an overview of their structural support systems. Background on the current design guidelines for fatigue loading and their origins is also provided.

- Chapter 3 presents an overview of the general approach and methodology used in this research project. Field data collected for both the DMS and the RICWS are used to validate numerical models of the two sign structures. In the case of the DMS, the validated numerical model is used to evaluate the fatigue life of the support structure, specifically in the friction fuse connection. In the case of the RICWS, the validated numerical models are used to identify potential modifications for reducing the amplitude of the oscillations experienced by the sign under wind loading.

- Chapter 4 describes the experimental setup and data collection procedures used in the field monitoring portion of the DMS support system.

- Chapter 5 presents an overview of the analysis of the DMS field data. The findings from this analysis are used to validate the finite element model of the DMS.

- Chapter 6 discusses the fatigue life of the specific DMS panel and support system instrumented in the field. A fatigue stress limit is determined based on the current specification and supporting literature. Results of the numerical simulations and guidelines for fatigue design from the AASHTO 2015 LRFD Specification for SLTS are used to determine whether the wind-induced fatigue stresses within the friction fuse connection are within the fatigue stress limit.

- Chapter 7 describes the field data collection system and instrumentation scheme for the RICWS. Laboratory experiments done on a scaled model of the RICWS by researchers at the St. Anthony Falls Laboratory (SAFL) are also presented in this chapter.

- Chapter 8 addresses the RICWS behavior under wind loading, as well as potential modifications for reducing the large amplitude oscillations in the structure. One modification implemented in the field is discussed. Validation of the FEM and computational fluid dynamics (CFD) models with the SAFL and field data is also presented in this chapter.

- Chapter 9 summarizes the conclusions and recommendations.

CHAPTER 2: BACKGROUND

2.1 DMS STRUCTURE

Dynamic Messaging Signs (DMS) display words, numbers or symbols to communicate real-time roadway and traffic information to drivers. The DMS fulfill a variety of applications including: emergency incident management, traffic management, maintenance activity updates, environmental condition warnings, and traveler information (MnDOT, 2000). An example of a typical roadside DMS is shown in Figure 2.1. MnDOT has found the roadside support structure for the DMS to be a cost-effective alternative to the overhead truss type or cantilever supports for these systems (MnDOT, 2016).

The DMS feature Type A breakaway posts suitable for placement in the clear zone. The clear zone is a roadside border area that extends a sufficient distance beyond the road to allow drivers to stop or navigate back to the roadway before meeting a hazard (McGee, 2010). Sign support structures within the clear zone must feature breakaway or yielding supports to limit injury to vehicle operators and damage to vehicles (AASHTO, 2015). The Type A posts used with the DMS feature a slip base and a friction fuse connection located just below the sign panel. The friction fuse connection consists of two plates, the fuse plate and the hinge plate. The plates are used to splice the two lengths of the support posts together. When a vehicle impacts the post, the post slips off the foundation at the base connection and then rotates around the weakened portion of the fuse plate (plate positioned nearest oncoming traffic), allowing the vehicle to pass safely under the sign (McGee, 2010).

Figure 2.2 displays the slip base connection of the DMS and the fuse plate located just below the sign. The hinge plate, is identical to the fuse plate except the four holes used to weaken the fuse plate are not present. Sample details of the friction fuse connection are shown in Figure 2.3.

Another key component of the DMS support structure is the attachment between the DMS panel and the support posts. Each post is attached with two “Z-Bar” mounts, located approximately 5.25 in. from the top and bottom of the sign panel. Figure 2.4 provides a side view of the DMS, illustrating the attachment of the sign panel to the supports. Knowledge of the location of these attachment points is necessary for idealizing how the wind-induced load on the sign panel is transferred from the panel to the support posts.

The DMS are much larger and heavier than signs typically placed on the Type A breakaway posts. Signs range from 6 ft. x 14 ft. to 8 ft. x 18 ft., weighing over 1500 lbs. (MnDOT, 2016) with post heights (taken from the ground to the top of the sign) ranging from 15.5 ft. to 22 ft. (Kimley Horn, MnDOT, 2015). Due to the excessive size and weight of the DMS, there is interest in investigating potential wind-induced vibrations not previously seen in the Type A post supports. Vibrations could lead to concerns with fatigue of the friction fuse plate. As a consequence, the current DMS with Type A post support may be structurally inadequate. MnDOT currently has approximately 40 of these signs in service with plans to install more in the future (MnDOT, 2016). If the current Type A post support design is inadequate, modifications may be needed that could negatively impact the breakaway status of the support system.

In such a case, guardrails, or other energy absorbing barrier systems, would be needed to protect drivers from such supported DMS structures placed in the clear zone (McGee, 2010).

2.2 RICWS STRUCTURE

Rural Intersection Conflict Warning Signs (RICWS) are installed in high risk intersections to warn drivers approaching from a minor roadway of high speed traffic traveling on the major roadway. Many severe collisions consist of two-vehicle, right-angle impacts that occur primarily at rural "Thru-STOP" controlled intersections where approaching traffic must stop or yield to traffic already in the intersection (CH2MHill, 2015). High speeds, and visual obstructions, such as vegetation, hills, and skewed roadways increase the risk of serious and fatal accidents at rural intersections (MnDOT, 2015). The RICWS are intelligent sign structures with yellow flashing lights at the top of the sign that flash when an oncoming vehicle approaches the intersection and traffic is present on the major roadway (MnDOT, 2015). If traffic does not exist on the major roadway, the yellow lights will not flash. An example of a RICWS structure is shown in Figure 2.5.

Similar to the DMS, the RICWS features breakaway supports for use in the clear zone. The RICWS is supported by two, 2 in. x 2 in. tube posts with slip base supports as shown in Figure 2.6. When a vehicle impacts the sign, the impacted post will fracture, bend, or pull from the ground, allowing the vehicle to pass through the sign with minimal damage to the vehicle (McGee, 2010). The slip base increases the safety of the sign and makes repair easier. The broken stub of the post can simply be removed from the base sleeve and replaced without having to re-drive the post (McGee, 2010).

MnDOT districts have noticed excessive swaying of the RICWS under wind loading, in some cases even to the point of full blow over (MnDOT, 2016). The electronic signs and mounted lights are much heavier than the typical flat sheet panel signs placed on the 2 in. x 2 in. tube post support systems. It is hypothesized that the added weight of the signs has brought the natural frequency of the RICWS too close to the frequency of the wind excitations (MnDOT, 2016). One solution has been to place a knee brace on the back of the sign, but the added brace removes the breakaway status of the RICWS. The additional support requires the signs to be either moved from the clear zone or have guardrail placed around them (McGee, 2010). This is undesirable. Strategies are needed to reduce the movement of the RICWS systems while maintaining the breakaway status of the base connection (MnDOT, 2016).

2.3 FATIGUE DESIGN AND CURRENT SPECIFICATIONS

Fatigue, damage resulting from stress fluctuations, is a primary concern for vibrating structures (AASHTO, 2015). Fatigue design can be done on either a finite life or infinite life basis. To design using the finite life approach an accurate estimate of the stress range and corresponding number of cycles is needed for the lifespan of the structure (AASHTO, 2015). This is difficult to achieve, especially for unpredictable wind-induced loading. In contrast, the infinite life approach identifies a Constant Amplitude Fatigue Threshold (CAFT) in which fatigue stresses below this limit result in the theoretical infinite fatigue life of the structure. Design with this method requires only the fatigue limit state stress range expected by the structure. A previous NCHRP study found that premature fatigue failure occurred

in structures where more than 0.05 percent of the fatigue stress ranges observed in the structure were greater than the CAFT (Fisher, Nussbaumer, Keating, & Yen, 1993). Based on these results, the fatigue limit state load range was recommended to be that which produces a fatigue stress range with 0.01 percent or less of exceedance (Kaczinski, Dexter, & Van Dien, 1998).

The AASHTO 2015 LRFD Specification for Structural Supports for Highway Signs, Luminaires, and Traffic Signals (SLTS) recommends an infinite life fatigue design approach. Critical details are separated into detail categories with uniform fatigue resistance design parameters across each category (AASHTO, 2015). A nominal stress methodology is then used to estimate the wind-induced stress in the detail. Stresses are calculated based on the application of equivalent static pressures that are intended to produce a static response in the structure similar to that produced by the actual dynamic wind loading on the structure (Kaczinski, Dexter, & Van Dien, 1998). For infinite life design, the wind load induced fatigue stress should be below the detail's factored Constant Amplitude Fatigue Threshold (CAFT), as seen in the equation below (AASHTO, 2015).

$$\gamma(\Delta f)_n \leq \varphi(\Delta F)_{TH} \qquad \textbf{(AASHTO, 2015)} \qquad \textbf{(2.1)}$$

where:

$\gamma =$ Load factor per the Fatigue I limit state, 1.0

$(\Delta f)_n =$ Wind-induced nominal stress range

$\varphi =$ Resistance factor, 1.0

$(\Delta F)_{TH} =$ CAFT

There are limitations to the infinite life fatigue approach specified by the AASHTO 2015 LRFD Specification for SLTS. First, wind is not a static load. The equivalent static pressures are a simplification of the loading behavior on the structure. They are back calculated to produce stresses similar to those produced via more complex spectral analysis (Dexter & Ricker, 2002). The resulting equivalent static pressures are then somewhat specific to the structures and wind loading used in the analysis. The fatigue limit-state load range of 0.01 percent exceedance is also difficult to estimate. Research to develop equivalent static pressures was sometimes done using only the upper bound of the observed wind load ranges, which was thought to be sufficient to ensure the fatigue life exceeded the serviceability life of the structure (Kaczinski, Dexter, & Van Dien, 1998).

The AASHTO LRFD Specification for SLTS, its interims, and previous research do not yet address fatigue design for the DMS, RICWS, or other similar roadside signs. Roadside signs are not cited as a concern, "Common light poles and roadside signs are not included because they are smaller structures and normally have not exhibited fatigue problems" (AASHTO, 2015). The AASHTO 2015 LRFD Specification

for SLTS identifies only five structure types in which fatigue is a necessary consideration in the design process.

1. overhead cantilevered sign structures
2. overhead cantilevered traffic signal structures
3. high-mast lighting towers (HMLT)
4. overhead non-cantilevered sign structures
5. overhead non-cantilevered traffic signal structures

Previous wind loading concerns on these structural support systems inspired research to understand the dynamic behavior of these structures under wind loading. Equivalent static wind loads were then developed for use in the fatigue design of these structures under different wind loading phenomena (AASHTO, 2015). The advancement of roadside signs such as the DMS and RICWS feature larger mass and size than typically supported on their support systems has sparked concern that these structures may also be susceptible to fatigue under wind loading.

2.4 WIND LOADING PHENOMENA

Four wind loading phenomena have been found to produce wind-induced vibrations in structures: galloping, vortex shedding, natural wind gusts, and truck induced wind gusts. Not all wind phenomena may be applicable to the DMS and RICWS, but each will be reviewed for completeness.

2.4.1 Galloping

Galloping is an aeroelastic phenomenon that results from the coupling between the aerodynamic forces acting on a structure and the oscillations of the structure (Kaczinski, Dexter, & Van Dien, 1998). As the structure oscillates, the angle at which the wind collides with the structure changes. The variation in the buffeting angle causes the oscillations in the structure to increase until the structure is thought to gallop. The oscillations occur transverse to the wind in asymmetric structures as shown in Figure 2.7, and are generally seen in uniform steady winds (Garlich & Thorkildsen, 2005). Generally, the oscillations occur at wind velocities oscillating around the natural frequency of the structure, but it has been observed that once the vibrations have begun they will continue to increase as the wind velocity increases (Kaczinski, Dexter, & Van Dien, 1998)

Galloping is most common in flexible, lightly damped structures. Structures exhibiting galloping must be susceptible to torsion, because to gallop the structure generally exhibits a transverse motion and twisting (Dexter & Ricker, 2002). Non-cantilevered structures or four chord cantilevered trusses, generally do not need to consider galloping in the design because these structures are less susceptible to torsion. Galloping is most prevalent in cantilevered structures with sign or single attachments. The arrangement of the signs, as well as the wind direction plays a role in the intensity of the vibrations (AASHTO, 2015).

Oscillations due to galloping can be mitigated by changing the dynamic characteristics or aerodynamic properties of the structure. Although stiffness and mass can also be manipulated, AASHTO LRFD

Specification for SLTS allows the use of “effective vibration mitigation devices” in place of designing the structure to resist oscillations due to galloping directly (AASHTO, 2015). Consequently, it is more common to change the mechanical damping of the structure when modifying dynamic characteristics. Galloping can only occur if the effective damping of the structure is negative, thus the minimum wind speed required to initiate galloping is proportional to the mechanical damping of the structure (Kaczinski, Dexter, & Van Dien, 1998).

The DMS and RICWS were assumed to behave similarly to an overhead non-cantilevered sign structure because the structures do not feature traffic signals and are supported at both ends. Fatigue design considerations for the overhead non-cantilevered sign structure does not include galloping. Galloping would produce vertical oscillations in the sign structures, which was thought unlikely to occur with both sides of the structures supported. Consequently, the DMS and RICWS are not susceptible to galloping.

2.4.2 Vortex Shedding

Vortex shedding occurs when fluid flows around a bluff body. The flow separates around the object and pressure vortices build on the leeward side of the object. The pressure vortices cause pressure differentials around the object, forcing the object to shift. By shifting, the object causes the vortices to form in a different location. The process repeats itself, resulting in oscillations (Ahearn & Puckett, 2010). Vortex shedding is thus an aeroelastic phenomenon that occurs through the coupling of the aerodynamic forces acting on the structure and the oscillations of the structure (Kaczinski, Dexter, & Van Dien, 1998).

Lock-in, the event of large amplitude oscillations, occurs when the shedding frequency matches the frequency of the structure’s oscillations. For structures with a large mass ratio this occurs around one of the natural frequencies of the structure (Williamson & Govardhan, 2004). Vortex shedding occurs under steady uniform flow and the oscillations are seen normal to the direction of the wind as illustrated in Figure 2.8 (Garlich & Thorkildsen, 2005). Generally, this phenomenon occurs within a small window of wind velocities. Wind speeds over approximately 35 mph are generally too turbulent to allow vortex shedding to occur and wind speeds below 10 mph do not generate aerodynamic forces with magnitudes large enough to cause the object to oscillate (Kaczinski, Dexter, & Van Dien, 1998). Vortex shedding is highly dependent on the Reynolds number and the Strouhal number (Ahearn & Puckett, 2010). The phenomenon is most common in pole structures, such as luminaires, but the masts of cantilever structures have also been known to exhibit vibrations due to vortex shedding when attachments (e.g., signs and signals) are not present (Garlich & Thorkildsen, 2005). Tapered luminaires have also been known to experience vortex shedding induced vibrations (Dexter & Ricker, 2002).

Oscillations due to vortex shedding can be mitigated by changing the dynamic characteristics or aerodynamic properties of the structure. Mechanical dampers are commonly employed in luminaires to reduce the amplitudes of the oscillations (Dexter & Ricker, 2002). Suspension bridges that have experienced vibrations due to vortex shedding have also successfully employed guide vanes to change the aerodynamic properties of the structure (Larsen, Esdahl, Andersen, & Vejrum, 2000).

Structures with attachments rarely experience vibrations due to vortex shedding (Garlich & Thorkildsen, 2005), but wind flow around the structures will always generate vortices (Williamson & Govardhan, 2004). In the wake of rigid objects vortex shedding indeed occurs, generating periodic eddies, also known as Karman streaks, evolving coherently up to order of 10 characteristic length scales of the object.

Depending on the likelihood for fluid-structure interaction, the shedding vortices may or may not couple with the oscillations of the structure to produce lock-in. With the DMS, it seemed unlikely that the shedding vortices would couple with the oscillations of the signs to produce lock-in. Fluid-structure interaction was thought to be more likely for the RICWS than the DMS due to the slender shape of the RICWS panel. The assumption that vortex shedding would not induce fluid-structure interaction in the case of the DMS is revisited in Chapter 5.

2.4.3 Natural Wind Gusts

Natural wind gusts buffet a structure with gusts fluctuating in magnitude and direction, causing the structure to oscillate. This phenomenon is applicable to all structures. Oscillations due to natural wind gusts can occur over a broad range of frequencies due to the natural turbulence in the wind (Kaczinski, Dexter, & Van Dien, 1998). Natural wind gusts result in a primarily horizontal displacement as shown in Figure 2.9, but there may be a vertical displacement component as well in cantilevered structures (Garlich & Thorkildsen, 2005). The impact of the atmospheric boundary layer on the mean wind speed acting on the sign at a given height is also not directly accounted for in the current AASHTO LRFD Specification for SLTS (Ahearn & Puckett, 2010). Equivalent static pressures were developed considering the mean wind speed at the height of the sign (Dexter & Ricker, 2002), but based on the AASTHO LRFD Specification for SLTS a single mean wind speed is used regardless of the height of the structure. The wind speed is known to vary with height because of the effects of the atmospheric boundary layer (Ahearn & Puckett, 2010). Little research has been done to explore the effects of natural wind gusts in combination with other wind loading phenomenon (Dexter & Ricker, 2002).

Flexible and lightly damped structures are most susceptible to damage from natural wind gusts (Garlich & Thorkildsen, 2005). Increasing the stiffness of the structure will allow the structure to resist larger wind loads, but will not necessarily reduce the dynamic response to loading (Kaczinski, Dexter, & Van Dien, 1998). Because wind velocities have significant excitation over such a broad range of frequencies the most effective method to reduce oscillation amplitudes is mechanical dampers (Kaczinski, Dexter, & Van Dien, 1998).

Natural wind gusts are applicable to all sign and signal structures and were assumed to be the predominant wind loading phenomena acting on the DMS and RICWS.

2.4.4 Truck Induced Wind Gusts

Truck-induced wind gusts are produced when a truck passes beneath, or near, a sign. As a truck passes beneath a sign, the vehicle distorts the airflow around the sign applying aerodynamic forces in both the

horizontal and vertical directions. This scenario most often results in displacements in the vertical direction as seen in Figure 2.10. Signs with large horizontal projections are most susceptible to forces from the trucks passing below. The larger the frontal area of the sign, the larger the force expected (Kaczinski, Dexter, & Van Dien, 1998). Truck-induced wind gusts became extremely relevant with the advancement of large Visual Message Signs (VMS) being installed over highways (Dexter & Ricker, 2002). Designing for truck-induced wind gusts is not required with structures that contain only signals (AASHTO, 2015).

The most effective method for reducing oscillations from truck-induced wind gusts is to increase the clearance between the sign and the truck passing below (Kaczinski, Dexter, & Van Dien, 1998). Forces on the structure reduce as the clearance between the truck and sign structure increases. Pressure from truck-induced wind gusts is assumed to be negligible at 33 ft. (AASHTO, 2015).

Truck-induced wind gusts are not applicable to the DMS or RICWS. The DMS are typically located approximately 30 ft. from the edge of the through lane (Martinez, 2015), making oscillations due to truck-induced gusts unlikely. The RICWS are located much closer to the road than the DMS, but the large frontal area of the RICWS faces the minor roadway where vehicle speeds were expected to be low as vehicles entered the intersection. Truck-induced gusts were consequently unlikely to occur in the RICWS at the speeds vehicles were passing the sign.

2.5 SUMMARY

DMS and RICWS are roadside signs that feature breakaway support posts with larger and heavier signs than typically used on these support systems in the past. The added weight and size of the DMS could potentially cause vibrations, and consequently fatigue problems in the weakened portion (i.e., the fuse plate) of the breakaway connection. Large amplitude oscillations have already been observed in the RICWS and need to be addressed.

Four wind loading phenomena are known to induce vibrations in sign and signal structures. Previous research has been done to explore the causes of these wind loading phenomena, as well as potential methods for reducing the resulting vibrations. Equivalent static pressures for fatigue design based on these four wind loading phenomena were also developed. Fatigue design for roadside signs, like the DMS and RICWS, have not yet been addressed in the current AASHTO LRFD specification for SLTS.

Figure 2.1 – Example of DMS

(a) Slip base

(b) Fuse plate

Figure 2.2 – Example of DMS breakaway connection

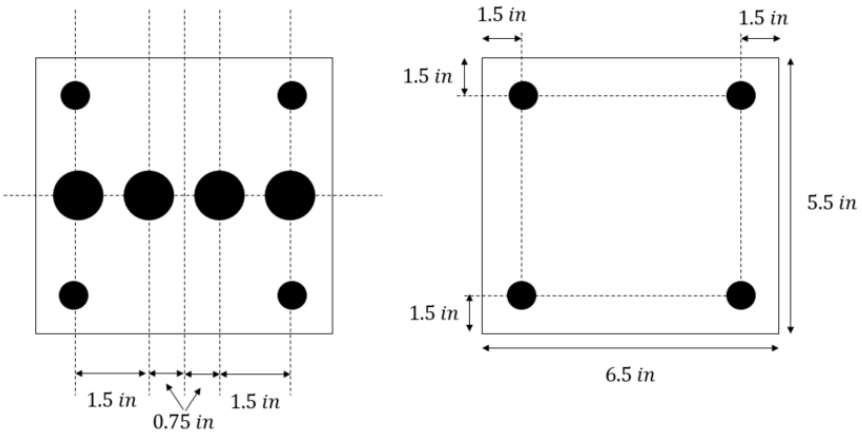

(a) Fuse plate (left) and hinge plate (right) sample details (not to scale)

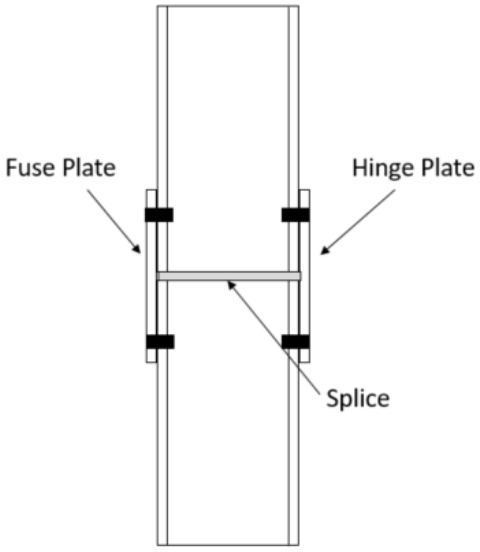

(b) Sample details for post splice (not to scale)

Figure 2.3 – Sample details for friction fuse connection

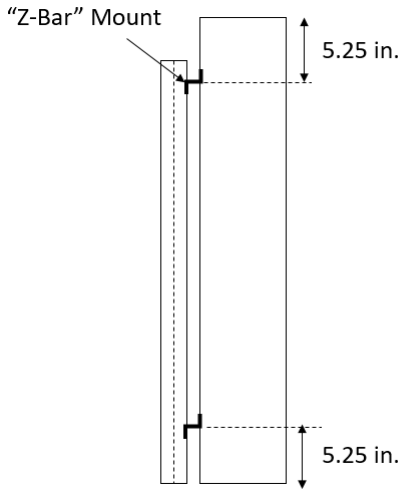

Figure 2.4 – Illustration of Z-Bar mounts used to attach DMS panel to supports (not to scale)

Figure 2.5 – Example of RICWS

Figure 2.6 – Example of RICWS breakaway connection

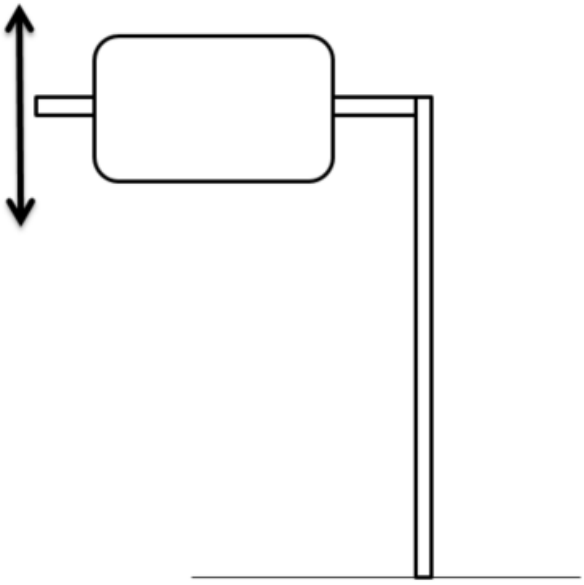

Figure 2.7 – Illustration of galloping for wind flow into page

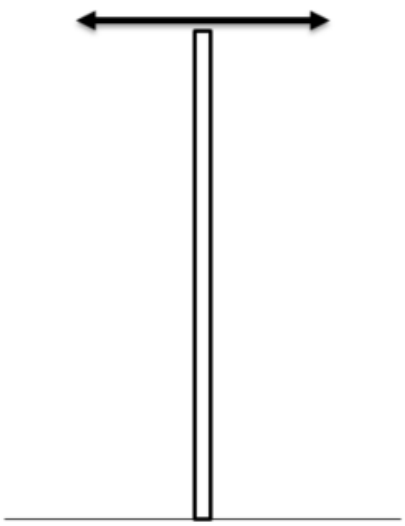

Figure 2.8 – Illustration of vortex shedding for wind flow into page

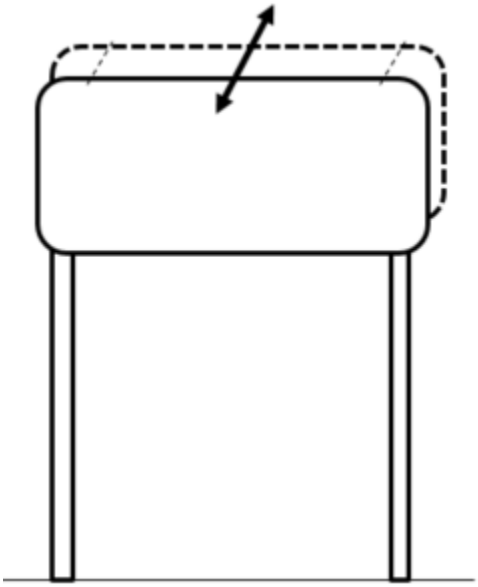

Figure 2.9 – Illustration of natural wind gusts for wind flow into page

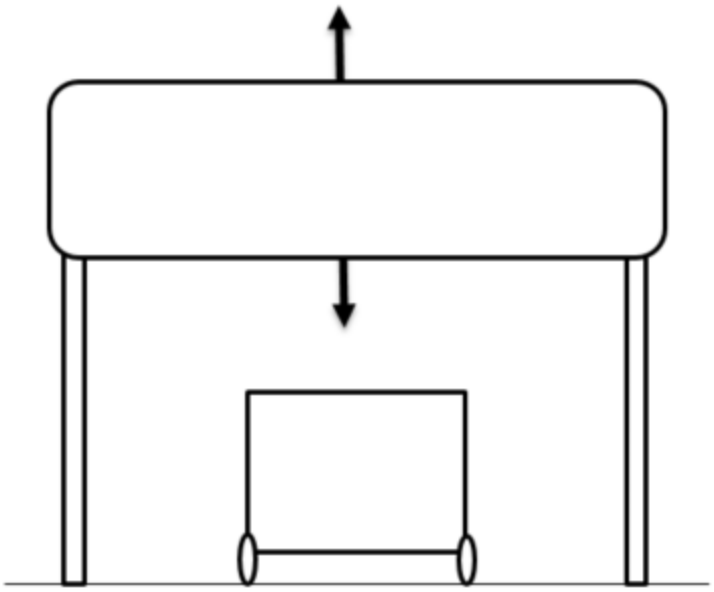

Figure 2.10 – Illustration of truck-induced wind gusts for wind flow into page

CHAPTER 3: APPROACH AND METHODOLOGY

3.1 RESEARCH GOALS

This research aimed to address concerns associated with wind-induced vibrations in the DMS and RICWS structures. Both signs are much larger and heavier than signs traditionally supported on their specific support structures potentially resulting in wind-induced vibrations not normally seen in typical roadside signs. The current AASHTO LRFD Specification for SLTS does not yet address vibration design for these nontraditional roadside signs. Vibration issues with roadside signs are ignored in the specification because vibration problems have not previously been a concern in traditional roadside signs.

The DMS Type A support system, specifically the friction fuse connection, is susceptible to the formation of stress concentrations and potentially fatigue issues. This research assessed the fatigue life of the Type A support system with the current DMS design. Large amplitude oscillations under wind loading have already been observed in the RICWS. Research was done to explore the wind-induced dynamic behavior of the RICWS to identify potential modifications to the RICWS support system for reducing the amplitude of the wind-induced oscillations.

3.2 APPROACH

The general approach for addressing both the DMS and the RICWS research goals included finite element method numerical (FEM) modeling validated with measurements from field monitoring. The validated numerical models were used to explore the behavior of the signs under various wind loading conditions to address the specific research goals for the two types of signs.

3.2.1 Methodology Specific to the DMS

The data collection system deployed to monitor the behavior of the DMS under wind loading was specifically tailored for validating the FEM model used to evaluate the fatigue life of the DMS support structure. Instrumentation was placed to capture the overall behavior of the DMS structure, as well as the local behavior within the friction fuse connection. The overall behavior was observed by monitoring accelerometers placed on the sign panel, as well as strain gages located at the base of the supports and distributed along the length of the post. Local behavior within the friction fuse connection was observed by monitoring numerous strain gages located on both the fuse plate and the hinge plate of the connection. Chapter 4 describes the setup for the DMS field monitoring in greater detail. Data collected along the posts was used to validate the overall behavior of the FEM model, while strain data specifically from the friction fuse connection was used to validate the behavior of the friction fuse connection in the model. The friction fuse connection was considered the critical fatigue detail in the structure, and consequently the connection was modeled in more detail within the FEM model. Chapter 5 provides the details for the FEM model and the validation process.

Wind loading models used to evaluate the fatigue life of the DMS support system were developed based on previous research exploring the wind loading phenomena known to induce vibrations in sign and

signal structures. Based on the findings in Chapter 2, wind loading models used to generate the fatigue stress range of the DMS were developed assuming loading predominantly from natural wind gusts. Guidelines from the AASHTO LRFD Specification for SLTS, wind data from the field observation period, and previous research in fatigue loads due to natural wind gusts were used to develop the wind loading models used in the FEM simulations for evaluating the fatigue life of the current DMS support system.

The stress range computed using the validated FEM model and prescribed wind loading models was compared with the estimated fatigue threshold for the friction fuse connection. The threshold was determined based on the recommendations of the AASHTO LRFD specifications for SLTS and other literature related to fatigue stress limits for details similar to the friction fuse connection. Final recommendations on the fatigue life of the DMS support system were based on the comparison of the simulated fatigue stress ranges and the estimated fatigue stress threshold. The selection of the fatigue threshold and evaluation of the fatigue life of the DMS support system are presented in Chapter 6.

3.2.2 Methodology Specific to the RICWS

The dynamic behavior of the RICWS under wind loading was explored using data collected from the field, data collected from scaled experiments done at the St. Anthony Falls Laboratory (SAFL), and numerical models of the structure validated with both the field data and experiments done at SAFL. The RICWS was modeled using a FEM model of the structure coupled with a computational fluid dynamic (CFD) model to capture the fluid-structure interaction between the RICWS and the wind loading.

The data from the field monitoring and SAFL experiments were used to validate and inform the RICWS numerical models. The field data collection system to capture the displacement of the structure and the experiments conducted at SAFL are described in detail in Chapter 7. The experiments at SAFL were used to capture fluid structure interaction characteristics that were not easily obtained in the field, specifically those related to vortex shedding which was thought to be one of the predominant wind loading phenomena acting on the RICWS based on the findings in Chapter 2. Two major experiments were done: drag experiments and wake experiments. Drag experiments were done to identify the drag coefficient and shedding frequency of the sign. Wake experiments were done to confirm the shedding frequency determined by the drag experiments. The wake experiments also provided important inflow turbulent boundary layer conditions for the CFD model, as well as a means for validating the resulting wake profiles predicted by the CFD model.

Field data was intended to validate the coupled FEM and CFD model because the displacements measured in the field indirectly contained the effects of the fluid structure interaction between the RICWS and wind. The analysis of the field data and validation of the RICWS models are presented in Chapter 8. Based on the observed behavior of the RICWS, the most appropriate modifications for reducing the amplitude of the observed oscillations were identified. The proposed options include altering the dynamic properties, reducing the form drag through aerodynamic modifications of the sign or adding a mechanical damping device. The recommended modifications are presented in Chapter 8. One modification approach to adjust the stiffness was implemented in the field and the results are presented in Chapter 8.

3.3 SUMMARY

The chapter presented the approach and methodology used to explore the dynamic behavior of the DMS and RICWS under wind loading.

CHAPTER 4: DMS FIELD MONITORING

4.1 FIELD OBSERVATION SETUP

The Type A post-mounted DMS (DMS 169-142.45 NB) located on 169 North within the Brooklyn Park area was instrumented in the field to investigate its structural performance under dynamic wind loading. Loads on the friction fuse connection and the fatigue lifetime of the Type A post support system were given specific attention when selecting and applying instrumentation. The final instrumentation setup is shown in Figure 4.1 through Figure 4.4. Images of the applied instrumentation are shown in Figure 4.5.

DMS 169-142.45 was selected for instrumentation primarily for its North-South orientation and its proximity to the University of Minnesota (UMN). Winds were expected primarily in the North-South directions, and the DMS 169-142.45 was oriented such that the normal surface of the sign was approximately perpendicular to the prevailing wind where moderate winds were expected regularly. This orientation was ideal for observing large strains (stresses) in the support system. Routine visits to the sign to check on instruments and data collection were more manageable with a sign located near the UMN.

The instrumentation consisted of two accelerometers, two cup and vane anemometers, one temperature probe, and 76 strain gages. The accelerometers were used to investigate the dynamic behavior of the DMS. The cup and vane anemometers measured the mean wind speed and direction. The strain gages were used to measure the dynamic response in the Type A post support system and the friction fuse connection under loading. Two of the total 76 strain gages were used to instrument two steel coupons placed on the ground near the base of each post. Because of the wide range of temperatures experienced in the field, the unstressed coupons provided a means to correct the gage readings for temperature effects. Although the strain gages used were temperature-compensated for steel attachments, the compensation was linear within a limited temperature range of 68 to 96^{o} F. The model number, manufacturer, and resolution of all instruments are provided in Appendix A. A layout of the instrumentation on the DMS is shown in Figure 4.1. General layouts for the strain gages are provided in Figure 4.2 through Figure 4.4. As built dimensions for the gages are provided in Appendix A.

The DMS support structure was expected to experience strong axis bending, weak axis bending, shear and torsion. The strain gage orientation shown in Detail A of Figure 4.2 (i.e., two rosettes on each face of the web, four strain gages on the flange tips, and two strain gages at the center of the flange face) provided some redundancy to facilitate investigation of these behaviors. The setup was also intended to enable shear strains generated from torsion to be distinguished from shear strains generated from bending. Detail A was positioned at the base of each post, as the greatest bending moments, shears and torsions were expected to occur there. The same strain gage orientation was distributed at two additional locations up the west post to capture the loading behavior over the height of the support to facilitate further comparison with the FEM model.

Detail B of Figure 4.2 was used to monitor shear transfer through the friction fuse connection. There was a visible gap between the two sections that made up each post (i.e., above and below the friction fuse connections). Shear could not be transmitted via friction through the webs of the two sections. Consequently, the rosettes of Detail B were located approximately 3 in. above and below the interface to avoid nonlinear effects due to St. Venant at the discontinuities.

Detail C of Figure 4.2 shows both plates of the friction fuse connection (i.e., the hinge plate and the fuse plate) instrumented with multiple strain gages to capture the strain behavior in the connection. The hinge plate was instrumented with five, 0.236 in (6 mm) gages as shown in Figure 4.2, and the fuse plate was instrumented with two, 0.236 in (6 mm) gages and three, 0.118 in (3 mm) gages. Smaller gages were used on the fuse plate to improve the fit of the gage within the limited space between the holes in the plate. The behavior of the friction fuse connection was especially important for model validation because the friction fuse connection was a likely location for stress (strain) concentrations and potential fatigue issues. It was not possible to detect local strain concentrations with the gages due to their finite size; the gages provided an averaged strain over their gage length. The averaged strains from the collected field data were later used to validate the FEM model by comparing the measured results with strains from the FEM model. This procedure is explained in detail in Chapter 5.

Due to challenges avoiding the existing conduit located on the east post of the Type A support system, some strain gages were not placed as illustrated in the details provided in Figure 4.2 through Figure 4.3. Gages 66 and 68, see Figure 4.4, were not installed because of conduit covering those locations on the hinge plate, and gages 37, 38, and 39, see Figure 4.3, were placed on the inside of the post flange instead of on the exterior of the flange to avoid the conduit on the post.

Strain gages were installed using CN-Y adhesive and installation procedures recommended by Texas Measurements. The galvanization at gage locations on both posts and both friction fuse connections was removed using an angle grinder. The surface was then smoothed using a rotary sander and later by hand for fine smoothing. Grinding the surface of the fuse plate and the hinge plate was especially difficult due to the presence of the bolts in the connection. The face of the grinder did not fit well between the bolts, and grinding in these areas was quite crude. The red circle on the fuse plate in Figure 4.5 highlights an example of a poorly grinded surface. The surface was smoothed as much as possible with the rotary sander and sand paper applied by hand. After installation, all strain gages were protected environmentally with SB tape and aluminum foil tape. The gages on the friction fuse plate in Figure 4.5 are shown before the protective tape was applied.

Data was collected using a CR9000X Campbell Scientific data logger. The two accelerometers, two anemometers, temperature probe, and 54 of the total 74 strain gages installed could be monitored simultaneously by the data logger. Three groupings of instrumentation were used during the monitoring period. In the first phase, the accelerometers, anemometers, temperature probe, and gages 1 through 54 were connected for data collection. This grouping of gages was used to capture the loading behavior vertically along the post of the support system. In the second grouping, gages 13 through 36 were replaced with gages 55 through 74 to target the loading in the friction fuse connection. A third group was utilized to confirm the findings from group 1 as well as maintain the observation of the friction fuse

connection. In this group, gages 2 and 5 were replaced with gages 14 and 17, and gages 26 and 29 were added. Group 3 was used for most of the data collection period. Figures of each gage grouping are provided in Appendix A, as well as a log stipulating when during the data collection period each gage grouping was utilized.

Temperature, wind speed and direction were sampled at the peak sampling rate of the cup and vane anemometers selected for instrumentation, which was 1 Hz. The values of these quantities were not expected to change at a rate much faster than 1 Hz. The strain and acceleration data were sampled much faster (i.e., at 200 Hz) to capture higher frequency response of the structure and provide opportunity for filtering the data to remove any high frequency noise. A cellular modem was used to access the data collection system and data remotely.

The primary data of interest were collected at a fast rate on an event basis. Additionally, the wind speed and direction, air temperature, and the strain at each of the connected gages were continuously collected at five-minute intervals, and the average values over five-minute periods (5-minute averages) were stored. These averages were collected primarily for investigating long-term data trends and diagnostic purposes. The fast rate dynamic data (i.e., raw sampled measurements) were saved when a measurement threshold had been exceeded. Three different types of thresholds were set: maximum wind speed (31.3 mph), maximum strain (100 $\mu\varepsilon$), or a maximum acceleration (1g). In all events recorded, the maximum wind speed triggered the wind event. Limiting fast data collection to events beyond the threshold increased the quality of the data being saved by increasing the probability that some strain data would be above the noise floor of the gages. Observing the data through unique, individual events enabled a more detailed exploration of the sign behavior under wind from specific directions.

4.2 DATA COLLECTION PERIOD

Field data collection for the DMS began on August 8th, 2017. A log of all major changes to the data collection system is provided in Appendix A, but some notable data collection milestones are summarized here:

- Reliable data collection began on August 17th after adjustments were made to the initial setup of the system.
- Between September 14th and October 31st, the data collection system was not fully operational because of problems with the power supply to the system.
- On September 19th the accelerometers were glued directly to the support post instead of attached using a steel plate as seen in Figure 4.5. This was done to remove any frequency content of the steel plate in the accelerometer data.
- On September 29th Accelerometer 1 was moved to the web (orthogonal to original position on the flange) of the west support post to capture frequency content for the second mode shape, as shown Figure 5.18. The accelerometer could only capture motion within the axis in which it was applied. Consequently, the accelerometer had to be moved to capture motion in the East-West direction.

- On October 31st, the anemometer located at the bottom of the DMS sign panel was removed for use in the instrumentation system installed on the RICWS. Wind data collected after October 31st was based on the readings from the top anemometer only.

High speed wind events were rare during August and September, with very few wind events exceeding 31.3 mph (14 m/s). Data collected in November and December generally consisted of much larger wind speeds than those recorded during August and September. Consequently, in November and December multiple wind events were collected for a wind speed threshold of 31.3 mph (14 m/s). Critical wind events from November and December are described in Chapter 5 during field data reduction.

4.3 SUMMARY

A Type A post-mounted DMS (DMS 169-142.45 NB) was instrumented in the field to observe its behavior under a measured wind loading. The instrumentation setup included accelerometers, anemometers, a temperature probe, and numerous strain gages. Sensors were located to validate the FEM model. Two different types of data sets were recorded: 5-minute averages over the course of the measuring period and fast rate triggered event-based dynamic data. The data collection period began in August, but wind events with higher wind speeds were primarily collected in November and December. Data collection was ongoing throughout the duration of the project, but wind data used to generate the conclusions provided in Chapter 9 are based on wind events in November and December only due to limited high wind events in the spring.

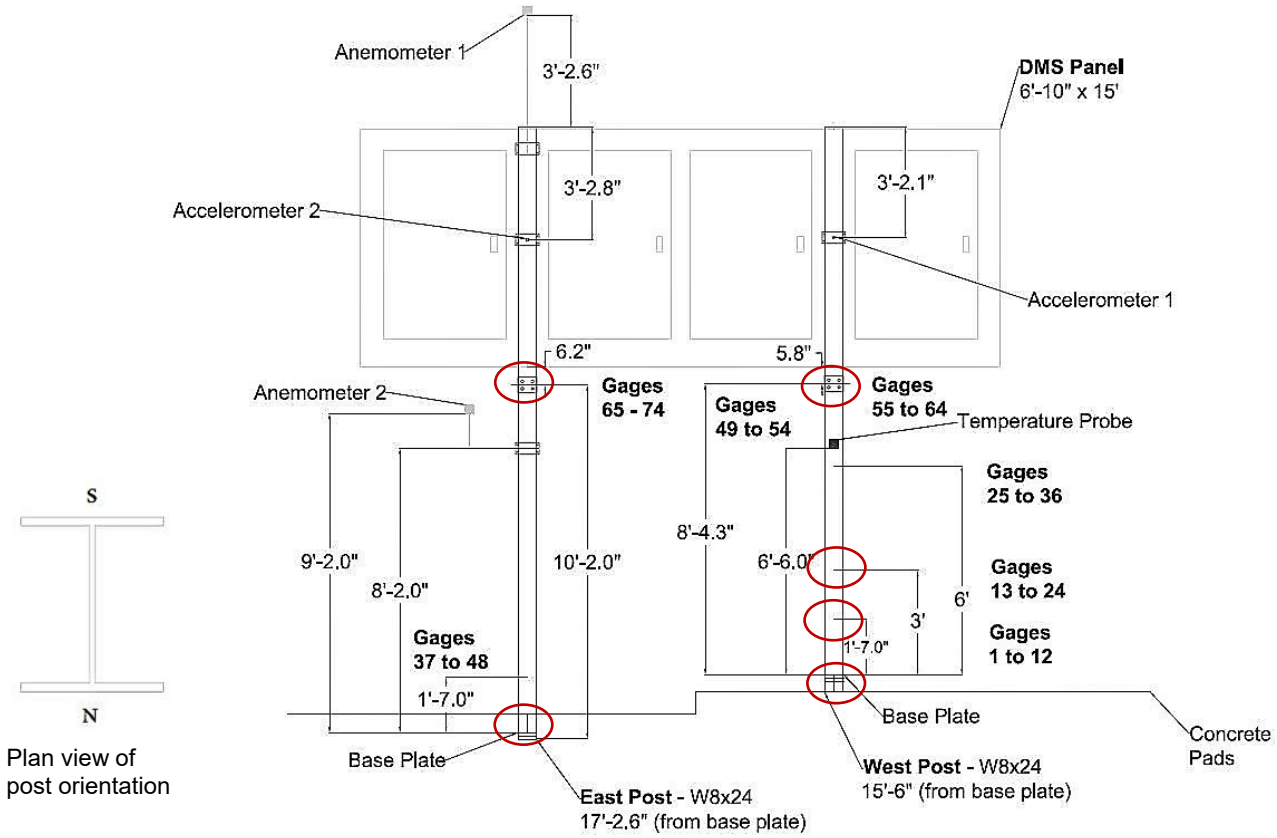

Note: The concrete pad was used as a reference point for dimensions, but the posts were imbedded into the ground adjacent to the concrete pad. The concrete pad protruded just a few inches from the surface of the ground.

Figure 4.1 – Instrumentation layout for DMS

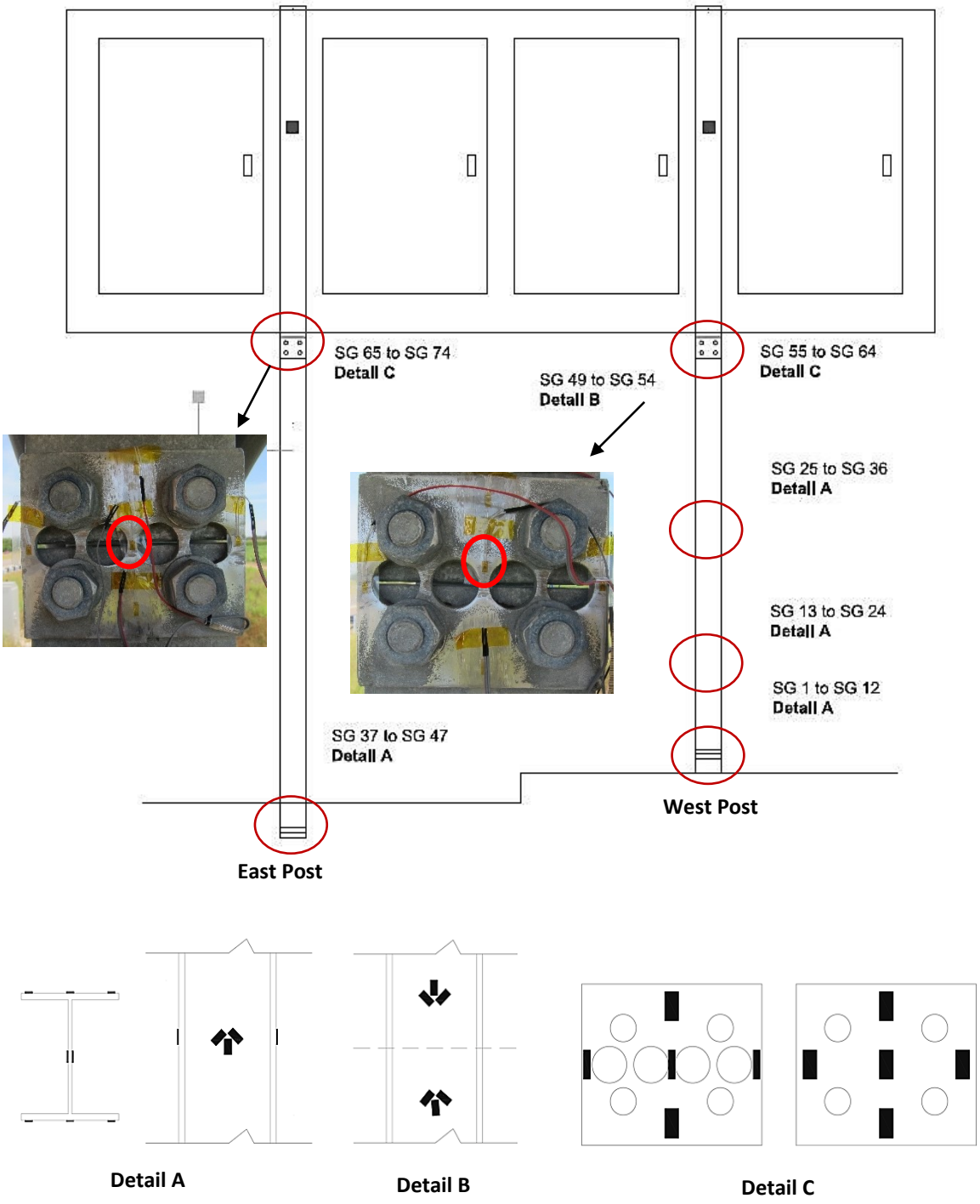

Figure 4.2 – Strain gage details (detail subsets not to scale)

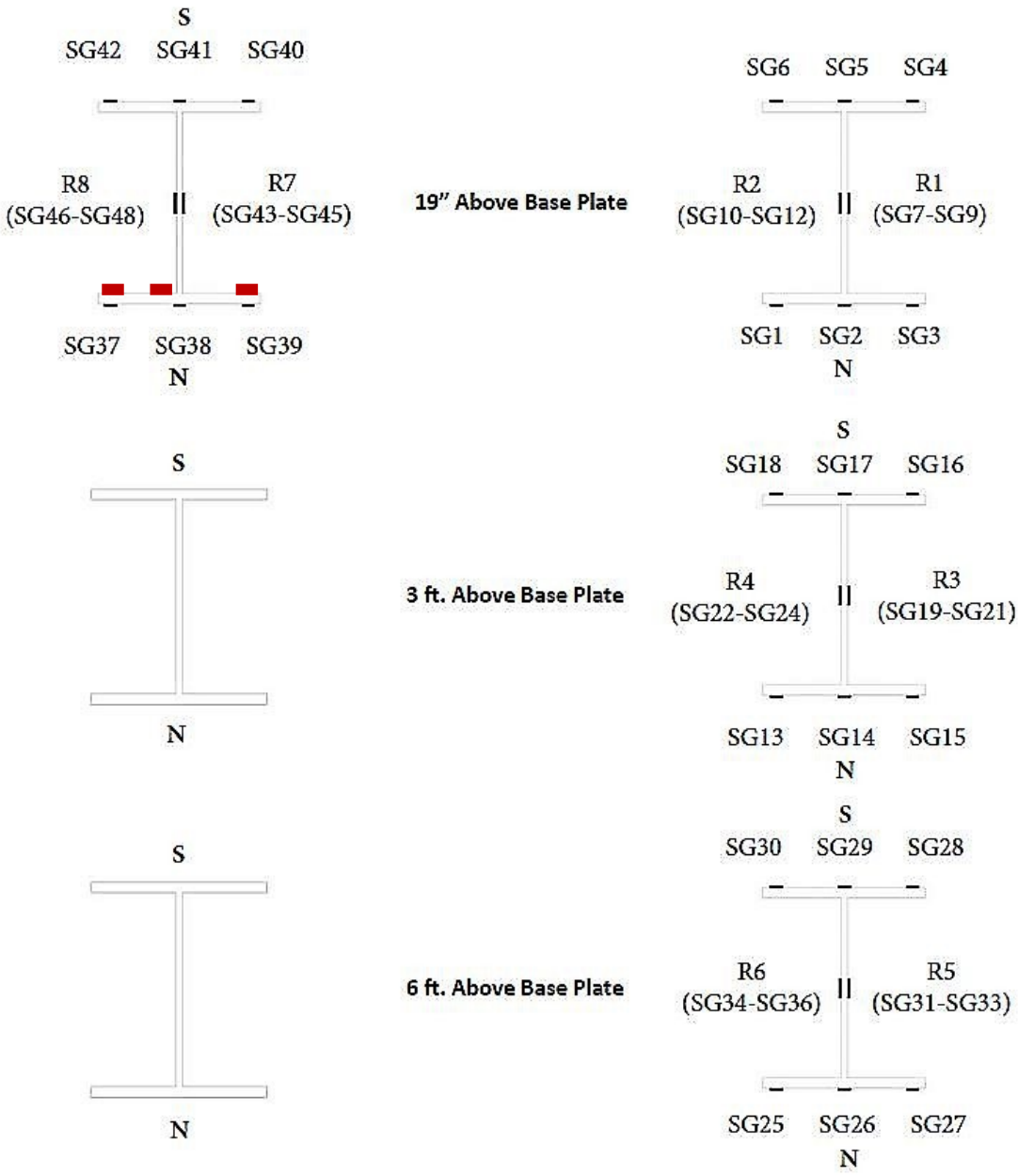

Figure 4.3 – Strain gage layout for gages 1 through 48 (not to scale)

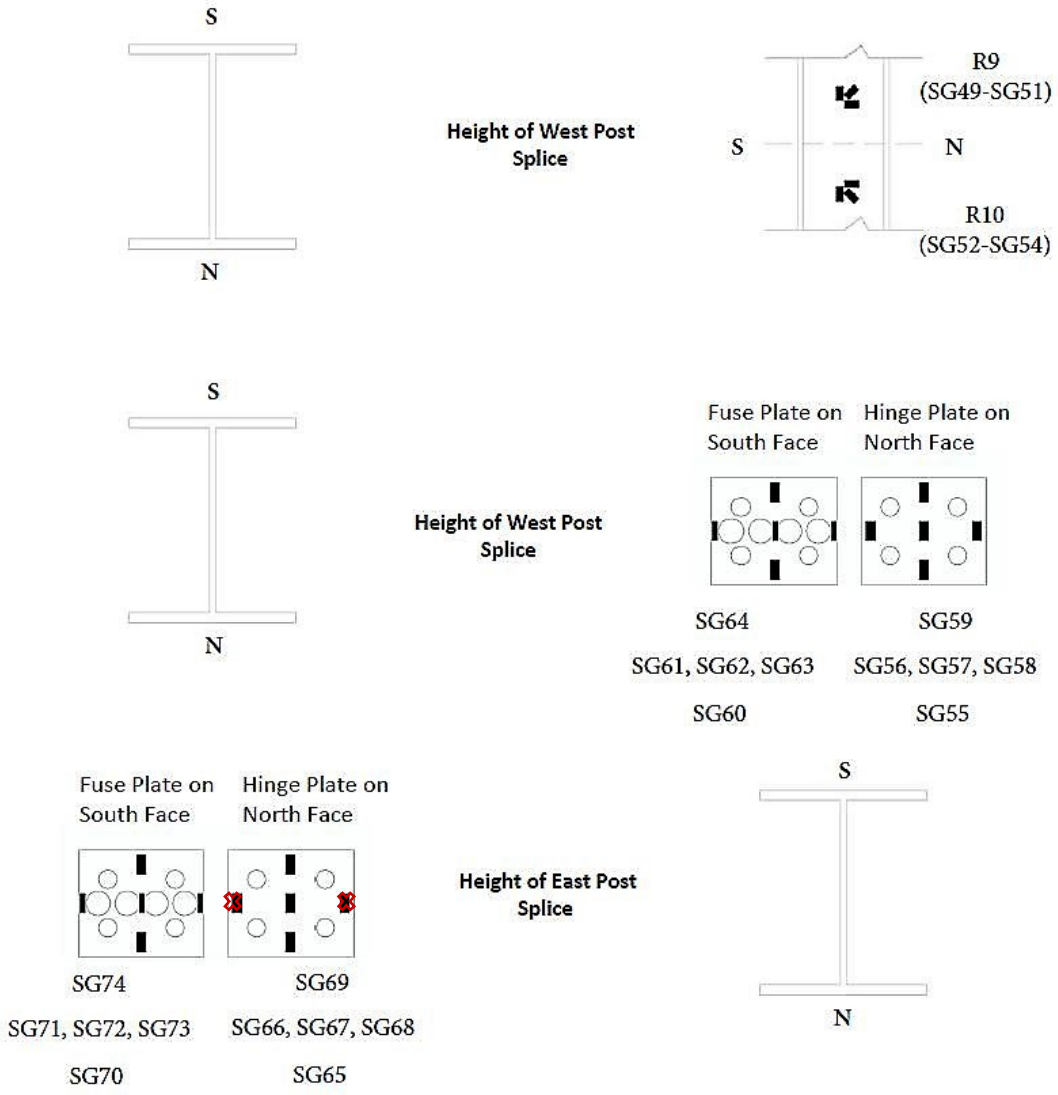

Figure 4.4 – Strain gage layout for gages 49 through 74 (not to scale)

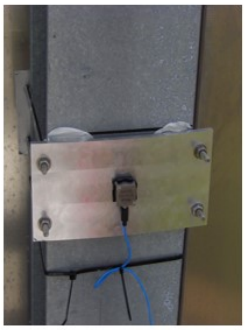

Accelerometer

Strain Gages

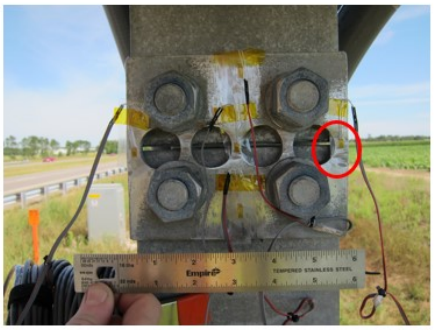

Friction Fuse
Strain Gages

Temperature Probe

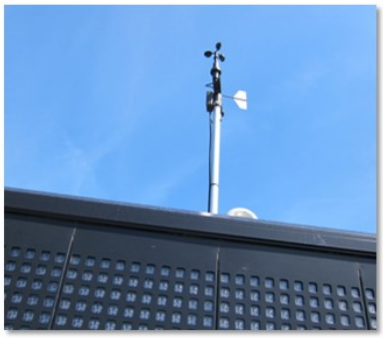

Upper Anemometer

Lower Anemometer

Figure 4.5 – Examples of DMS instrumentation

CHAPTER 5: ANALYSIS OF DMS WITH TYPE A SUPPORT SYSTEM

5.1 FIELD DATA REDUCTION

The DMS 169-142.45 NB structure was instrumented as described in Chapter 4 to determine the behavior of the DMS sign structure subjected to wind loading. The measured data were subsequently used to validate the FEM model of the DMS and Type A support system. The validated FEM model could then be used to investigate different wind scenarios and local strain fields of interest in the friction-fuse plate.

Wind events with wind speeds that exceeded a threshold of 31.3 mph were used for the validation. A threshold speed of 31.3 mph was thought to be large enough to produce strains that exceeded the noise floor of the gages (i.e., $\pm\, 3\mu\varepsilon$, see Section 5.1.1) in most of the support structure. Of the several wind events triggered during November and December of 2017, eight critical wind events were selected for detailed analysis. Events were designated using the month/day and time in which the event occurred. Critical wind events were selected based on the peak wind speed exhibited in the event and/or the primary wind direction of the event. The wind rose and wind speed history for each of the eight critical wind events is given in Figure 5.1 (Event 11/01 at 1506 through 11/09 at 1506), Figure 5.2 (11/10 at 1608 through 12/04 at 2321), and Figure 5.3 (Event 12/05 at 1321 and Event 12/13 at 1038).

Note that the wind speed history includes plots for the raw wind speed, normal wind speed, and the tangential wind speed. All speeds are absolute values. The raw wind speed represents the raw wind speed value recorded relative to magnetic north, whereas, the normal and tangential wind speeds are the components of the raw wind speed separated to explore the effects of normal and tangential loading on the sign. The normal and tangential wind speeds were computed using trigonometry and the known offset, approximately 52 degrees, between the direction normal to the North face of the DMS and magnetic north. The reference for the direction normal to the North face of the DMS is indicated in the wind roses shown in Figure 5.1 through Figure 5.3 by “Sign North.” Also note that for cleaner comparison between the three speed plots, only the magnitude of each wind velocity component was displayed. The wind rose illustrates the direction winds were coming from, i.e., North, South, East, or West.

5.1.1 Challenges

A few challenges were encountered in analyzing the field data. The first challenge dealt with the effect of temperature on the strain gages. For comparison with the FEM model, the mechanical strains due to wind loading needed to be separated from the strains due to temperature. Although the strain gages were temperature compensated for steel, they were only compensated between 68 to 96 ^{o}F as described in Appendix A. Fluctuation in temperature outside of this temperature range resulted in measured changes in strain due to thermal effects. During the six-month observation period from August to January, the temperature regularly exceeded the temperature range in which the gages were temperature compensated. Long-term temperature data for the DMS is shown in Figure 5.4. To

overcome this challenge, only the change in strain throughout a wind event was analyzed. Wind events were 5 minutes in length. During a wind event temperature changes were not sufficient to induce changes in strain due to thermal effects. Instrumented unstressed steel coupons were used to investigate the effects of temperature on the long term (5-minute average) strains. Although the coupons did not account for the impact of differential exposure to sunlight at various positions on the structure, the coupons served as an average measure of the change in strain due to temperature.

The coupons were primarily used to estimate the noise in the measured strain data. Figure 5.5 displays the normal wind speed, air temperature, strain in the coupon located on the ground near the east post, and strain in the gage located at the base of the north center flange of the east post. The trend observed in the strain data for the gage located on the support post clearly follows the trend observed in the wind speed data, indicating that the gage was indeed responding to the wind loading. As expected, the strains observed in the coupon did not resemble the trend observed in the wind data. The fluctuations observed in the coupon strain measurements were significantly smaller than those observed in the gage on the support structure. Changes in the strains measured in the coupon represent noise in the gage, but the absolute magnitude of the strain is likely due to temperature-induced strain sustained from changes in temperature beyond the zero-conditions the gage was installed in. Based on similar analysis with other critical wind events, it was determined that the coupons did not respond to wind loading on the structure. Consequently, they could be used as a representation of the noise in the gages on the supporting structure.

The second challenge dealt with the variation in the sampling frequency of the data. Wind speed, wind direction, and air temperature were sampled at 1 Hz, while strains and acceleration were sampled at a much faster sampling rate of 200 Hz. Sampling the strains and accelerations at the higher frequency allowed the sensors to detect response in the sign at frequencies less than 100 Hz. For example, response due to high frequency buffeting or vortex shedding could potentially be detected in the strain and acceleration data. Wind gusts that may have caused the response, however, could not be measured because of the limited sampling rate of the anemometer. Without the known wind loading, it was difficult to reliably distinguish response from noise in the higher frequency data of the strains and accelerometers.

Consequently, much of the exploration of the strain data was done at a 1 Hz sampling rate. This was done for two main reasons. First, strain data collected at 200 Hz was very noisy. Filtering and downsampling to a sampling rate of 1 Hz smoothed the data significantly and made observing basic trends in the data much easier. Second, because the wind data was collected at 1 Hz sampling, it was not possible to develop an accurate estimate of the pressure, and consequently the force on the structure for changes greater than 1 Hz. Any comparison done with the field data, for example comparison with the FEM model, required knowledge of the force applied to the structure. Comparisons had to be performed at a sampling rate of 1 Hz because any comparison done at a faster sampling rate would require extrapolation of the wind loading behavior beyond that which was measured. There would be no way to verify the accuracy of the extrapolation. The natural frequency of the DMS support structure was between 3 and 4 Hz, see Section 5.2.1. Consequently, a sampling frequency of 1 Hz was

not sufficient to capture any resonant behavior in the strain data. Resonant behavior was explored in Section 5.2.1 through an analysis of the strain data.

The strain amplitude measured in the coupons, or assumed noise in the gages, was also evaluated at 1 Hz. Figure 5.6 displays the average strain amplitude in each coupon at 1 Hz sampling for each of the critical wind events. As seen in Figure 5.6, the strain variation in the coupons ranged from approximately $\pm 1\ \mu\epsilon$ to $\pm 3\ \mu\epsilon$, with the smaller variations in strain consistently observed in the coupon near the west post. The variation in the two coupons was a limited representation of the noise experienced in all 76 gages utilized in the experiment. The maximum error observed in the coupons, $\pm 3\ \mu\epsilon$, was assumed to be a reasonable representation of the error present in all the gages throughout the DMS support structure.

The remainder of the analysis presented in this chapter was done assuming an error of $\pm 3\ \mu\epsilon$ in each strain gage. For clarity, subsequent figures in this chapter, except those referring to the validation of the model under tangential loading, use data from Wind Event 11/09 at 0553 as seen in Figure 5.1. Wind Event 11/09 at 0553 was selected because the wind direction was primarily normal to the sign and featured relatively large normal wind speeds. A primarily normal wind event was desired for most comparisons because the area of the sign surface exposed to the normal component of the wind was much larger than the surface of the sign exposed to the tangential loading of the sign. The response of the sign due to normal loading was thought to control over the response due to tangential loading. Validation of the FEM model, seen in Section 5.2 was done dynamically using field data.

5.1.2 Static and Dynamic Model Investigation

Based on the evaluation of the estimated strains in the base of the support posts, it was determined that a dynamic FEM model was necessary for simulating the strains in the DMS support structure. Note that the base of the post refers to the strains at the first set of gages on each post, which reside 19 in. above the base plate. See Figure 4.1. The estimated change in strain was computed by two approaches. The first assumed the static application of wind pressure to the DMS. In the second case, the response of the structure was investigated using a dynamic model.

The estimated static strain was based on the change in measured wind speed and corresponding change in pressure. The pressure was computed using the wind speed at two specified points in time, see (5.1) and (5.2), and then the difference in pressure was used to calculate the resulting change in applied force. Drag force was computed by multiplying the pressure by the area of the sign exposed to the wind loading as shown in (5.3). Wind loading was assumed constant over the entire area of the sign. The normal component of the wind loading was assumed to control because the exposed area of the sign was much larger than the area exposed to the tangential component of the wind loading. The tangential component of the wind load was consequently neglected, and the normal wind pressure was computed using only the normal component of the wind velocity. The expected change in strain at the base of the post was calculated using statics and the cantilever models shown in Figure 5.7. A fixed base was assumed for each support. The point loads shown in Figure 5.7 correspond to the location of the “Z-Bars” used to connect the sign to the W8x24 support posts as discussed in Chapter 2. Two Z-Bars were

used to connect each post, for a total of four Z-Bars. For this analysis, the force on the sign was assumed to distribute evenly between the four attachment locations.

$$P = \frac{1}{2}\rho C_d V^2 \quad (5.1)$$

$$C_d = 1.0 + 0.02\left(\frac{w}{h} + \frac{h}{w}\right) \quad (5.2)$$

$$\mathrm{F_d} = \mathrm{PA} \quad (5.3)$$

where:

$P =$ Pressure, lb/ft^2

$\rho =$ Density of air, 0.75$\frac{lb}{ft^3}$

$C_d =$ Drag coefficient, 1.64

$\mathrm{V} =$ Wind velocity, ft/s

$w =$ Width of sign, 6.64 ft.

$h =$ Height of sign, 14.85 ft.

$F_d =$ Drag force, lb

$A =$ Area of the sign, 98. 6 ft^2

The strain distribution through the I-Section at the base of the post was evaluated for pairs of gages at the N and S flange tips. Evaluating the strain distribution across the section instead of comparing expected strains to individual strain measurements reduced the likelihood of forming a conclusion based on data from a potentially faulty individual gage reading. A map of the strain distribution was developed from the measured strains that extended from flange tip to flange tip across the section. The expected static strains were computed at the center of each flange. Strains on opposite flanges of the same post were assumed to be equal and opposite, with a linear distribution in strain across the section. Zero strain was expected at the center of the web (i.e., neutral axis).

Figure 5.8 illustrates the force history for Wind Event 11/09 at 0553 and the corresponding strain in gages located on the north flange of the respective posts. The measured strains clearly exhibited trends like those observed in the forces calculated in each post. The markers located on the plot represent the

points in which the change in strain was evaluated in the I-Section. Expected static strains were computed as described previously, and the change in measured strain was determined by simply taking the difference in the measured strains at the two points.

The black markers shown in Figure 5.8 mark the locations for the change in force resulting in the change in strain shown in Figure 5.9. In Figure 5.9, the red line corresponds to gages on the west flange tips of the section, the green line corresponds to gages on the east flange tips of the section, and the black line corresponds to the estimated, or calculated, strain at the center of the flanges. Although gages did exist at the center of the flanges, data from this event was taken while gages from Group 3 were connected to the logger. Consequently, for this event no measured data was available for strain at the center of the flanges. The subset image within Figure 5.9 shows the location of each strain measurement in the cross section. The south flange of the section is located at an x-value of -4 in. and the north flange is located at an x-value of 4 in. on the plot. The measured strains at the north flange of the east support were located at an adjusted x-value of 3.6 in. due to adjustments made in the field to avoid conduit on the north flange of the east post. Error bars of $\pm 3\ \mu\varepsilon$ are shown on all calculated values. Error bars were always placed on the calculated values because the measured strains were expected to be within the bounds of the calculated strains considering the resolution of the data (i.e., $\pm 3\ \mu\epsilon$).

For primarily normal wind loading assuming there is no change in axial load in the post, the distribution of changes in strain in the I-Section should be symmetrical about the centroid of the section. Strains on the flange closest to the oncoming wind should be in the greatest tension and strains on the other flange should be in greatest compression. The strain distribution in Figure 5.9 shows the south flange in compression, i.e., a negative change in strain, and the north flange in tension for all measured and expected strains, which was logical for the wind loading direction observed in this event. Also note that strains measured on the west flange tips (circled in red) and the east flange tips (circled in green) crossed within $\pm 3\ \mu\varepsilon$ of zero-strain at the center of the I-section suggesting that the measured strain distribution within the I-section was indeed symmetrical in magnitude. In both the east support and the west support, the measured strains (red and green) were not within the $\pm 3\ \mu\varepsilon$ of the expected static strains (black).

Figure 5.10 was developed using the change in strain computed for the change in force corresponding to the gray markers shown in Figure 5.8. In this case, the measured and estimated strains also exhibited compression on the south flange and tension on the north flange. The magnitude of the measured strains at the center of the I-section were again within $\pm 3\ \mu\varepsilon$ of zero strain at the center of the I-section suggesting that the measured strain distribution within the I-section was symmetrical in magnitude. However, the difference between the estimated strains (black) and the measured strains (red and green) for this change in force was much larger than seen previously in Figure 5.9.

A simple dynamic analysis of the DMS was conducted (i.e., second model) to determine if the difference in strains between the predicted and measured results assuming the static behavior could be attributed to dynamic effects. The dynamic model encompassed other factors that affect the strains in the supports, such as the inertia of the sign and support posts. The simple dynamic model was developed assuming a fixed-free support condition and two posts of equal height. The two posts instrumented in

the field were not the same length, but this assumption simplified the model and served as a good initial comparison with the experimental data. The mass of the sign was applied to the finite rectangular prism with dimensions of the sign panel as shown in Figure 5.11. The model was developed using the Assumed-Modes Method (5.4). The post was assumed to follow the deformed shape of a vertical cantilever with a point load at the free end as shown in Figure 5.11. For use as a shape function, the deformation function was normalized such that the displacement at the free end of the cantilever was equal to one. The final equation of motion is given by (5.5). The equation of motion was converted to a state space formulation and Simulink was then employed to solve for the time-dependent function, $q(t)$, based on the applied forcing function, $F(t)$, computed from the experimental wind data. The longitudinal strain history in the flange of the I-section nearest to the oncoming wind was then computed using (5.6).

$$\mathbf{v(x,t) = \psi(x)q(t)} \tag{5.4}$$

$$\left[\frac{33}{140}M_t + M_s\left(1 + (w^2 + h^2)\left(\frac{3}{2L}\right)^2\right)\right]\ddot{q}(t) + c\dot{q}(t) + \left[\frac{3EI}{L^3} - g\left(\frac{48M_s+15M_t}{40L}\right)\right]q(t) = F(t) \tag{5.5}$$

$$\boldsymbol{\varepsilon_{xx} = yv'' = y\psi''(x)q(t) = y\left(\frac{3}{L^2} - \frac{6x}{2L^3}\right)q(t)} \tag{5.6}$$

where:

$\boldsymbol{v(x,t)} =$ Lateral displacement as a function of space and time

$\boldsymbol{\psi(x)} =$ Shape function

$\boldsymbol{q(t)} =$ Time function

$\boldsymbol{M_t} =$ Mass of the support post, 48 $\frac{lb}{ft}$

$\boldsymbol{M_s} =$ Mass of the sign, 1414 lb.

$\boldsymbol{w} =$ Width of sign, 14.85 ft.

$\boldsymbol{h} =$ Height of sign, 6.64 ft.

$\boldsymbol{L} =$ Length of post, from base plate to the bottom of the sign, 9.29 ft.

$\boldsymbol{c} =$ Damping coefficient, assumed 2% damping

$\boldsymbol{E} =$ Elastic modules of steel post, 29000 ksi

$I =$ Moment of inertia in the strong axis for W8x24 post, 82.7 in^4

$g =$ Gravity constant, 32.17 ft/s^2

$F(t) =$ Forcing function due to wind loading

$\varepsilon_{xx} =$ Longitudinal strain on the flange of the support post

$y =$ Distance from centroid of I-Section to exterior flange edge, 3.96 in

The response history results of the strain computed using the analytical dynamic model could not be directly compared to the measured strains without first removing the transient response of the model and then adjusting both the measured data and the predicted strains such that they had the same initial strain. The results of the dynamic model were dependent upon the initial conditions applied to the model, but because the wind loading before the wind event began was unknown, it was not possible to apply the same initial conditions observed in the field to the model. Instead, the transient response of the dynamic model, approximately the first 10 seconds of the simulation, was removed from both the simulated strain history and the measured strain history such that the effects of the initial conditions would be negligible in the strain results. The measured strains and predicted strains were then compared by adjusting the initial value of the data sets such that the first point of each response history was set to zero after the initial condition effect had been eliminated. Adjusting the zero-value of the data sets removed the effects of temperature change and prior wind loading from the magnitude of the measured data so that the fluctuation in the measured strains could be compared directly with the fluctuation in strains predicted by the simple dynamic model.

Figure 5.12 displays the response history of the measured and predicted strains for Wind Event 11/09 at 0553. The strains predicted by the dynamic model include the $\pm 3\mu\varepsilon$ error expected in the measured strains. The strains predicted by the dynamic model observe trends very similar to those seen in the measured strains. Measured strains are within $\pm 3\mu\varepsilon$ of the dynamic prediction for the east post. The measured strains are very close to the strains predicted by the dynamic model in the west post, but some measured strains exceed the error bars on the dynamic prediction. The small misalignment between the measured and predicted dynamic strains in the west post is likely due to the dynamic model assuming two posts of equal length.

The measured strain distribution previously shown in Figure 5.10 was compared to the strain distribution predicted by the dynamic model in Figure 5.13. As seen in Figure 5.13, the strain distribution predicted by the dynamic model (pink) aligns much better with the measured strains (green and red) than those strains predicted via the static model (black). Based on the improved fit of the strains predicted by the dynamic model, it was determined that a dynamic FEM model was needed to accurately simulate the strains in the DMS support structure.

5.1.3 Implications of Dynamic Model

The improved fit of the strains predicted by the simple dynamic model over those predicted by the static model had important implications for the analysis of the DMS. First, considering the effects of the inertia was important in the development of the response of the structure. Without considering the inertia, i.e., the static model, the strains predicted did not align well with the measured data. The large mass of the DMS compared to signs typically placed on the Type A support structure was a key concern for this research, and the improved fit of the strains predicted by the simple analytical dynamic model implied that the mass of the DMS had a significant role on the response of the structure. In the case presented here, the improved fit of the strains predicted by the simple analytical dynamic model implied that the mass of the DMS was beneficial in reducing the response in the DMS. It should be emphasized that this is not always true. The effects of the mass on the field DMS and other variations of the DMS in service is explored further in Chapter 6.

Although the strains predicted by the dynamic model were smaller than those estimated by the static model, it did not imply that fatigue was a non-concern in the DMS. Strains within the friction fuse connection evaluated under different wind loading conditions may still correspond to fatigue stresses beyond the fatigue stress limit. The response of the DMS structure under different wind loading conditions was explored in Chapter 6. In addition, the dynamic amplification of the strains needed to be considered. Wind loading near the natural frequency of the sign could result in resonance and increased stresses in the support structure. Future simulations done with the validated FEM model, see Chapter 6, were consequently done at a sampling rate large enough to capture any potential amplification of the stresses due to resonance.

Utilizing a dynamic FEM model also required the use of dynamic wind loading functions as inputs to the model. A static wind speed and corresponding static pressure could not be used to accurately simulate the wind loading on the model. Instead, pressure functions were developed directly from wind loading events measured in the field, as well as through appropriate wind spectrum. Wind loading events measured in the field were used to validate the FEM model. Wind spectrum were used to generate random wind speed histories possible within the state of Minnesota to evaluate the fatigue stress range in the friction fuse connection.

5.2 NUMERICAL MODEL VALIDATION

The FEM model of the sign structure was developed to evaluate the fatigue stress generated in the DMS friction fuse connection during wind loading. Abaqus© (version 6.13) was used to create the structural model of the DMS and Type A structural support system shown in Figure 5.14. Three main components made up the model; the friction fuse connection, the support posts, and the sign panel. The friction fuse connection was modeled as a separate detailed three-dimensional component because the friction fuse connection, specifically the fuse plate, was most likely to feature stress concentrations of interest to evaluate potential fatigue issues. The support posts were modeled using standard Hermite beam elements and the panel was modeled using standard four-node shell elements. The sign was assumed to act as a rigid plate. Constraints were applied between each of the components to ensure the posts and

sign acted together under loading. A coupling constraint was used to tie displacements between the post and the panel together. The model was linear elastic, and all structural components were modeled using ASTM A36 steel. A damping ratio of 2% was assumed for all dynamic analyses with the model.

The three-dimensional friction fuse connection model was run separately from the overall structural model to reduce computational costs. Stresses in the friction fuse connection were simulated by applying tractions over the inner surface of the plates in contact with the post. These tractions simulated the friction forces in the connection and were produced using the moment and shear generated in the main structural model at the connection location. There was a visible gap between the two post segments spliced by the friction fuse connection. Consequently, all axial and shear load was transferred through the connection by the two plates alone. Bending in the plates due to the eccentric loading was prevented by displacement constraints that prevented the plates from pulling away from the post. The stress distribution within the friction fuse plate for a unit traction is shown in Figure 5.15 for a moment acting about the strong-axis of the post and in Figure 5.16 for a moment acting about the weak axis of the post. Note that in both Figure 5.15 and Figure 5.16 the tractions were not applied over the center strip of the plate where the splice between the two posts would be.

5.2.1 Comparison with Field Data

The FEM model of the DMS was validated using the data collected in the field. The accelerometer data were used to compute the frequency response of the structure. Natural frequencies and mode shapes predicted by the FEM model are given in Figure 5.17. The first natural frequency of the field DMS was found to vary from 3 Hz to 4 Hz. Figure 5.18 illustrates the variation in the first and second natural frequencies of the structure with changing air temperature. Based on the trends observed in Figure 5.18, it was hypothesized that the natural frequency of the sign increased with colder temperatures and decreased with warmer temperatures. During colder temperatures the ground was assumed to freeze, resulting in a stiffer connection at the base and an increased first natural frequency. The fluctuations in the natural frequencies implied that the connection at the base of the DMS support structure was brought closer to a fixed condition when the ground froze.

The variation in the fixity of the base connection with temperature was not possible to capture with the FEM model with one consistent post height. To utilize a fixed condition at the base of the support posts of the FEM model, the posts needed to be elongated to achieve the flexibility of the base connection observed in the field DMS. The model was adjusted such that the first natural frequency was approximately 3.2 Hz. A first natural frequency of 3.2 Hz was chosen because it was close to the natural frequency observed when the ground was not frozen, which was true for most of the critical wind events analyzed, specifically those recorded earlier when the FEM model was being developed. The wind also has a lower frequency content, so utilizing the lower natural frequency of the structure was a conservative approach. Length was added through an iterative process until the desired first natural frequency was achieved. A natural frequency of 3.2 Hz was achieved in the FEM model by adding an additional 3 ft. of length to each post, beyond the length of the post measured aboveground in the field. The support posts of the DMS were embedded approximately 12 ft. into the ground (Kimley Horn, MnDOT, 2015), so it was thought that the added 3 ft. of length was a reasonable approach to simulating

the dynamic response of the field DMS with a fixed base in the model. Note that all previous models in Section 5.1.2 were done with the length of the posts measured aboveground. Only, the FEM post length was extended to reflect the flexibility of the base connection observed in the field.

Strains from the FEM analysis and measured field data were compared for multiple wind events. The results of the comparison for Wind Event 11/09 at 0553 are shown in Figure 5.19 through Figure 5.25. Note that during the temperature conditions under which Wind Event 11/09 at 0553 occurred, the field DMS had a predominant first frequency of 3.3 Hz, which aligned closely with the first natural frequency of the model. Strains in the FEM model were produced using pressure history functions computed from the normal component of the wind speed data for each critical wind event. All pressure functions and strains generated in the FEM model had a sampling rate of 1 Hz because wind loading from the field was not known at a faster sampling rate. To properly compare the FEM strains to the measured strains, both sets of strains were scaled and approximately the first 50 seconds of the simulation was removed such that impact of the initial conditions in both systems would be negligible. Adjustments to the zero-value were done as previously described in Section 5.1.2 with the simple dynamic analytical model. Note that strains in the FEM model were sampled at a single point that aligned with the center of the strain gage instead of averaged over the area the strain gage covered. Consequently, strains sampled from the FEM model could be more extreme than those measured in the field. This was appropriate for evaluating the fatigue life and was considered sufficient for validation. The FEM strains are shown with $\pm 3\mu\varepsilon$ error bounds. These error bounds reflect the resolution of the measured field strains based on the noise levels observed in the coupons.

The measured strains at the base of the support posts are compared to the strains from the FEM model in Figure 5.19 through Figure 5.22. The measured strains aligned well with the strains from the model and are generally within the $\pm 3\mu\varepsilon$ error bounds. The measured strains of the east post, north center flange shown in Figure 5.21 just exceeded the error bounds relative to the FEM strains. This was hypothesized to be because of the conduit located on this portion of the support post. The conduit forced the relocation of the gage slightly off the center of the I-section and onto the inner face of the flange. Because the conduit was not modeled, potential damping effects may be present that were not considered in the model. Overall it was found that the FEM model adequately aligned with the strains measured at the base of the supports for primarily normal loading.

Figure 5.23 through Figure 5.26 compare the strains measured in the friction fuse connection with those obtained from the FEM model at the same location. Although multiple strain gages were placed on the friction fuse and hinge plates in the field, only a few gages recorded strains related to the mechanical response of the structure. Many gages measured only noise, with trends like those seen in the coupons not located on the structure. The reason for this discrepancy is not known. One hypothesis is that the grinding performed during the installation of the gages may have reduced the quality of the bond between the gage in the plate surface. These gages were ignored in the validation of the friction fuse connection.

Figure 5.23, Figure 5.25, and Figure 5.26 show good correlation between the measured strains and the strains obtained from the FEM model. The measured strains in Figure 5.23 and Figure 5.25 were very

small, and well within the noise of the gages. However, the trends and magnitude observed in the measured and simulated strains were very similar. The measured strains in Figure 5.26 exceeded the expected noise of the gage and aligned well with the strains from the FEM model. Figure 5.24 does not exhibit strains of the same magnitude as those of the FEM model. The general trend in the FEM strains did, however, feature some of the characteristics of the measured strains. As seen in Figure 4.2, the gage associated with the measured data shown in Figure 5.24 (west post) was located on the friction fuse slightly higher than the gage associated with the measured data shown in Figure 5.26 (east post). Based on the stress distribution in the fuse plate shown in Figure 5.15, it seems likely that the strain measured by the gage shown in Figure 5.24 (located in the light blue zone in Figure 5.15) would be less than the strain measured by the gage in Figure 5.26 (located in the yellow zone in Figure 5.15). For both Figure 5.24 and Figure 5.26 the strains in the FEM model were sampled from the very center of the plate, which explains the alignment between the FEM model strains and measured strains in Figure 5.24 when the gage was centered and not in Figure 5.26 when the gage was slightly above the center of the plate.

The behavior of the FEM model under tangential loading was verified using field data from a primarily tangential event, Event 11/30 at 0035. Similar to the validation for normal wind loading, strains in the FEM model were produced using pressure history functions computed from the appropriate component of the wind speed data. All pressure functions and strains generated in the FEM model had a sampling rate of 1 Hz because wind loading from the field was not known at a faster sampling rate. Both sets of strains were adjusted as described previously in Section 5.1.2 and approximately the first 50 seconds of the simulation were removed such that impact of the initial conditions in both systems would be negligible. The FEM strains are shown with $\pm 3\ \mu\varepsilon$ error bounds. These error bounds reflect the resolution of the measured field strains based on the noise levels observed in the coupons.

Figure 5.27 and Figure 5.28 compare the strains measured at the base of the support with strains obtained from the FEM model when only the tangential component of the pressure for Wind Event 11/30 at 0035 was considered. In both Figure 5.27 and Figure 5.28 the strains measured in the field are significantly larger than those from the FEM analysis. It was hypothesized that the normal component of the pressure controlled the response of the structure because of the surface area of the sign in the normal direction was much larger than that in the tangential direction.

Figure 5.29 and Figure 5.30 compare the strains measured in the field with those obtained from the FEM model when both the tangential and normal component of the wind loading were considered. To do this, tangential and normal loading functions for Wind Event 11/30 at 0035 were applied to the FEM model separately and then the resulting strains in the FEM model were combined in Figure 5.29 and Figure 5.30. Strains measured in the field are much closer to those predicted by the FEM model when the normal component of the wind pressure is considered. This is clearly seen in Figure 5.30 for the base of the east post. Strains measured in the base of the west post, Figure 5.29, are still slightly larger than those predicted by the FEM model. Wind Event 11/30 at 0035 features winds from the west and any shedding occurring around the structure would produce larger strains in the post closest to the oncoming wind (west post) that could not be captured by the FEM model without considering fluid-structure interaction using a computational fluid dynamics (CFD) model. Consequently, it seems logical

that the strains measured at the base of the west post would be slightly larger than those obtained from the FEM model.

Strains in the friction fuse connection of the FEM model were also sampled for combined normal and tangential wind loading. Figure 5.31 through Figure 5.34 compare strains measured in the field at the friction fuse connection with those obtained from the model for combined tangential and normal loading. The alignment between the FEM strains and those measured in the field is quite good for gages located at the center of the fuse plate as seen in Figure 5.32 (recall this gage is not positioned exactly centered on the plate) and Figure 5.34, however the strain measured in gages located at the edge of the plate where tangential loading was thought to control was significantly overestimated by the FEM model as seen in Figure 5.31 and Figure 5.33. Recall, these gages had previously only registered noise when validating the model under primarily normal wind events and they were considered unreliable for direct comparison with the model.

To determine if the normal component of the wind loading did indeed control the analysis, Figure 5.35 and Figure 5.36 (base of posts) and Figure 5.37 to Figure 5.40 (friction fuse plate) compare the field and FEM model strains when only the normal component of the wind loading for Wind Event 11/30 at 0035 was considered. The correlation between the measured strains and those in the FEM model at the base of the support when only normal loading was considered is similar to the correlation when both the tangential and normal component of the wind loading was considered, implying the normal component of the wind loading did control the response. Measured strains and strains produced in the FEM model were much closer in the friction fuse plate when only the normal component of the wind loading was considered. The improvement is clearly seen by contrasting Figure 5.37 and Figure 5.40 with Figure 5.31 and Figure 5.33. The gages compared in these figures, however, were considered unreliable. The true response at the outer edge of the plate is unclear.

Limited field data were available for comparison with the FEM model in the friction fuse connection. One of the two gages on the friction fuse plate was not completely centered on the fuse plate and was consequently not in the location of greatest strain in the fuse plate under normal wind loading. The strains produced in the FEM model aligned well with the strains of the single gage positioned correctly. Through the tangential validation of the FEM model it was found that the normal component of the wind loading controlled the response of the structure. When only the normal component of the tangential wind event was considered, the strains in the FEM model compared reasonably well with the strains measured in the field. Strains in the FEM model when the tangential component of the pressure was considered overestimate the strains in the friction fuse connection for locations near the edge of the fuse plate. The gages in these locations, however, were considered unreliable. The FEM model was considered validated, based on the strong alignment between the strains in the FEM model and measured strains at the base of the supports as well as the alignment between the available field data at the friction fuse connection and the strains at the friction fuse connection of the FEM model. Future research should work to confirm the strains in the friction fuse connection at the edge of the fuse plate under primarily tangential loading.

All comparisons between the strains in the FEM model with those measured in the field were done at a sampling rate of 1 Hz, which was not sufficient to capture any potential dynamic amplification that could be occurring in the structure. A sampling rate of at least 10 Hz would be needed to capture resonance at the natural frequency of the field DMS. A loading rate at this frequency was not possible due to the limited sampling rate of the anemometer used in the field. Strain data from the field was observed at 1 Hz and at 10 Hz to determine if the amplification of the amplitude of the strains on the support structure at 10 Hz compared to those measured at 1 Hz exceeded the amplification observed for the same sampling rates for the strains on the coupons. If the amplification of the strains measured by the gages on the support structure exceeded those measured by the gages on the coupons, then resonance behavior, and not just amplified noise, was present. It was found that the amplification between strains at 10 Hz and at 1 Hz for gages on the support structure was similar to those gages on the coupons. This implied that the validation for the FEM model done at 1 Hz was suitable for use at larger sampling frequencies.

Resonance behavior due to vortex shedding, or lock-in, was also not considered during the comparison between the strains in the FEM model and those measured in the field. Vortex shedding occurs under specific conditions, generally between 10 and 35 mph, and is highly dependent on the shedding frequency of the structure (Kaczinski, Dexter, & Van Dien, 1998). The Strouhal number (5.7) can be used to estimate the wind velocity under which vortex shedding is likely to occur. Experimental testing done at SAFL was not performed for the DMS, so the shedding frequency and Strouhal number of the DMS were not known. A Strouhal number of 0.2 was considered appropriate for a rectangular panel, and the natural frequency of the DMS was used as an estimate for the shedding frequency (Kaczinski, Dexter, & Van Dien, 1998). The velocity required for lock-in could then be calculated for both tangential and normal loading based on the horizontal length across the sign panel in each direction.

$$S_t = f_s \frac{L_d}{u} = 0.2 \qquad (5.7)$$

where:

$S_t =$ Strouhal number

$f_s =$ Shedding frequency, assumed 3.2 Hz

$L_d =$ Horizontal length across section, in

$u =$ Homogeneous upstream velocity, in/sec

For normal wind loading, the horizontal length was taken as 97.25 in. resulting in a wind velocity of 88.4 mph (39.5 m/s). For tangential wind loading, the horizontal length was taken as 17.75 in. or 25.75 in. resulting in a wind velocity of 16 mph (7.2 m/s) and 23.5 mph (10.5 m/s) respectively. The two different lengths in the tangential direction considered the horizontal length of the sign panel alone (17.75 in.)

and the horizontal length of the sign panel including the extent of the attached support posts (25.75 in.). Wind speeds required to produce lock-in in the normal direction were well beyond the acceptable range for vortex shedding, but required speeds in the tangential direction were within the target range of 10 to 35 mph. The required speeds in the tangential direction were also within the typical wind speed range exhibited in the field. Consequently, although lock-in has not previously been a problem for structures with attached signs (Garlich & Thorkildsen, 2005), lock-in could be a plausible cause for wind-induced vibrations in the DMS for wind in the tangential direction. Further research is needed to understand the impact of vortex shedding on the response of the DMS. Experimental work at SAFL is recommended. Analysis done in this project was done neglecting the effects of vortex shedding because the FEM model utilized could not account for the effects of fluid-structure interaction, and a computational fluid dynamics (CFD) model was not considered in the original scope of the work related to the DMS.

5.3 SUMMARY

The FEM model of the Type A structural support system was validated using data from the field. Based on the analysis of the strains at the base of the support it was determined that a dynamic FEM model would more accurately capture the response of the structure under wind loading than a static model. Consequently, the potential for dynamic amplification of stresses in the structure were considered in future analyses with the dynamic FEM model. Strains obtained from the FEM model near the base of the support post and at the friction fuse connection were compared to strains measured in the field at the same locations. The measured strains and those obtained from the FEM model aligned well when the normal component of the wind loading was considered. The normal component of the wind loading was found to control the response of the structure even under primarily tangential wind events. Several gages in the friction fuse plate gave results that were considered unreliable. The FEM model was considered validated based on the available instrumentation. Future research is needed to verify the behavior of the fuse plate under primarily tangential loading and to investigate the impact of vortex shedding on the response of the DMS.

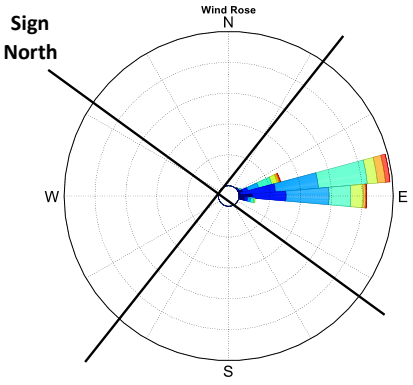

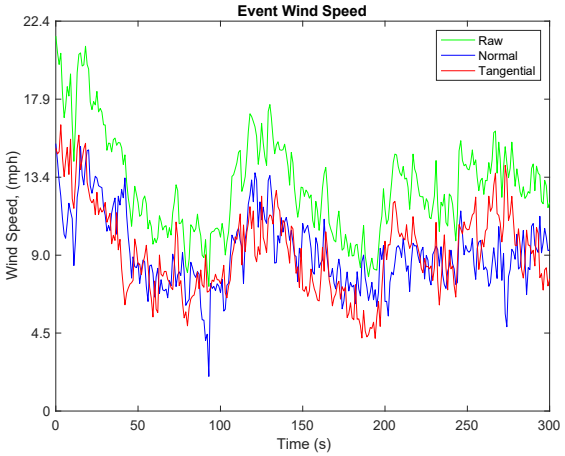

11/01 at 1506

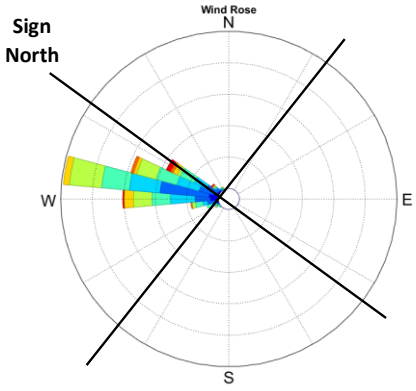

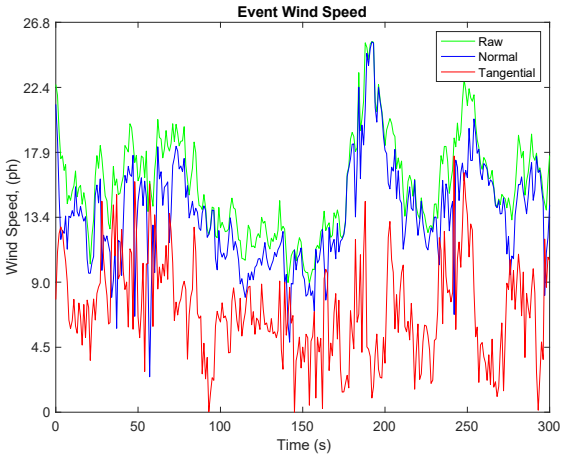

11/09 at 0553

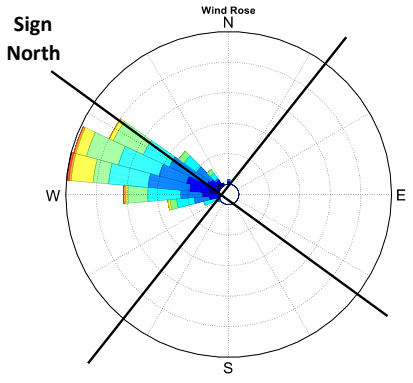

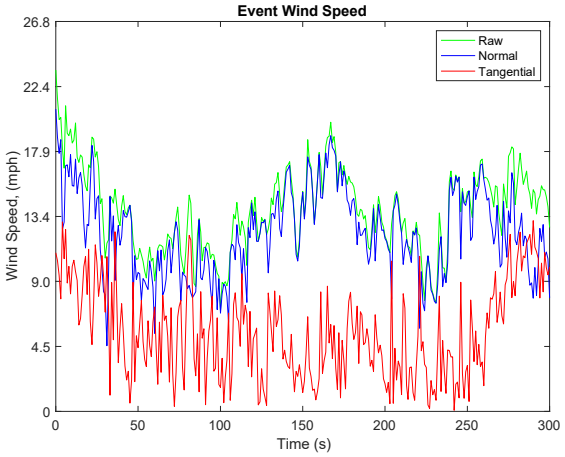

11/09 at 1521

Figure 5.1 – Wind rose and wind speed history for critical wind events 11/01 at 1506 through 11/09 at 1521

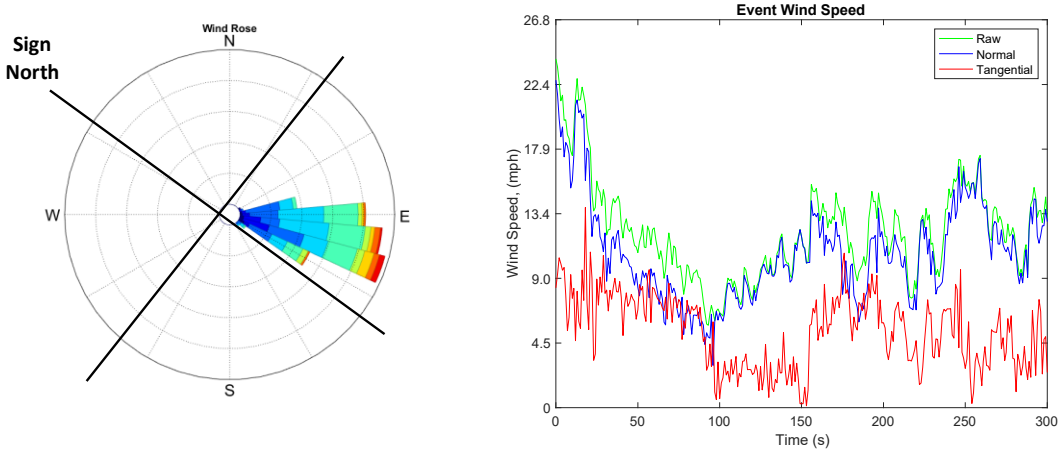

11/10 at 1608

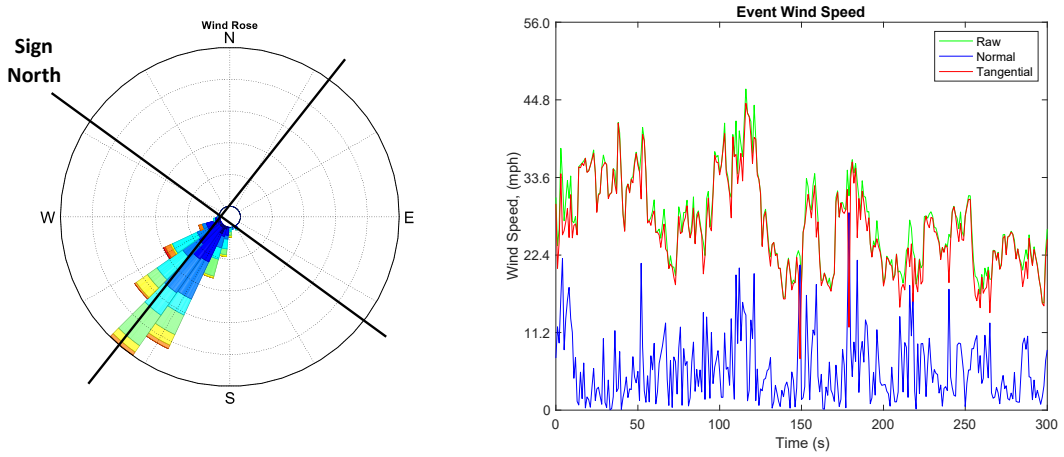

11/30 at 0035

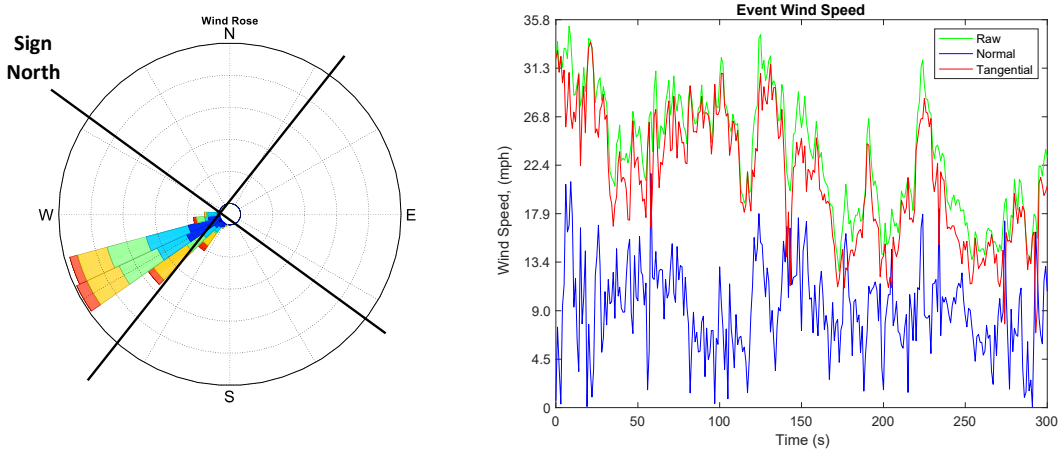

12/04 at 2321

Figure 5.2 – Wind rose and wind speed history for critical wind events 11/10 at 1608 through 12/04 at 2321

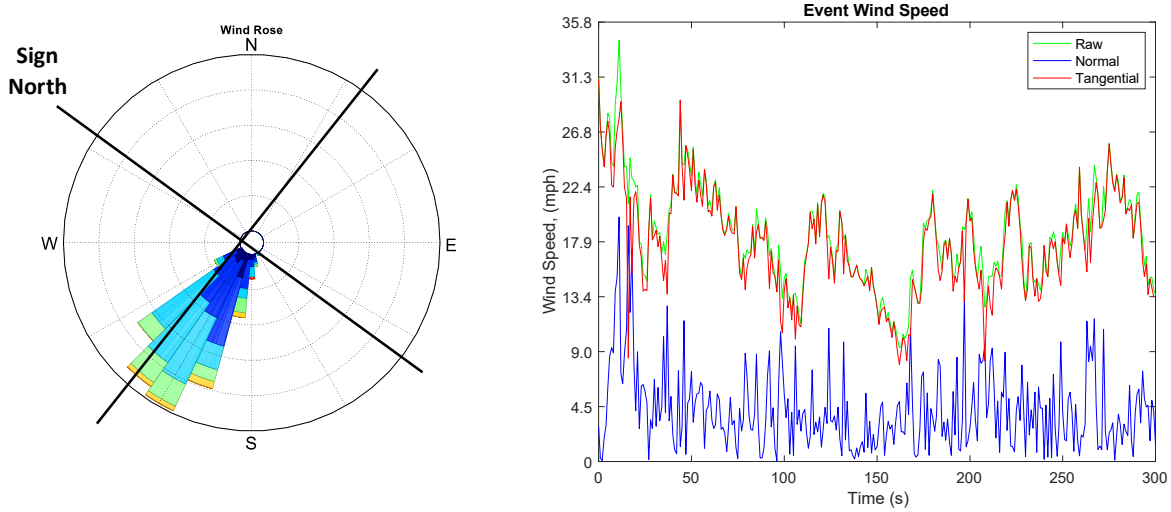

12/05 at 1321

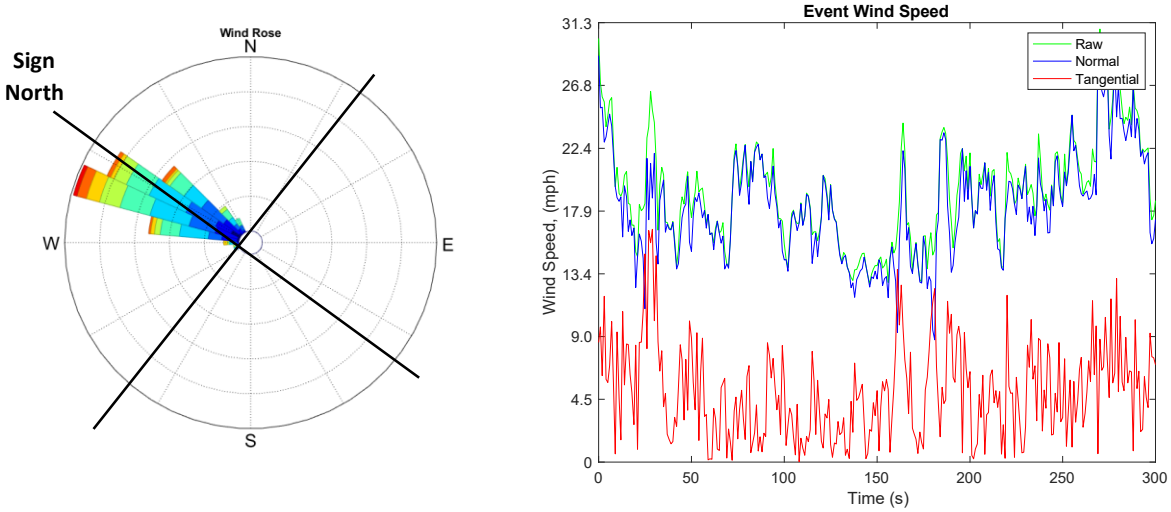

12/13 at 1038

Figure 5.3 – Wind rose and wind speed history for critical wind events 12/05 at 1321 through 12/13 at 1038

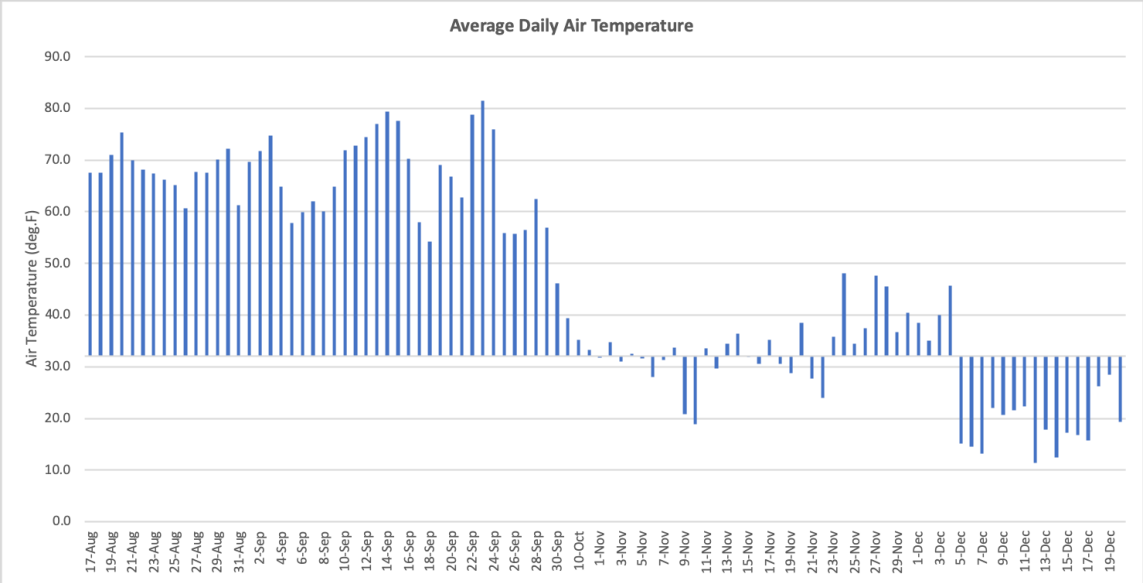

Figure 5.4 – Average daily air temperature throughout data collection period

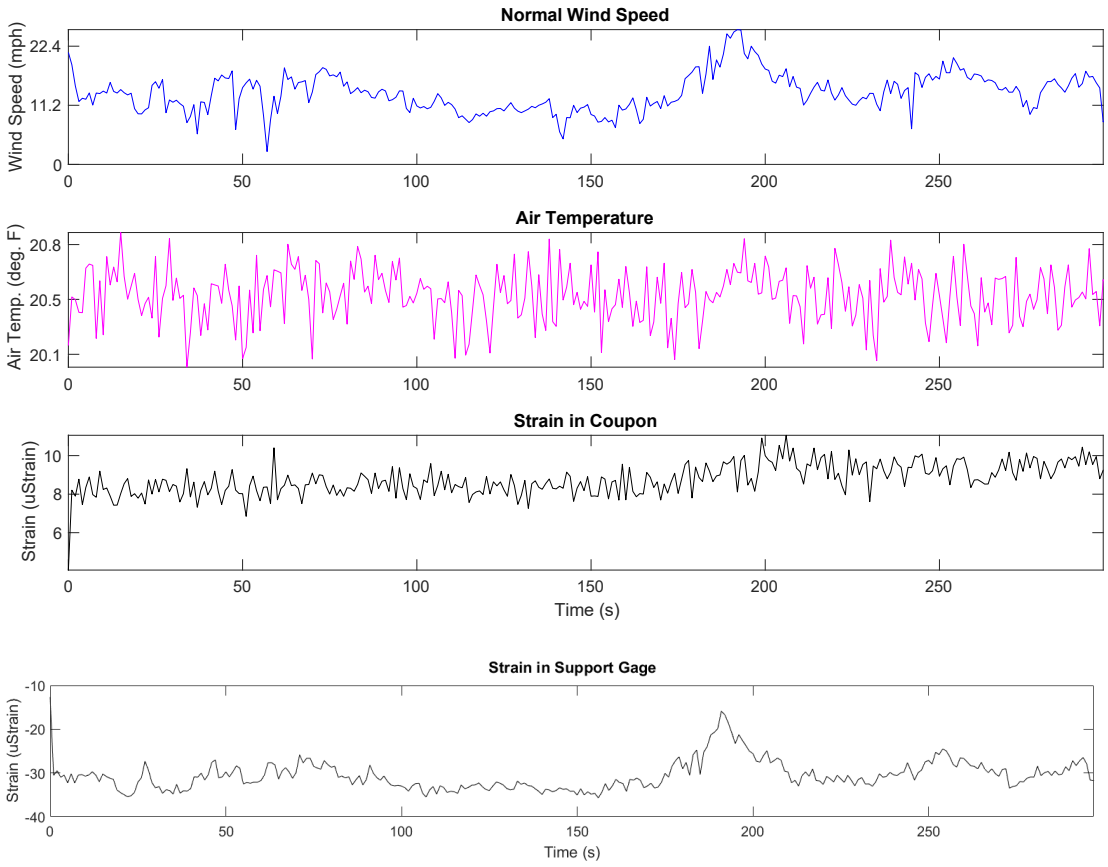

Figure 5.5 – Behavior of support gage and coupon during wind loading (for 11/09 at 0553)

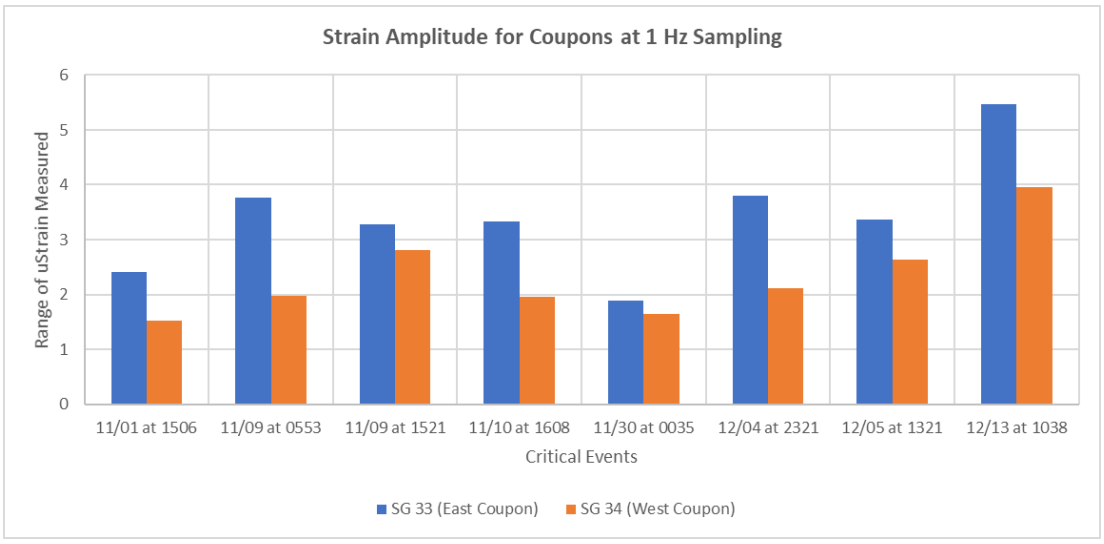

Figure 5.6 – Strain amplitude in coupons at 1 Hz sampling rate for critical events

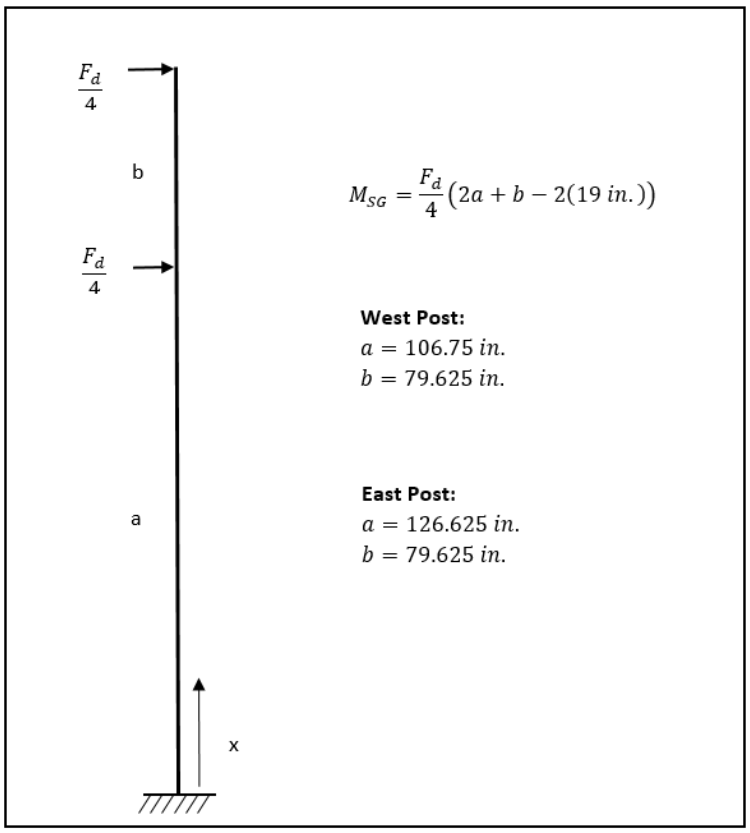

Figure 5.7 – Beam models used to estimate strain in the support posts

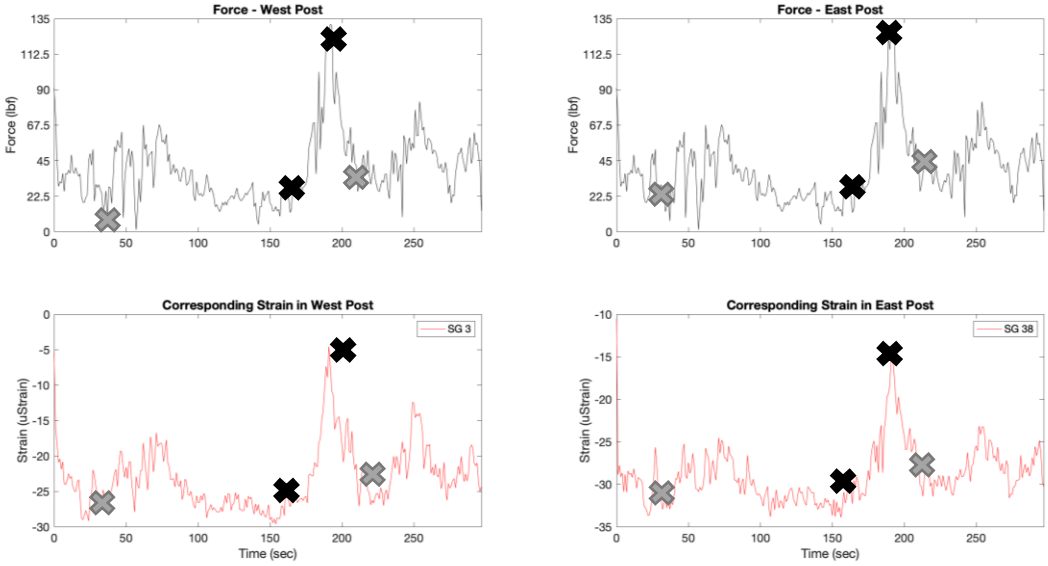

Figure 5.8 – Calculated force in each post compared to measured strain at base of each post (11/09 at 0553)

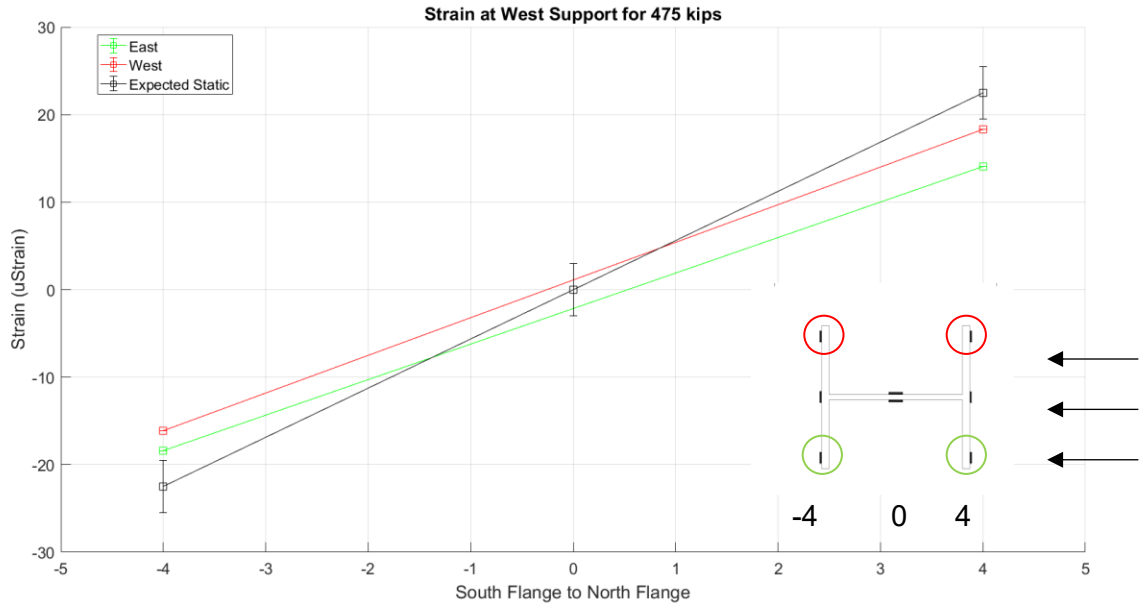

(a) Strain distribution in west support

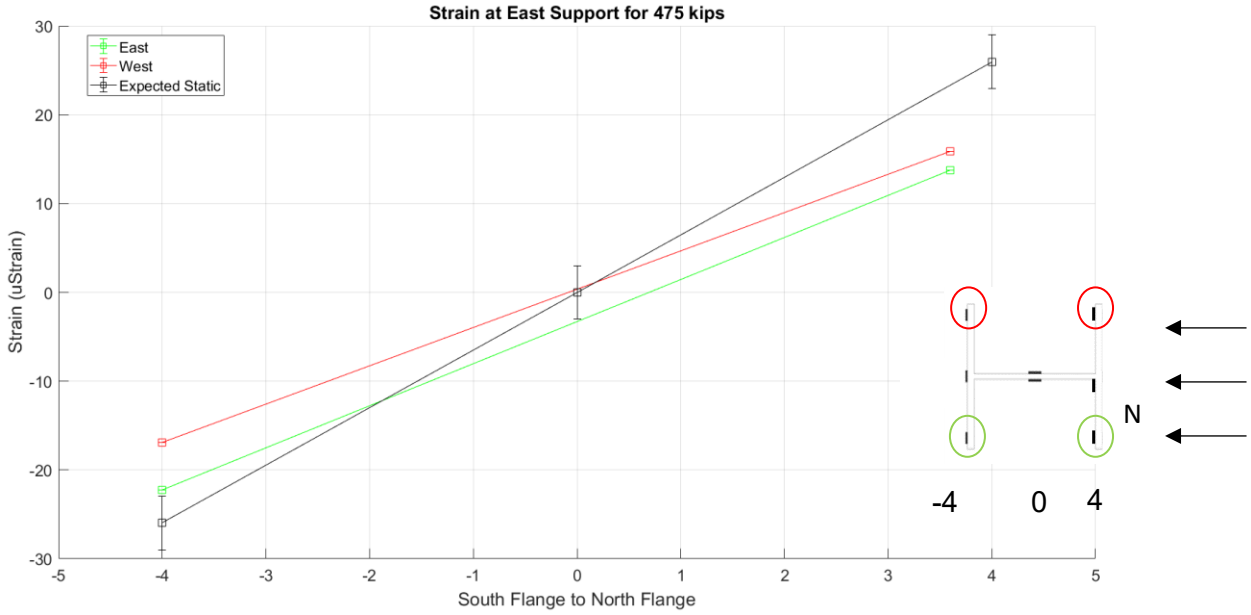

(b) Strain distribution in east support

Figure 5.9 – Strain distribution through I-section for change in force between black markers (Figure 5.8)

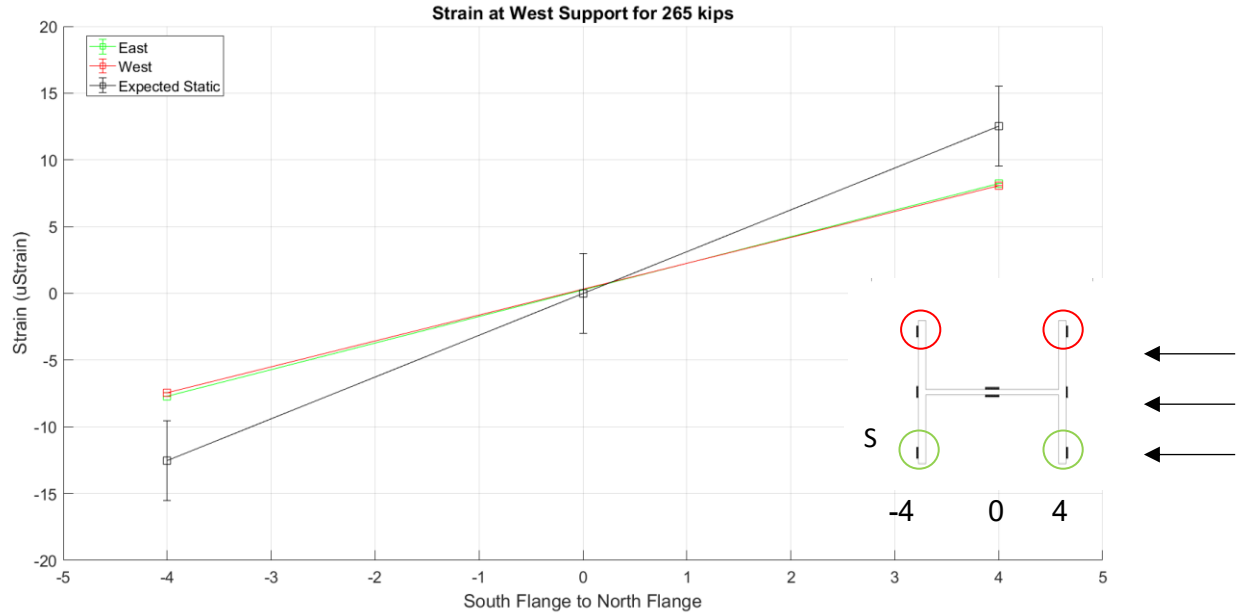

(a) Strain distribution in west support

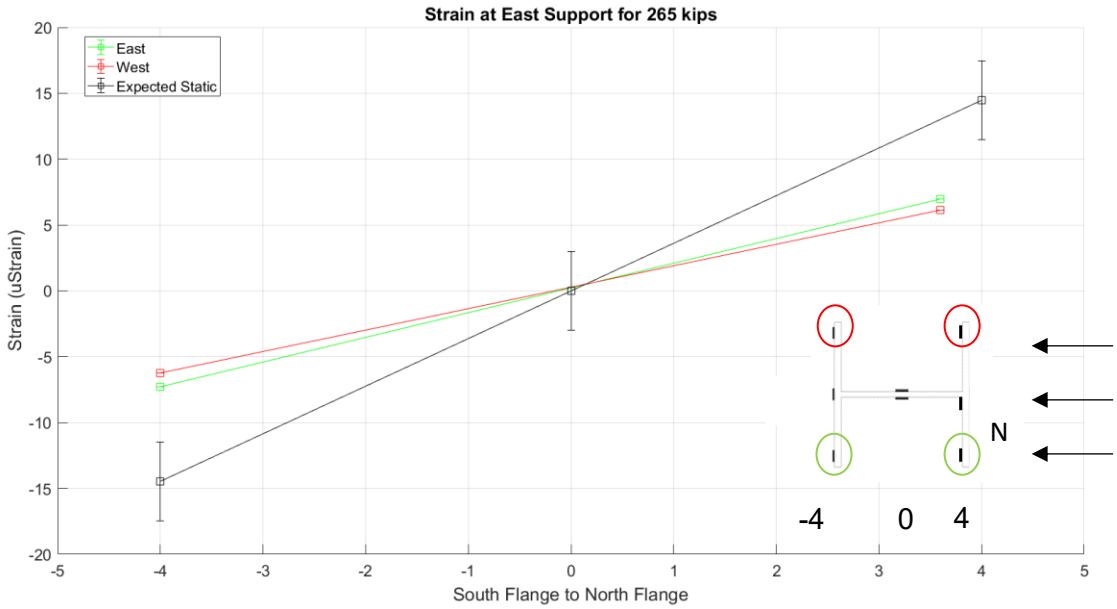

(b) Strain distribution in east support

Figure 5.10 – Strain distribution through I-section for change in force between gray markers (Figure 5.8)

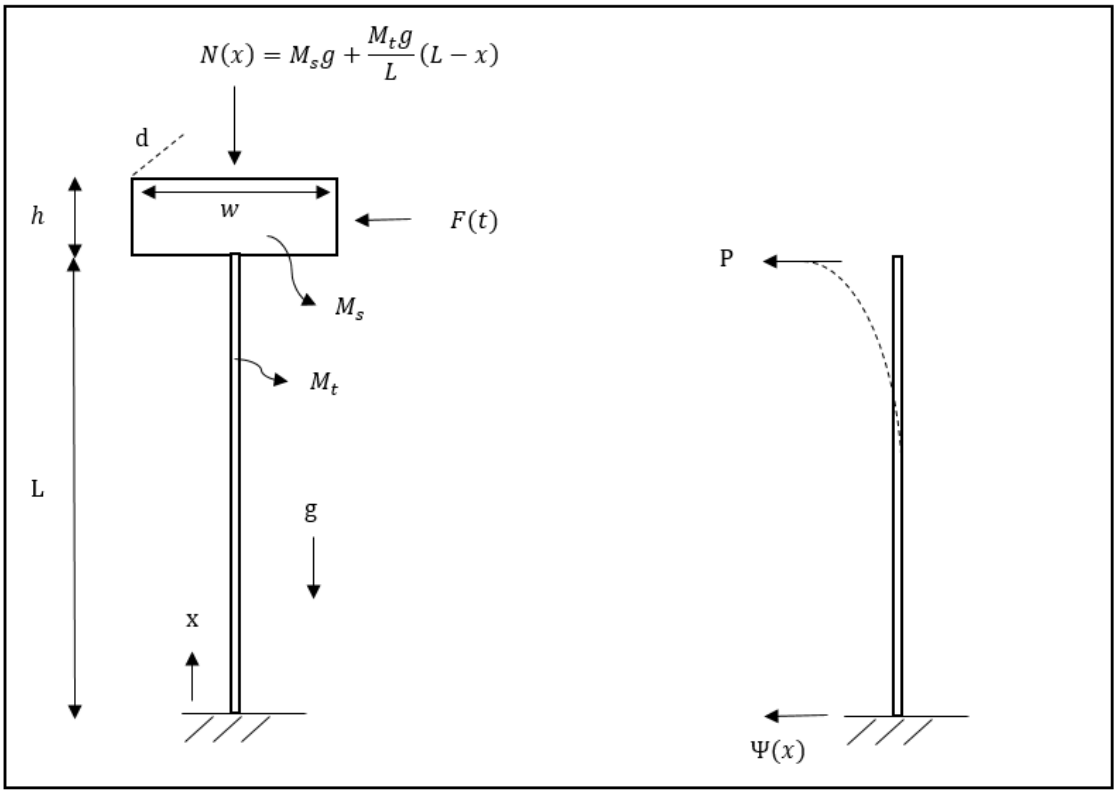

Figure 5.11 – Assumptions for dynamic model

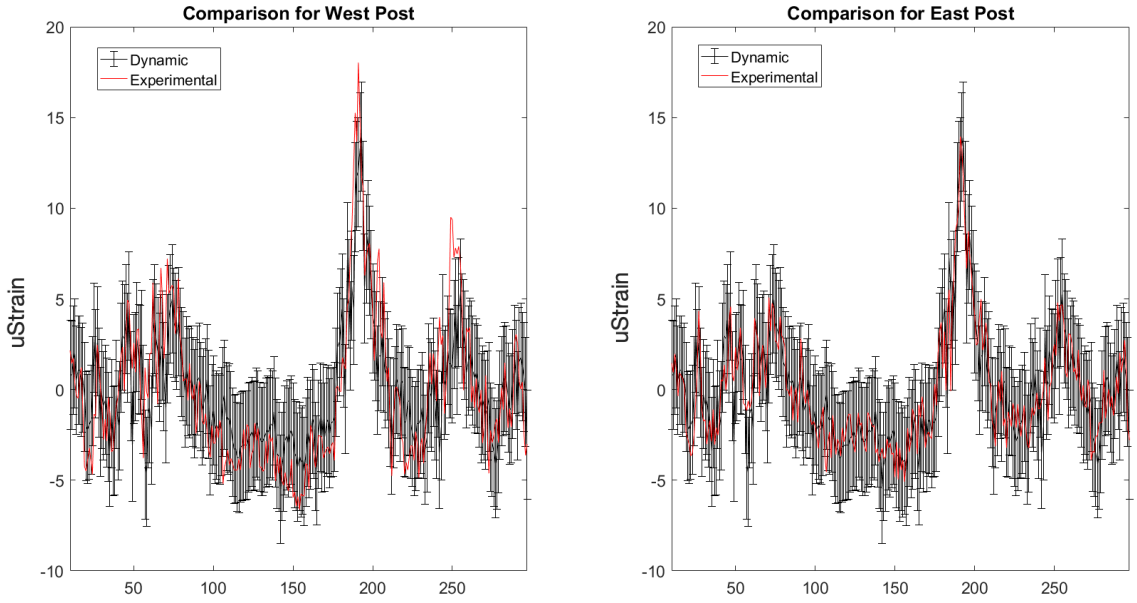

Figure 5.12 – Measured strain compared to predicted strain of dynamic model (11/09 at 0553)

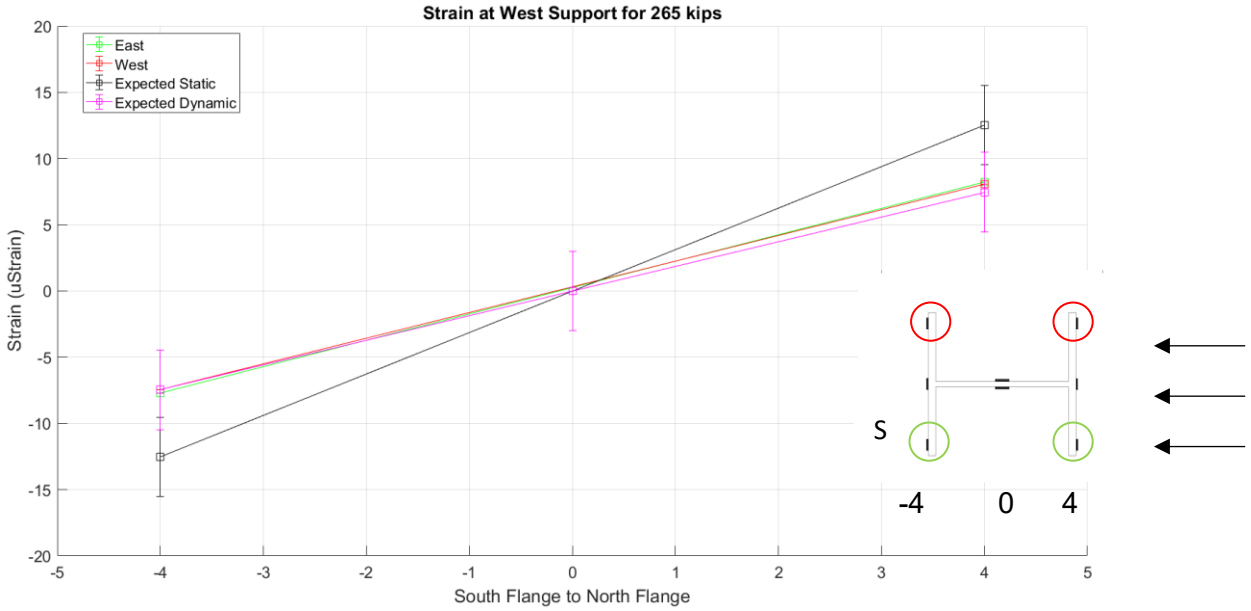

(a) Strain distribution in west support

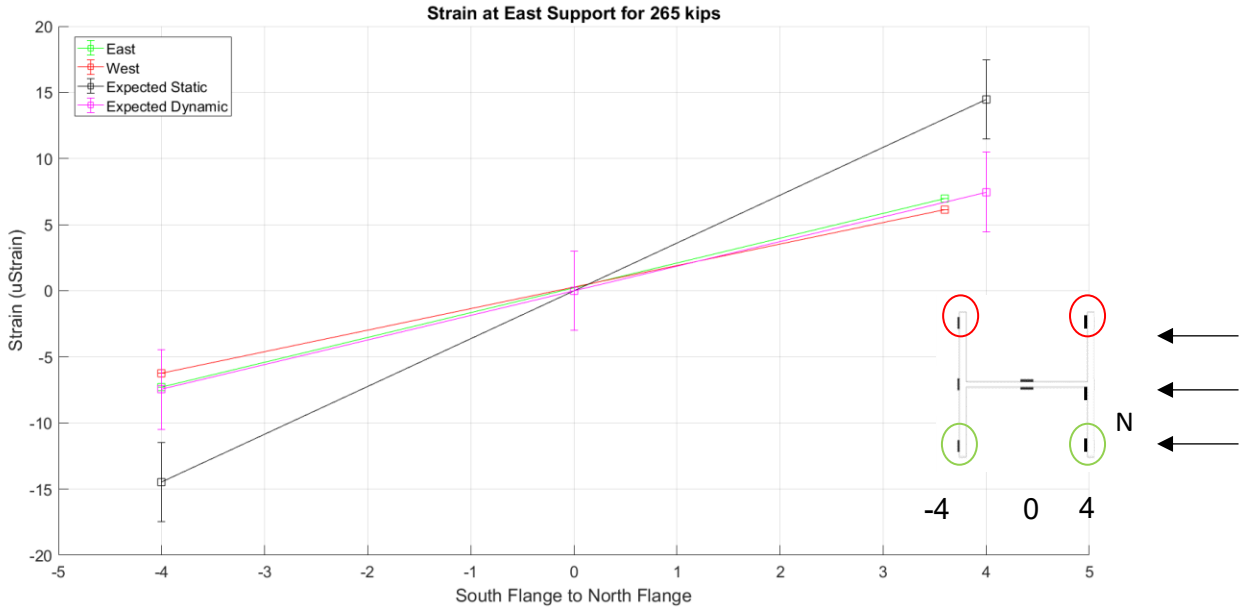

(b) Strain distribution in east support

Figure 5.13 – Updated strain distribution through I-section for change in force between gray markers (Figure 5.8)

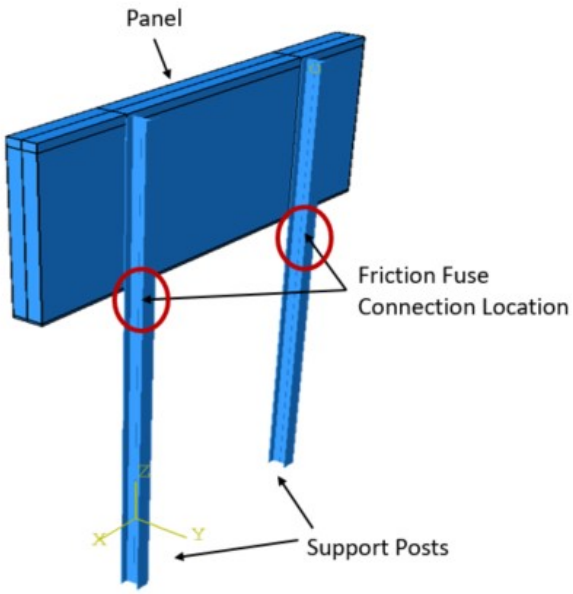

Figure 5.14 – DMS FEM model with friction fuse connection

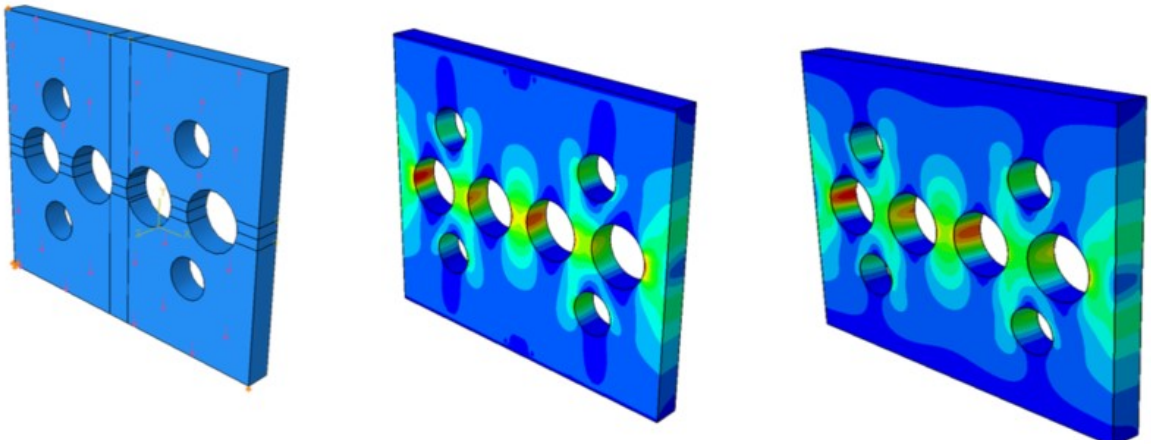

(a) Loading (b) Stress on internal face (c) Stress on external face

Figure 5.15 – Stress distribution in the fuse plate for moment acting about the strong axis of the support post

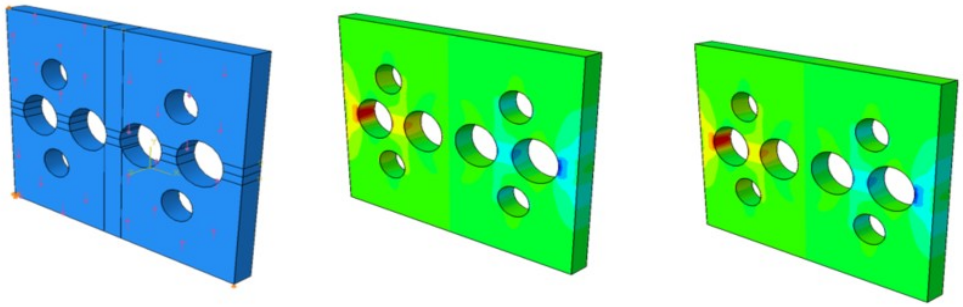

(a) Loading (b) Stress on internal (c) Stress on external face

Figure 5.16 – Stress distribution in the fuse plate for moment acting about the weak axis of support post

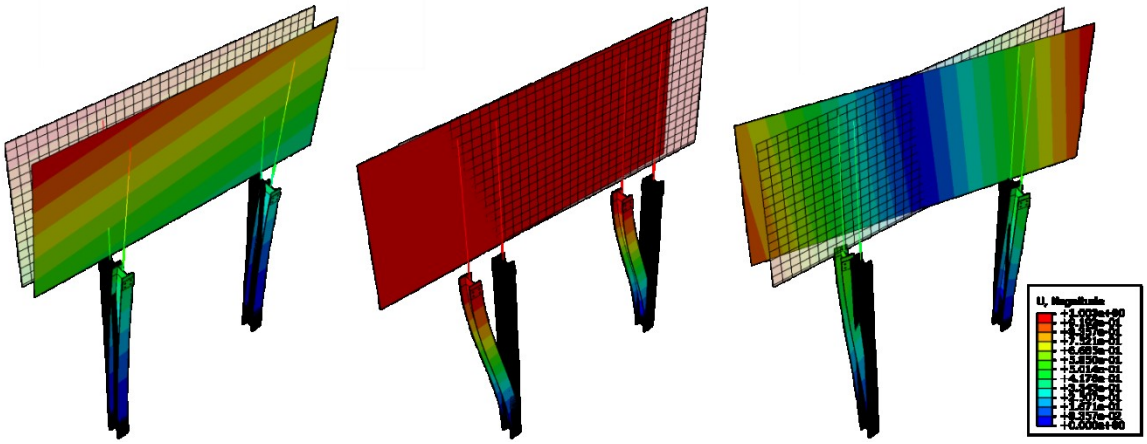

3.2 Hz 4.14 Hz 8.28 Hz

Figure 5.17 – DMS FEM model natural frequencies and mode shapes

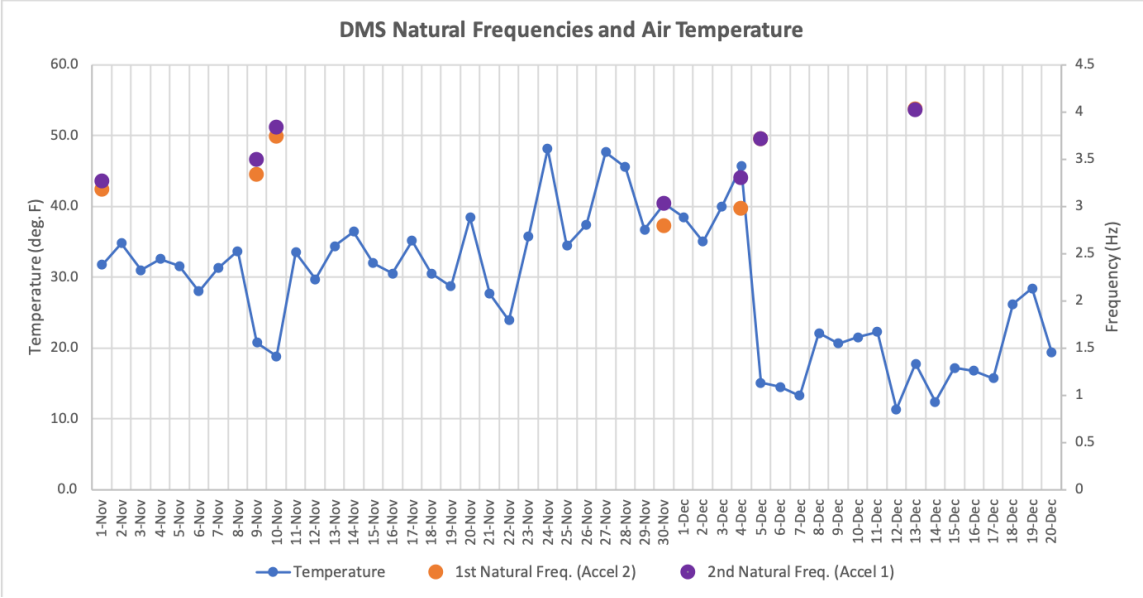

Figure 5.18 – Natural frequency variation with temperature

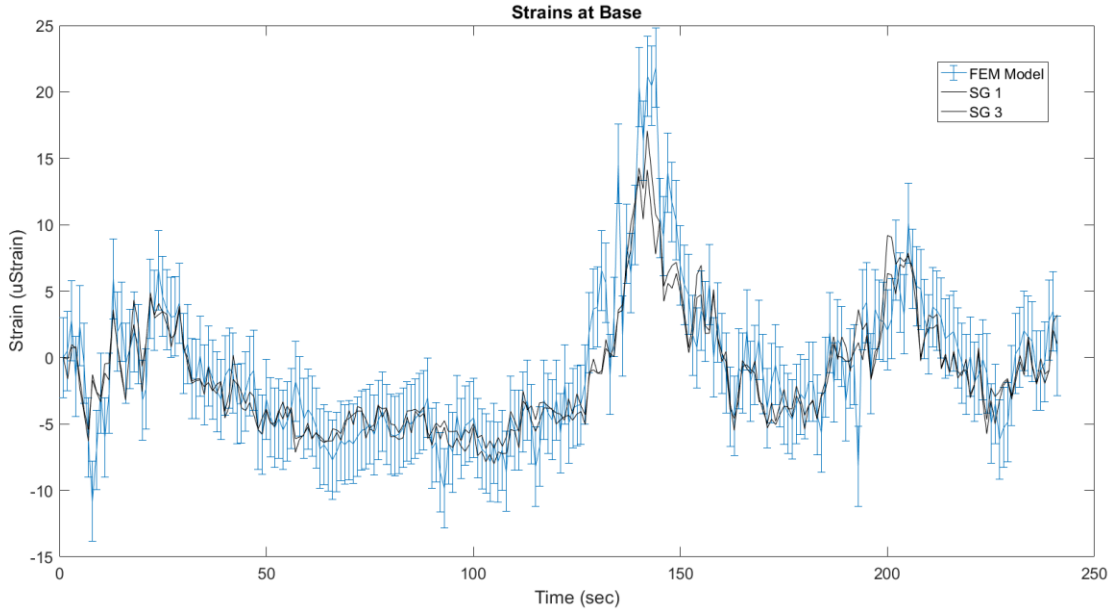

Figure 5.19 – Strains from FEM model and experimental strains in north center flange at base of west support post (11/09 at 0553)

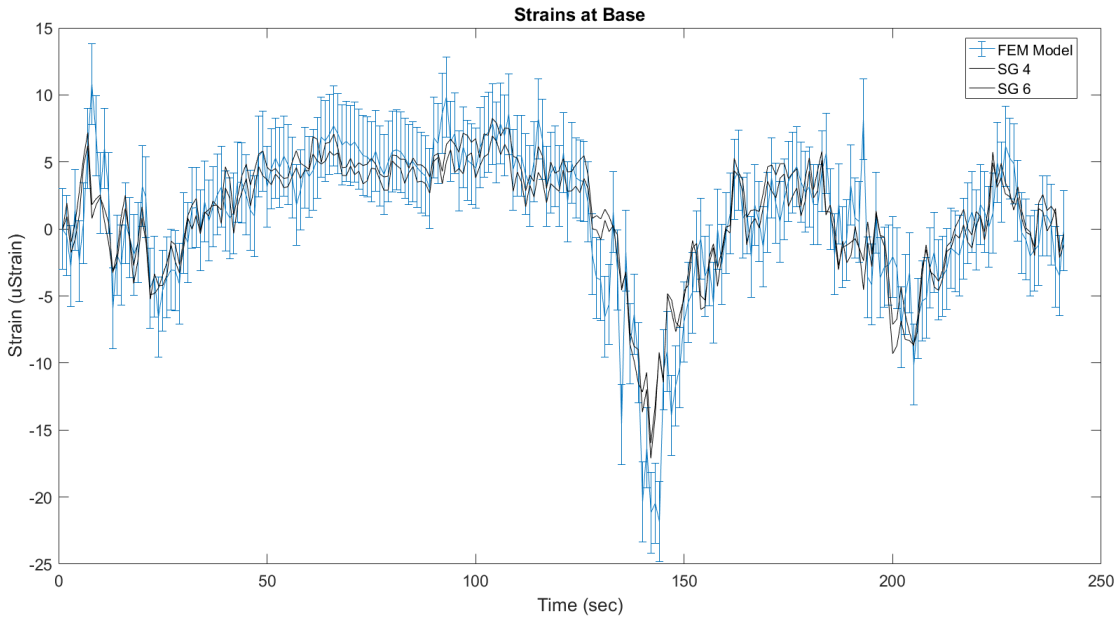

Figure 5.20 – Strains from FEM model and experimental strains in south center flange at base of west support post (11/09 at 0553)

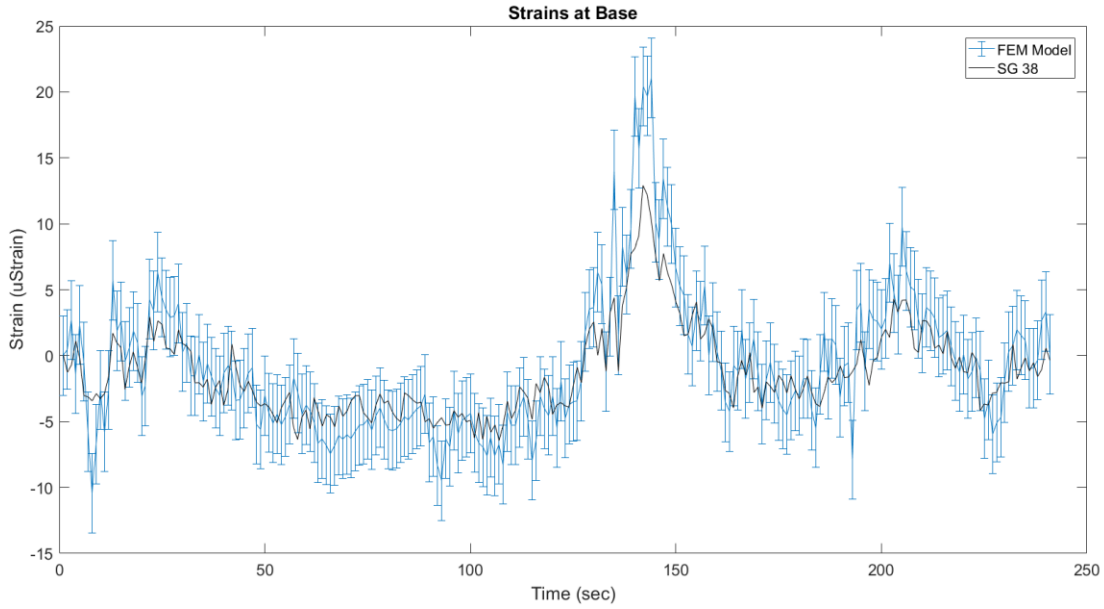

Figure 5.21 – Strains from FEM model and experimental strains in north center flange at base of east support post (11/09 at 0553)

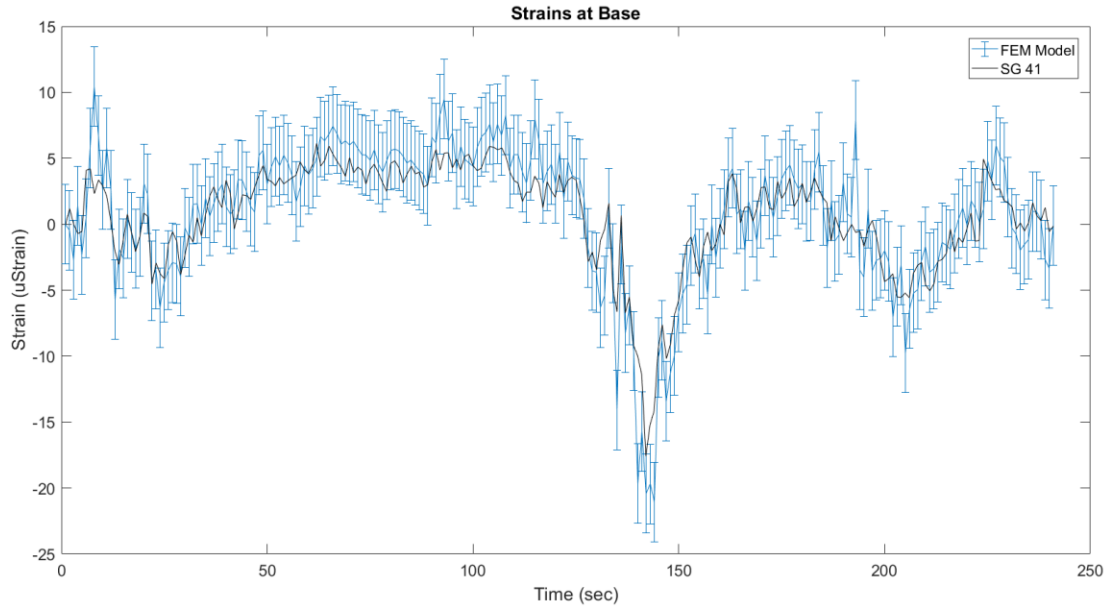

Figure 5.22 – Strains from FEM model and experimental strains in south center flange at base of east support post (11/09 at 0553)

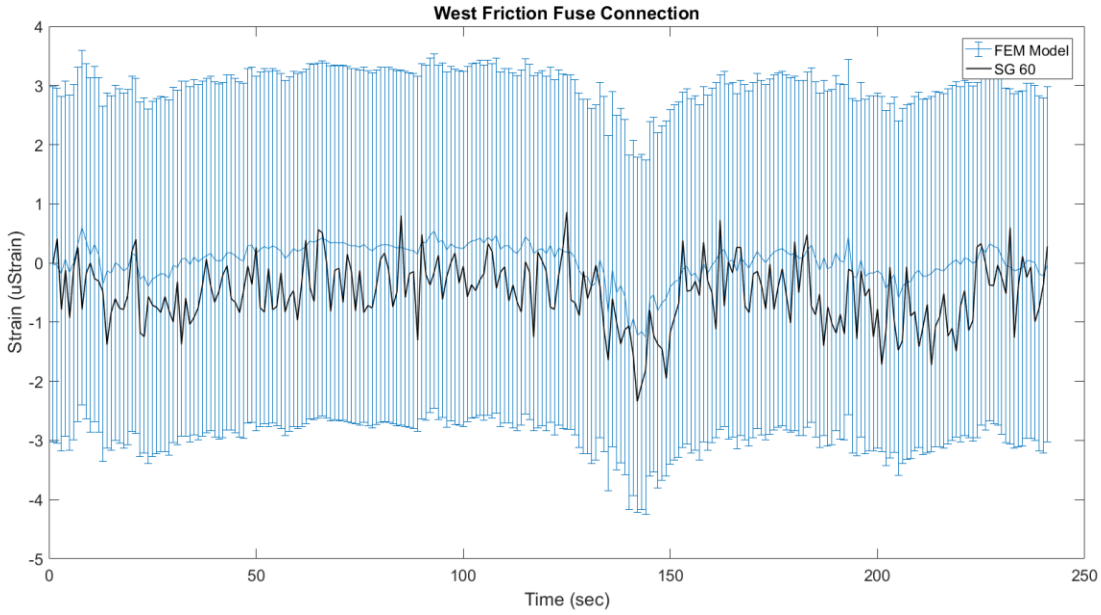

Figure 5.23 – Strains from FEM model and experimental strains in west friction fuse plate, SG 60 (11/09 at 0553)

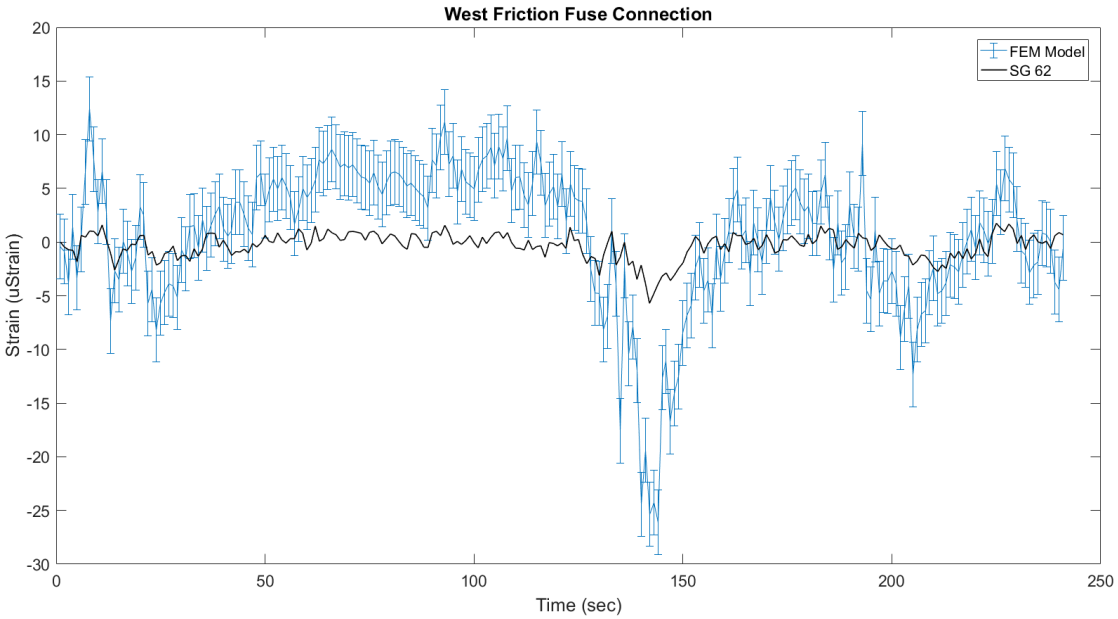

Figure 5.24 – Strains from FEM model and experimental strains in west friction fuse plate, SG 62 (11/09 at 0553)

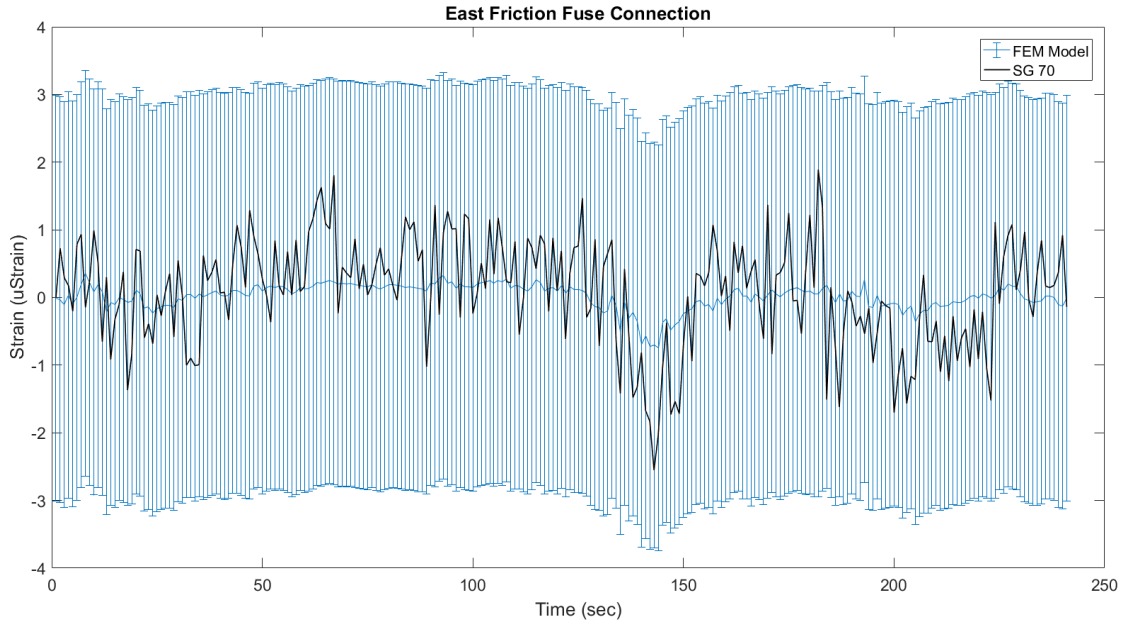

Figure 5.25 – Strains from FEM model and experimental strains in east friction fuse plate, SG 70 (11/09 at 0553)

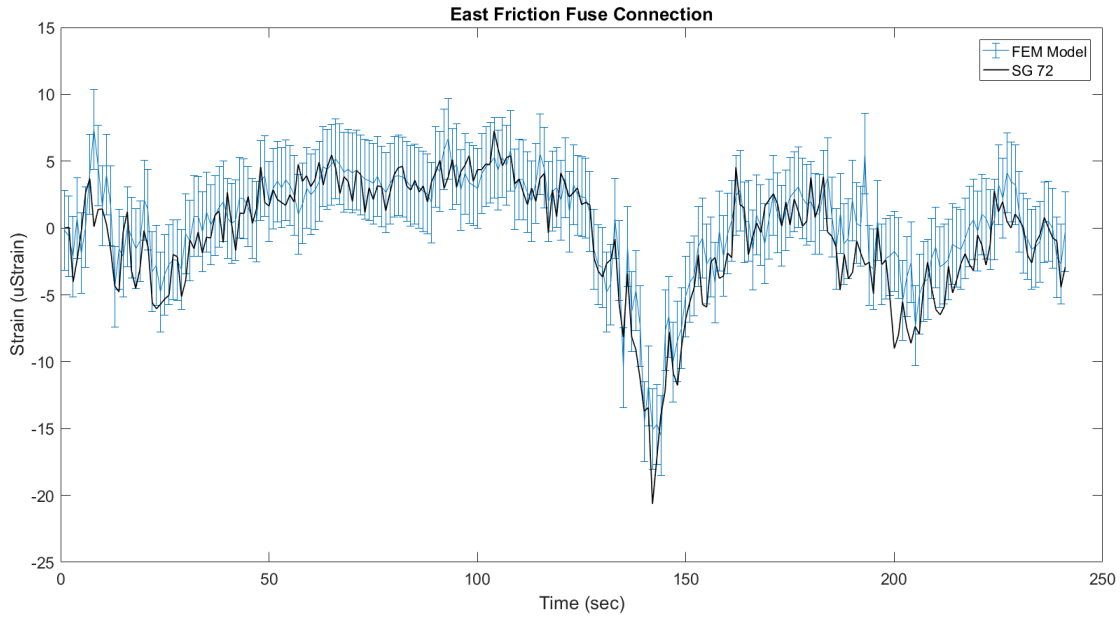

Figure 5.26 – Strains from FEM model and experimental strains in east friction fuse plate, SG 72 (11/09 at 0553)

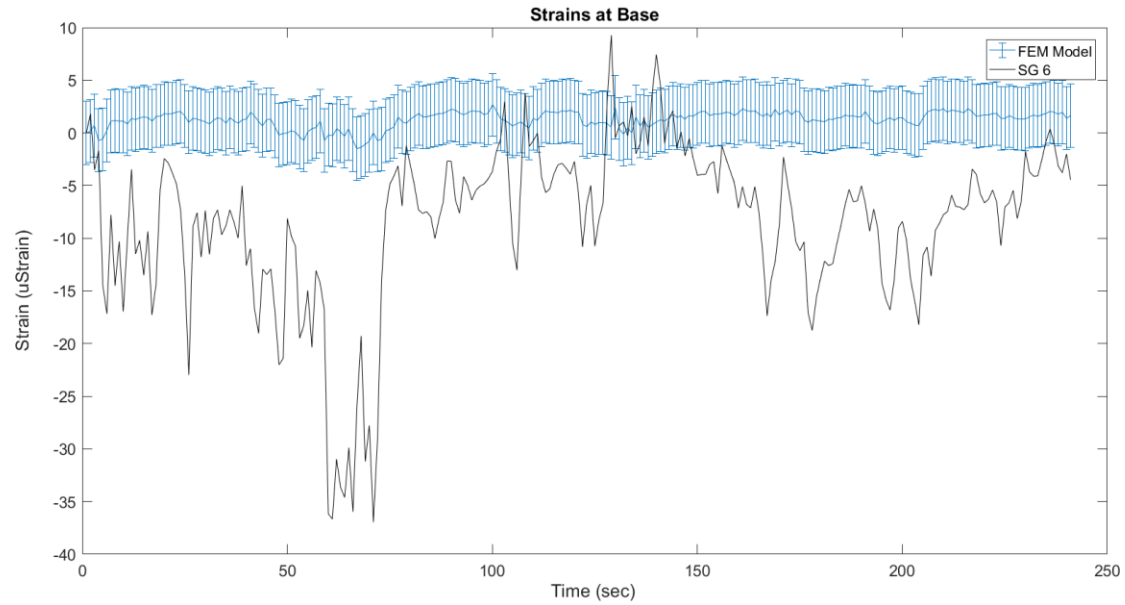

Figure 5.27 – Strains from FEM model in response to only the tangential pressure component and experimental strains in east tip of south flange of west post (11/30 at 0035)

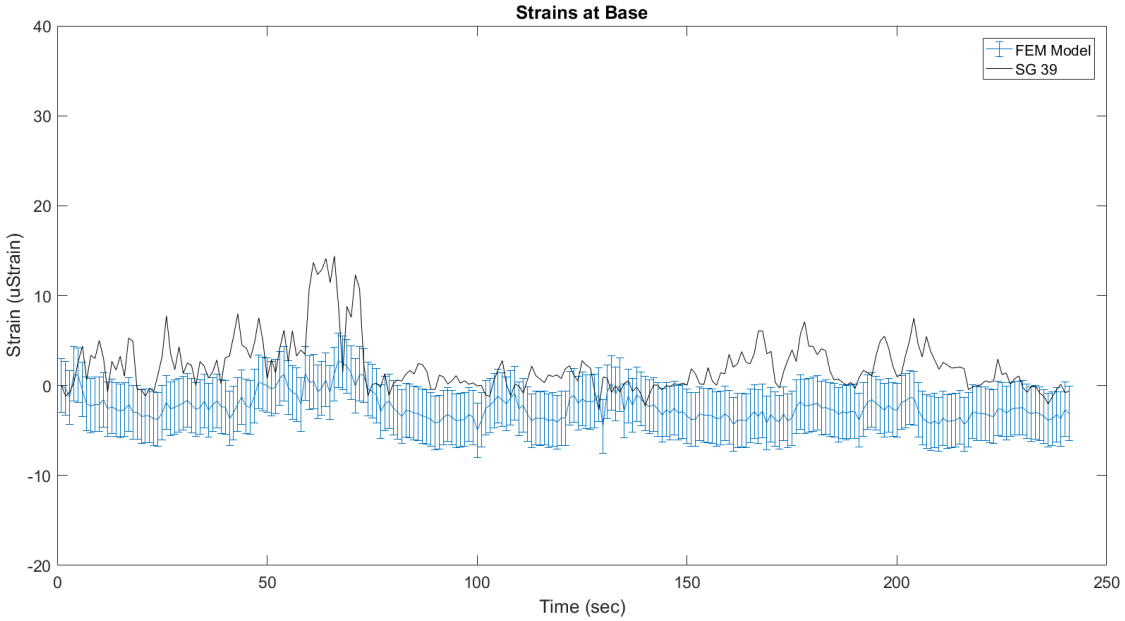

Figure 5.28 – Strains from FEM model in response to only the tangential pressure component and experimental strains in west tip of north flange of east post (11/30 at 0035)

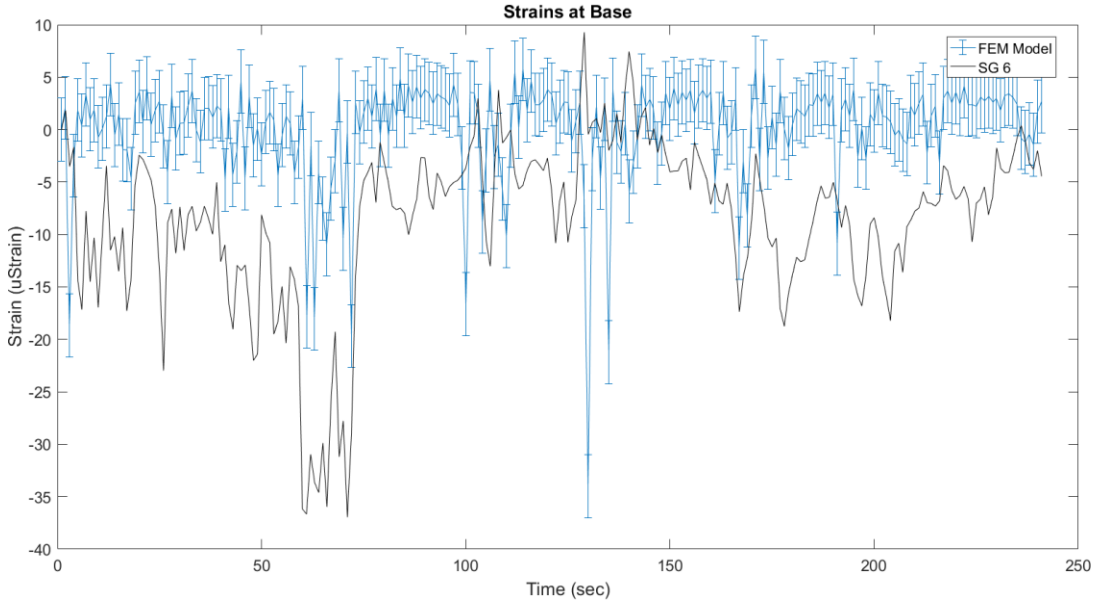

Figure 5.29 – Strains from FEM model in response to the combined tangential and normal pressure components and experimental strains in east tip of south flange of west post (11/30 at 0035)

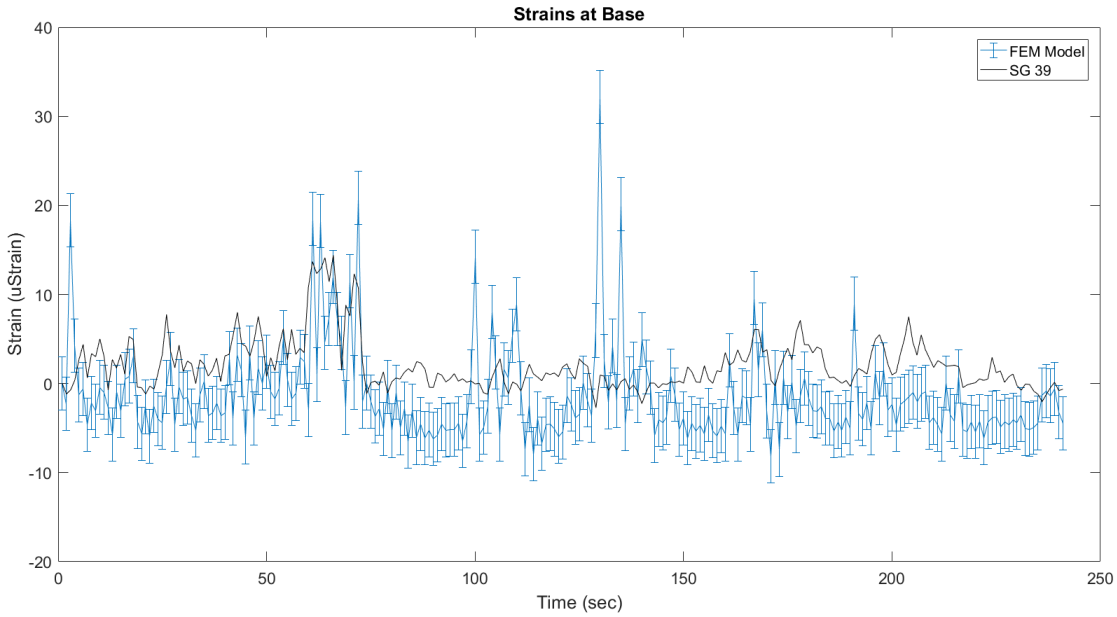

Figure 5.30 – Strains from FEM model in response to the combined tangential and normal pressure components and experimental strains in west tip of north flange of east post (11/30 at 0035)

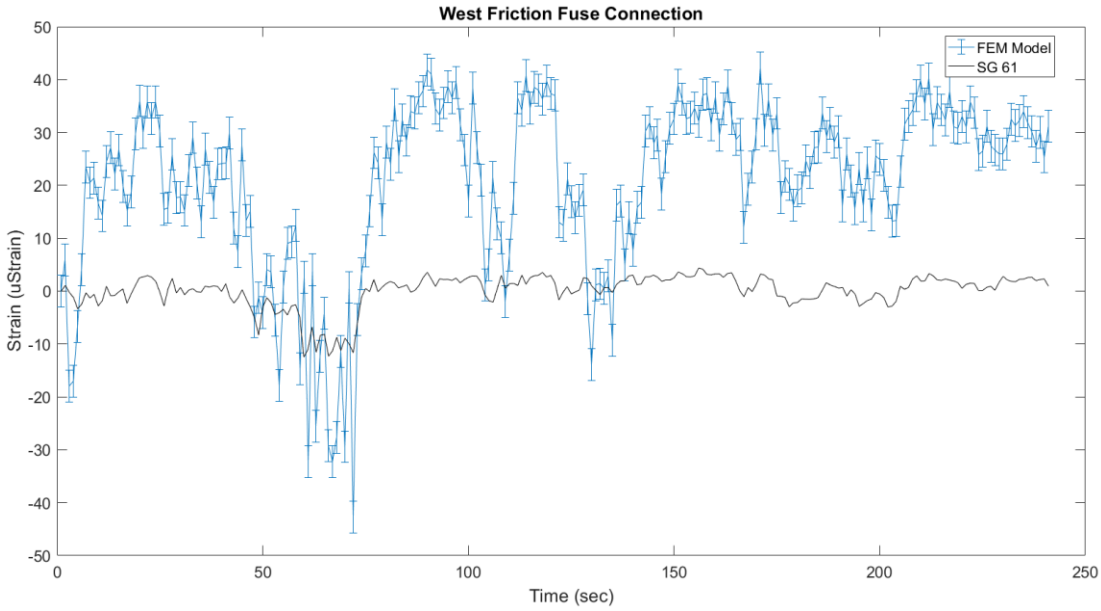

Figure 5.31 – Strains from FEM model in response to the combined tangential and normal pressure components and experimental strains in west friction fuse plate, SG 61 (11/30 at 0035)

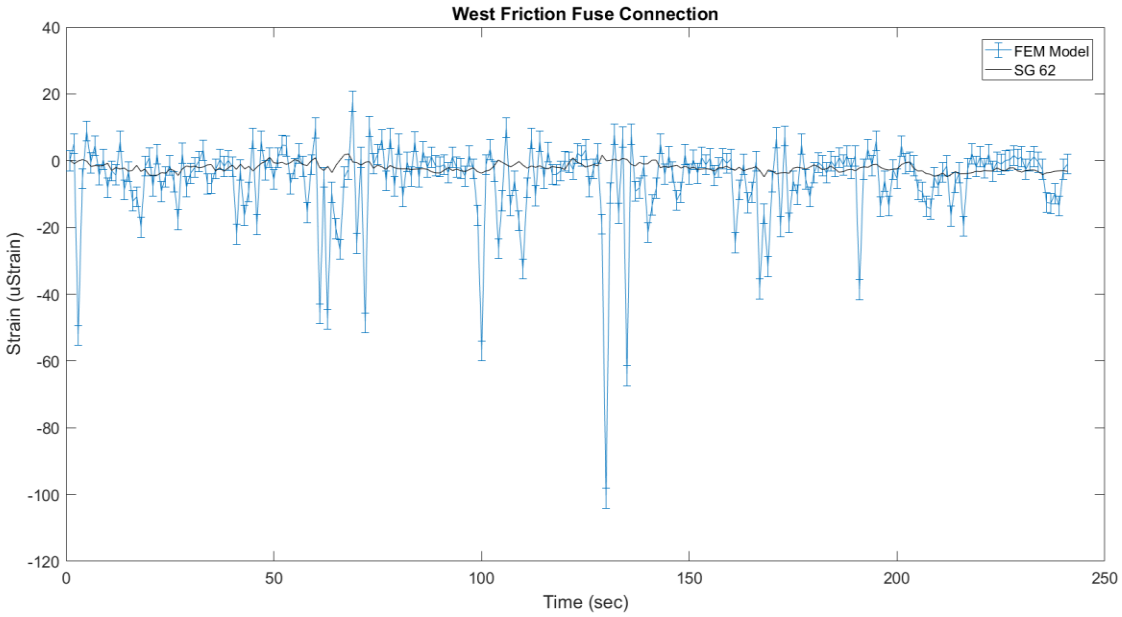

Figure 5.32 – Strains from FEM model in response to the combined tangential and normal pressure components and experimental strains in west friction fuse plate, SG 62 (11/30 at 0035)

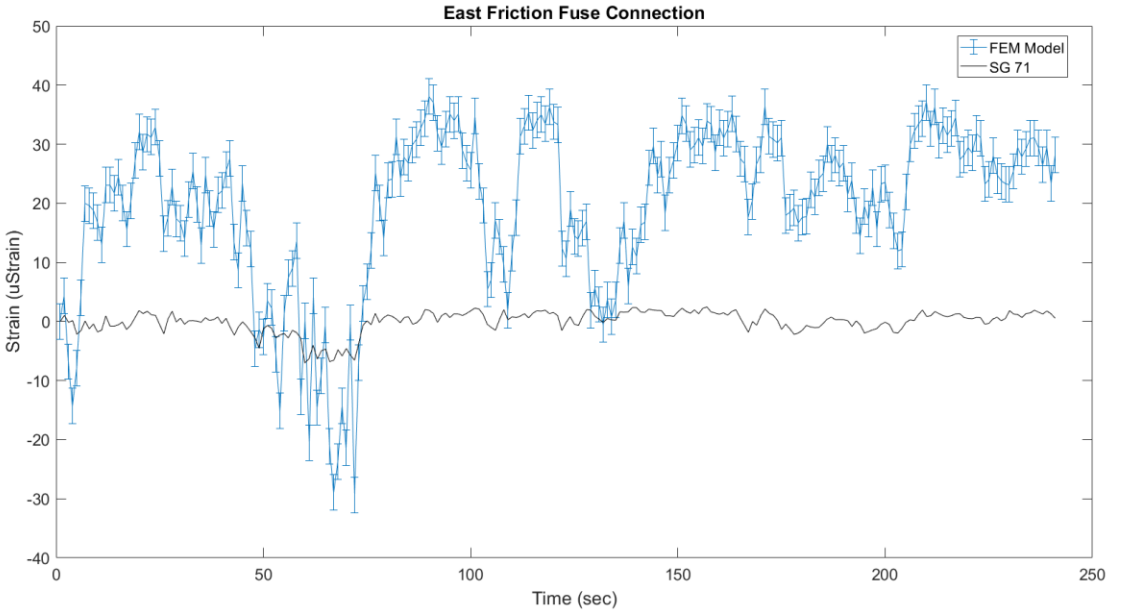

Figure 5.33 – Strains from FEM model in response to the combined tangential and normal pressure components and experimental strains in east friction fuse plate, SG 71 (11/30 at 0035)

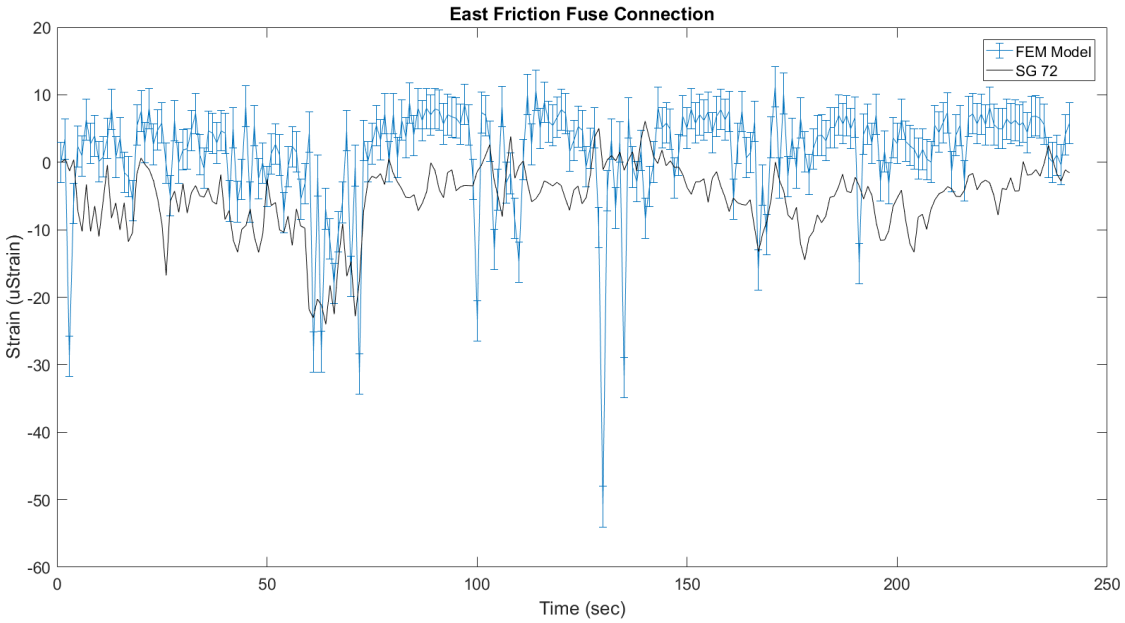

Figure 5.34 – Strains from FEM model in response to the combined tangential and normal pressure components and experimental strains in east friction fuse plate, SG 72 (11/30 at 0035)

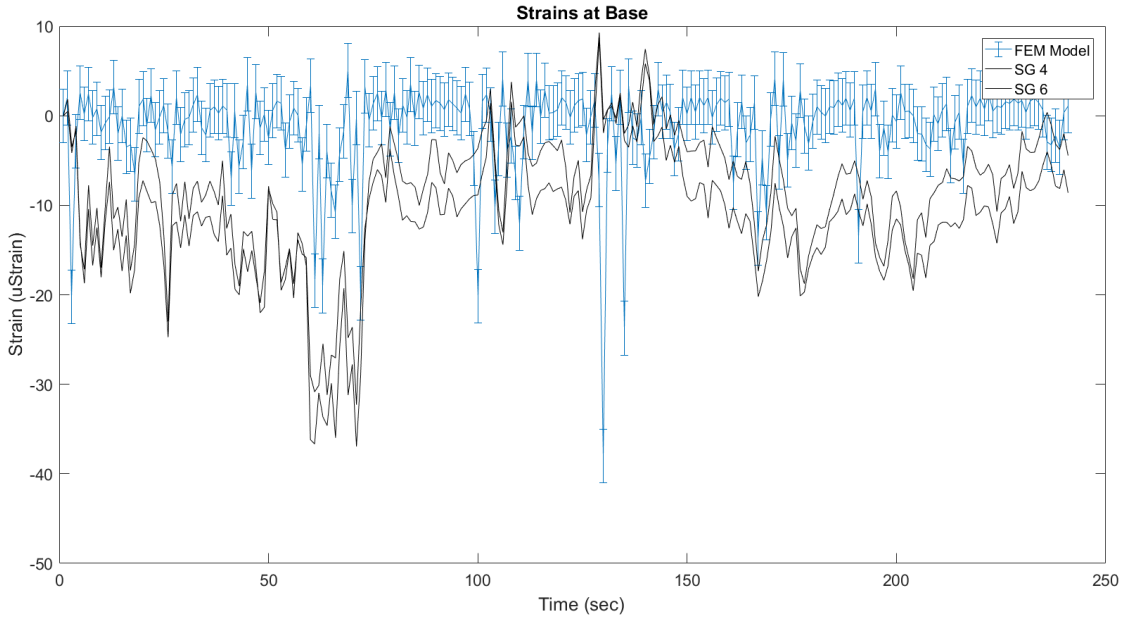

Figure 5.35 – Strains from FEM model in response to only the normal pressure component and experimental strains in south flange of west post (11/30 at 0035)

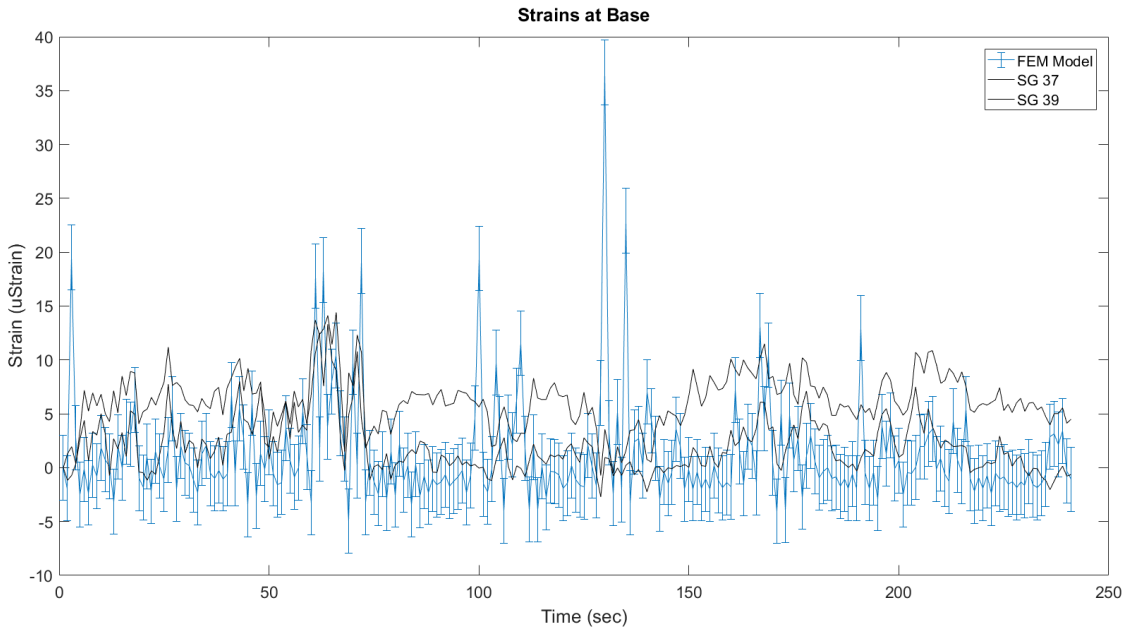

Figure 5.36 – Strains from FEM model in response to only the normal pressure component and experimental strains in north flange of east post (11/30 at 0035)

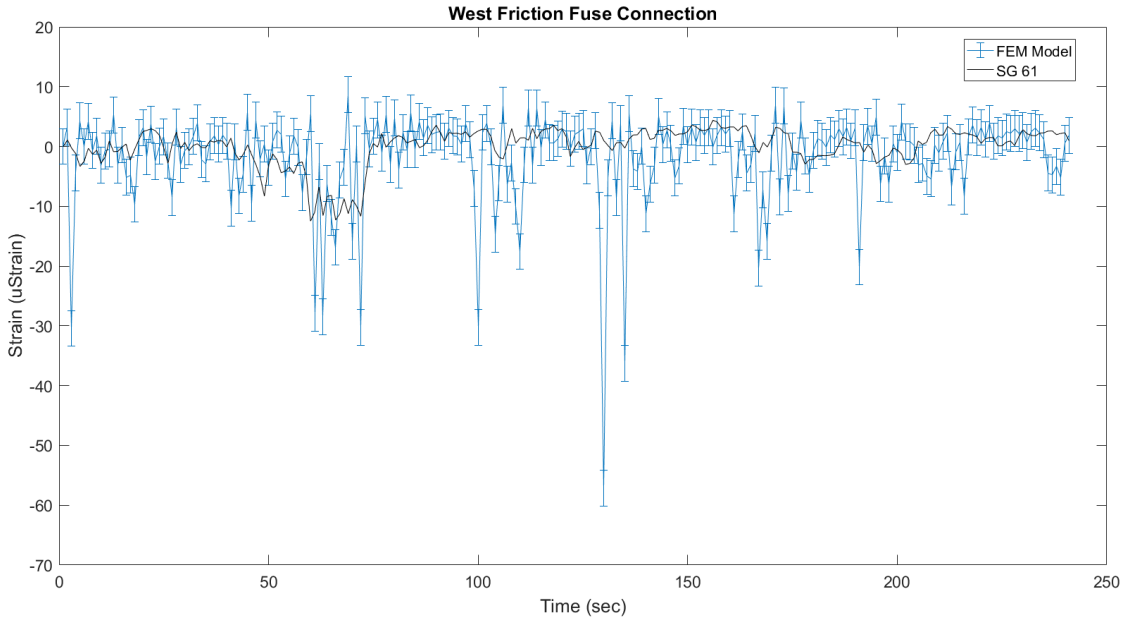

Figure 5.37 – Strains from FEM model in response to only the normal pressure component and experimental strains in west friction fuse plate, SG 61 (11/30 at 0035)

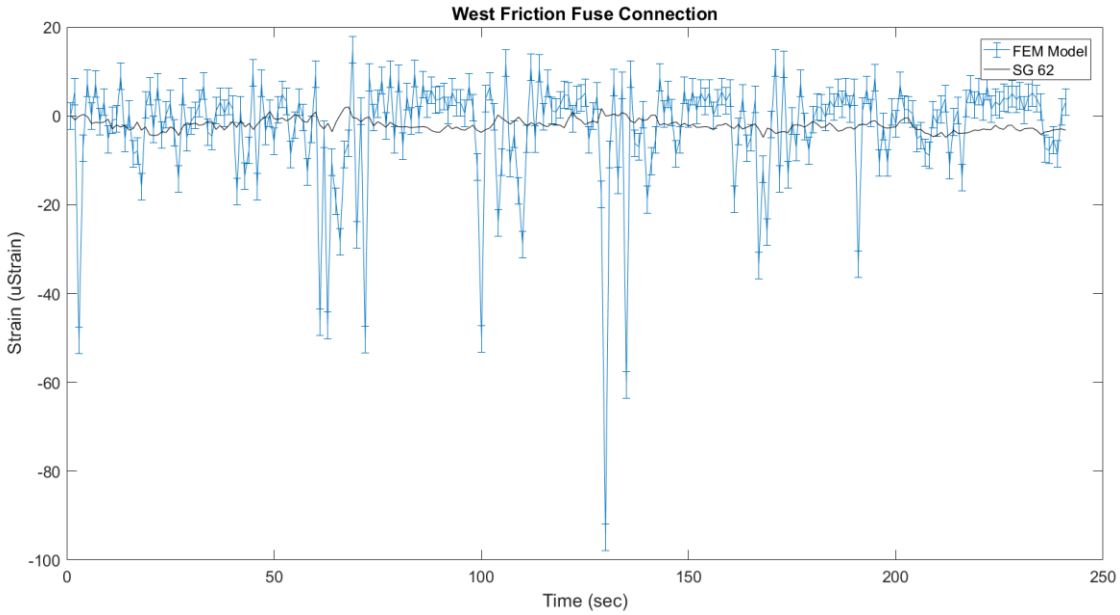

Figure 5.38 – Strains from FEM model in response to only the normal pressure component and experimental strains in west friction fuse plate, SG 62 (11/30 at 0035)

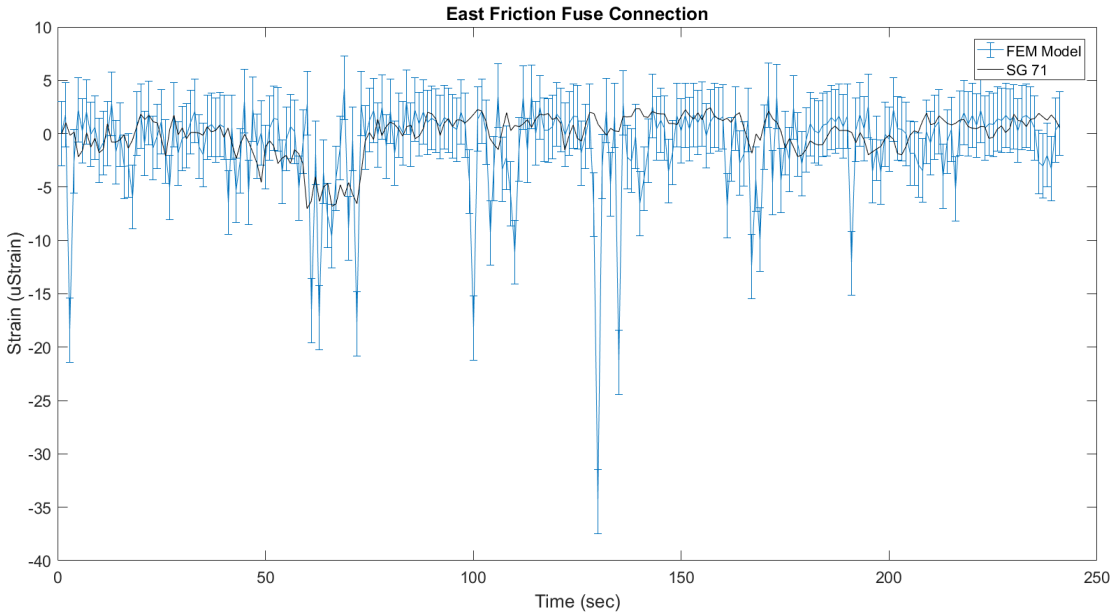

Figure 5.39 – Strains from FEM model in response to only the normal pressure component and experimental strains in east friction fuse plate, SG 71 (11/30 at 0035)

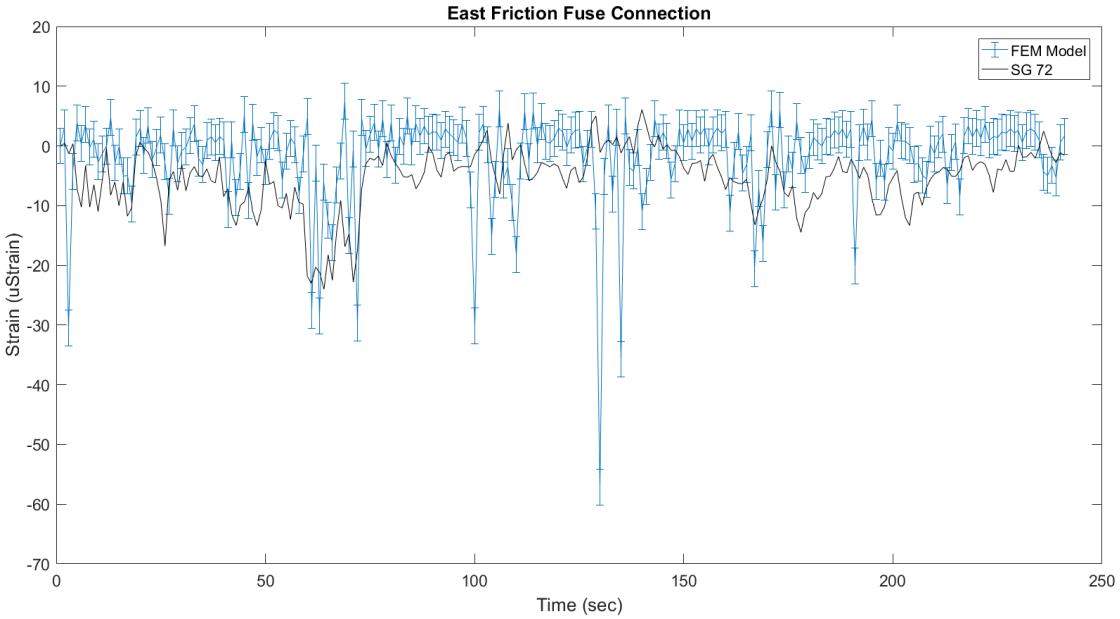

Figure 5.40 – Strains from FEM model in response to only the normal pressure component and experimental strains in east friction fuse plate, SG 72 (11/30 at 0035)

CHAPTER 6: FATIGUE LIFE OF CURRENT DMS SYSTEM

The primary objective of the research targeting the DMS structure was to identify the fatigue characteristics of the fatigue critical detail, the fuse plate, to assess the fatigue life of the structure. The AASHTO 2015 Specification for SLTS recommends fatigue design be done on an infinite life basis. Fatigue stresses below the constant amplitude fatigue threshold (CAFT) theoretically result in the infinite fatigue life of the structure. The code states that the fatigue demand in a support structure can be computed using the equivalent static pressure equations provided in Article 11.7 of the AASHTO 2015 Specification for SLTS or using a dynamic analysis in conjunction with "appropriate dynamic load functions derived from reliable data" (2015). Infinite fatigue life design requires only the CAFT be met for the fatigue sensitive details and the fatigue limit-state stress range expected by the structure (Kaczinski, Dexter, & Van Dien, 1998).

The fatigue design category and corresponding CAFT for the fuse plate is determined in Section 6.1. The fatigue limit-state stress range and corresponding limit-state wind loading are identified in Section 6.2. The dynamic loading functions for the limit-state wind loading used to load the dynamic FEM model validated in Chapter 5 are described in Section 6.3. Section 6.4 evaluates the limit-state fatigue stress demand in the friction fuse plate using two approaches: (1) using the equivalent static pressure equations provided in Article 11.7 of the AASHTO 2015 Specification for SLTS and (2) using the dynamic FEM model. The final fatigue life of the DMS structure was assessed through comparison of the fatigue limit state demand with the S-N curve for the appropriate fatigue detail category.

6.1 FATIGUE STRESS LIMIT

The AASHTO 2015 Specification for SLTS, its interims, and previous research currently do not address fatigue design for the DMS structure. The friction fuse connection, which is considered the fatigue sensitive detail within the DMS support system, is not present in the fatigue sensitive details catalogued in Table 11.9.3.1-1 of the AASHTO 2015 Specification for SLTS and its interims. Details 2.1 and 2.2 of Table 11.9.3.1-1 refer to mechanically fastened connections relevant to the DMS friction fuse connection. However, the prominent feature of the friction fuse connection, the open holes, is not accounted for in these fatigue sensitive details.

Further exploration for an appropriate CAFT for the friction fuse connection was done using the AASHTO LRFD Bridge Design Specification (6th Edition) with 2012 and 2013 interims. Table 6.6.1.2.3-1 of the AASHTO LRFD Bridge Design Specification lists detail categories for load-induced fatigue. An excerpt from Table 6.6.1.2.3-1 is shown in Figure 6.1. Detail 1.5 refers to open holes in members. The detail is classified as Category D with a corresponding CAFT of 7.0 ksi. Brown et al. performed the research used to establish the CAFT associated with this detail (2007).

The research done by Brown et al. explored the effects of the hole manufacturing process on the strength, ductility, and fatigue performance of structural steel plates and connections. Figure 6.2 illustrates the fatigue results of plate specimens with open holes from research specifically done by Brown et al. as well as previous research done by others (Alegre, Aragon, & Gutierrez-Solana, 2004;

Brown, Lubitz, Cekov, Frank, & Keating, 2007; Gutierrez-Solana, Pesquera, & Sanchez, 2004; Rassati, Swanson, & Yuan, 2004). In Figure 6.2 data marked as “Other-Punched” or “Other-Drilled” was not the work of Brown et al. The results obtained by Brown et al. aligned well with the previous research. Based on these findings, fatigue detail Category C was found to be an acceptable lower bound for plate specimens with drilled holes and Category D was thought appropriate for plate specimens with punched holes. Brown et al. also explored fatigue performance in steel connections. Bearing type connections were found to satisfy fatigue detail Category C regardless of hole type, and slip-critical connections were found to satisfy Category B regardless of hole type. (Brown, Lubitz, Cekov, Frank, & Keating, 2007)

Galvanization was found to significantly reduce the fatigue performance of the plate specimens. Brown et al. recommended that all galvanized plates with open hole connections be classified as fatigue Category D (2007). Furthermore, Brown et al. recommended that all bolted connections in galvanized structures be taken as Category D, specifically those connections in the highway industry where the use of galvanization is prominent and the control of bolt tightening in secondary structures, such as sign and signal supports, is not as reliable as in bridge construction (2007). Much of the exploration done by Brown et al. on the impact of galvanization was done using a previous study by Valtinat and Huhn (2004). Brown et al. did not conduct fatigue tests of their own to explore the effects of galvanization (2007), and Valtinat and Huhn only explored the effects of galvanization in steel plates with open holes (2004).

The DMS friction fuse connection contained a combination of pre-tensioned bolted connections and open holes. The connection was galvanized and assumed to be manufactured with punched holes. Based on the recommendations of Brown et al. and the AASHTO LRFD Bridge Design Specification, fatigue Category D and a corresponding CAFT of 7.0 ksi were used in the evaluation of the fatigue life of the DMS supports.

6.2 LIMIT-STATE WIND LOADING

NCHRP 412 was the primary report used to establish the equivalent static pressure equations used to compute fatigue design loads for the sign and signal structures specified in the AASHTO 2015 LRFD specification for SLTS. NCHRP 412 argues that the fatigue limit-state stress range should be that with 0.01 percent or less of exceedance (Kaczinski, Dexter, & Van Dien, 1998). This argument was based on previous research done by NCHRP 354, which found that premature fatigue failure occurred in structures where more than 0.05 percent of cycles had a fatigue stress greater than the CAFT and theoretical infinite life resulted when 0.01 percent or fewer of the cycles had fatigue stress ranges exceeding the CAFT (Fisher, Nussbaumer, Keating, & Yen, 1993; Kaczinski, Dexter, & Van Dien, 1998). NCHRP 412 assumed that the fatigue limit-state stress range was produced by the mean hourly wind speed with 0.01 percent exceedance (Kaczinski, Dexter, & Van Dien, 1998). In NCHRP Report 469, a follow-up report to confirm the methods recommended by NCHRP 412, the fatigue limit-state stress range was also computed from the mean hourly wind velocity with 0.01 percent exceedance (Dexter & Ricker, 2002). Consequently, the limit-state wind speed for this analysis was based on the mean hourly wind speed with 0.01 percent exceedance.

The limit-state wind speed was estimated from the annual mean wind speed in the region. Figure 6.3 displays the annual mean wind speed for the state of Minnesota at a height of 262 ft. WINDExchange, a resource that shares wind energy information relevant to the installation of wind turbines, was used to develop Figure 6.3. Although speeds at 262 ft. are appropriate for wind turbine related work, wind speeds at 33 ft. were required for the analysis of the DMS and other sign and signal support structures. The annual mean wind speed near the instrumented DMS at a height of 33 ft. was determined to be 12.7 mph (5.7 m/s). This speed was calculated using the power law (6.1) assuming open coast terrain (Liu, 1991). Open coast terrain was thought to conservatively account for terrain conditions during winter when snow on the ground was common, effectively smoothing obstructions in the terrain around the DMS. Using the Rayleigh distribution and an annual mean wind velocity of 12.7 mph (5.7 m/s), the mean hourly wind speed with 0.01 percent of exceedance was estimated to be 42.5 mph (19 m/s) (Liu, 1991).

$$V(z) = V_1 \left(\frac{z}{z_1}\right)^{\alpha} \qquad \text{(Liu, 1991)} \qquad (6.1)$$

where:

$V(z) =$ Wind velocity at height z, 12.7 mph (5.7 m/s) at 33 ft.

$V_1 =$ Wind velocity at height z_1, 15.6 mph (7 m/s) at 262 ft.

$\alpha =$ Terrain factor, $\frac{1}{10}$ for open coast

6.3 DYNAMIC WIND LOADING PRESSURE FUNCTIONS

A static wind speed and corresponding pressure were no longer appropriate for the dynamic FEM model. Wind speed histories were needed to determine pressure histories to apply to the model. Various spectra exist in the literature to simulate wind speeds in the field, with the most prominent being the Davenport, Kaimal, and von Karman spectra (Bec, 2010). To determine the most appropriate spectra for the Minnesota region, the power spectral density of wind speed data collected in the field was compared with the Davenport (6.2), Kaimal (6.5), and von Karman (6.8) spectra. The power spectral density of the wind speed data for each of the eight critical wind events identified in Chapter 5 was computed independently. Then, the power spectral densities of all the critical wind events were averaged together to obtain a more comprehensive description of the overall wind behavior in the area. For the field data, only frequency content up to 0.5 Hz was available due to the 1 Hz sampling rate of the anemometer. Figure 6.4 displays the averaged spectrum from the field data, as well as the non-normalized Davenport, Kaimal, and von Karman spectra. The Davenport, Kaimal, and von Karman spectrum were computed in Figure 6.4 using the mean wind speed of the eight critical wind events for direct comparison with the averaged spectrum of the field wind data. Of the three spectra, the Davenport spectrum aligned best with the field data. The fit between the Davenport spectrum and the field data, however, was not ideal.

$$S_v(f) = \frac{4{x_1}^2{\bar{u}_*}^2}{(1+{x_1}^2)^{\frac{4}{3}}}$$ **(Davenport, 1961)** **(6.2)**

where:

$${u_*}^2 = k{\bar{u}_{10}}^2$$ **(6.3)**

$$x_1 = \frac{1200f}{\bar{u}_{10}}$$ **(6.4)**

$S_v(f) =$ Velocity power spectral density

$k =$ Terrain coefficient, assumed 0.005

$\bar{u}_{10} =$ Mean hourly wind speed at 33 ft. (10 m)

$f =$ Frequency

$$S_v(f) = \frac{105x{u_*}^2}{(1+33x)^{\frac{5}{3}}}$$ **(Beaupuits, et al., 2004; Bec, 2010)** **(6.5)**

where:

$$u_* = \frac{k\bar{u}_z}{ln\left(\frac{z}{z_o}\right)}$$ **(6.6)**

$$x = \frac{fz}{\bar{u}_z}$$ **(6.7)**

$S_v(f) =$ Velocity power spectral density

$k =$ Von Karman's constant, 0.4

$\bar{u}_z =$ Mean hourly wind speed at height z

$z =$ Height of spectra, assumed 20 ft.

$z_o =$ Terrain roughness parameter, assumed 1 ft.

$\boldsymbol{f} =$ Frequency

$$S_v(f) = \frac{24 x_u {u_*}^2}{(1+70.7 {x_u}^2)^{\frac{5}{6}}} \quad \text{(Bec, 2010)} \quad (6.8)$$

where:

$$u_* = \frac{k\bar{u}_z}{ln\left(\frac{z}{z_o}\right)} \quad (6.9)$$

$$x_u = L_{ux} x \quad (6.10)$$

$$L_{ux} = 300\left(\frac{z}{350}\right)^{\frac{1}{k}} \quad (6.11)$$

$$\frac{1}{k} = 0.437 + 1.53 log(z_o) \quad (6.12)$$

$$x = \frac{fz}{\bar{u}_z} \quad (6.13)$$

$\boldsymbol{S_v(f)} =$ Velocity power spectral density

$\boldsymbol{k} =$ Von Karman's constant, 0.4

$\boldsymbol{\bar{u}_z} =$ Mean hourly wind speed at height z

$\boldsymbol{z} =$ Height of spectra, assumed 20 ft.

$\boldsymbol{z_o} =$ Terrain roughness parameter, assumed 1 ft.

$\boldsymbol{f} =$ Frequency

In Figure 6.4 the Davenport spectrum was generated assuming a terrain factor of 0.005 for open, unobstructed terrain (Davenport, 1961). In Figure 6.5 the Davenport spectrum was generated assuming a terrain coefficient of 0.008, which falls somewhere between Davenport's terrain factors for unobstructed terrain and terrain with low obstructions (Davenport, 1961). The fit between the field data

and the Davenport spectrum in Figure 6.5 was significantly improved, suggesting the terrain near the field DMS falls somewhere between unobstructed terrain and terrain with low obstructions. Figure 6.6 displays the averaged power spectral density for field events occurring only in December as well as the Davenport spectrum generated assuming a terrain factor of 0.005 for open, unobstructed terrain. The alignment between the field data and the Davenport spectrum in Figure 6.6 was quite good, suggesting that the terrain of the region varies with conditions such as snow, which likely smooth obstructions near the DMS.

Based on the strong alignment of the Davenport spectrum with the field data when the appropriate terrain coefficient was selected, the Davenport spectrum was used to generate the wind speed and subsequent pressure functions for use with the dynamic FEM model. A terrain coefficient of 0.005 for open, unobstructed terrain was used in the analysis because this would produce the greatest wind speeds and reflects the most conservative conditions in the region. A mean hourly wind speed of 42.5 mph (19 m/s) at 33 ft. was used in the Davenport spectrum. This is the limit-state fatigue wind loading found in Section 6.2 at the height of the DMS.

Wind speed functions were generated using Simulink and a shaping filter resembling the Davenport spectrum. The filter, designated “Davenport filter” herein, was applied to a white noise input with unit covariance to produce a zero-mean wind speed history with variance appropriate for the applied Davenport spectrum. The non-normalized Davenport spectrum shown in Figure 6.4 through Figure 6.6 is given in spectral density units, which in this case are units for velocity squared per frequency. To obtain the correct units of velocity for the zero-mean wind speed history, the Davenport filter was developed by curve fitting to the square root of the Davenport spectrum (Gawronski, 2002). The simulation model and Davenport filter are described in Figure 6.7.

Figure 6.8 compares the Davenport filter and the desired Davenport spectrum, while Figure 6.9 compares the Davenport spectrum and the power spectral density (PSD) of the wind speeds generated using the Davenport filter. The corresponding wind speeds generated using the Davenport filter can be seen in Figure 6.10. Good alignment was seen between the Davenport filter and the Davenport Spectrum shown in Figure 6.8, indicating the curve fitting function was sufficient. Good alignment was also seen between the Davenport filter and the PSD of the generated wind speeds shown in Figure 6.9. The alignment between the magnitude of the Davenport filter and the PSD of the generated wind speeds suggests the Davenport filter design was adequate. Consequently, the Davenport filter was thought to be appropriate for generating the loading functions for the dynamic FEM model.

The pressure loading functions for the dynamic FEM model were developed from the generated wind speed histories using a variation of the methods presented in Section 2.2.6 of NCHRP 469 (Dexter & Ricker, 2002). In NCHRP 469, the spectral force density was computed from the spectral velocity density obtained from the Davenport spectrum. The spectral force density was then applied directly to the model, and the resulting root-mean-square (RMS) of the spectral fatigue stress density was scaled to determine the effective stress range (Dexter & Ricker, 2002). The FEM model used in this analysis had already been validated using pressure functions developed directly from field data. Loading history functions were preferred over the application of the spectral density functions to maintain the same

analysis procedures used previously in the validation process and to maintain the ability to conveniently compare the wind speed histories applied to the FEM through pressure loading functions with those collected in the field. Consequently, the analysis done in this exploration was done using the square root of the spectral velocity density instead of the spectral velocity density. The pressure loading function for the dynamic FEM model was derived using the following methodology.

The drag force, F, acting on the surface of the sign was taken as:

$$F = \frac{1}{2}\rho C_d A V^2 \qquad (6.14)$$

where:

$\rho =$ Density of air, 0.75$\frac{lb}{ft^3}$

$C_d =$ Drag coefficient of the sign, 1.7 (AASHTO, Table 3.8.7-1)

$A =$ Area of the sign, 98. 6 ft^2

$V =$ Velocity, ft/s

The velocity was further separated into two components, the mean velocity, V_m, and the fluctuating velocity, V_w.

$$F = \frac{1}{2}\rho C_d A (V_m + V_w)^2 \qquad (6.15)$$

$$F = \frac{1}{2}\rho C_d A \left[{V_m}^2 + 2V_m V_w + {V_w}^2\right] \qquad (6.16)$$

The term, ${V_w}^2$, was neglected because its magnitude was negligible compared to the other velocity terms (please note that cup and vane sensor operating at 1Hz are not designed to resolve turbulence fluctuations, implying that V_w is underestimated). The drag force was then separated into its mean, F_m, and fluctuating components, F_w.

$$F = F_m + F_w \qquad (6.17)$$

$$F_{m=} \frac{1}{2}\rho C_d A {V_m}^2 \qquad (6.18)$$

$$F_w = \rho C_d A V_m V_w \qquad (6.19)$$

The shape of the square root of the spectral velocity density was assumed to have the same shape as the square root of the spectral force density such that,

$$\frac{\sqrt{S_v}}{V_w} = \frac{\sqrt{S_f}}{F_w} \tag{6.20}$$

$$\sqrt{S_f} = \left(\frac{F_w}{V_w}\right)\sqrt{S_v} \tag{6.21}$$

Combining (6.19) and (6.21),

$$\sqrt{S_f} = \left(\frac{\rho C_d A V_m V_w}{V_w}\right)\sqrt{S_v} \tag{6.22}$$

The square root of the spectral velocity density was taken as the output of the Davenport filter, i.e., a wind speed history with zero mean. To achieve the total drag force applied to the sign, the mean drag force was combined with the fluctuating drag force (6.19) such that,

$$F(t) = \rho C_d A\left(\frac{1}{2}{V_m}^2 + V_m V(t)\right) \tag{6.23}$$

In which $V(t)$ is the velocity output of the Davenport filter and $F(t)$ is the forcing function on the sign. The corresponding pressure history was computed as,

$$P(t) = \rho C_d\left(\frac{1}{2}{V_m}^2 + V_m V(t)\right) \tag{6.24}$$

An example of a pressure loading function developed using this methodology is shown in Figure 6.11. Figure 6.10 displays the output of the Davenport filter used to generate the specific pressure history given in Figure 6.11.

In NCHRP Report 469 the RMS of the stress resulting from only the fluctuating force was used to compute the fatigue limit-state stress range. In the analysis prescribed here, the gravity loads were thought to play a critical role in the sign of the stresses within the friction fuse connection because of the large mass of the sign transmitting compressive stresses through the connection. It was possible that the wind-induced fatigue stresses in the friction fuse connection might not have been large enough to overcome the compressive stresses due to gravity. Utilizing the combined mean and fluctuating pressure, instead of the fluctuating pressure only, was thought to give a more realistic representation of the magnitude of the fluctuating tension stresses in the friction fuse connection. The final pressure loading function used included both the fluctuating pressure and the mean pressure. The fatigue limit-state stress range was taken as the amplitude of the tension stress within the friction fuse connection.

6.4 FATIGUE STRESS DEMAND IN FRICTION FUSE CONNECTION

The fatigue demand in the friction fuse connection was computed two ways: (1) using the equivalent static pressure equations provided in Article 11.7 of the AASHTO 2015 Specification for SLTS, and (2) using the dynamic FEM model with the dynamic loading functions developed in Section 6.3.

6.4.1 Static Analysis with Equivalent Static Pressures

In Article 11.7.1 of the AASTHO 2015 Specification for SLTS, equivalent static pressure equations are provided to compute the fatigue demand from three of the four main wind loading phenomena on sign and signal structures; galloping, natural wind gusts, and truck-induced wind gusts. The fourth wind loading phenomenon, vortex shedding, is outlined specifically in Article 11.7.2, "High-Mast Lighting Towers Fatigue." As explained in Chapter 2, natural wind gusts and vortex shedding were considered the most applicable wind loading phenomena for the DMS. The equation provided for vortex shedding in Article 11.7.2, however, was intended specifically for high mast light towers of 55 ft., and was not appropriate for use with the DMS. In the static analysis presented here, only the methodology prescribed in Article 11.7.1.2 for natural wind gusts was used.

The equivalent static pressure equation for natural wind gusts referenced in the AASHTO 2015 Specification for SLTS was developed through the dynamic analysis done in NCHRP Report 412 and NCHRP Report 469. Stresses calculated using the equivalent static pressure equation were intended to resemble the stresses computed using the dynamic analysis from these reports. The dynamic analyses done in NCHRP Report 412 and NCHRP Report 469 were based off an annual mean wind speed of 11.2 mph (5 m/s). Similar to the methodology described in Section 6.2, the annual mean wind speed was then used in conjunction with the Rayleigh distribution to produce the hourly mean wind speed with 0.01 percent exceedance, i.e., the fatigue limit-state wind loading. According to Article 11.7.1.2 of the AASTHO 2015 Specification for SLTS, the equivalent static pressure equation for natural wind gusts can be adjusted to compensate for annual mean wind speeds that exceed 11.2 mph. The adjusted natural wind gusts equation (6.25) was required for this analysis because the annual mean wind speed at the location of the instrumented DMS was estimated to be 12.7 mph (5.7 m/s).

$$P_{NW} = 5.2 C_d I_f \left(\frac{V_{mean}}{11.2\ mph}\right)^2 \qquad \text{(AASHTO, 2015)} \qquad (6.25)$$

where:

P_{NW} = Pressure due to natural wind gusts, lb/ft^2

C_d = Drag coefficient of the sign, 1.7 (AASHTO, Table 3.8.7-1)

I_f = Fatigue importance factor, 1.0 (AASHTO, Table 11.6-1)

V_{mean} = Annual mean wind velocity for region in mph

The fatigue demand in the friction fuse connection was estimated using the pressure computed from (6.25), assuming an annual mean wind speed of 12.7 mph (5.7 m/s), a fatigue importance factor of 1.0, and drag coefficient of 1.70. The pressure was applied horizontally to the exposed area of the DMS in both the normal direction and tangential direction. Static analysis was used to compute the resulting stresses in the friction fuse connection for each independent loading direction. For this analysis, only the stresses in the friction fuse plate will be discussed, as this is the portion of the friction fuse connection most likely to experience fatigue issues.

The stresses in the friction fuse plate due to normal wind loading were computed based on the loading assumptions shown in Figure 6.12. Pressure applied to the normal surface of the sign was assumed to resolve at the centroid of the sign. Load was assumed to distribute evenly between the two support posts. The moment at the friction fuse connection of a single post was computed by multiplying half the resolved force by the distance from the mid-height of the sign to the center of the friction fuse connection. The force couple acting on the friction fuse plate was estimated by dividing the moment acting at the friction fuse connection by the depth of the W8x24 post section. Fatigue stresses in the friction fuse plate were based on the force in the fuse plate and the critical net section area, where the four holes pierced the cross section. An extra 1/16” was added to the diameter of each hole to account for damage in the section during the hole manufacturing. A diagram of the fuse plate and corresponding critical net section area is shown in Figure 6.13. For normal loading, fatigue stresses in the fuse plate of the west post controlled over those in the east post because the distance from the bottom of the sign panel to the center of the friction fuse connection was slightly larger in the west post generating a larger moment at the friction fuse in that leg.

Forces due to pressure applied to the tangential area of the DMS were assumed to travel through the support structure via the frame emphasized in Figure 6.14. The area of the tangential face of the DMS included the depth of the support posts attached to the sign structure because the posts contributed directly to the area opposing winds from the tangential direction as illustrated in Figure 2.4. Load was assumed to distribute equally between the two columns of the frame shown in Figure 6.14. The moment at the friction fuse connection was computed using the three column models shown in Figure 6.15. Assumed dimensions for the columns and the distance from the mid-height of the sign to the friction fuse connection are provided in Figure 6.15. All dimensions refer to the dimensions measured directly in the field. No length was added to posts to simulate the flexibility of the base connection as was done for the FEM model in Chapter 5.

The three models used were thought to bound the analysis between the three behaviors: (1) fixed-free, (2) fixed-side sway, and (3) pinned-side sway. Note that Model 1 produces a moment with a sign different than the other two loading models. The focus of the analysis was on bounding the magnitude of the fatigue moment demand at the friction fuse connection, so the sign of the moment was ignored. The structure was hypothesized to behave most closely to Model 2, but bounding the analysis in this fashion encompassed the uncertainty in the flexibility of the field DMS base connection. The stress in the friction fuse plate was computed from the moment at the friction fuse connection divided by the

appropriate section modulus for the friction fuse plate at the depth of the four empty holes as shown in Figure 6.16. Half of the moment due to tangential loading was assumed to be resisted by the hinge plate and half by the fuse plate. This methodology produced the worst-case stress in the friction fuse plate due to tangential loading. For tangential loading, stresses in the fuse plate controlled in the east post for Model 2 and Model 3 because the east post was taller than the west post. For Model 1, stresses in the west fuse plate controlled because the loading model was only dependent on the distance between the attachment point of the sign and the mid-section of the friction fuse connection. This distance was larger in the west post.

The stresses in the fuse plate were evaluated using the loading combinations specified in Table 3.9.3-1 of the AASHTO 2015 LRFD Specification for SLTS. Fatigue stress demand for natural wind gusts must be considered for all wind directions (AASHTO, 2015). The combinations specified in Table 3.9.3-1 of the AASHTO 2015 LRFD Specification for SLTS are provided in Table 6.1. Because combining raw wind loads would not be appropriate for evaluating the stress in the friction fuse plate, the combinations in Table 6.1 were applied to the fatigue stress demand due to normal or tangential loading instead of the applied load as originally specified in the AASHTO 2015 LRFD Specification for SLTS. As shown in Table 6.1, the combined loading case, Case 3, stipulates that 75 percent of the stress due to normal loading should be combined with 75 percent of the stress due to tangential loading. The combined loading case conservatively accounts for oncoming wind at a 45 degree angle. Case 3 was found to control the analysis for Model 3 only, likely because this model produces the largest demand at the friction fuse plate due to tangential loading. For all other models the normal loading controlled. Figure 6.17 and Figure 6.18 display the final results for the analysis in the east and west post respectively. The stresses for only normal loading, only tangential loading, and combined loading are shown for each of the three tangential loading models. Fatigue detail category limits for fatigue Category A through fatigue Category E' are also shown in Figure 6.17 and Figure 6.18. Fatigue Category D, the fatigue category of the fuse plate, is the most relevant for the analysis of the friction fuse connection.

For comparison, Figure 6.19 and Figure 6.20, show the final results obtained for the east post and west post, respectively, for an annual wind speed of 11.2 mph. This is the wind speed the AASHTO 2015 LRFD Specification for SLTS defaults to for the evaluation of natural wind gusts.

Using an annual wind speed of 12.7 mph, see Figure 6.17, produced a maximum fatigue stress in the fuse plate of 7.2 ksi, which was just above the CAFT for Category D of 7.0 ksi. An annual wind speed of 11.2 mph, see Figure 6.19, produced a maximum fatigue stress in the fuse plate of 5.5 ksi. In both cases, Model 3 with combined loading controlled in the east post. If the true behavior of the DMS were assumed to resemble Model 2, the maximum fatigue stress in the fuse plate would be 5.2 ksi and 4.0 ksi for a mean annual wind speed of 12.7 mph and 11.2 mph respectively. In this case, normal loading controls in the west post.

Based on the static analysis recommended by the AASHTO 2015 Specification for SLTS, the fatigue demand in the friction fuse plate was not satisfactory for infinite life design if Model 3 most accurately represented the tangential behavior of the structure. If Model 1 or Model 2 most accurately represented the behavior of the DMS when subjected to tangential wind loading, then the fatigue

demand in the friction fuse plate did not exceed the CAFT of 7.0 ksi, and the structure could be assumed to have infinite fatigue life.

6.4.2 Dynamic Analysis

The dynamic analysis was performed using the validated FEM model and the pressure functions developed in Section 6.3. The dynamic pressure functions for both tangential and normal loading were developed using a drag coefficient of 1.7 as recommended by the AASHTO LRFD Specification for SLTS (2015). It is important to note that when validating the FEM model in Chapter 5, the drag coefficient was taken as 1.63 using (5.2) for normal loading and 1.78 for tangential loading. The drag coefficient recommended by the AASHTO LRFD Specification for SLTS was used to develop the dynamic pressure functions for the dynamic analysis with the FEM model, so that the results achieved with the dynamic simulation could be compared directly to the fatigue stress range predicted by the equivalent static pressure equations.

Five simulations were run with different pressure functions generated using the same limit-state wind speed of 42.5 mph (19 m/s) and terrain coefficient of 0.005 for unobstructed terrain. Different pressure loading functions were obtained by changing the seed value in the Band-Limited White Noise Block (MathWorks, 2018) used in Simulink to generate the white noise input to the model shown in Figure 6.7. Seed values were taken as 3312, 9845, 21375, 18491, and 22396. The five simulations were done to determine an average wind-induced fatigue stress range in the connection. A sampling frequency of 10 Hz was used to capture any potential amplification due to resonance. Each of the five pressure loading functions were applied to the FEM model twice, once with the effects of gravity included on the stresses in the friction fuse and once neglecting the effects of gravity.

In the analysis, the pressure functions were applied to the normal and the tangential face of the DMS independently. The area of the tangential face of the DMS included the depth of the support posts attached to the sign structure because the posts contributed directly to the area opposing winds from the tangential direction as illustrated in Figure 2.4. Winds in the normal direction were applied from the south and winds in the tangential direction were applied from the east. The resulting stresses for each loading were sampled from the critical locations in the fuse plate illustrated in Figure 6.21. These locations were thought to be the critical locations in the plate based on the stress distribution shown in Figure 5.15 and Figure 5.16. Only fatigue stresses in the fuse plate were pulled from the FEM model because the fuse plate was the component of the friction fuse connection most likely to fatigue. Stresses in the fuse plate of the FEM model were computed using the same methodology described when validating the model in Section 5.2.

The stresses in the fuse plate due to both normal and tangential loading were evaluated using the combinations specified in Table 3.9.3-1 of the AASHTO 2015 LRFD Specification for SLTS and shown in Table 6.1. Table 6.2 and Table 6.3 display the average wind-induced fatigue stress ranges at the 11 sampled locations for the east and west post respectively without considering the effects of gravity.

Table 6.4 and Table 6.5 display the average wind-induced fatigue stresses for the same 11 locations after considering the effects of gravity on the fatigue stress range.

In the east and west fuse plate, combined loading controlled when the effects of gravity were neglected. When the effects of gravity were considered in the analysis, the combined loading controlled in the east fuse plate, and normal loading controlled in the west fuse plate. Without considering gravity, stresses in both the east and west fuse plate exceeded the CAFT of 7.0 ksi, with fatigue stresses as large as 11.4 ksi in the west post. Including the effects of gravity reduced the fatigue stresses in both fuse plates, but stresses in the west fuse plate still exceeded the CAFT at sample locations B, D, E, G, H, and J. Location B had the greatest fatigue stress demand of 9.27 ksi. The stress range in the west post was consistently greater than that in the east post. From the analysis done in Chapter 5, the true behavior of the friction fuse connection in both the field and the FEM model under primarily tangential loading was not verified due to unreliable gages at the locations on the friction fuse where tangential loading was thought to control. However, because the dynamic analysis was controlled by normal loading in the west post, this uncertainty did not impact the overall results of the dynamic analysis with FEM model.

6.5 FATIGUE LIFE OF THE DMS SUPPORT SYSTEM STUDIED IN THE FIELD

The wind-induced stress range within the fuse plate of the friction fuse connection was evaluated using the equivalent static pressure equations provided in Article 11.7 of the AASTHO 2015 LRFD Specification for SLTS and the validated FEM model. The CAFT was not exceeded when the fatigue stress demand was computed using the equivalent static pressure equation in Article 11.7.1.2 for tangential loading Model 1 and Model 2, however it was exceeded when Model 3 was used. The fatigue stress demand exceeded the CAFT when computed using the dynamic analysis with the validated FEM model. Fatigue stresses computed with the validated FEM model controlled, with a peak fatigue stress demand of 9.27 ksi.

The effects of some of the key assumptions within the development of the wind-induced stress range should be noted to fully appreciate the results of the analysis.

The mean annual wind speed at the location of the field DMS was computed from the mean annual wind speed at 262 ft. assuming open coast terrain. This resulted in a mean annual wind speed at the field DMS of 12.7 mph (5.7 m/s) at the height of the DMS. Open coast terrain was thought to be suitable for heavy snowfall conditions possible in the winter. If open terrain had been assumed, the resulting mean annual wind speed would have been 11.5 mph (5.1 m/s) in the same location (Liu, 1991). The change in wind speed would have been reflected in the mean annual wind speed used in the equivalent static pressure analysis and the mean hourly wind speed used in the dynamic analysis.

The mean hourly wind speed was taken as that with 0.01 percent exceedance. A mean hourly wind speed with a larger percentage of exceedance would have resulted in a lower mean hourly wind speed in the dynamic analysis with the FEM model. The methodology prescribed in Article 11.7.1.2 of the AASHTO 2015 LRFD Specification for SLTS, however, was also developed assuming a mean hourly wind speed with 0.01 percent exceedance (2015).

Open, unobstructed terrain was assumed in the Davenport spectrum used to develop the dynamic pressure functions for the FEM model. This terrain coefficient resulted in the greatest wind speeds.

Unobstructed terrain, however, fit well with wind data collected during the winter, suggesting this terrain coefficient was appropriate for the location of the instrumented DMS.

For the analysis using the equivalent static pressure equation provided in Article 11.7.1.2, the DMS was assumed to be a fatigue category I structure, resulting in an importance factor of 1.0. A fatigue category II or fatigue category III structure would have resulted in lower pressures applied to the DMS in the equivalent static pressure analysis only.

Based on these assumptions and the results of the dynamic analysis with the validated FEM model, the wind-induced stress range within the DMS friction fuse connection exceeded the fatigue stress limit needed to ensure the infinite fatigue life of the connection. The finite life of the field DMS can be estimated using the S-N curve provided by Brown et al. in Figure 6.2 (2007).

Based on Figure 6.2, the critical fatigue stress amplitude of approximately 10 ksi corresponds to a fatigue life of 2×10^6 cycles. During the field analysis between September and February, the 1-second wind speed exceeded the mean hourly limit-state wind speed of 42.5 mph (19 m/s) approximately 27 times, with the peak speed being 46.6 mph (20.8 m/s). If this trend were extrapolated, the 1-second wind speed would exceed the mean hourly limit-state wind speed approximately 70 times a year. It is very conservative to then assume that the yearly 1-second wind speed occurrence at or beyond 42.5 mph (19 m/s) represents the yearly incidence of the mean hourly wind speed at or beyond the limit-state wind speed. The field DMS was assumed to undergo 4 cycles every second based on the structure's natural frequency. Every wind incident at or above the limit-state wind speed was assumed to last for 5 minutes, which is the same length as the analysis done with the FEM model used to produce the fatigue stress demand of 10 ksi. Based on these assumptions, the structure would be expected to undergo a tensile stress range of approximately 10 ksi for approximately 84,000 cycles each year. With a fatigue life of 2×10^6 cycles, the service life of the field DMS would be estimated to be approximately 23.8 years. It should be reiterated that a number of conservative assumptions were used to obtain this estimate.

- A 1-second wind speed was compared with a limit-state mean hourly speed.
- The instances in which the 1-second speed exceeded the limit-state mean hourly speed in a year were taken as equivalent to the instances in which the mean hourly wind speed exceeded the limit-state mean hourly wind speed in a year. Equating a 1-second speed to a mean hourly speed is very conservative.

6.6 FATIGUE LIFE OF OTHER DMS IN SERVICE

The behavior of the DMS investigated in the field does not fully represent the behavior of every DMS in service. DMS signs range from 6 ft. x 14 ft. to 8 ft. x 18 ft. (MnDOT, 2016) with post heights (from the ground to the top of the sign) ranging from 15.5 ft. to 22 ft. (Kimley Horn, MnDOT, 2015). The DMS instrumented in the field was approximately 6 ft. - 10 in. x 15 ft. with an average post height of 15.5 ft. To investigate the behavior of other DMS in service two approaches were used: (1) FEM analysis of two other large DMS in service, (2) a simple analytical model to explore the effects of various sign sizes and post heights.

The dynamic FEM methodology used to evaluate the DMS investigated in the field was extended to the fatigue life of two other large DMS in service (Figure 6.22). The first (DMS – L1) was considered an extreme case with a panel of 8 ft. x 18 ft. and post height clearance of 14 ft. The second (DMS – L2) corresponds to an existing DMS (DMS-S15 on NB35) with a panel of 6.75 ft. x 21 ft. and variable post clearance heights of 11.75 ft. and 9.75 ft (MnDOT, 2008). FEM models similar to those in Section 5.2 were developed with W8x24 steel posts. In the models, each post is connected to the panel at two locations: 4.125" below the top of the panel and 1.125" above the bottom of the panel. A fixed connection is used at the bottom of each post within the model, but in practice the posts are embedded in the ground and are not entirely restrained from rotating at the base. In order to account for this difference, an additional length of 3.75 feet was added to each post in the model as was done previously. The friction fuse connection is located 6" below the bottom of the sign panel.

Ten different simulations were run for each model with the same pressure functions, which included the 5 pressure functions developed in Section 6.4.2 and 5 new pressure functions generated with the same limit-state wind speed of 42.5 mph (19 m/s) and a terrain coefficient of 0.005 for unobstructed terrain. Different pressure loading functions were obtained by changing the seed value in the Band-Limited White Noise Block (MathWorks, 2018) used in Simulink to generate the white noise input to the model shown in Figure 6.7. The new seed values were taken as 834, 15306, 15843, 19820, and 21801. The ten simulations were done to determine an average wind-induced fatigue stress range in the connections. Each of the ten pressure loading functions were applied to the FEM model, which included gravity.

The dynamic analysis followed the same methodology as in Section 6.4.2. In the analysis, the pressure functions were applied to the normal and the tangential face of the DMS independently. Stresses in the fuse plate of the FEM model were computed using the same methodology described when validating the model in Section 5.2. In these models, out of the three combinations valuated using the combinations specified in Table 3.9.3-1 of the AASHTO 2015 LRFD Specification for SLTS and shown in Table 6.1, the normal loading case controlled.

The average maximum tensile stress in the friction fuse plate for DMS-L1 was 12.0 ksi. Using the stress range vs. cycles to failure for category D in Figure 6.2, an estimate of the fatigue life corresponding to 12 ksi is 1.3×10^6 cycles. With the conservative assumption of 84,000 cycles each year determined from the instrumented DMS, the service life of DMS-L1 would be estimated to be approximately 15.5 years.

The average maximum tensile stress in the friction fuse plate for the DMS-L2 was 11.4 ksi. From Figure 6.2, an estimate of the fatigue life corresponding to 11.4 ksi is 1.5×10^6 cycles. Using the same conservative assumption of cycles per year, the service life of DMS-L2 would be estimated to be approximately 18 years.

A few assumptions used to obtain these estimates in both models should be reiterated:

- The friction fuse was assumed to be 6" below the bottom of the sign panel. A larger distance would lower the stress demand.
- The steel posts were assumed to be W8x24 for DMS-L1.

- The posts in the model were assumed to extend the same distance into the ground as the field model to capture the dynamic behavior.
- The same conservative number of cycles each year of exceeding the fatigue stress demand was use as the field DMS.

The simple analytical model used in Chapter 5 was employed to explore the effects of various sign sizes and post heights on the demand at the friction fuse connection. In this analysis, both posts were assumed to be of equal length for all simulations. The first simulation was performed by applying the pressure function shown in Figure 6.11 to the analytical model from Chapter 5. Pressure was only applied to the normal surface of the sign. A sampling rate of 10 Hz was used to capture any dynamic amplification present. The strong axis moment was computed at the friction fuse connection, which was assumed to be 6 in. below the bottom of the sign, using (6.26). More details on the analytical dynamic model are provided in Chapter 5.

Figure 6.23 illustrates the various sign sizes and heights explored with the analytical model. These represent the extreme sign sizes and post heights currently in service for the DMS. The same pressure function was applied to every sign variation shown in Figure 6.23. The control structure for the exploration was a 6 ft. - 10 in. x 15 ft. DMS with two 15.5 ft. equal length posts, which was similar to the field DMS but with equal length posts. Figure 6.23 displays the ratio of the moment demand due to wind loading at the friction fuse connection for each sign variation to that of the control.

A second simulation was done to explore the response ratio of the structure under a unit step loading. The response ratio is given in (6.27) for an underdamped system and provides an estimate of the ratio of the dynamic response to the static response for a step input. Figure 6.24 displays the dynamic amplification for each of the structures shown in Figure 6.23. The data was normalized such that the static response of the control structure was 1.0.

$$M_x = EIv'' = \left(\frac{3}{L^2} - \frac{6x}{2L^3}\right) q(t) \qquad (6.26)$$

where:

$\boldsymbol{E} =$ Elastic modulus of steel, 29000 ksi

$\boldsymbol{I} =$ Strong axis moment of inertia, 82.7 in^4

$\boldsymbol{v(x,t)} =$ Displacement function

$\mathbf{q(t)} =$ Time function

$\boldsymbol{L} =$ Length of post from base plate to the bottom of the sign, see Figure 6.23

$\mathbf{x} =$ Location evaluating moment measured from base plate, (L-6")

$$R(t) = 1 - e^{-\xi\omega_n t}\left(\cos\omega_d t + \frac{\xi\omega_n}{\omega_d}\sin\omega_d t\right) \qquad (6.27)$$

where:

$\boldsymbol{R(t)} =$ Response ratio

$\boldsymbol{\xi} =$ Viscous damping factor

$\boldsymbol{\omega_n} =$ Undamped circular natural frequency, rad/s

$\boldsymbol{t} =$ Time

$\boldsymbol{\omega_d} =$ Damped circular natural frequency, rad/s

As seen in Figure 6.24 the overall response of the structure changed both dynamically and statically as the post height and panel size was varied. Increasing the size of the panel increased the static response, but changing the post length had no effect on the static response for normal wind loading when the panel size was kept constant. Changing the post height did, however, effect the dynamic response. This is clearly seen in Figure 6.24 for the structure with the smallest sign panel and explains why the stress

scale factor differed for two structures with the same size panel in Figure 6.23. Panels larger than the control resulted in greater fatigue demand at the friction fuse connection.

It is also important to emphasize that the posts shown in Figure 6.23 are drawn with the dimensions given for the structures in the field. No additional length was added to the support posts to modify the flexibility of the structure as was done in the FEM model in Chapter 5 to account for the base connection at the ground not being fully fixed. The maximum lengths shown in Figure 6.23 may need to be extended to account for the effect of the base connection on the flexibility of the sign.

The location of the DMS may also play a role on the fatigue stress in the friction fuse connection. The DMS instrumented in the field was not located in the region of the state subjected to the largest mean annual wind speed as shown in Figure 6.3. DMS in regions with greater mean annual wind speeds would need to be analyzed with the corresponding speed for that region, which would increase the magnitude of the pressure predicted by the equivalent static pressure equation as well as the magnitude of the dynamic pressure functions applied to the FEM model. The increased loading on the sign would likely result in an increased fatigue stress range for both analysis methods.

Symmetry also may have a significant impact on the magnitude of the fatigue stress in the friction fuse connection. In the dynamic analysis done with the FEM model, the fatigue stresses in the west connection were significantly larger than those in the east connection. Fatigue stresses in the east fuse plate never exceeded the CAFT when gravity loads were considered, while several locations in the west fuse plate featured stresses beyond the CAFT. The west post was approximately 2 ft. shorter than the east post. When the sign deflected under load, the east post, and more flexible post, deflected more than the west post and changed the load distribution within each post. Load distributed evenly between each post, but the distribution of the load into the support through the Z-Bar attachment points was different in each sign. More load was distributed in the attachment point furthest from the friction fuse connection in the west post, resulting in a greater demand and greater fatigue stress at the west friction fuse connection. Utilizing two equal length posts would result in both posts deflecting an equal amount, which may reduce the difference in demand at the two connections and equalize the fatigue stress in each connection.

Finally, the location of the friction fuse connection along the height of the posts also impacts the fatigue stress in the connection. The further the friction fuse connection is from the base of the sign panel, the larger the stresses produced in the connection from winds applied to the normal surface of the sign. This trend was evident in the analysis done with the equivalent static pressure equation for natural wind gusts. In the field DMS, the friction fuse connection on the west post was further from the base of the sign panel than the connection on the east post, resulting in a greater normal wind fatigue stress demand in the west fuse plate. For a tangential wind loading however, placing the friction fuse connection further from the base of the sign (lower on the structure) resulted in an increased fatigue demand at the friction fuse connection via Model 1, decreased demand via Model 2, and decreased demand via Model 3. Both tangential loading and normal loading should be considered when determining the optimal location for the friction fuse connection.

The support system and DMS instrumented in the field did not meet the requirements for infinite fatigue life using what are believed to be conservative assumptions. Other DMS in service may also be subjected to fatigue stresses beyond the CAFT depending on the size of the sign panel, height of the posts, sign location, and the relative location of the friction fuse connection. In the two different approaches for investigating other DMS in service, the taller DMS with larger panels had a greater fatigue stress demand. While the stress ratios between the FEM analyzed structures and those developed with the simplified analysis can't be directly compared, the simplified analysis likely provides a conservative assumption when considering other DMS in service.

6.7 SUMMARY

The fatigue life of the DMS instrumented in the field was investigated. The friction fuse plate, the fatigue sensitive detail within the support system, was assumed to be a fatigue Category D detail with corresponding CAFT of 7.0 ksi. The limit-state stress range was developed using the limit-state wind loading recommended by NCHRP 412 and NCHRP 469, as well as reliable wind data for the region. Fatigue stresses in the fuse plate were evaluated using the applicable equivalent static pressure equations provided in Article 11.7 of the AASHTO LRFD Specification for SLTS and the validated FEM model.

The CAFT was not exceeded when the fatigue stress demand was computed using the applicable equivalent static pressure equations in Article 11.7 when tangential loading Model 1 or Model 2 were assumed to represent the behavior of the DMS subjected to tangential loading. However, it was exceeded when Model 3 was used. The fatigue stress demand computed using the dynamic analysis with the validated FEM Model also exceeded the CAFT. Fatigue stresses produced by the FEM model controlled the analysis. Based on the dynamic analysis, the field DMS did not meet the requirements for infinite fatigue life. Other DMS in service may also be subjected to fatigue stresses beyond the CAFT depending on the size of the sign panel, height of the posts, sign location, and the relative location of the friction fuse connection. For example, the two large DMS considered numerically resulted in fatigue stress limits above the CAFT and the instrumented DMS. A service life of 23.8 years was conservatively estimated for the field DMS.

Table 6.1 – Wind load combinations per AASHTO LRFD Specification for SLTS modified for application with fatigue design (AASHTO, 2015)

Load Case	Normal Component	Tangential Component
1	$1.0(\sigma_N)$	$0(\sigma_T)$
2	$0(\sigma_N)$	$1.0(\sigma_T)$
3	$0.75(\sigma_N)$	$0.75(\sigma_T)$

σ_N = Stress demand from normal loading only

σ_T = Stress demand from tangential loading only

Table 6.2 – Average fatigue stress range for east post of field DMS excluding effects of gravity

Loading	A	B	C	D	E	F	G	H	I	J	K
Normal (ksi)	2.84	6.45	4.09	5.23	5.92	4.35	5.91	5.22	4.07	6.40	2.82
Tangential (ksi)	0.00	0.00	0.00	0.00	0.00	0.26	1.23	2.04	2.01	3.68	1.76
Combined (ksi)	2.13	4.84	3.07	3.92	4.44	3.46	5.35	5.44	4.56	**7.56**	3.44

Table 6.3 – Average fatigue stress range for west post of field DMS excluding effects of gravity

Loading	A	B	C	D	E	F	G	H	I	J	K
Normal (ksi)	5.06	**11.33**	**7.20**	**9.19**	**10.4**	**7.72**	**10.4**	**9.19**	**7.17**	**11.29**	5.03
Tangential (ksi)	0.00	0.00	0.00	0.00	0.00	0.00	0.82	1.96	2.06	3.92	1.90
Combined (ksi)	3.79	**8.50**	5.40	6.89	**7.81**	5.79	**8.41**	**8.36**	6.92	**11.40**	5.20

Table 6.4 – Average fatigue stress range for east post of field DMS including effects of gravity

Loading	A	B	C	D	E	F	G	H	I	J	K
Normal (ksi)	2.02	4.63	2.93	3.75	4.24	3.10	4.23	3.73	2.91	4.58	2.00

Tangential (ksi)	0.00	0.00	0.00	0.00	0.00	0.00	0.00	0.82	1.11	2.34	1.17
Combined (ksi)	1.51	3.47	2.20	2.81	3.18	2.32	3.17	3.42	3.02	5.19	2.37

Table 6.5 – Average fatigue stress range for west post of field DMS including effects of gravity

Loading	A	B	C	D	E	F	G	H	I	J	K
Normal (ksi)	4.12	**9.27**	5.88	**7.51**	**8.52**	6.30	**8.50**	**7.51**	5.86	**9.22**	4.10
Tangential (ksi)	0.00	0.00	0.00	0.00	0.00	0.00	0.00	0.55	1.01	2.36	1.20
Combined (ksi)	3.09	6.95	4.41	5.63	6.39	4.72	6.38	6.05	5.15	**8.69**	3.98

Description	Category	Constant A (ksi^3)	Threshold $(\Delta F)_{TH}$ ksi	Potential Crack Initiation Point	Illustrative Examples
Section 1—Plain Material away from Any Welding					
1.1 Base metal, except noncoated weathering steel, with rolled or cleaned surfaces. Flame-cut edges with surface roughness value of 1,000 µ-in. or less, but without re-entrant corners.	A	250×10^8	24	Away from all welds or structural connections	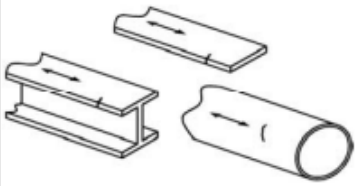
1.2 Noncoated weathering steel base metal with rolled or cleaned surfaces designed and detailed in accordance with FHWA (1989). Flame-cut edges with surface roughness value of 1,000 µ-in. or less, but without re-entrant corners.	B	120×10^8	16	Away from all welds or structural connections	
1.3 Member with re-entrant corners at copes, cuts, block-outs or other geometrical discontinuities made to the requirements of AASHTO/AWS D1.5, except weld access holes.	C	44×10^8	10	At any external edge	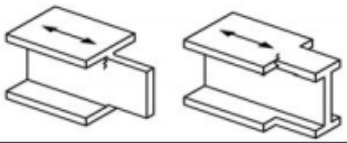
1.4 Rolled cross sections with weld access holes made to the requirements of AASHTO/AWS D1.5, Article 3.2.4.	C	44×10^8	10	In the base metal at the re-entrant corner of the weld access hole	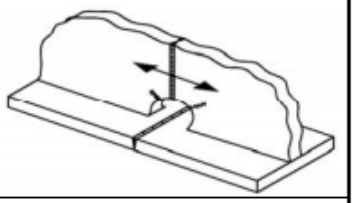
1.5 Open holes in members (Brown et al., 2007).	D	22×10^8	7	In the net section originating at the side of the hole	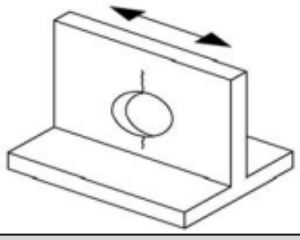

Figure 6.1 – Excerpt from Table 6.6.1.2.3-1 of the AASHTO LRFD Bridge Design Specifications (AASHTO, 2012)

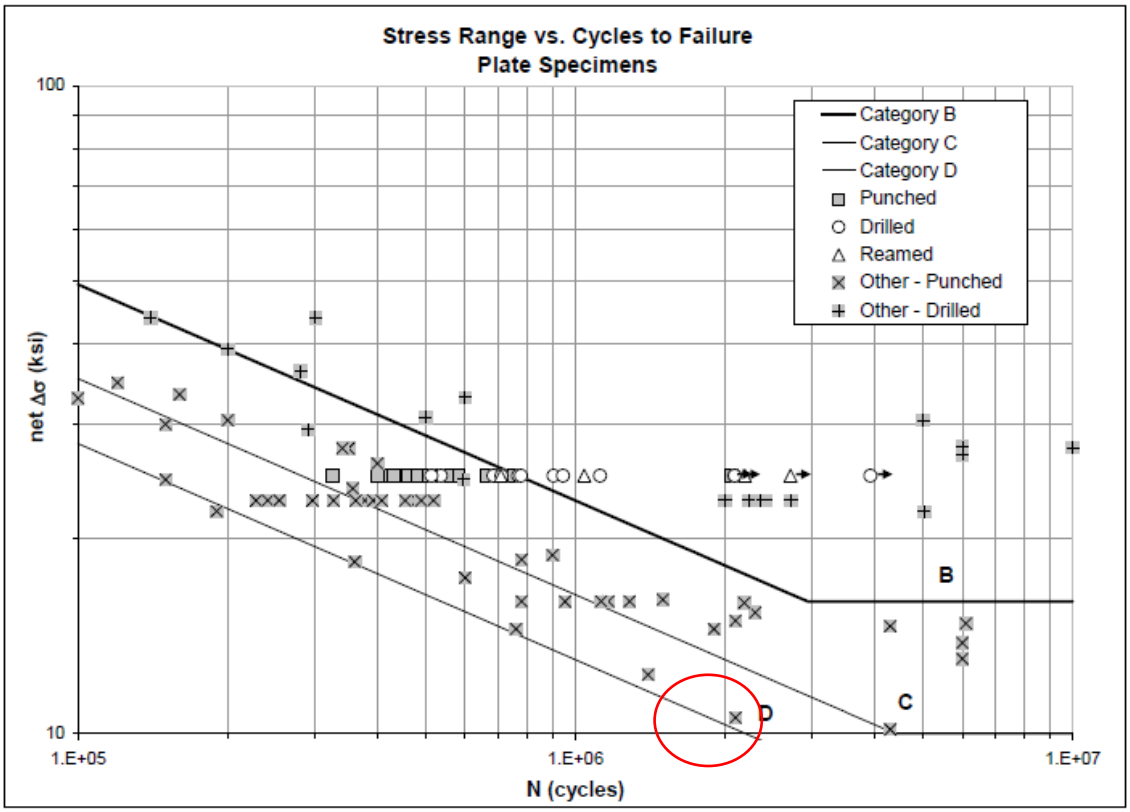

Figure 6.2 – Comparison of fatigue results for plates with open holes from Brown et al. with other research (Brown, Lubitz, Cekov, Frank, & Keating, 2007)

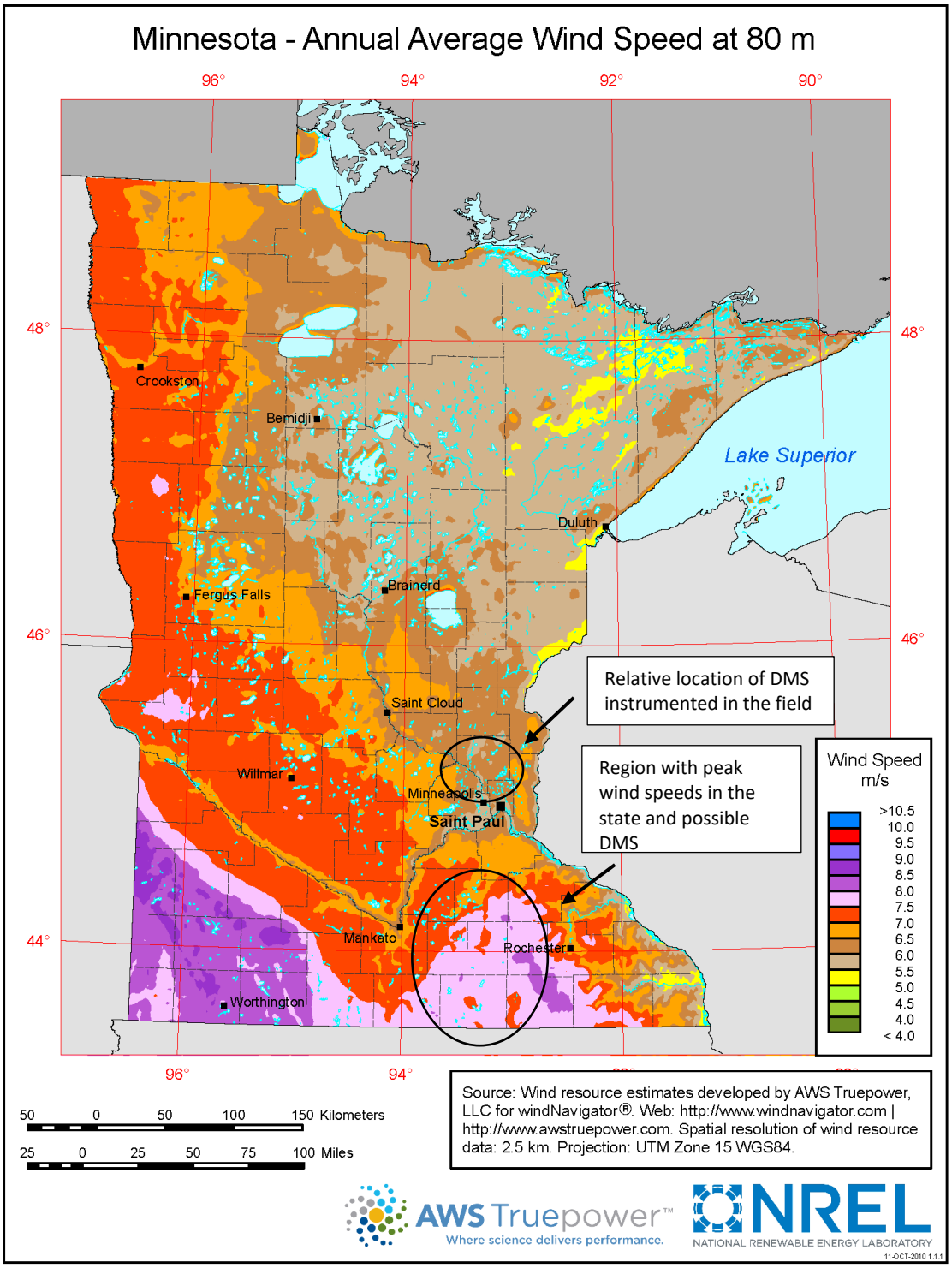

Figure 6.3 –Average annual wind speed at 262 ft. (80 m) (AWS Truepower, 2010)

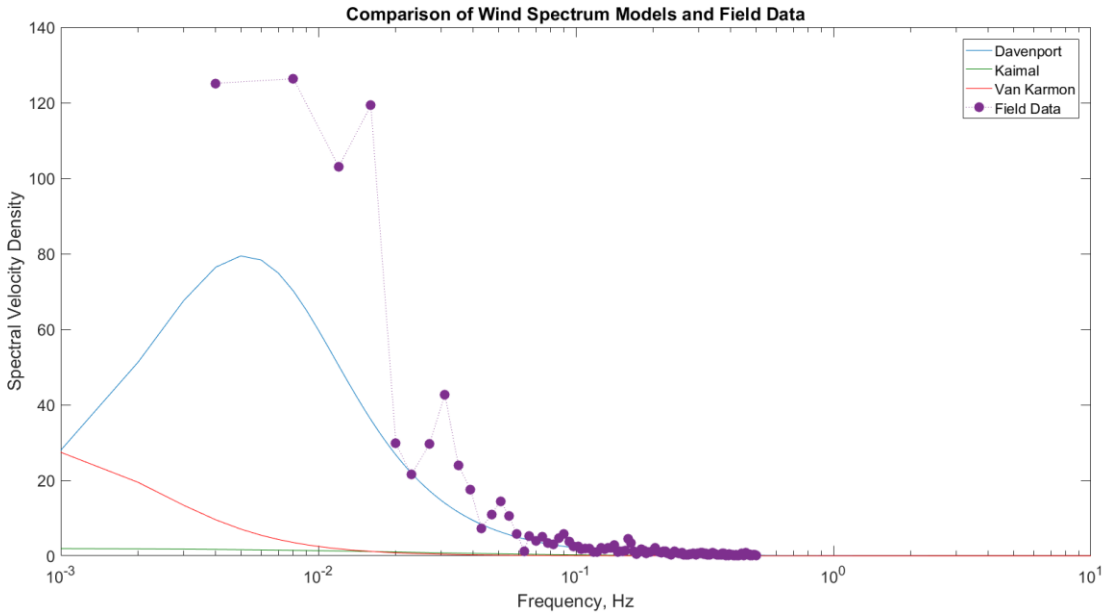

Figure 6.4 – Comparison of Davenport, Kaimal, and Van Karmon spectrum with average velocity spectrum of critical wind events (k=0.005)

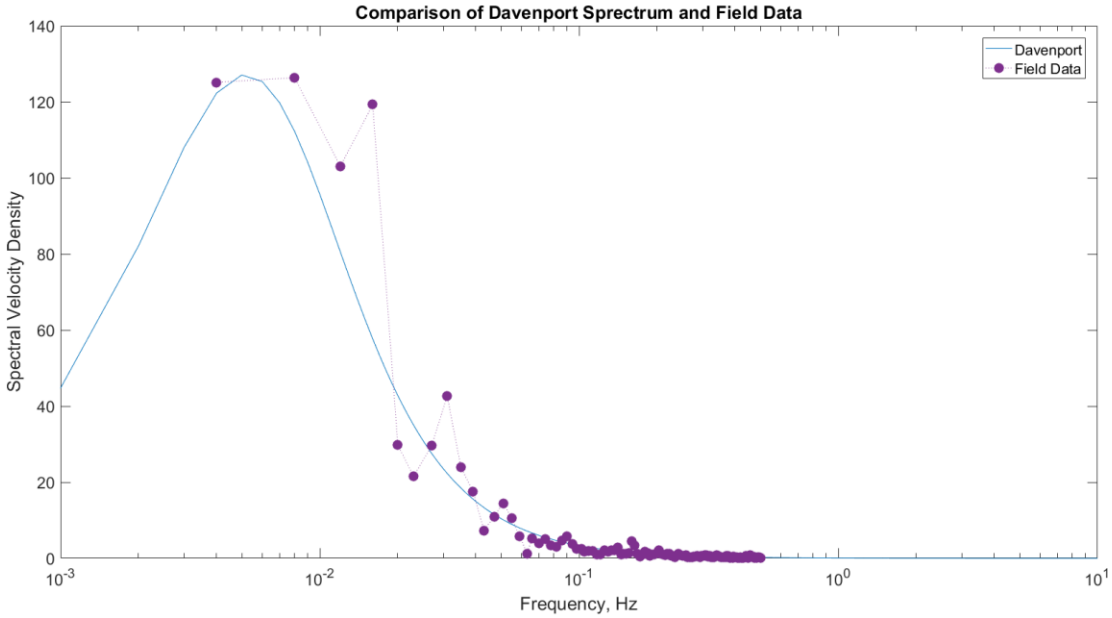

Figure 6.5 – Comparison of Davenport spectrum with average velocity spectrum of critical wind events terrain between unobstructed and low obstruction (k=0.008)

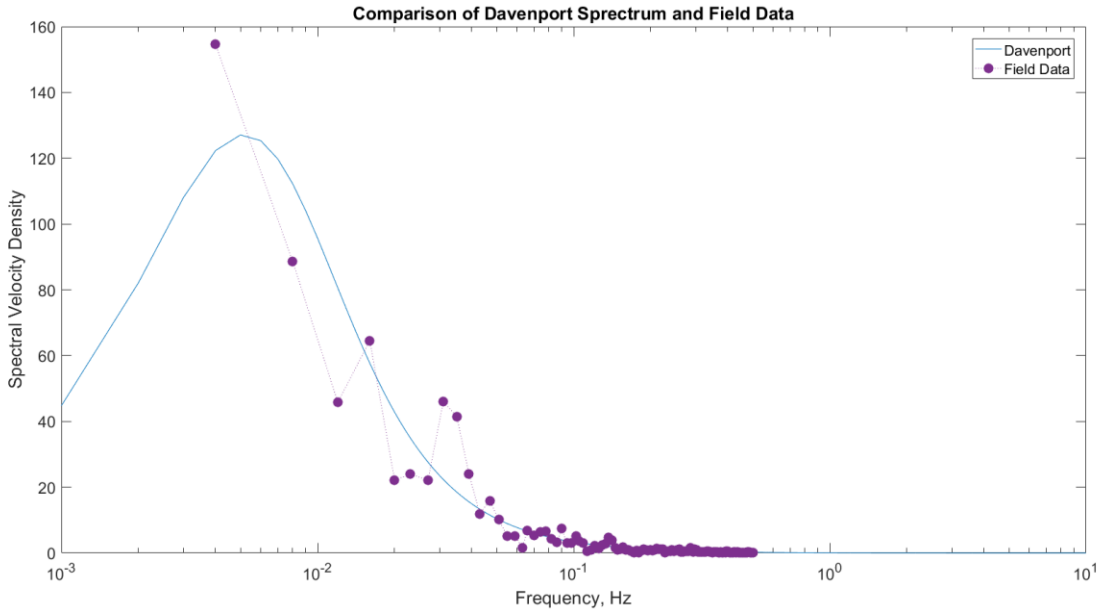

Figure 6.6 – Comparison of Davenport spectrum with average velocity spectrum of critical wind events in December with unobstructed terrain (k=0.005)

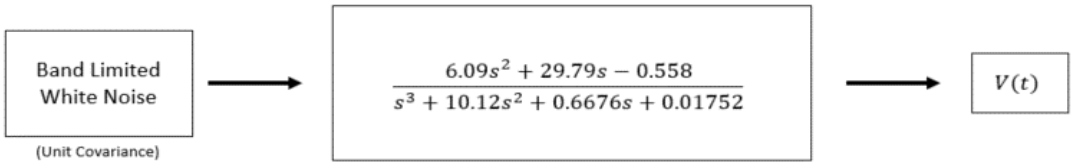

Figure 6.7 – Simulation model

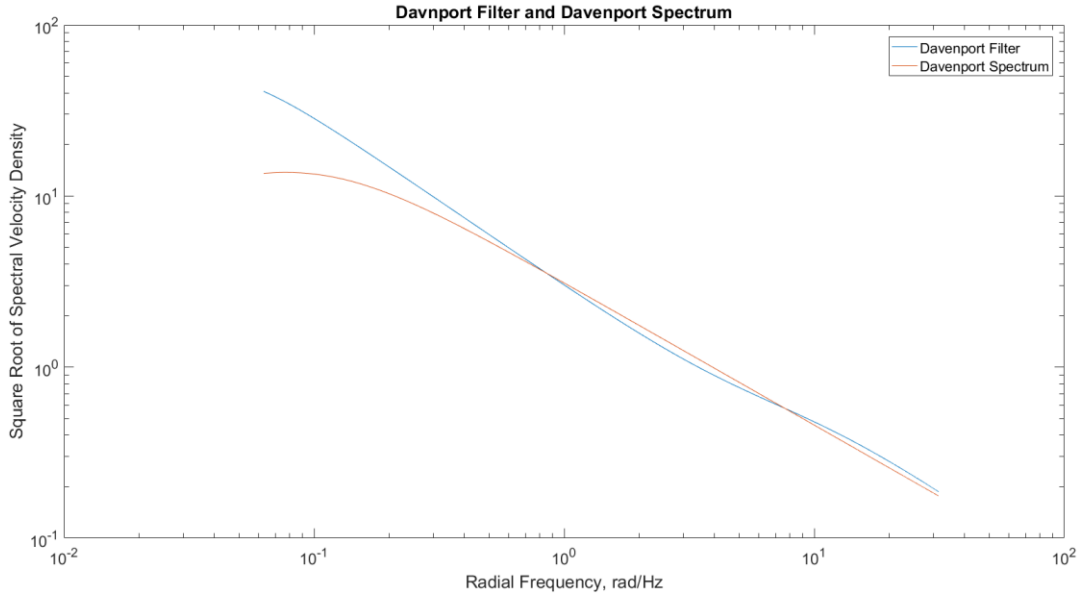

Figure 6.8 – Comparison of Davenport filter and Davenport spectrum at 42.5 mph (19 m/s)

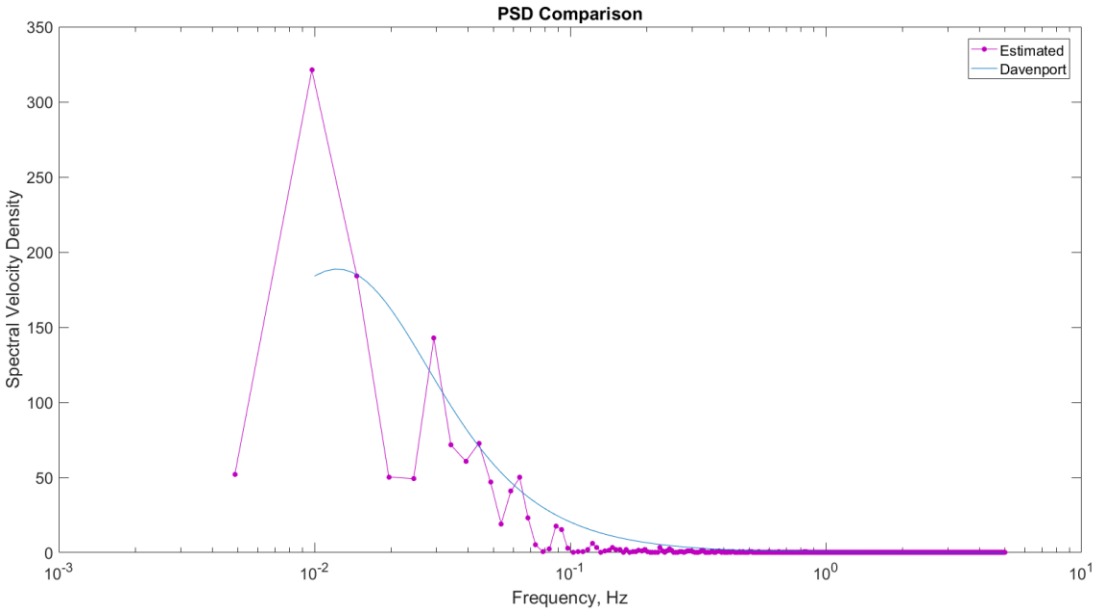

Figure 6.9 – Comparison of Davenport spectrum and PSD of wind speeds generated using the Davenport filter (seed = 3312)

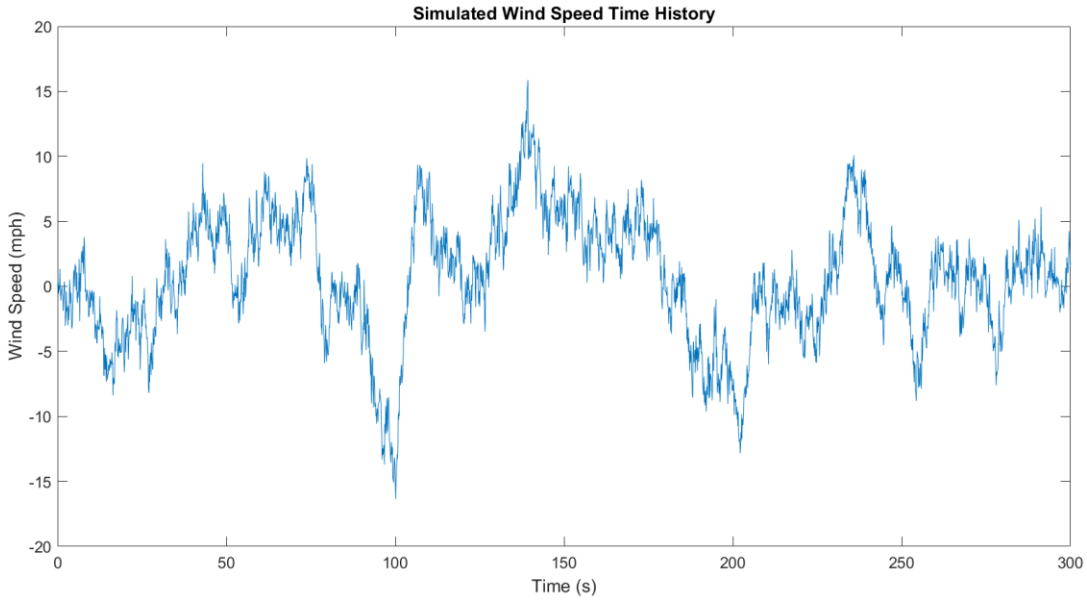

Figure 6.10 – Example wind speed history generated with Davenport filter (seed = 3312)

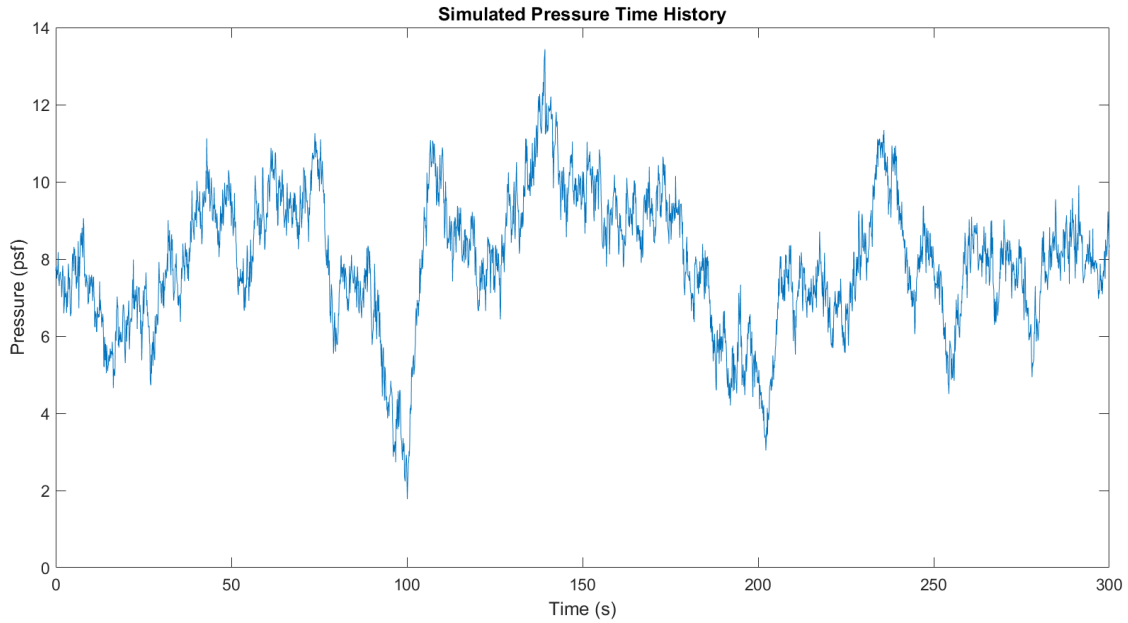

Figure 6.11 – Example wind pressure history generated with Davenport filter (Seed = 3312)

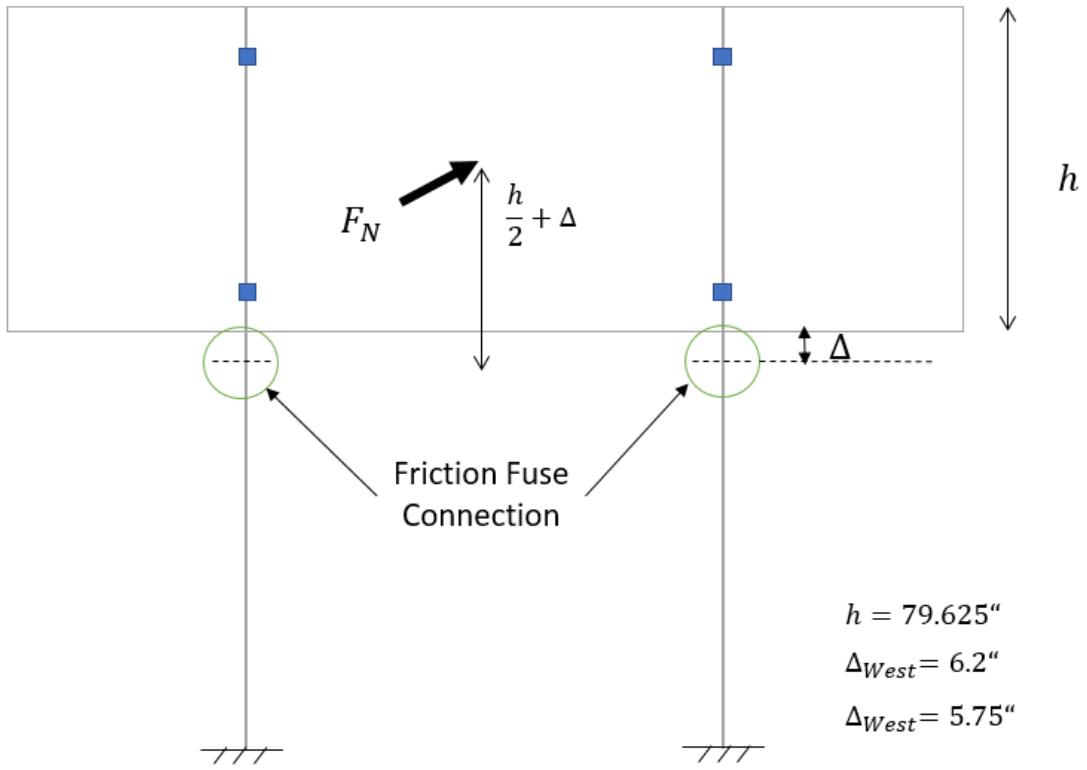

Figure 6.12 – Application of normal wind loading to sign (not to scale)

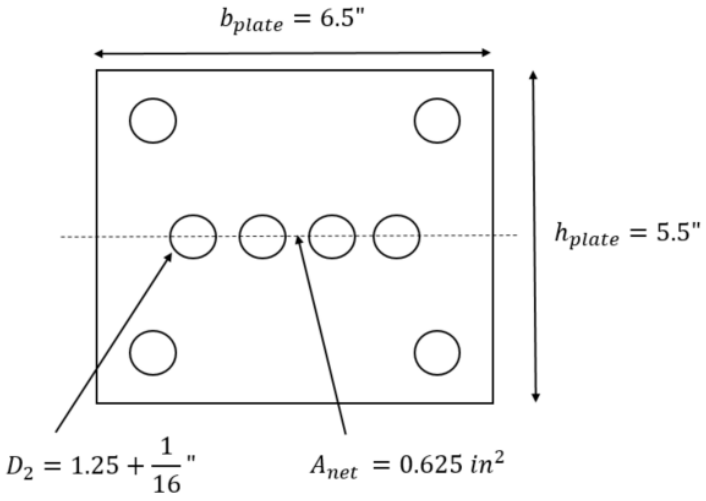

Figure 6.13 – Diagram of fuse plate emphasizing the critical net area (not to scale)

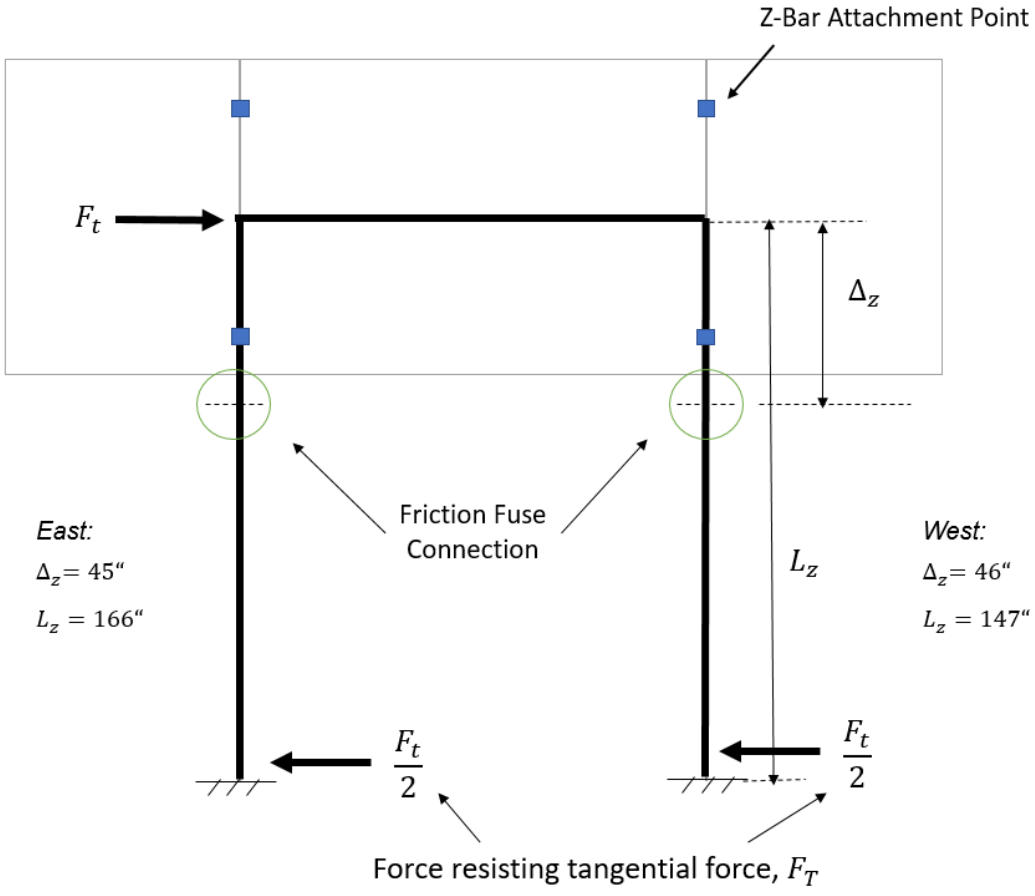

Figure 6.14 – Application of tangential wind loading to sign (not to scale)

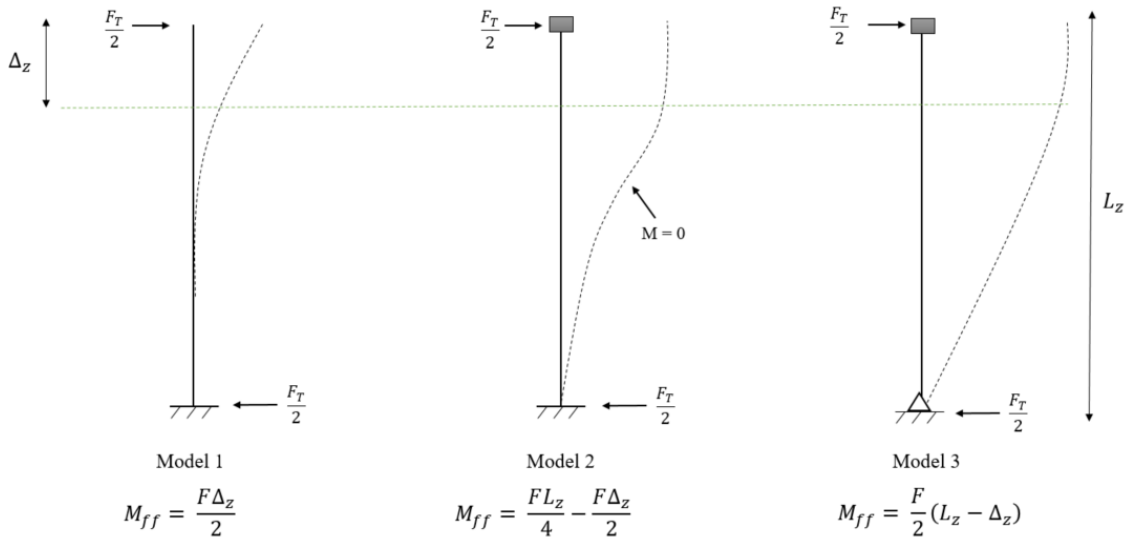

Figure 6.15 – Tangential wind loading column models (not to scale)

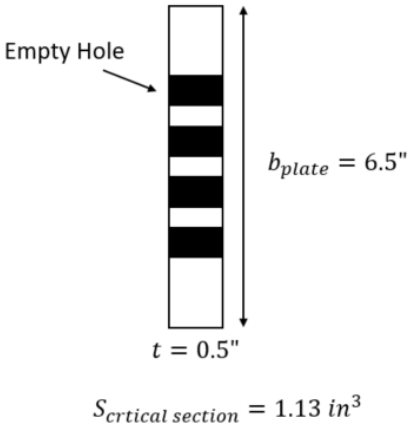

Figure 6.16 – Plan view of critical section used to determine section modulus for tangential loading acting on fuse plate (not to scale)

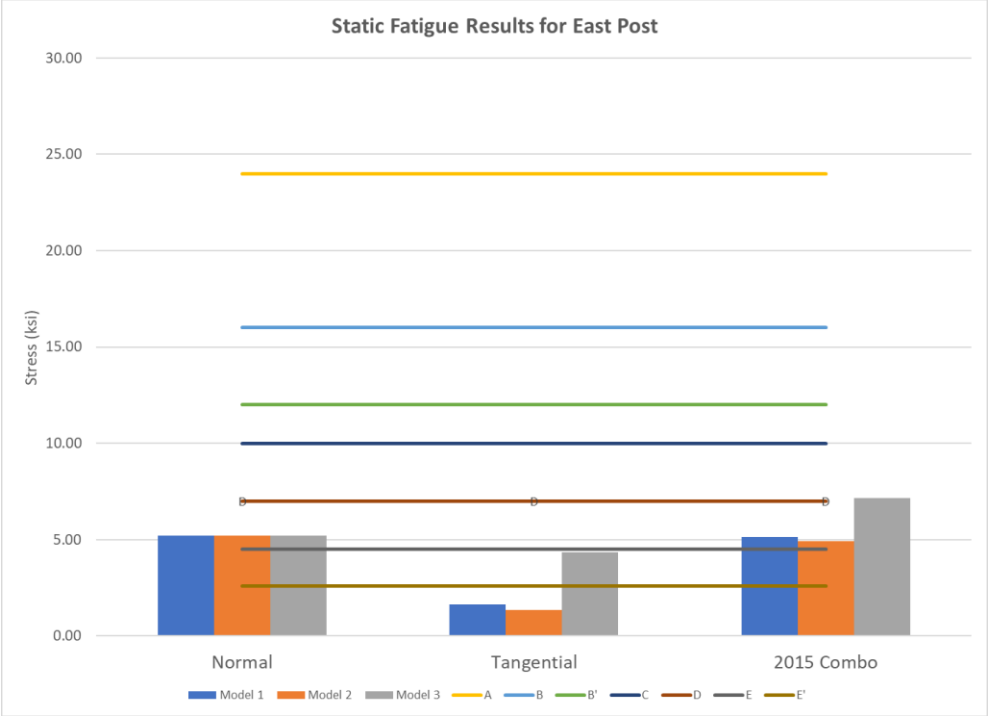

Figure 6.17 – Results of static fatigue analysis in east post for 12.7 mph (5.7 m/s) mean annual wind speed and methods suggested in Article 11.7 (AASHTO, 2015)

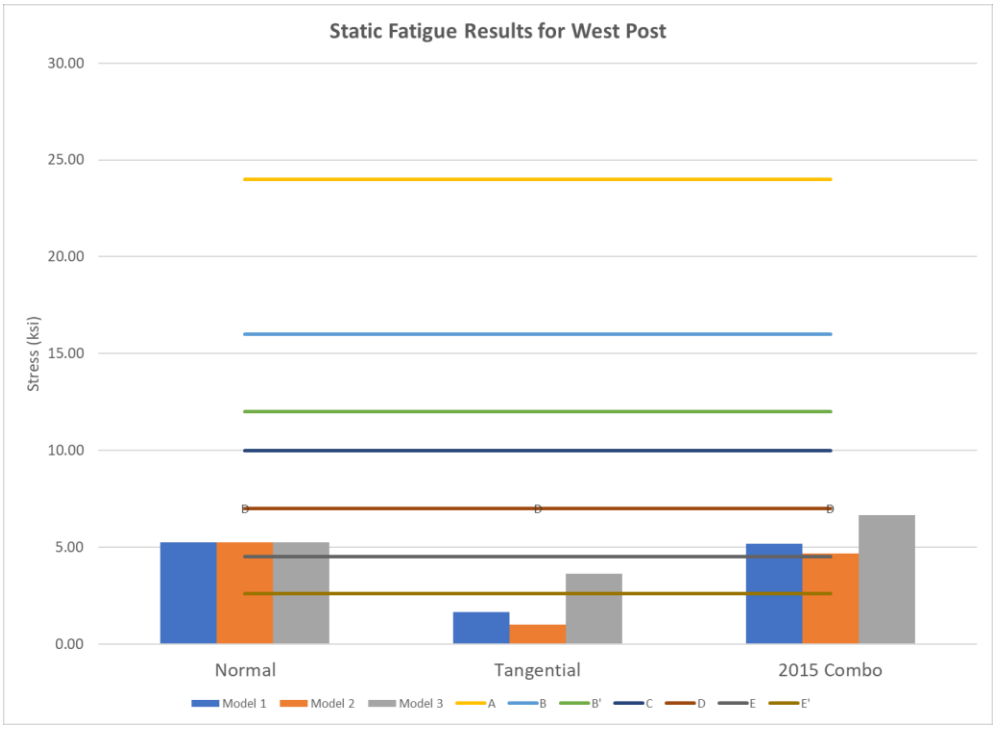

Figure 6.18 – Results of static fatigue analysis in west post for 12.7 mph (5.7 m/s) mean annual wind and methods suggested in Article 11.7 (AASHTO, 2015)

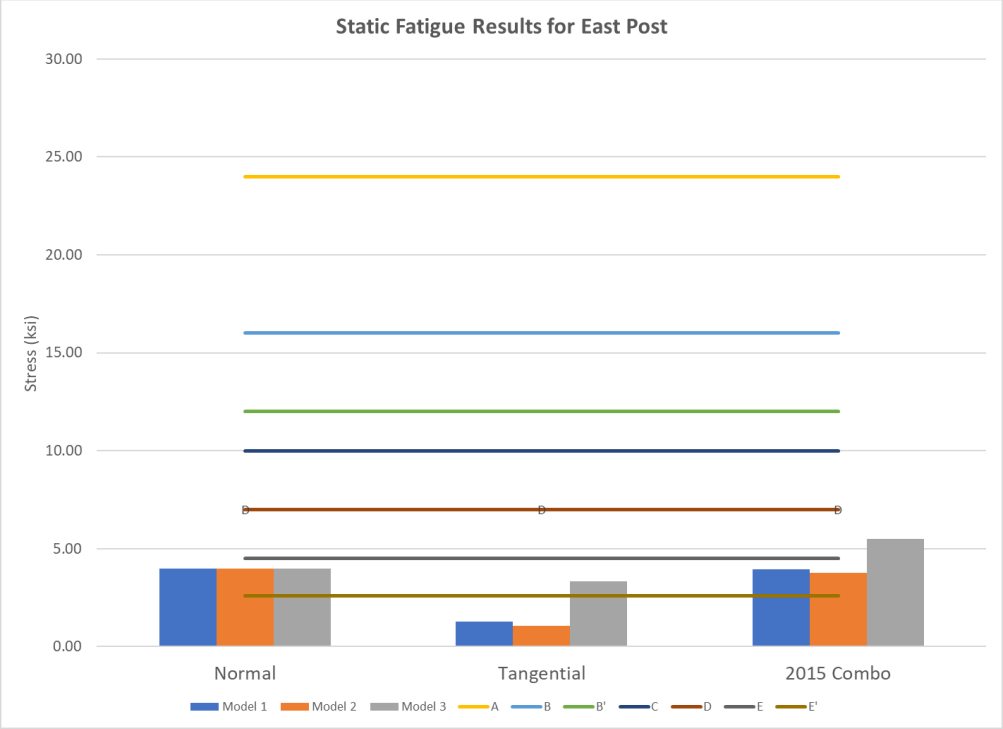

Figure 6.19 – Results of static fatigue analysis in east post for 11.2 mph (5 m/s) mean annual wind and methods suggested in Article 11.7 (AASHTO, 2015)

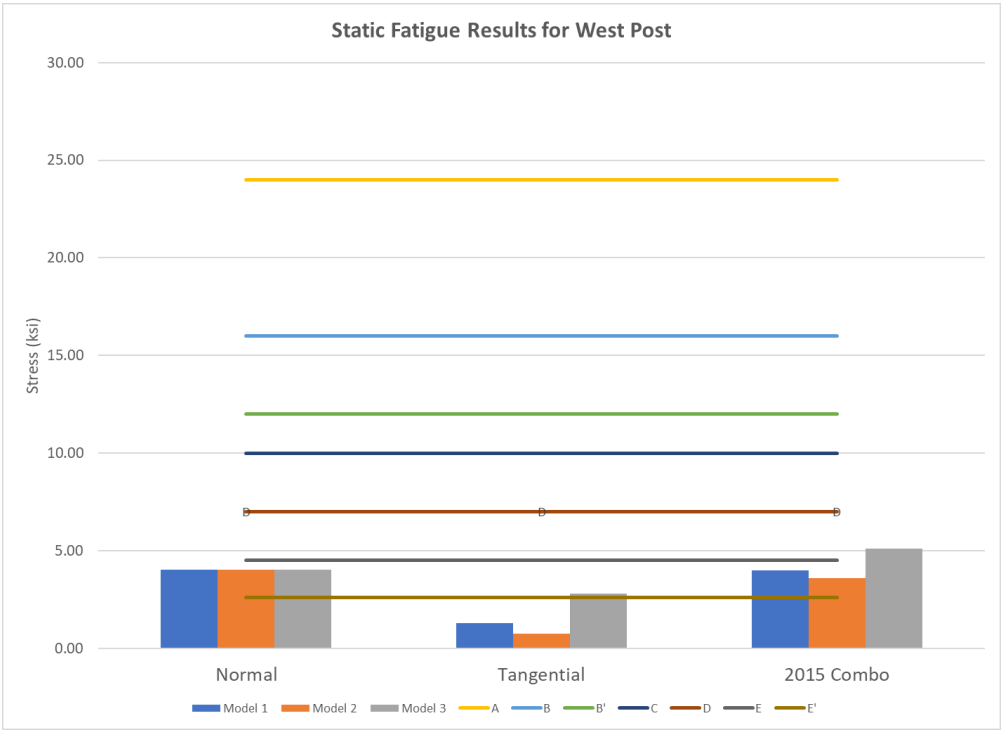

Figure 6.20 – Results of static fatigue analysis in west post for 11.2 mph (5 m/s) mean annual wind and methods suggested in Article 11.7 (AASHTO, 2015)

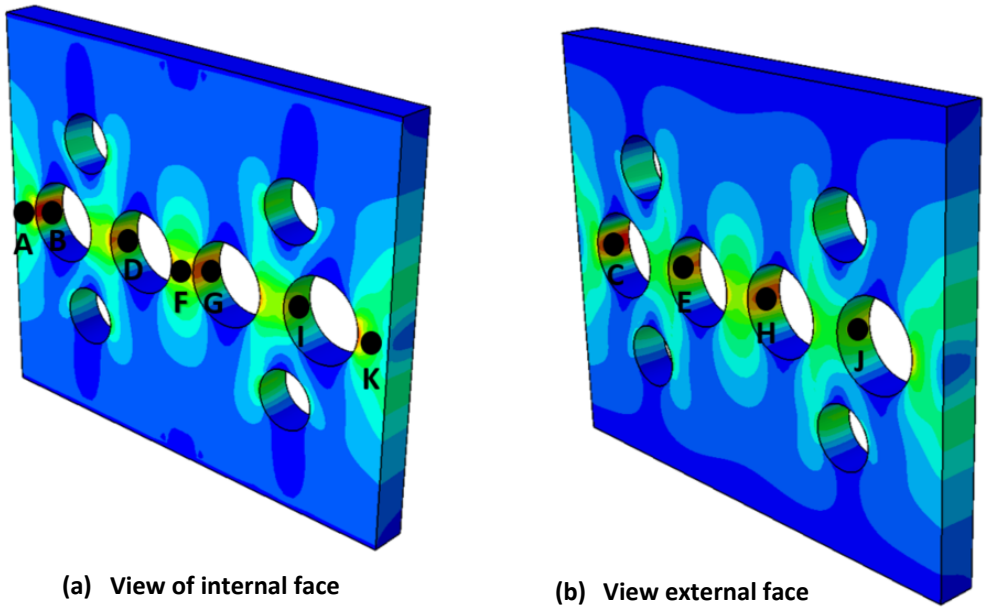

(a) View of internal face

(b) View external face

Figure 6.21 – Stress locations sampled on the fuse plate

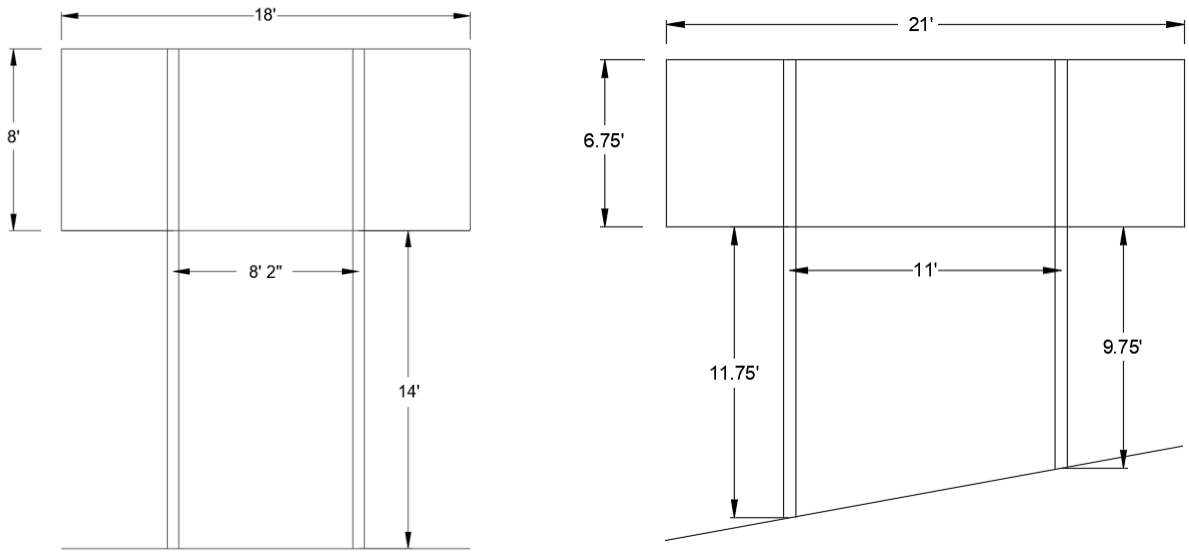

(a) DMS – L1 **(b) DMS – L2**

Figure 6.22 – Other DMS in service evaluated with FEM analysis method.

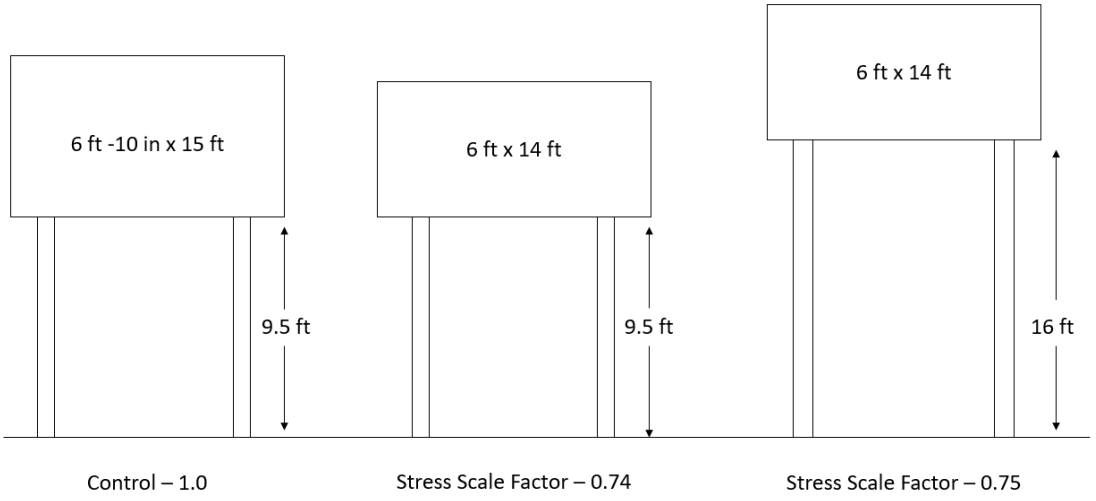

(a) Control compared to smallest DMS panel in service

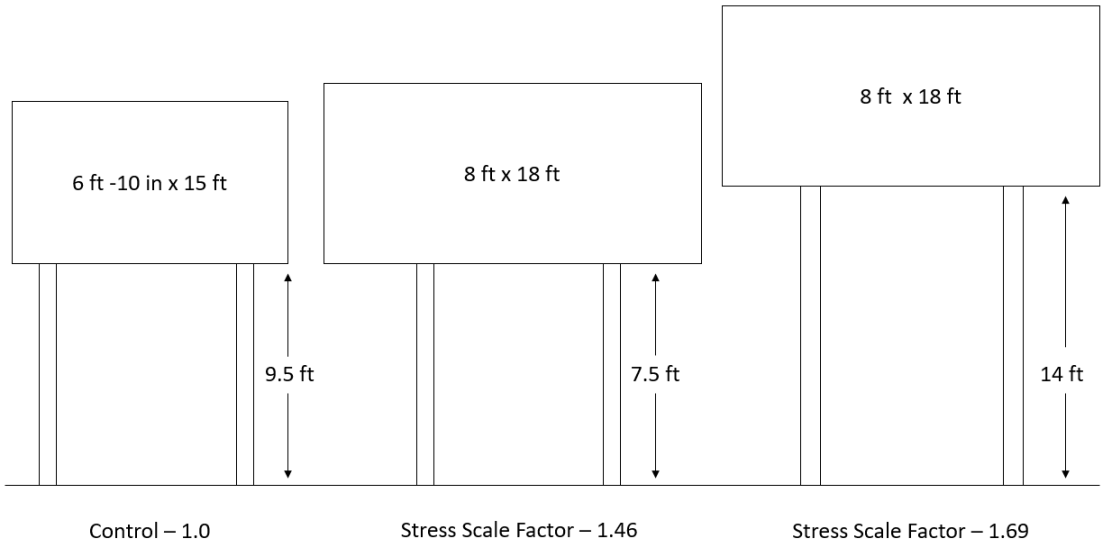

(b) Control compared to largest DMS panel in service

Figure 6.23 – DMS variations and stress scale factor in friction fuse plate

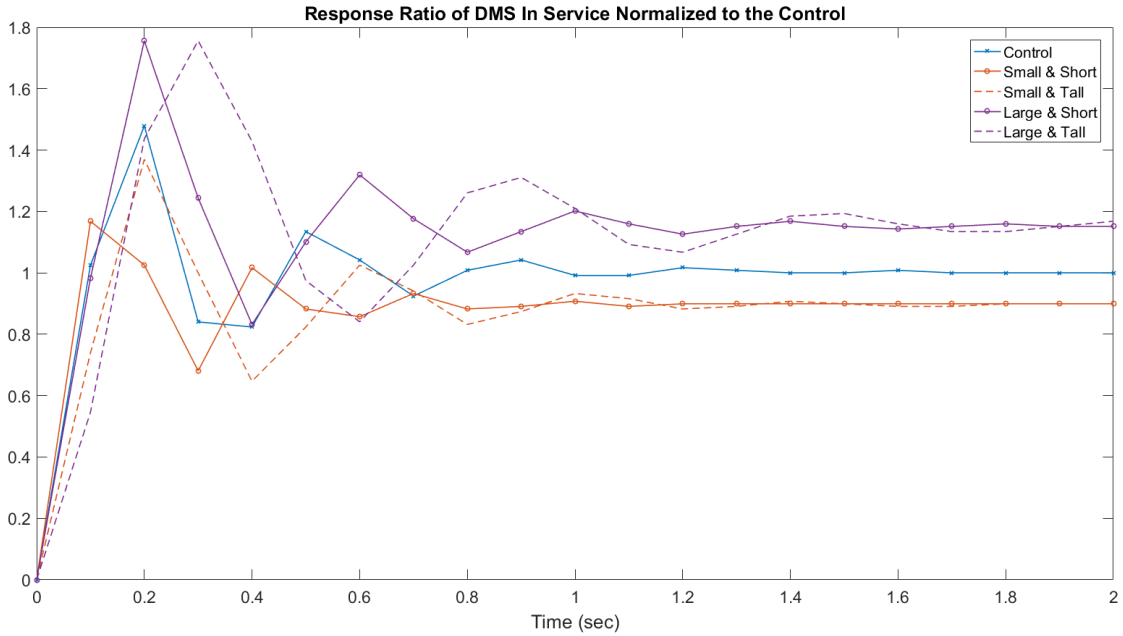

Figure 6.24 – Dynamic amplification: response ratio of DMS in service normalized to the control

CHAPTER 7: RICWS EXPERIMENTAL WORK

7.1 FIELD OBSERVATION SETUP

The Rural Intersection Conflict Warning Sign (RICWS) located on the south side of the intersection of TH-7 and CSAH-1 was instrumented to investigate the dynamic characteristics of the sign subjected to wind loading and to provide data for validating and informing the FEM model and CFD model of the RICWS. The front face of the sign is oriented 15 degrees clockwise from north. Figure 7.1 shows the dimensions for the RICWS instrumented. The final instrumentation setup, shown in Figure 7.2 and Figure 7.3, was selected with consideration for large amplitude displacements that have been observed in the field.

Two accelerometers, two string potentiometers, one cup and vane anemometer, and one temperature probe were installed to monitor the behavior of the RICWS under wind loading. The accelerometers were attached directly to the RICWS at the location specified in Figure 7.2 and were used to capture the dynamic motion of the sign. The two string potentiometers measured the change in displacement between the sign supports and a "fixed" reference point. The wires of the string potentiometers were attached to the RICWS supports at a height of 4 ft.-6in. above ground level (attachment points are shown in Figure 7.2). The housings of the two string potentiometers were attached to a single post placed 3 ft. directly south of the RICWS at the same height, 4 ft.-6 in., to ensure the wires were level. The cup and vane anemometer was used to measure the mean wind speed and direction. Due to the large amplitude oscillations expected of the RICWS, the anemometer and temperature probe were externally mounted adjacent to the sign. These sensors were mounted on a post located 5 ft. directly west of the RICWS. The anemometer was placed 8 ft.-4 in. above ground level and the temperature probe was placed at 7 ft.-4 in. above ground level. A plan view of the sensor layout is shown in Figure 7.3, and an elevation view of the anemometer and temperature probe setup can be seen in Figure 7.4. Examples of the deployed instrumentation are shown in Figure 7.5.

7.1.1 Data Collection Procedures

Data was collected using a CR1000 Campbell Scientific data logger. Unlike with the DMS, the data logger used with the RICWS could support readings from all sensors deployed simultaneously. Data was collected in the field and then transferred via modem to a server accessible by the research team. Wind speed, wind direction, and air temperature were sampled at 1 Hz, while the accelerations and displacements were sampled at 100 Hz. The cup and vane anemometer selected for the instrumentation was limited to a peak wind speed sampling rate of 1 Hz. Temperature and wind direction were not expected to change at a rate faster than 1 Hz, so for simplicity these values were sampled at the same rate as the anemometer. Displacement and acceleration data were sampled at 100 Hz to capture the higher frequency response of the structure and provide opportunity for filtering the data to remove any high frequency noise. The maximum sampling rate of the CR1000 data logger limited the sampling rate of the displacements and accelerations to 100 Hz.

Data collection for the RICWS was also primarily event focused to improve the quality of the data collected. The wind speed, wind direction, air temperature, and two displacement readings were continuously collected at five-minute intervals, and the average values over five-minute periods (5-minute averages) were stored. These averages were collected primarily to investigate long-term data trends and for diagnostic purposes. The fast rate dynamic data (i.e., raw sampled measurements) were saved when a wind speed threshold had been exceeded. The wind speed threshold varied throughout the data collection period and is stipulated in Table B.2.

7.1.2 Data Collection Period

Field data collection for the RICWS began on November 17th, 2017 and continued through May 2020. The majority of the data analyzed is from November 2017 through May 2018. The modification of the RICWS was analyzed between January and May 2020. A log of all major changes to the data collection system is given in Appendix B. High-speed wind events were most prominent during winter and spring months. Field data collection for the RICWS continued over the course of the project.

7.2 LABORATORY EXPERIMENTS AT THE ST. ANTHONY FALLS LABORATORY (SAFL)

The dynamic behavior of the RICWS was also explored with laboratory experiments conducted on a small-scale model at the St. Anthony Falls Laboratory (SAFL). Experiments were done to measure key characteristics of the RICWS behavior that could not be easily measured in the field. These characteristics were later used to validate and inform the CFD model. Two major experiments were done: drag experiments and wake experiments. The same model of the RICWS, as seen in Figure 7.6, was used in both experiments. It was fabricated from stainless steel and scaled approximately 1:18, apart from the plate thickness, with respect to the RICWS instrumented in the field. The thickness of the plates (0.25 in.) was not to scale and was instead chosen to improve the rigidity of the model. The dimensions of the scaled model are given in Figure 7.7. The two lights at the top of the sign structure were designed to be detachable to explore the effect of the lights on the dynamic response of the scaled RICWS model.

7.2.1 Drag Experiments – Tow Tank Tests

The drag experiments were conducted in the main channel facility at SAFL during November 9-10, 2017. The drag experiments were done to identify the drag coefficient of the RICWS and to identify the primary shedding frequency of the structure.

The drag sensor experimental setup is shown in Figure 7.8(a). Five one-dimensional load cells were precisely located and collectively used to measure the forces on the model in the streamwise direction (parallel to flow) and spanwise direction (perpendicular to flow) and the moment in the same plane. Both the instrumentation and the model were attached to the data acquisition cart positioned above the main channel as seen in Figure 7.8(b). Upon command, the data acquisition cart submerged the model at a specified angle and then towed the model through the main channel at a specified speed.

The main channel had no inflow or outflow discharge and was thus considered a still water basin. Therefore, the flow relative to the model was spatially uniform and steady at the speed of the cart. Force measurements were sampled at 50 Hz while the model was towed through the main channel.

The following characteristics were identified from the drag experiments:

- The drag coefficient of the RICWS model, including the lights, was $C_d = 1.34 \pm 0.19$ and was found to be independent of the Reynolds number for the range of tow velocities tested in the experiment (see Figure 7.9).
- Including the lights at the top of the sign increased the mean force and variance measured. The lights were thought to contribute proportionally to the overall drag behavior of the model because the increase in force was proportional to the area contribution of the two lights (the drag coefficient remained essentially unchanged).
- The primary shedding frequency of the model under flow normal to the sign was identified in the spectral analysis of the drag force and was described by a dimensionless Strouhal number of 0.2, determined by (7.1). The Strouhal number of 0.2 was determined based on frequency content in the force component parallel to the relative flow. The natural frequency of the sign model was estimated at around 10Hz and 8Hz for the streamwise and spanwise components of the force, respectively. As clarified later this is due to the larger stiffness of the RICWS sign model, as compared to the real sign.
- For cases with yaw, that is flow at an angle to the sign, the drag coefficient is observed to decrease while the lift coefficient becomes relevant exhibiting a maximum value around 0.75in the range between 45^0 and 60^0 (Figure 7.10).
- The shedding and natural frequencies remained the same under different yaw conditions.

$$S_t = f_s \frac{L_d}{u} = 0.2 \qquad (7.1)$$

where:

$S_t =$ Strouhal number

$f_s =$ Shedding frequency

$L_d =$ Horizontal length across diamond plate

$u =$ Homogeneous upstream velocity

The drag coefficient and shedding frequency were later used to validate the CFD model developed for the scaled model of the RICWS by comparing the drag coefficient and shedding frequency predicted by the experiments done at SAFL with those predicted by the CFD model.

7.2.2 Wake Experiments – Wind Tunnel Testing

Wake experiments were conducted in the wind tunnel facility at SAFL during January 8-10, 2018. Experiments were done to characterize the vertical wake profiles resulting from the inflow turbulent boundary layer. The inflow turbulent boundary layer for three different experimental cases were characterized for use as input conditions to the CFD model. The experimentally measured wake profiles were used to validate the CFD model subject to the respective input conditions.

The inflow boundary layer is the portion of air inflow at the measurement location that varies from zero velocity at the disturbing surface, that is, the wall of the tunnel, to the free-stream velocity achieved at some distance from the wall. In this experiment the boundary layer was classified as turbulent. The vertical wake profile describes the variation in velocity with respect to height within the downstream wake of the RICWS model. Wake experiments were also done to further characterize the shedding behavior of the scaled RICWS model. The scaled model used in the wake experiments was the same as that used with the drag experiments.

The wind tunnel facility at SAFL is a closed-loop boundary layer wind tunnel, which features a turbulence trip at the leading edge of the tunnel. The turbulence trip, composed of wooden spikes on the tunnel floor, disturbs the air flow in the tunnel and develops a turbulent boundary layer that is fully developed at the measurement location shown in Figure 7.11. At the measurement location the test cross section was 5.6 ft. x 5.6 ft. Within the specified cross section, the scaled RICWS model was mounted to the floor of the wind tunnel upstream of a hot-wire anemometer sensor system connected to a motorized traverse system. The motorized traverse system was used to position the hot-wire sensor at various points relative to the RICWS model.

Measurements from the hot-wire sensor were used to describe the wake characteristics of the RICWS model for the applied boundary layer profile. For each measurement location, data was collected for 75 seconds at a sampling rate of 10,000 Hz. In addition to the measurements from the hot-wire sensor, videos were used to capture the horizontal deflections due to the model vibrating under wind loading in the tunnel. Five 20-second videos were taken at 120 frames per second.

The following outcomes were achieved from the wake experiments:

- The inflow turbulent boundary layer for three different experimental cases were characterized for use as input conditions to the CFD model. The experimentally measured wake profiles are used to validate the CFD model subject to the respective input conditions (see Figure 7.12).
- The primary shedding frequency identified in the spectral analysis of the wake velocity matched the shedding frequency identified from the Strouhal number in the drag experiment.

- The observed sign oscillation frequencies were observed to be consistent with the tow tank experiments (Figure 7.12). By reducing the height of the sign the oscillation frequency increased, suggesting an increased stiffness and an increased natural frequency (case 3).

7.3 SUMMARY

The RICWS was instrumented in the field to observe its dynamic behavior subjected to wind loading and to provide field data for validating the coupled FEM and CFD models of the RICWS. The instrumentation setup included accelerometers, string potentiometers, a cup and vane anemometer, and a temperature probe. Sensors were placed to capture the dynamic motion of the sign and accommodate the large amplitude oscillations anticipated. Data collection began in November and continued through the project.

Laboratory experiments were performed to address characteristics of the RICWS behavior that could not be measured in the field. Drag experiments were performed to estimate the drag coefficient and the primary oscillation frequency of the RICWS. Experiments were run at different velocities to distinguish between the natural frequency (invariant with respect to the towing velocity) and the shedding frequency (depending on the towing velocity). Both characteristics were needed for validation of the CFD model. Wake experiments were done to confirm and further characterize the primary shedding frequency of the RICWS. The wake experiments also provided important inflow turbulent boundary layer conditions to be applied to the CFD model. The CFD model will be validated by comparing the resulting wake profiles of the CFD model with those obtained experimentally for the same input turbulent boundary layer conditions.

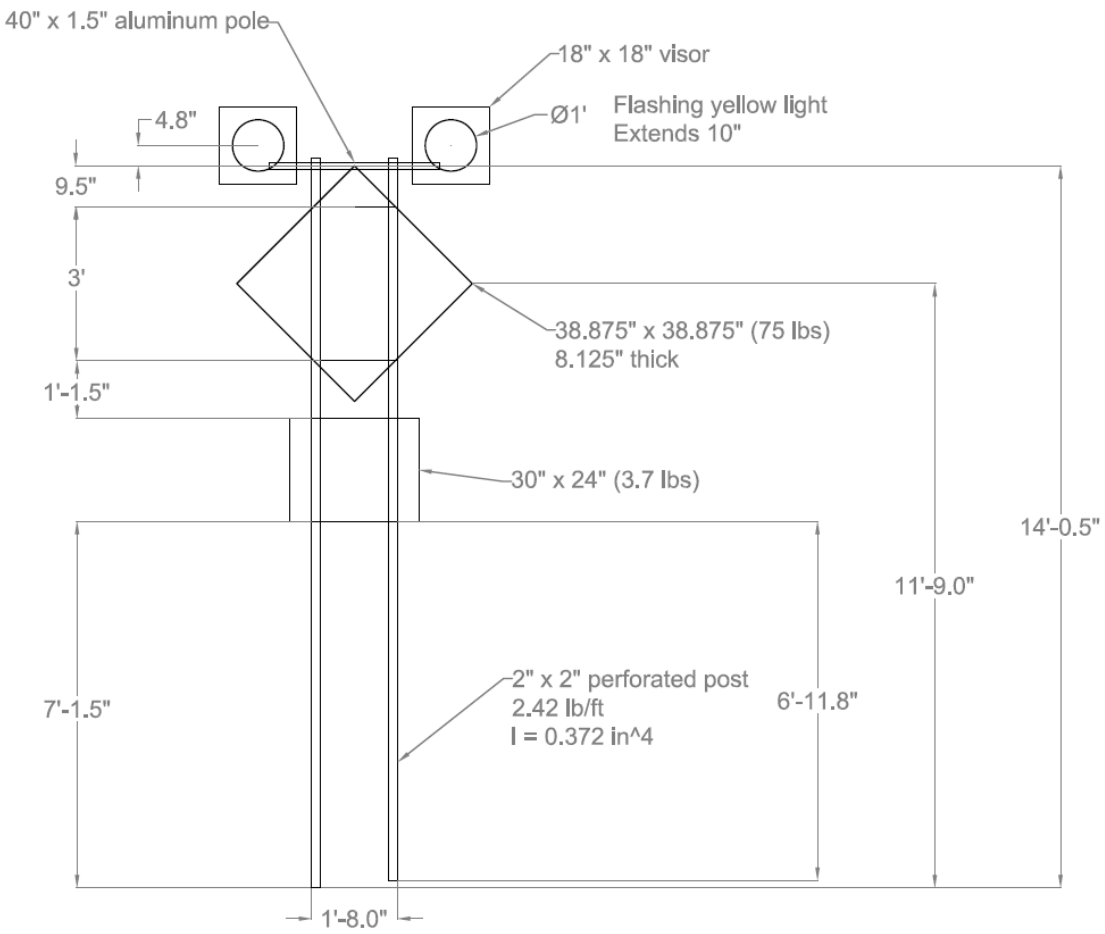

Figure 7.1 – Dimensions of field RICWS

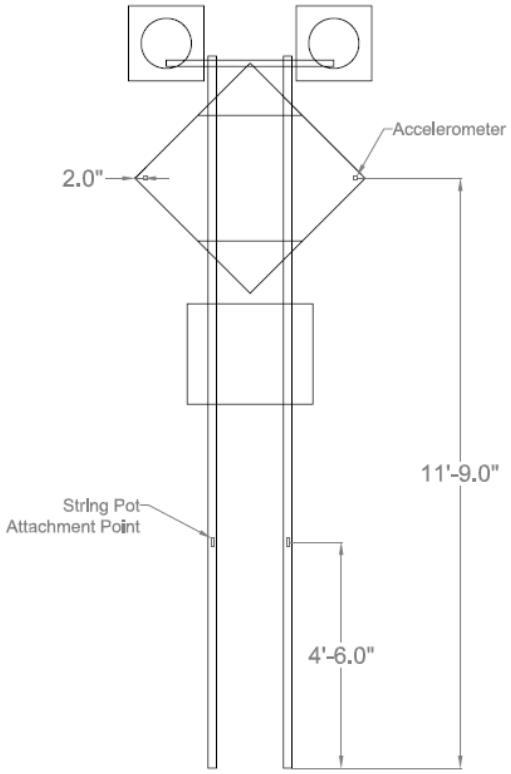

Figure 7.2 – RICWS instrumentation layout

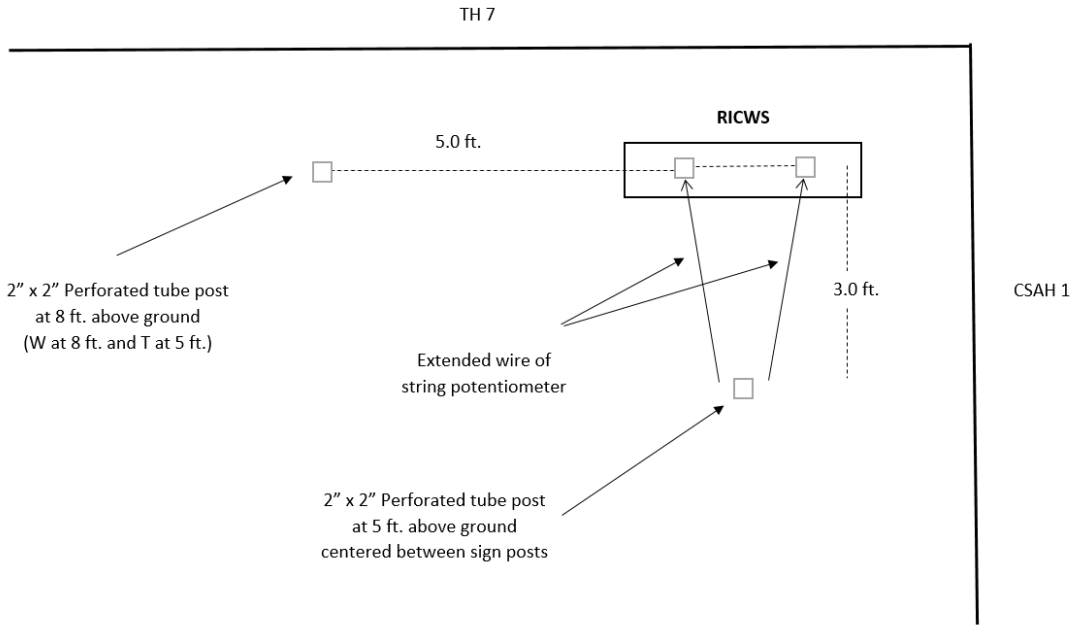

Figure 7.3 – Plan view of sensor layout

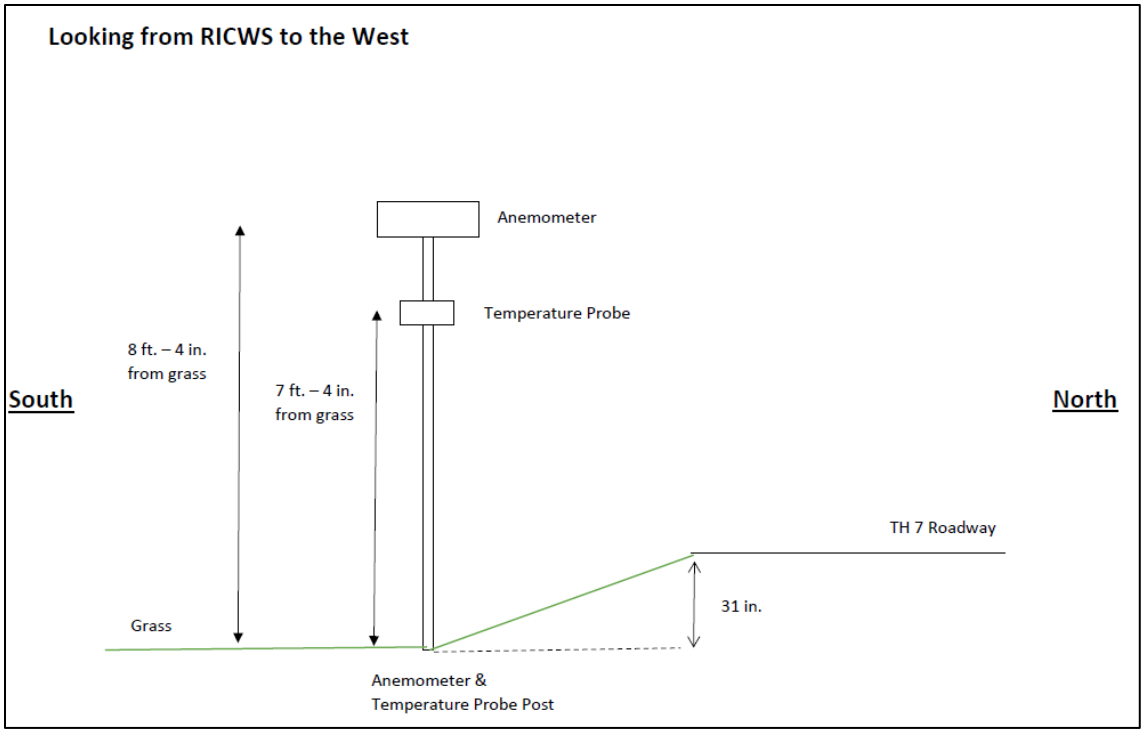

Figure 7.4 – Elevation view of anemometer and temperature probe setup

(a) Anemometer and temperature probe **(b) String potentiometers** **(c) Accelerometers**

Figure 7.5 – RICWS instrumentation

Figure 7.6 – Scale model of steel RICWS with plastic mount

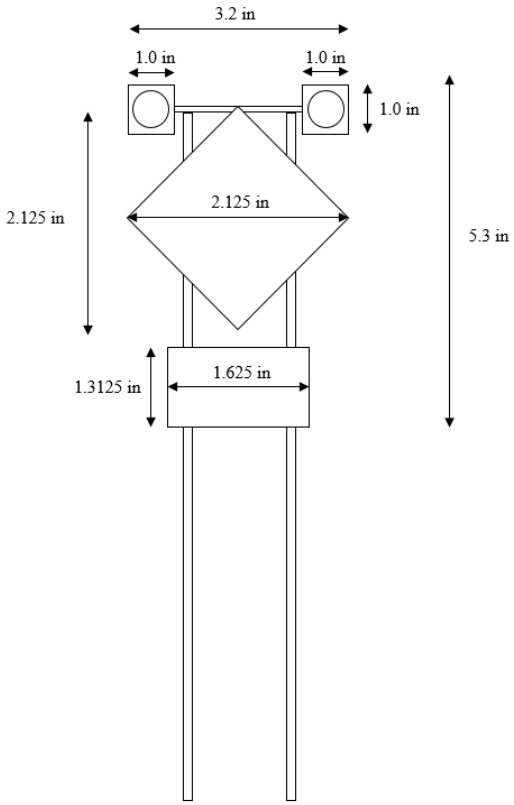

Figure 7.7 – Dimensions of RICWS scale model

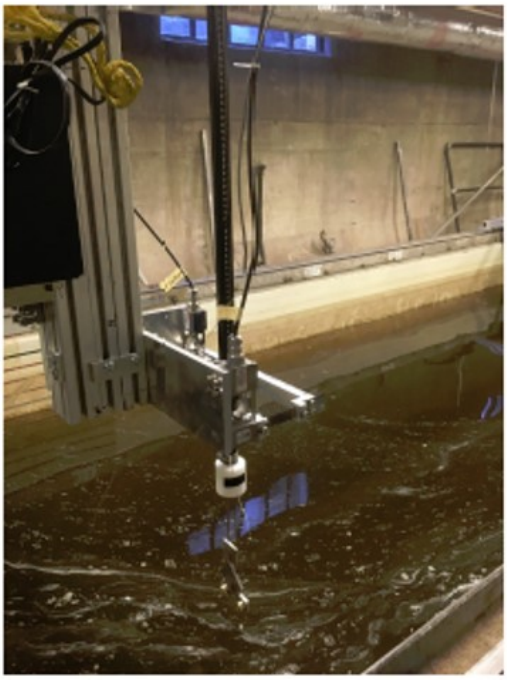

(a) Orientation of model relative to data acquisition cart

(b) Model and instrumentation mounted to data acquisition cart

Figure 7.8 – Drag experiment set up in main channel facility at SAFL

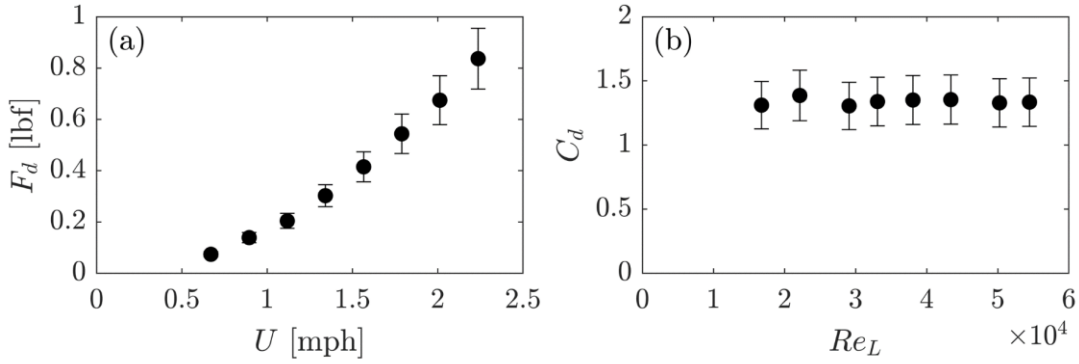

Figure 7.9 - Drag parameters for yaw angle of 0 degrees and lights intact: (a) drag force F_d as a function of inflow velocity U; (b) drag coefficient C_d as a function of Reynolds number Re_L.

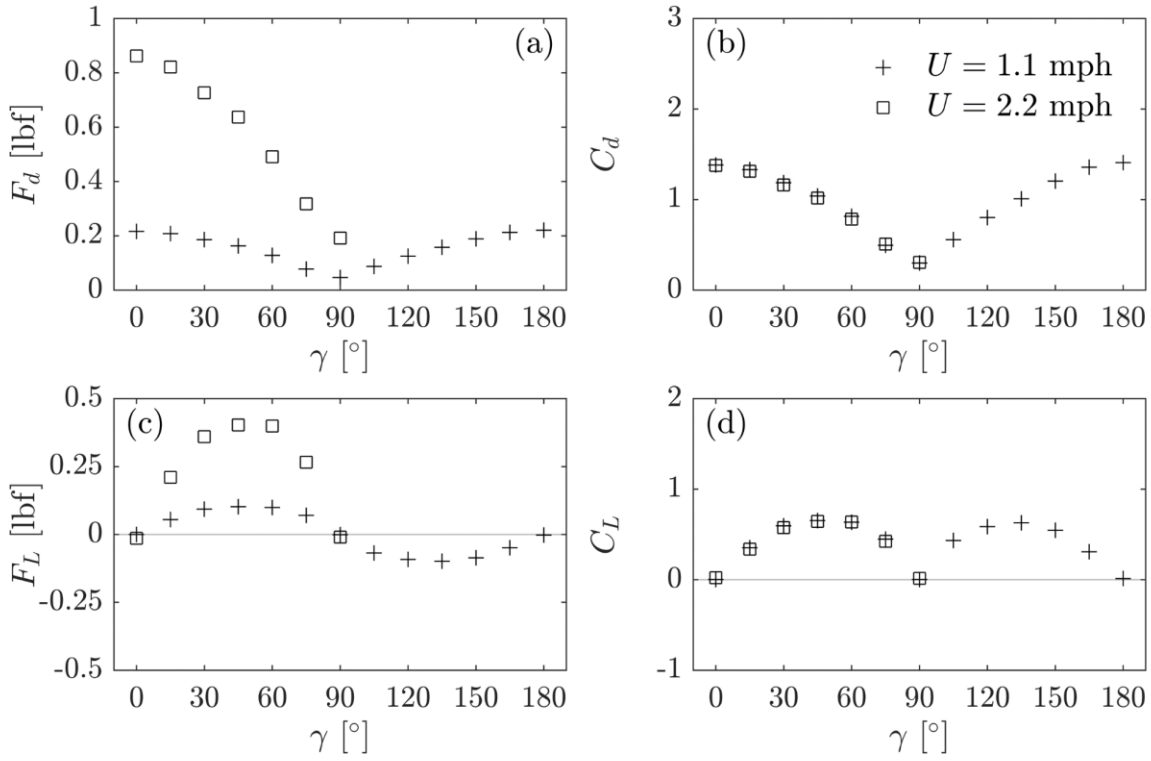

Figure 7.10 - Calculated drag and lift parameters for inflow speeds of 1.118 mph (0.5 m/s) and 2.237 mph (1.0 m/s), as specified in legend graphed as a function of yaw angle between the inflow direction and a vector normal to the face of the model: (a) drag force F_d; (b) drag coefficient C_d; (c) lift force F_L; (d) lift coefficient C_L.

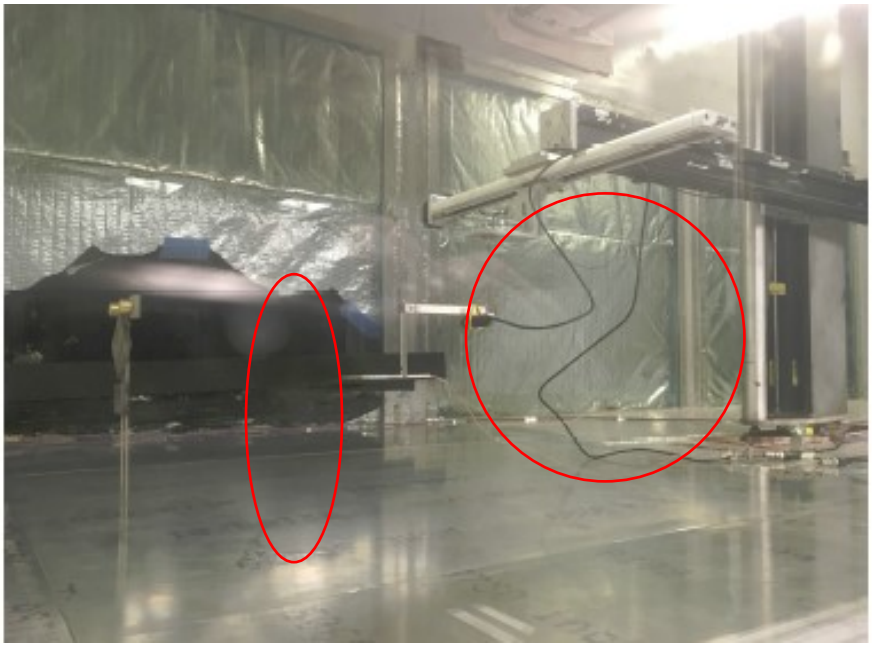

Figure 7.11 – RICWS model and hot-wire probe connected to traverse system in wind tunnel Analysis of RICWS

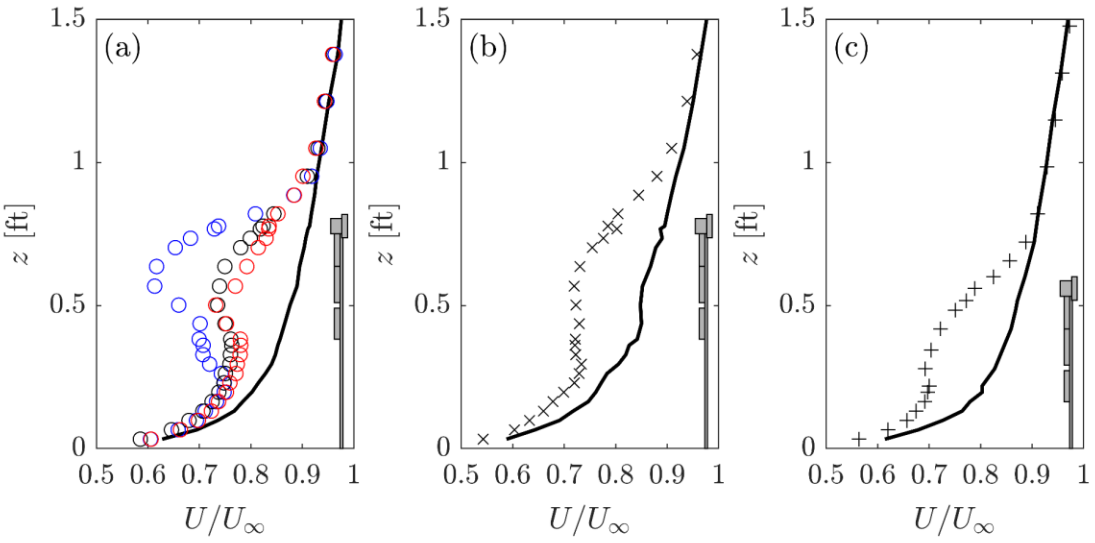

Figure 7.12 - Profiles of the mean velocity U relative to the free-stream velocity U_∞ as a function of height z (0 to 1.5 ft) in the wake (symbols) and inflow (black lines) conditions: (a) case1 U_∞ =16.78 mph (7.5 m/s) ; (b) case2 U_∞ = 7.83 mph (3.5 m/s); (c) case3 U_∞ = 16.78 mph (7.5m/s) (reduced height). Data marker colors indicate downwind distances 2H (blue), 4H (black), and 6H (red), where H = 0.8 ft (specimen height).

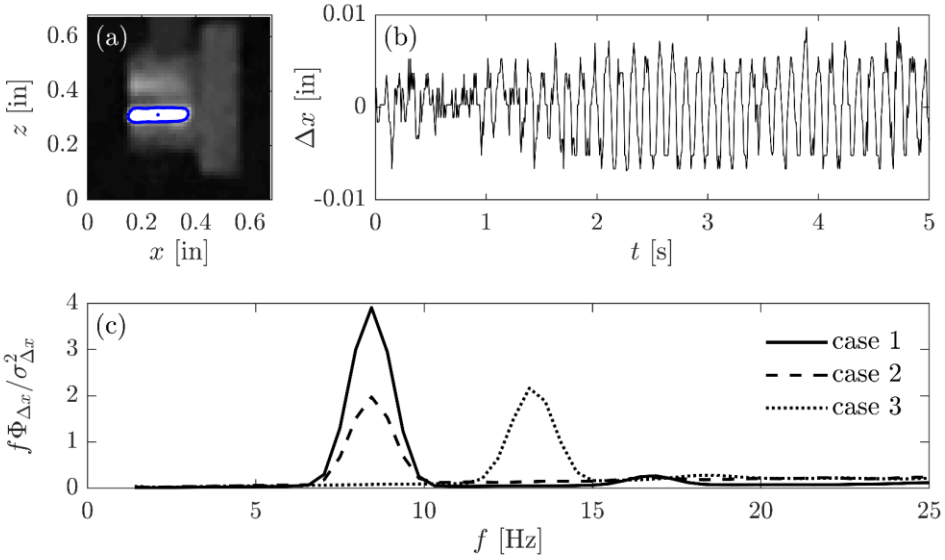

Figure 7.13 - Vibration analysis from video of the sign model: (a) example video frame showing the side of the top plates, the detected reflection from the cylindrical plate (blue outline), and centroid of the reflection (blue dot); (b) example 5-second time series of the horizontal deflection Δx calculated as the displacement of the reflection centroid; (c) pre-multiplied energy spectra of the deflections Δx as a function of frequency f, normalized by the deflection variance: case1 U_∞ = 16.78 mph (7.5m/s) ; (b) case2 U_∞ = 7.83 mph (3.5 m/s); (c) case3 U_∞ = 16.78 mph (7.5m/s) (reduced height and increased stiffness).

CHAPTER 8: ANALYSIS OF RICWS

The RICWS located at the south side of the intersection of TH-7 and CSAH-1 was instrumented to observe the behavior of RICWS subjected to wind loading. An FEM model and CFD model were developed to explore the wind-induced behavior of the RICWS. The field data helped quantify the possibility of resonance and vortex shedding. Additionally, the field data was used to validate the FEM model, as well as the coupled FEM and CFD model of the RICWS. The CFD model was also validated and informed using data collected through the experiments at SAFL. The validated models and field data informed possible modifications to reduce the structural response: adjusting dynamic behavior, aerodynamic modification, and use of a non-commercial damper. One proposed modification was implemented in the field and evaluated for effectiveness.

8.1 FIELD DATA ANALYSIS

Of the several wind events triggered during the analysis of the RICWS field data, fourteen critical wind events were selected for detailed analysis. Critical wind events were selected based on the peak wind speed exhibited in the event and/or the primary wind direction of the event (Table 8.1 and Table 8.2). Additional wind events were selected between November 2017 and March 2018 to generally study the dynamic behavior of the RICWS under different wind directions, and under different wind speed within a narrow range of directions (mostly normal to the wind).

All preliminary data analysis was done at a sampling frequency of 1 Hz. This was done for two main reasons. First, displacement data collected at 100 Hz was noisy. Filtering and downsampling to a sampling rate of 1 Hz smoothed the data significantly and made observing basic trends in the data much easier. Second, because the wind data was collected at 1 Hz sampling, it was not possible to develop an accurate estimate of the pressure, and consequently the force on the structure for changes occurring faster than a frequency of 1 Hz. Any comparison done with the field data required knowledge of the force applied to the structure, so comparisons needed to be performed at a sampling rate of 1 Hz.

8.1.1 Frequency Response -Vortex Shedding

The key concern for RICWS was the potential for large amplitude oscillations. Initial analysis of the displacement time histories and the corresponding wind speed and directions showed that ranges of wind speeds led to increased oscillatory response. Consequently, vortex shedding was considered to be a key to the system response and frequency response analysis of both the displacement and acceleration data was a critical component in the evaluation of the field data.

The frequency response analysis of the acceleration data identified two key natural frequencies. Figure 8.1 illustrates the two key natural frequencies identified by each accelerometer. The first natural frequency was found to vary from 0.7 to 1.1 Hz. The second peak in Figure 8.1 refers to the second significant frequency captured by the accelerometers. Because the accelerometers were placed normal to the sign, only mode shapes with movement normal to the sign was captured by the accelerometers.

The mode shape associated with Peak 2 has characteristics of a torsional mode, but due to the accelerometer placement it is unclear whether this frequency peak refers to the second or third mode.

The frequency response analysis of the displacement data only captures the first natural frequency, which aligns closely with frequency identified with accelerometer data. The spectral energy plotted in Figure 8.2 has a clear first frequency peak that ranges from 0.8 to 1.3 Hz. The large DC components in the plot are from the fixed offset of the potentiometer measurements and can be neglected. The potentiometers were not able to capture the higher frequency behavior.

The magnitude of the accelerometer and displacement spectral energy results do not vary linearly with wind speed (Figure 8.1 and Figure 8.2). This velocity dependent response supports the idea that vortex shedding may be occurring. The first natural frequency is largest from wind speeds that range from 15 to 18 mph (7 to 8 m/s). This range is not the same for the second peak, which suggests that resonance with the first natural frequency is more probable.

The relation between natural frequency and air temperature was not as prominent in the RICWS as it was in the DMS (Figure 8.3). The support posts of the DMS were extended from the base connection directly into the ground. The stiffness of the soil around the support posts likely directly affected the stiffness of the DMS base connection. In contrast, the slip base connection of the RICWS as shown in Figure 8.4 and Figure 8.5 was composed of three layers of square tube posts, in which each consecutive layer was placed within the previous. Furthermore, only one corner bolt was used to secure the tube post within the other two layers of tubing imbedded in the ground. A significant amount of slop was observed in the base connection when installing instrumentation in the field. It was hypothesized that the colder temperatures did result in the ground freezing, but the slop observed in the base connection reduced the effect of the frozen ground on the stiffness of the base connection.

To explore the potential for resonance in the sign, the first natural frequency identified from the displacement data and accelerometer data is compared with the shedding frequency. The shedding frequency was computed using the Strouhal number recommended by the drag and wake experiments done at SAFL of 0.2.

$$f_s = S_t \frac{u}{L_d} \qquad (8.1)$$

where:

$S_t =$ Strouhal number, 0.2

$f_s =$ Shedding frequency

$L_d =$ Horizontal length across diamond plate, 54.97 in

$\boldsymbol{u} =$ Homogeneous upstream velocity (in/s), see Table 8.1

The length of the diamond sign was taken as the widest length across the surface of the diamond, normal to the N-S direction, and the upstream velocity was taken as the raw mean wind speed of the event. This value varies with each wind event. Consequently, the shedding frequency varies with each wind event. Variation in the observed oscillating frequency f_o and in the expected shedding frequency f_e are plotted in Figure 8.6 for events with the wind normal to the sign at different speeds (Table 8.1). Additionally, variation in the observed oscillating frequency f_o and in the expected shedding frequency f_e are plotted in Figure 8.7 as a function of wind direction for wind events of approximately the same wind speed (Table 8.2). Note that the overlap between shedding and observed frequency is significant. Also consider that the estimated natural frequency from the accelerometer data is very close to the observed oscillation frequency determined from the displacement data.

Alignment between the shedding frequency, natural frequency, and oscillation frequency implies that vortex shedding, specifically the phenomenon of lock-in, may play a prominent role in the large amplitude oscillations observed in the RICWS (Williamson & Govardhan, 2004). Vortex shedding occurs within a small window of wind speeds, generally between 10 and 35 mph (Kaczinski, Dexter, & Van Dien, 1998). Figure 8.8 displays the long-term wind speed data observed for the RICWS. Wind speeds consistently fall into the range susceptible to vortex shedding, giving even stronger indication that vortex shedding likely plays a significant role in the dynamic behavior of the RICWS under wind loading.

8.2 NUMERICAL MODEL VALIDATION

A FEM model of the RICWS structure and a CFD model of the surrounding airflow were developed to consolidate the experimental observations reported in Sections 7.2 and 8.1 and to explore potential modifications of the RICWS configuration that reduce wind-induced vibrations. In the following, the results of two validation studies, one for the structural FEM model and one for the CFD model, are reported. The validation results confirm that both models represent all critical phenomena observed in the field and in the SAFL experiments to such an extent that qualitative and quantitative conclusions can be drawn from the coupled simulation results. These simulation results will be presented in Section 8.3.1.

8.2.1 FEM Model

Abaqus© (version 6.13.2) was used to create the structural model of the RICWS. The support posts were modeled using standard beam elements and properties specified by the manufacturer of the support posts, Telespar. The posts were assumed to be ASTM A36 steel, and the structure was assumed to be linear elastic. All sign panels and lights were modeled with rigid shells to eliminate any local plate deformation. The FEM model of the RICWS can be seen in Figure 8.9. The structure is discretized with Reissner-Mindlin shell elements (STRI65 in Abaqus) and beam elements (B32 in Abaqus), involving 3,100

elements in total. Coupling and MPC constraints are used to strongly enforce coupling between panels and beams.

Based on the slop observed in the base connection in the field and the variation in the natural frequency of the RICWS with air temperature, it was assumed that the base connection was not fully fixed at the ground. The length of the RICWS model was adjusted such that the first natural frequency was approximately 1.1 Hz. Adding an additional 3 ft. to the structure beyond the length of the post measured above ground reduced the stiffness of the model and more closely resemble the conditions observed in the field at the base connection. The length was added through an iterative process until the desired first natural frequency of 1.1 Hz was achieved. The natural frequencies and corresponding mode shapes of the RICWS predicted by the model can be seen in Figure 8.10. Figure 8.11 compares the high energy frequencies observed for Wind Event 11/29 at 2343 with the natural frequencies predicted by the FEM model. Good alignment was seen between the first natural frequency measured in the field and that predicted by the FEM model. The mode shape corresponding to the next frequency peak captured by the accelerometer data has characteristics of a torsional mode. Both the second and third mode predicted by the model feature characteristics of a torsional mode. It can be concluded that the accelerometer data is unable to capture the second significant frequency, but the next significant frequency captured by the accelerometer data corresponds to the third mode. The slight mismatch between the accelerometer data (5.0 Hz) and the FEM model (4.7 Hz) is likely to stem from the stiffness assumptions in the FEM model, in particular the one of rigid plate elements in all panels.

8.2.2 CFD Model

For the simulation of the airflow around the RICWS structure, a CFD model based on the finite element method is used. To this end, the airflow is modeled by the Navier-Stokes equations for momentum conservation and continuity equation for mass conservation under the assumption of incompressible flow. The finite element implementation used is based on linear basis function to discretize velocity and pressure. For propagating the solution in time, the generalized-α time integration scheme is employed. To account for turbulent effects in the flow, the variational multiscale (VMS) method is applied, which has been shown in the literature to be an effective subgrid-scale model for solution behavior that cannot be fully resolved by the grid. For further details on the variational multiscale method for turbulence modeling, interested readers are referred to (Bazilevs, Calo, Cottrell, Hughes, Reali, & Scovazzi, 2007). The VMS method has been shown to be the naturally emergent subgrid-scale model when the finite element method is used, versus the more well-known Spalart-Allmaras, k-epsilon and k-omega RANS models or dynamic Smagorinsky LES models which were designed for finite difference or finite volume schemes (Hughes, Mazzei, & Jansen, 2000, Stoter 2017, Stoter, Turteltaub, Hulshoff, & Schillinger, 2018). It is noted that the so-called SUPG, PSPG and LSIC terms as detailed in (Tezduyar & Osawa, 2008) are applied. The SUPG parameter relates the residual of the momentum equation and the fine-scale velocity, and the LSIC parameter relates the residual of the continuity equation and the fine-scale pressure. Based on the SUPG, PSPG and LSIC terms, further terms are added to arrive at the complete VMS model as detailed in (Bazilevs, Calo, Cottrell, Hughes, Reali, & Scovazzi, 2007). The CFD methods are implemented in the framework of the open-source software FEniCS (Logg, Mardal, & Wells,

2012). The resulting set of discrete nonlinear equations are solved via the Newton Raphson method, where each iteration uses an iterative GMRES solver and a preconditioner based on the algebraic multigrid method to guarantee fast convergence.

In the first step, the CFD model is validated against the results of the drag experiments in the SAFL tow tank, described in Section 7.2.1. To model the sign resistance, only the four components that make up the majority of the wind resistance are considered (two sign panels and two lighting components). To represent the conditions in the tank, the four relevant components of the structure are embedded in a box as shown in Figure 8.12. The computational flow domain is 3.9ft x 2.6ft x 2.6ft (1.2m×0.8m×0.8m). The open-source software Gmsh (Geuzaine & Remacle, 2009) is applied to construct a graded mesh that consists of approximately 4 million tetrahedral elements. With respect to the drag experimental set-up, the following boundary conditions are chosen. At the inlet, a constant inflow velocity of u = 0.67 mph (0.3 m/s) is prescribed, while the imposed condition at the outflow boundary is zero pressure. At all boundaries along the main velocity direction, symmetry boundary conditions are imposed. At the surfaces of the RICWS model, no-slip conditions are imposed. The time step size is $3 \cdot 10^{-4}$ s, and the number of time steps is 15,000. Thereby, the total simulated time is 4.5 seconds.

The mean drag coefficient ($\overline{C_d}$) and mean lift coefficient ($\overline{C_l}$) were calculated from the simulation using response data from the 5,000th time step to the 15,000th time step. The mean drag force of the simulation is 0.074 lbf (0.3298 N), and the mean drag coefficient of the simulation is $\overline{C_d} = 1.314$. This result compares well with the drag coefficient obtained from the experiment, which is $\overline{C_d} = 1.34$. In the simulation, the mean lift force is 3.14 x 10^{-4} lbf (0.0014 N), and the mean lift coefficient is $\overline{C_l} = 0.029$. This corresponds well to the lift coefficient measured in the experiment, which is $\overline{C_l} = 0.04$. The standard deviation of the drag force, F_d, is 0.009 lbf (0.04 N) in the simulation, and the experimental value is 0.014 lbf (0.066 N). The normalized (by mean drag force) standard deviation of F_d is 0.12, and the normalized standard deviation F_d from the experiment is 0.19. The computed primary shedding frequency is f_s = 0.67 Hz, which agrees reasonably well with the primary shedding frequency f_s = 1.00 Hz obtained from the drag experiment. These results are summarized in Table 8.3.

In the second step, the CFD model of the RICWS structure is validated with respect to the wake experiments described in Section 7.2.2, which were conducted in the SAFL wind tunnel with a small-scale RICWS model. The CFD simulation model and its most important parameters are as follows. The computational domain at the laboratory scale is 4.6ft x 3.3ft x 1.8ft (1.4m×1.0m×0.54m), which are meshed with approximately 5.1 million tetrahedral elements by the Gmsh software (Geuzaine & Remacle, 2009). Figure 8.13 illustrates the mesh and the position of the sign at the model scale that was used in the SAFL wind tunnel. Again, only the parts of the RICWS sign that represent serious obstacles to the airflow are taken into account. These are the two main panels and the top lights, including the smaller panels around the lights. The mesh near the obstacles is refined to help resolve boundary layers and in the wake region to capture vortices in the wake of the sign structure. No-slip boundary conditions are applied at the wind tunnel wall and at the surface of the RICWS structure, and zero pressure boundary conditions at the outlet. For all other boundaries, symmetry conditions are applied. The time

step is 4×10^{-4}s and the number of time steps is 40,000. The total simulated time therefore amounts to 16s, computed with 240 parallel cores on the Minnesota Supercomputing Institute's Mesabi cluster, where the computation time for each time step is about 6.0s. In order to represent the incoming turbulence of the wind at the inlet, a channel flow simulation without the sign structure was set up that was run to obtain corresponding inlet boundary conditions. The comparison of velocity results obtained from the channel simulation and a free channel wind experiment at SAFL is shown in Figure 8.14, which indicates good agreement. It is noted that the mean and standard deviation of the velocity exclude the first 10,000 time steps to make sure we do not account for effects from initial conditions. It is noted, however, that the difference between results of CFD simulations with incoming turbulence and with uniform inflow velocity were found to be negligible. Therefore, it was decided to apply uniform inflow boundary conditions at the inlet in all CFD simulations that are presented in the remainder of this report.

With the CFD model for the RICWS structure set up, the mean velocities and their root mean square in the wake of the RICWS structure can be computed. Their profiles are compared at three different positions in the wake of the structure (x = 2H, 4H, 6H, where H is the total height of the sign model), where corresponding measurements were taken in the SAFL wind tunnel (see Section 7.2.2). Figure 8.15 shows some of the results, where it can be observed that the general shape of the mean velocities and their root mean squares are in good agreement with the results from the wind tunnel experiments. It is noted that the x-direction is the main wind direction perpendicular to the sign panels of the RICWS and the y-direction is the in-plane axis of the sign panels tangential to the channel wall. Figure 8.16 plots some instantaneous and averaged solution fields over the central plane, spanned by the main wind direction and the axial direction of the sign structure. It can be observed that the CFD simulations successfully reproduce the shedding of vortical structures in the wake of the RICWS.

8.3 POTENTIAL MODIFICATIONS

Vortex shedding can be mitigated by changing the dynamic characteristics or aerodynamic properties of the structure. The dynamic characteristics of the sign, that is, stiffness or mass, can be modified such that the natural frequency of the structure no longer aligns with the shedding and oscillation frequency. Alternatively, the aerodynamic properties of the sign could be altered; for example, by removing the light background shields, the vortex shedding and the accompanying force would be reduced. A mechanical damper could also be employed to reduce the amplitude of the oscillations observed in the RICWS. Mechanical dampers are often used in luminaires to reduce the amplitude of the oscillations observed in the structures under vortex shedding (Dexter & Ricker, 2002).

8.3.1 Dynamic Characteristic Modification – Height Adjustment or Increased Fixity

Currently, the first natural frequency of the sign structure aligns with the shedding frequency over commonly observed wind speeds. This alignment leads to vortex shedding and increased dynamic response. Altering the natural frequency to be far from the shedding frequency would reduce the likelihood of vortex shedding and the associated dynamic response. Two possible modifications to adjust

the natural frequency are: altering the height of the structure, increasing the fixity of the base connection. Lengthening or shortening the supports would change the stiffness of the system to reduce or increase the natural frequency, respectively. Increasing the fixity of the base breakaway connection would increase the stiffness and the corresponding natural frequency. For both of these proposed modifications, the configurations would need to be reviewed such that they don't limit the effectiveness of the sign (e.g. height above the roadway) or the breakaway safety necessary to remain in the clear zone.

8.3.2 Aerodynamic Modification – Background Shield

Of particular interest are inexpensive and simple changes in the currently used configuration of the RICWS sign structure that effectively reduce wind-induced vibrations. This includes configurations that do not change the behavior of the RICWS in a car crash, do not affect the usability of the RICWS with respect to the current configuration, and can be easily fabricated. To this end, one basic idea is to remove the background shields around the lights at the top of the current RICWS structure. The basic line of thought is that these top panels act as additional wind resistance and, despite their relatively small area, have a significant impact on the dynamic behavior of the structure, because they are far away from the support. To corroborate this hypothesis, two different RICWS configurations that are illustrated in Figure 8.17 are analyzed. The first configuration corresponds to the currently used RICWS structure with top panels around the lights (see Figure 8.17 (a) and (b)), the second corresponds to the modified RICWS structure, where the top panels are removed (see Figure 8.17 (c) and (d)).

In the first step, the validated CFD and structural models are employed to simulate the effect of the airflow on the vibration behavior of the RICWS structure. To this end, velocity and pressure of the airflow are simulated until a quasi-steady state is reached. The traction on the panels of the RICWS structure are then imposed as transient traction boundary conditions on the structural model in Abaqus. This enables the simulation of the dynamic response of the RICWS structure that characterizes its vibration behavior. The CFD model has been validated in section 8.2.2 at the laboratory scale with respect to tow tank and wind tunnel experiments conducted at SAFL. This model is now enlarged to the field scale, with the understanding that the CFD model is able to reproduce all flow features at the larger scale that were successfully reproduced at the laboratory scale. The new computational domain has total dimensions of 39.4ft x 26.2ft x 32.8 ft (12.0m×8.0m×10.0m). The time step is chosen as 1×10^{-3}s, and a total number of 24,000 time steps are used. At MSI's Mesabi cluster, 360 cores are applied in parallel to simulate this problem, where the computation time for each time step is about 6.9s. To maximize the vibration response of the RICWS structure, the wind direction is chosen orthogonal to the RICWS sign panels, with a mean velocity at the inlet of U = 11.2 mph (5.0 m/s). If the length of the edge of the diamond panel is used as the characteristic length, this results in a vortex shedding frequency that is equivalent to the first natural frequency of the RICWS structure (see equation 8.1). The rest of the numerical set up of the CFD model corresponds to what has been described in Section 8.2.1 and 8.2.2. A graded mesh with 6.1 million elements is applied. Figure 8.18 illustrates the mesh size around the RICWS panels.

Figure 8.19 compares the mean velocity magnitude in the main wind direction from the CFD simulations of the two RICWS configurations. It can be observed that the simulated overall flow velocities around the RICWS structures do not change significantly when the top panels are removed, both in terms of the shape of the mean fields as well as their maximum values. We can observe, however, pronounced local differences in the flow field at the top of the diamond-shaped main panel (highlighted by white arrows). These results indicate that the removal of the panel enables a smooth flow around the structure, with a free shear layer that shows little deviation from the free-stream streamlines. The shear stresses in the shear layer of the new configuration are of lower intensity due to the lower velocity gradients across the layer. The high curvature of the shear layer at the flow separation point in the old configuration leads to significant flow disruption. This effect is reduced in the new configuration. This hypothesis is supported by Figure 8.20 and Figure 8.21 that plot the simulated turbulence kinetic energy and instantaneous vorticity for the two RICWS configurations. It can be observed that both the kinetic energy and the vorticity in the vicinity of the lights (local regions highlighted by circles) are significantly reduced after removal of the top panels.

The transient structural analysis of the two RICWS configurations in Abaqus is considered next, where the dynamic tractions from the CFD simulations are imposed as transient boundary conditions. The geometry and dimensions of the structure model correspond to the field scale (see Figure 8.22). To account for the flexibility in the support at the base of the RICWS structure, the height of the model is increased by 3 ft. (see Section 8.2.1). In order to transfer the wind traction from the CFD simulations to the structure model, the user subroutine DLOAD is employed that reads and interpolates the CFD traction data to the corresponding integration point in each element of the panels. The dynamic analysis uses implicit time integration. In order to analyze and compare the results of the dynamic analyses, the displacements at points A through D are monitored whose locations on the diamond-shaped panel are illustrated in Figure 8.22. To visualize the vibration behavior in the two configurations, Figure 8.23 (a) through (d) show plots of the displacements in the out-of-plane direction over time for each of the four points. It can be observed that the vibrations at each of the four points are synchronized. Therefore, the out-of-plane vibration of the panel, and hence that of the complete structure, must be close to the first mode of the structure. This confirms that the rationale behind the wind velocity at the inlet of the CFD simulations indeed leads to the anticipated structural response. It can be seen that the vibrations of the RICWS structure are reduced in the modified configuration, where the background shields around the two lights are removed. The maximum displacement of the configuration with top panels is 1.9in (48mm), while the maximum displacement of the RICWS configuration without top panels is only 1.4in (35mm). This shows that the magnitude of vibration after removing the top panels is significantly reduced. This is confirmed by Figure 8.23 (e) through (h) (the right-hand side plots) that compare the amplitudes of the vibration in the frequency domain. Both RICWS configurations show resonant behavior with peak amplitudes at 1 Hz. This is expected, as the first natural frequency is practically the same for both RICWS configurations. In the frequency ranges below and above the natural frequency, the vibration amplitudes are significantly smaller for the modified RICWS structure as compared to the currently used configuration.

In summary, the comparison between CFD simulation results for the currently used RICWS configuration and the modified configuration without background shields clearly shows that the modification reduces the form drag of the RICWS. In particular, it can be observed that the frequency components away from the resonance frequency are effectively reduced.

8.3.3 Non-Commercial Damping Device – Tuned Mass Damper

One proposed modification to reduce the magnitude of the RICWS response, particularly at resonance, is the addition of a tuned mass damper. A tuned mass damper can be thought of as an eccentric mass that is 'tuned' to transfer the response of the structure to the smaller system. For conceptual design and verification of the approach, a simplified numerical dynamic model was created to simulate and evaluate the effectiveness of the addition of a TMD to the sign structure.

A simplified dynamic model was created assuming the behavior in the direction of a wind acting on the sign face mimics that of a cantilever with an end mass. This parallels the assumptions made for a simplified dynamic model of the DMS used previously (Section 5.1.2). The model incorporates the geometry of the RICWS sign instrumented in the field. Figure 8.24 is a representation of the simplified RICWS sign model. The equivalent stiffness, k_{eq}, of the sign post is originally obtained from the derivation of the linearized equation of motion for the single-degree-of-freedom system with a fixed base connection in the absence of the TMD. The TMD is modeled as a simple pendulum with a mass on the end. The pendulum is free to rotate and is attached at the center of mass of the sign; while this is a major simplifying assumption, it is a good first step towards characterizing the potential impact of a supplemental device. In the model, the sign is loaded by a wind pressure distribution derived from observed wind loading on a RICWS sign in the field. The pressure distribution is considered an extreme wind event.

The model uses a fixed connection at the base of the sign, which is a simplifying assumption. In reality, there is likely to be some rotation at the base due to the breakaway connection. Recent field experimentation suggests that the equivalent stiffness of the sign in the field is less than the equivalent stiffness derived for a fixed base. A second model was constructed using the field determined equivalent stiffness. The fixed base equivalent stiffness (Model 1) is equal to k_{eq1} = 384.6 lb/ft and corresponds to a natural frequency of 1.27 Hz. The second equivalent stiffness was derived from a field experiment (Model 2) and is equal to k_{eq2} = 162.7 lb/ft, corresponding to a natural frequency of 0.83 Hz. Analysis of the field data shows that the natural frequency of the structure is approximately 1 Hz, so the actual stiffness of the sign lies between k_{eq1} and k_{eq2}. These two models and corresponding TMD designs bound the possible performance, as the fixed base and field equivalent stiffness are stiffer and softer than the true system, respectively.

The tuned mass damper (TMD) design was calibrated to each stiffness separately, resulting in two designs. The TMD mass was selected to produce the greatest reduction in the root mean square of the displacement response without making the mass unreasonably large. The root mean square (RMS) is related to the energy content of the sign's oscillation, so a smaller root mean square indicates less oscillation during a wind event. The pendulum lengths of the TMDs were chosen to correspond to the

natural frequency of the sign model. TMD 1 was calibrated to k_{eq1}, and TMD 2 was calibrated to k_{eq2}. TMD 1 has a mass of 13 lb (10.4% of the sign weight) and a pendulum length of 0.5 ft, while TMD 2 has a mass of 10 lb and a pendulum length of 1.184 ft.

An example of the displacement response with and without the TMD is provided in Figure 8.25. The displacement response of the center of the sign (Model 1) in response to the wind pressure distribution is compared to the response with TMD 1. The TMD reduced the root mean square of the displacement response by 15.7% but did not significantly reduce the peak displacement of the sign. An intrinsic damping of 10% was assumed in the model results presented; however, values between 2% and 10% were found to provide similar performance. Figure 8.26 displays the corresponding rotation angle of TMD 1 versus time to achieve this level of reduction. Ignoring the initial effect of loading, which is influenced by initial conditions, the largest rotation angle of the TMD is 23 degrees, which is not unreasonable for practical implementation. This level of rotation is representative of the different TMD and model combinations.

Figure 8.27 highlights the magnitude of the displacement of the sign (Model 1 with TMD 1) in the frequency domain under the same wind loading. In general, the TMD reduces the magnitude of the curve around the natural frequency of the sign, resulting in less oscillation. The area under on the curve could be considered as an analog for the RMS of the displacement response.

The effects of TMD 1 and TMD 2 were compared for both models, i.e. the TMDs were considered for both their corresponding design stiffness and the other effective stiffness. For Model 1 (k_{eq1}), TMD 1 and TMD 2 reduce the displacement RMS value by 15.8% and 7.89%, respectively. For Model 2 (k_{eq2}), TMD 1 and TMD 2 reduce the displacement RMS value by 6.38% and 16.0%, respectively. These results suggest that both TMD 1 and TMD 2 will provide significant reduction in the RMS response (at least equal to 6%) for an equivalent stiffness lying between the two values. In order to increase effectiveness, the TMD could be installed with an adjustable length to allow for more precise calibration to the actual stiffness of the sign in the field.

Although the model results indicate that the peak displacement of the sign is not significantly reduced by the TMD, the reduction in the RMS displacement is significant. The reduction in oscillation during wind loading could help to prevent large vibrations of the sign and related damage to the panel components. The model also shows that the rotation angle of the TMD will remain within an acceptable range during extreme wind loading. Thus, the TMD may not be sufficient by itself to prevent large displacements during extreme wind events, but it could be implemented alongside other modifications (such as aerodynamic modifications) to sufficiently reduce the dynamic response.

8.4 FIELD IMPLEMENTATION OF STIFFNESS MODIFICATION

Out of the proposed modifications in Section 8.3, a simple approach to modify the dynamic characteristics of the sign structure was selected for field investigation. The base of the RICWS structure supports was modified in the field by inserting a ‘shim’ in each of the slip-base connections on January

26, 2020. The objective was to increase the stiffness of the structure and eliminate slop in the connections, while maintaining their break-away status.

The gap in the sleeves in the base, which is visible in Figure 8.5, is 0.04 in. While this seems minimal, if the posts remain rigid, this gap accounts for approximately ±0.2 in. and ±0.8 in. of movement at the string pot fixture and panel center, respectively. The gap was filled by a 2 in. x 5 in. x 20 gage bar inserted at the base of each post (Figure 8.28). The shim goes down about 1.5 in. into the base. The shim was only inserted in the north side of the post due to a bolt located in the east-west direction. Therefore, some small movement is still possible.

To explore changes in the stiffness and corresponding displacement, the wind response of the modified RICWS was evaluated using field measurements recorded over April 22, 2020 to May 18, 2020. The primary measurements used were the displacements of the sign captured by the potentiometers connected to each post and the corresponding wind speed and direction. The data analysis was done at a sampling frequency of 1 Hz. This was done for two main reasons. First, because the wind data was collected at a 1 Hz sampling rate, it was not possible to develop an accurate estimate of the pressure, and consequently the force on the sign, for changes occurring faster than 1 Hz. Second, the average wind speeds normal to the sign during the monitoring duration were quite low (Figure 8.29), which led to noisier high frequency displacement data.

The structural stiffness of the sign in the field was estimated assuming a linear elastic force-displacement relationship. The key assumption is static equilibrium between the drag force and the elastic response of the sign structure. The force and stiffness, *k*, are then related using:

$$F_d = \frac{1}{2} C_d \rho A U^2 = k \Delta x \qquad (8.2)$$

where:

$C_d =$ Drag coefficient, 1.34

$\rho =$ Density of air, 0.0765 lbm/ft^3

$A =$ Total frontal area of the sign, 20.7 ft^2

$U =$ Measured wind speed, ft/s

$\Delta x =$ Horizontal displacement at sign centroid, ft

The drag coefficient is the value estimated in the SAFL experiments. The horizontal displacements are taken at the centroid of the diamond sign. The centroid of the diamond plate was selected as the representative location at which the wind drag force would be applied.

To estimate the stiffness, *k*, from the low frequency data, wind events normal to the sign and the corresponding displacements were considered. Only wind events with northerly (-40° < θ < 40°) or southerly (140° < θ < 220°) direction were considered. Additionally, only events with wind speeds greater than 11.2 mph (5 m/s) were considered to limit the impact of any slop in the connection on the stiffness estimate. The displacement offset under very low wind loads (less the 1 mph) was removed (Figure 8.30b) to isolate the change in displacement due to the wind loading. The slop in the base connection causes the resting point of the sign to shift, e.g. the sign does not always return to zero under no wind loading. The displacement at the centroid of the diamond plate was linearly extrapolated from the displacement measured at the height of the string potentiometers. Figure 8.31 shows the relationship between the measured (squared) wind velocity (U^2) and displacement Δx for the wind events that met these criteria. The slope of the relationship in Figure 8.31 can be expressed as $0.5C_d\rho A/k$ from Eq. 8.2 with *k* the only unknown; the stiffness was determined from linear fits of the points in Figure 8.31.

The two potentiometer sensors result in approximately the same stiffness estimate in each wind direction; however, there are several clusters of data. Due to uncertainty in the resting position under the varying conditions, the linear fit of the data did not impose the intercept to be at the origin. The difference in the reference displacement is clearest in the northerly wind results (Figure 8.31b) with the vertically offset linear trends in the clusters for the different sensor data. An individual linear fit was determined for the two sensors using the scattered data, leading to 4 estimates of the stiffness. The mean stiffness resulting from the fits was k = 132 lb/ft and the standard deviation was σ_k = 18 lb/ft.

This resulting stiffness is actually lower than the previous stiffness derived from field experiments of 162 lb/ft with a deviation of about 14 lb/ft. However, the results are similar within the variations. There are a few possible reasons for the small disparity including ground condition differences during the field tests and the limited number of high-speed wind events in the normal direction used to estimate the stiffness. Given the similarity in the stiffness results and the lower value for the modification, the shim is not an effective means to get significant change in the stiffness of the RICWS support structure. A different base connection design is recommended to improve the fixity and increase the stiffness. While the shim did not impact the stiffness of the sign supports, it did limit the slop as expected. Figure 8.30 compares the offsets considered when calculating the displacement change in the wind loading. The overall magnitude of the offset changes is smaller after the shim was inserted. Therefore, the total displacement magnitude under wind loading should decrease.

8.5 SUMMARY

Analysis of the RICWS field data suggests vortex shedding may have a significant role in the dynamic behavior of the RICWS subjected to wind loading. Alignment between the natural frequency, oscillation frequency, and shedding frequency of the sign suggests that lock-in could be possible. The wind speeds that lead to alignment are commonly observed in the field. As a result, the proposed modifications aim to reduce the possibility of vortex shedding and the corresponding amplitude of the dynamic response. The three proposed modifications are: altering the dynamic characteristic of the sign through height or

fixity changes, aerodynamic modification by removing the background shields around the lights, addition of a small pendulum-type TMD. Development of the aerodynamic modification leveraged the validated FEM and CFD models for implementation and evaluation. Out of the proposed modifications, a simple modification of inserting a shim into the slip-base connection was implemented in the field to increase the stiffness while maintaining the breakaway sign support. However, analysis of the field data reveals that the stiffness did not appreciably change due to this simple modification.

Table 8.1 – Reference events for computing shedding frequency of RICWS – Wind Events Normal to Sign

Event Label	Wind Event	Mean Speed, mph (m/s)
1N	1/22/18 at 0444	9.37 (4.19)
2N	1/22/18 at 1510	9.57 (4.28)
3N	1/22/18 at 0441	13.15 (5.88)
4N	2/22/18 at 1011	15.73 (7.03)
5N	11/27/17 at 1420	16.33 (7.30)
6N	04/13/18 at 1542	17.56 (7.85)
7N	04/13/18 at 2249	22.50 (10.06)

Table 8.2 – Reference events for computing shedding frequency of RICWS – Wind Events at Different Orientations to Sign at Similar Speeds

Event Label	Wind Event	Mean Speed, mph (m/s)	Wind direction from North, degrees
1D	1/22/18 at 0120	13.76 (6.15)	10.0
2D	4/13/18 at 1259	15.43 (6.90)	45.9
3D	3/5/18 at 1215	15.93 (7.12)	86.1
4D	2/18/18 at 0937	15.93 (7.12)	136.2
5D	1/17/18 at 1208	14.52 (6.49)	191.9
6D	11/29/17 at 2358	16.02 (7.16)	272.0
7D	12/4/17 at 2356	14.50 (6.48)	282.5

Table 8.3 – Comparison of RICWS characteristics simulated via the CFD model and found experimentally in SAFL drag experiment

Parameter	Experimental	Simulated with CFD
Mean Drag Coefficient, $\bar{C}_d$	1.34	1.314
Mean Lift Coefficient, $\bar{C}_l$	0.04	0.029
Primary Shedding Frequency, f_s	1.00 Hz	0.67 Hz

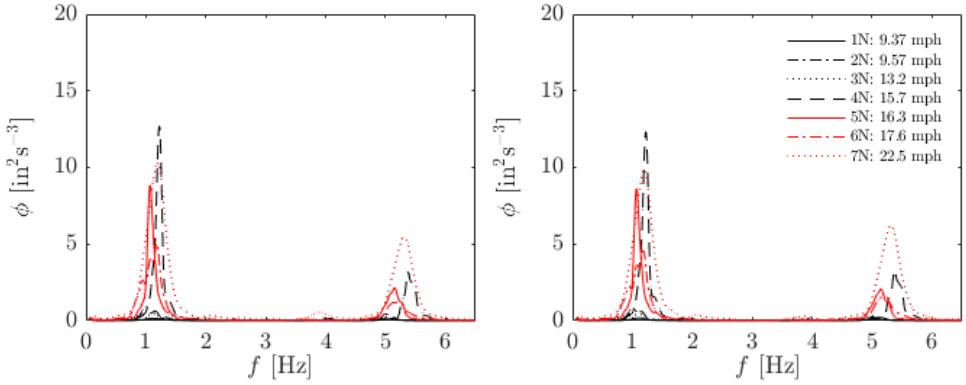

Figure 8.1 - Spectral energy of accelerometer data under for normal wind events under varying wind speeds (Table 8.1): (a) west accelerometer, (b) east accelerometer.

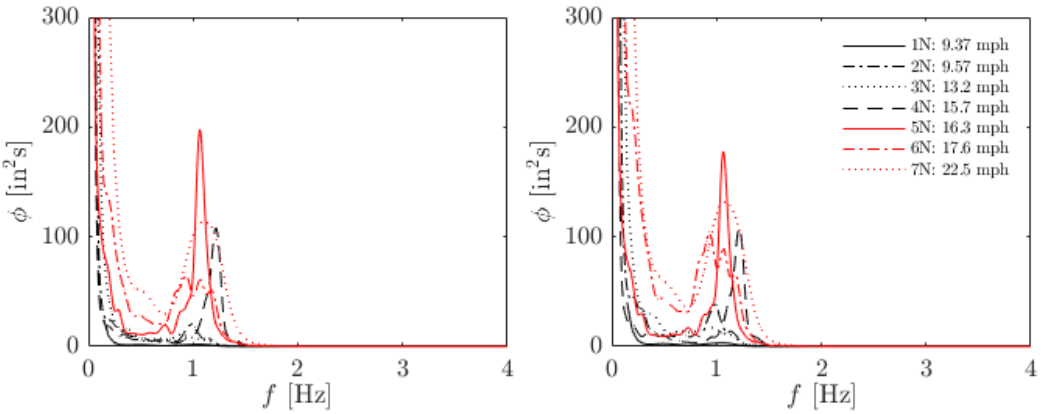

Figure 8.2 - Spectral energy of displacement data for normal wind events under varying wind speeds (Table 8.1): (a) west string potentiometer, (b) east string potentiometer.

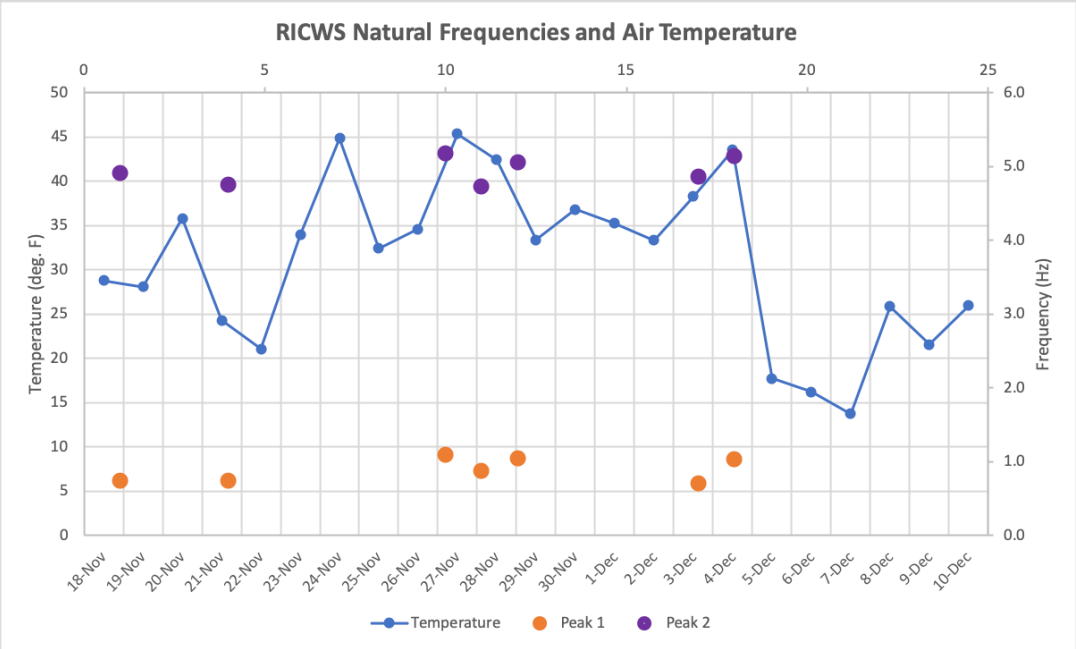

Figure 8.3 – Natural frequency variation with temperature

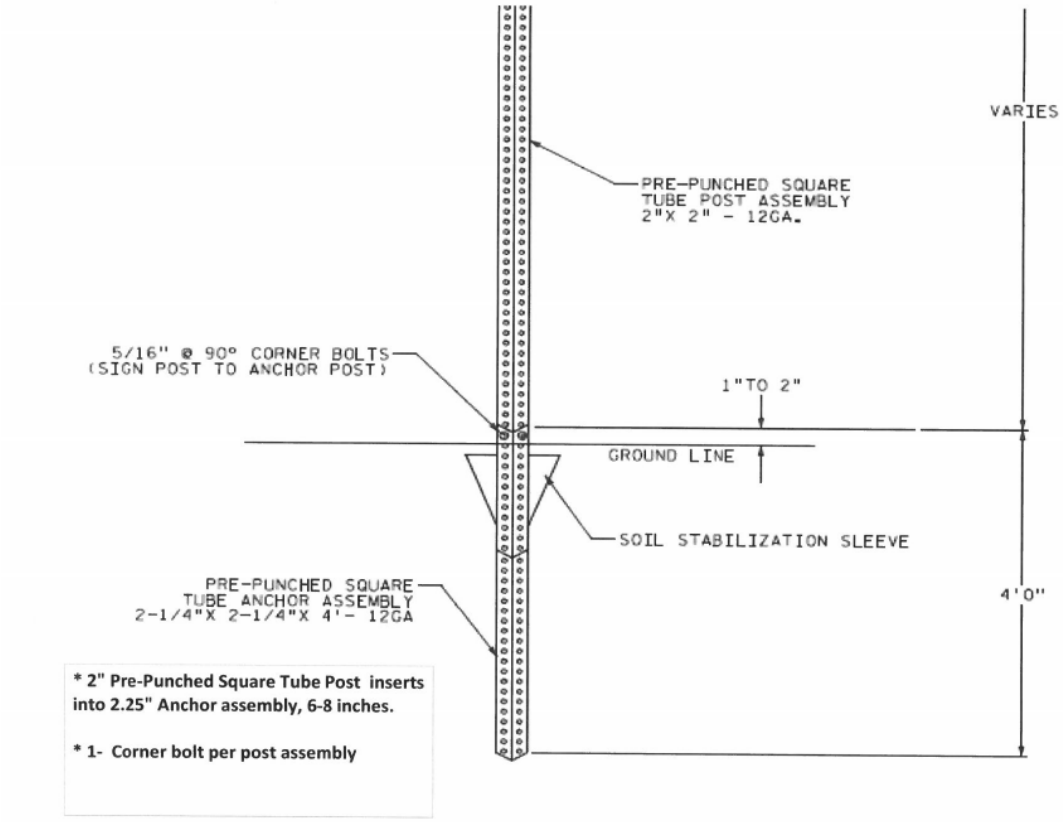

Figure 8.4 – RICWS slip base connection (shared by MnDOT, 2018)

Figure 8.5 – Image of breakaway base connection for RICWS

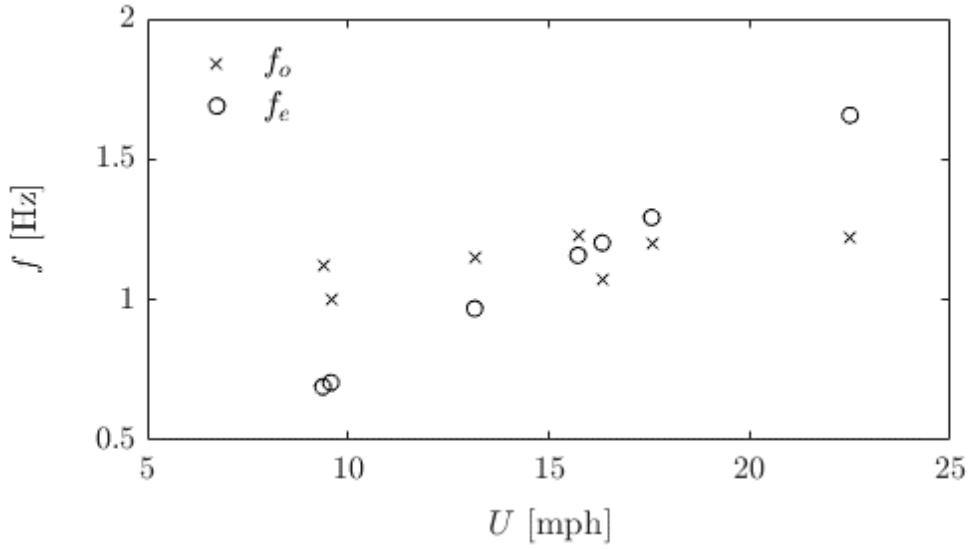

Figure 8.6 - Graph of first observed frequency f_o and expected shedding frequency f_e as a function of wind speed for events 1N through 7N (Table 8.1).

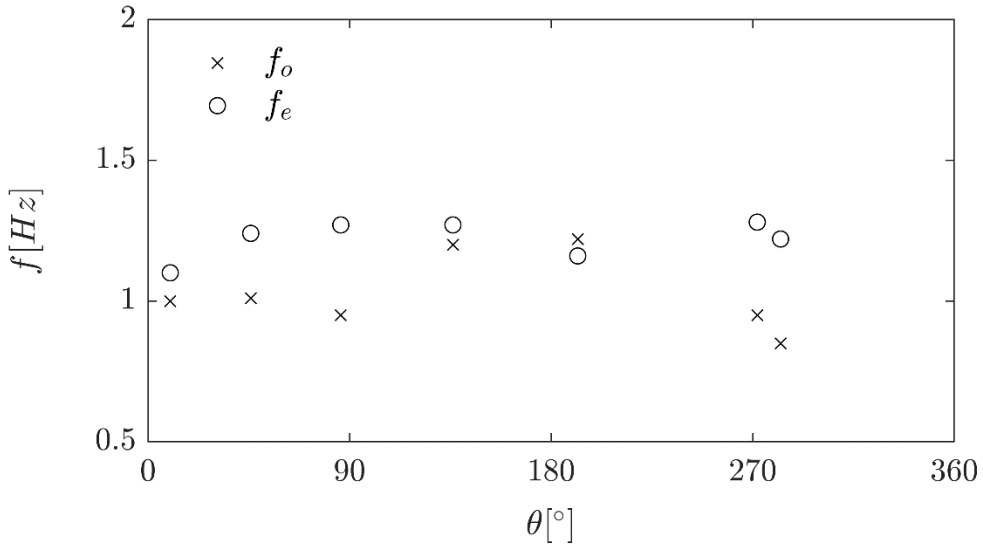

Figure 8.7 - Graph of first observed frequency f_o and expected shedding frequency f_e as a function of wind direction for high frequency events 1D through 7D (Table 8.2). f_e is varying based on the actual wind speed for the given direction assessed.

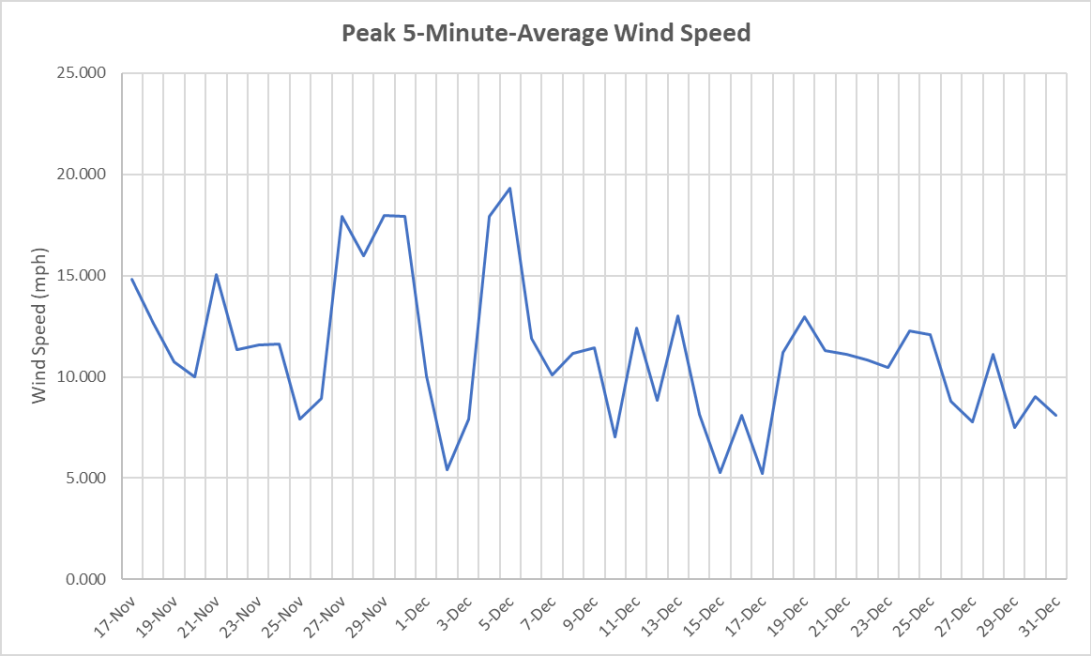

Figure 8.8 – Peak five-minute-average wind speed during November and December

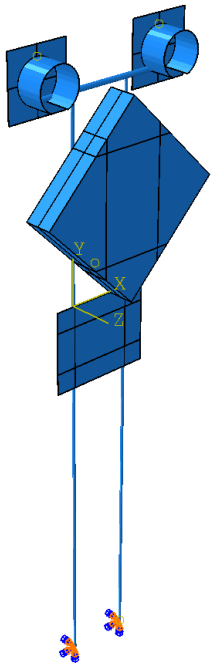

Figure 8.9 – The geometry of the RICWS sign structure in Abaqus

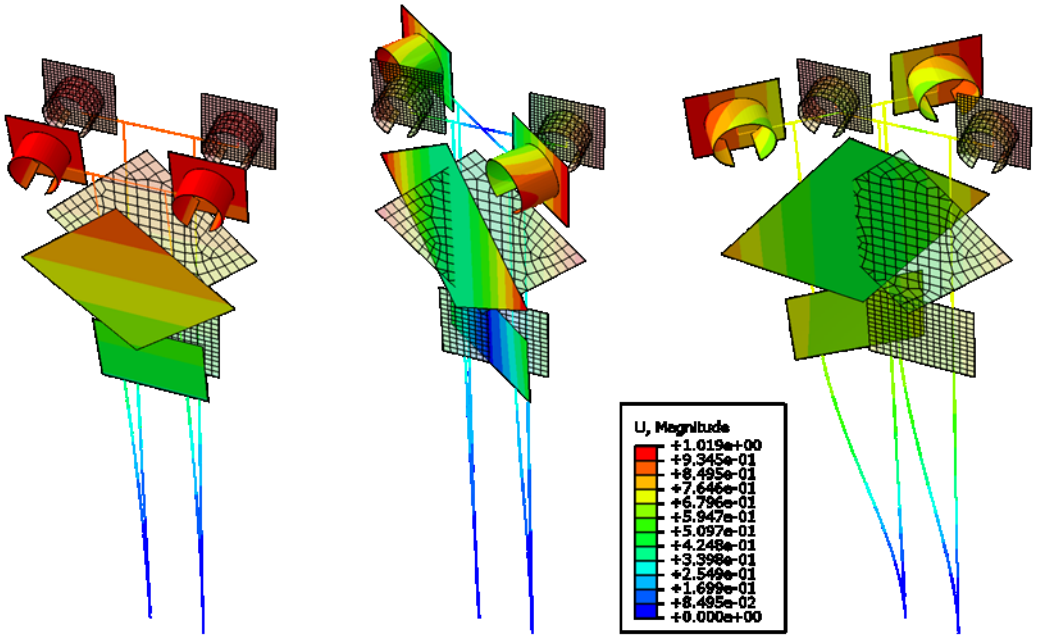

1.1 Hz 1.7 Hz 4.1 Hz

Figure 8.10 – Natural frequencies and mode shapes of the RICWS FEM model

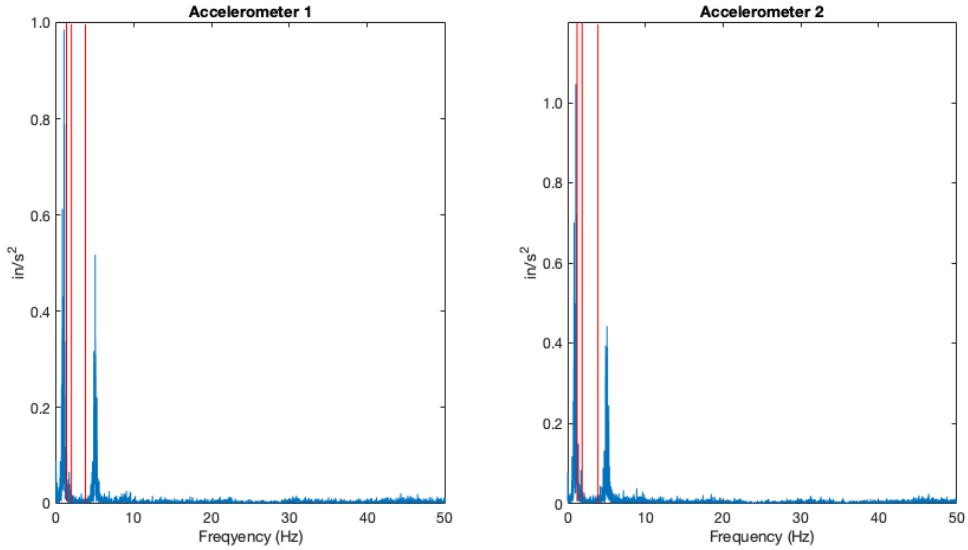

Figure 8.11 – Comparison of natural frequencies of FEM model and field RICWS for Event 11/29 at 2343 (the three red lines correspond to three first natural frequencies of Figure 8.10).

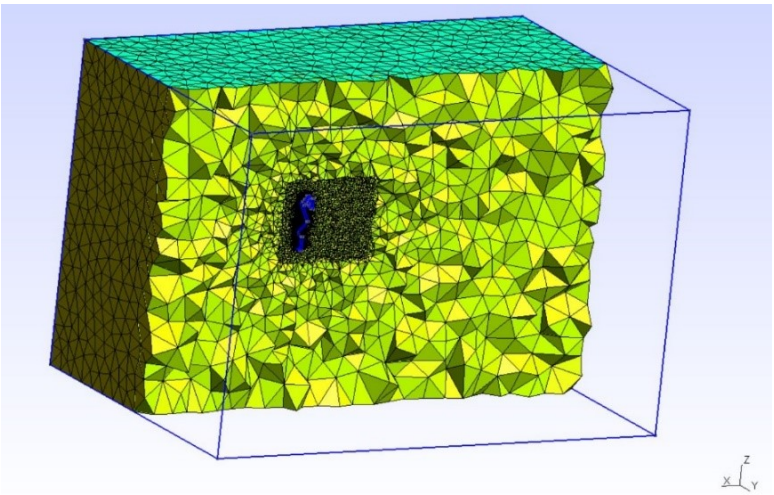

(a) Complete mesh of the flow domain

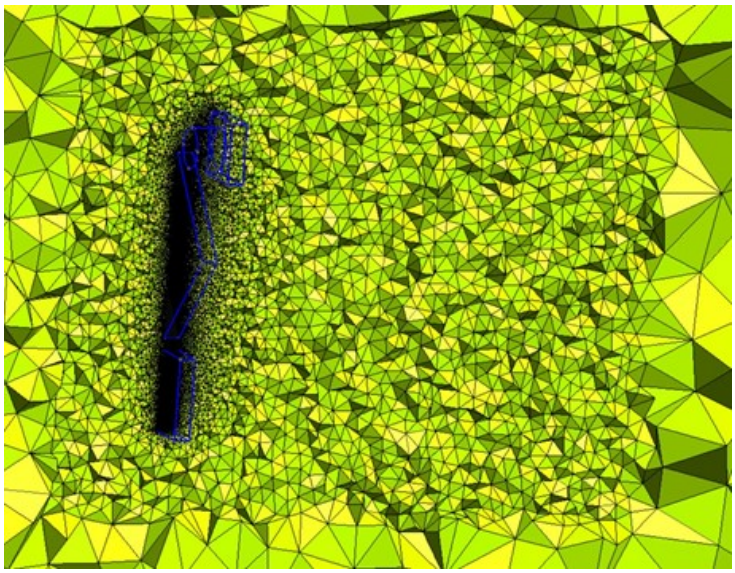

(b) Refined mesh near the RICWS

Figure 8.12– Elevation view of mesh of flow domain for the tow tank simulation.

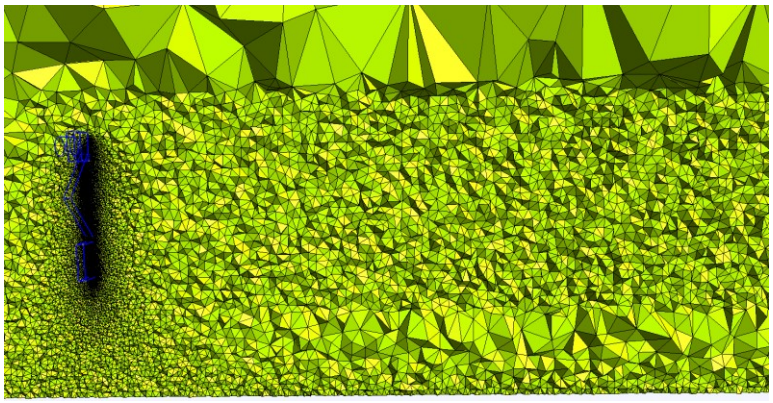

(a) Mesh of the complete computational domain

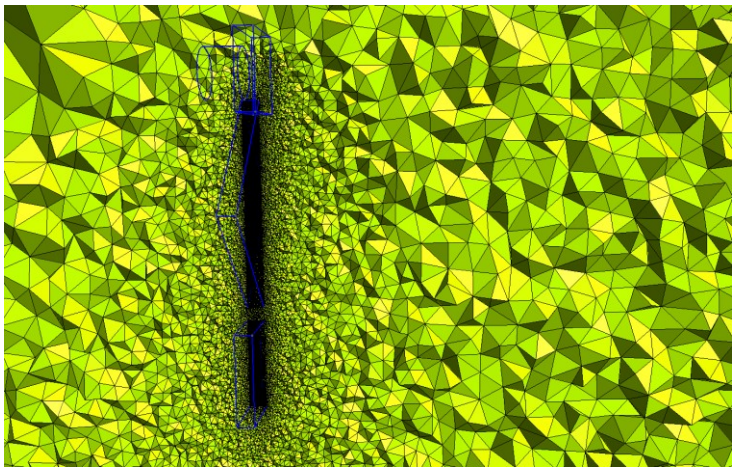

(b) Mesh in the vicinity of the sign panels

Figure 8.13 - Elevation view of mesh of flow domain for the wind tunnel simulation.

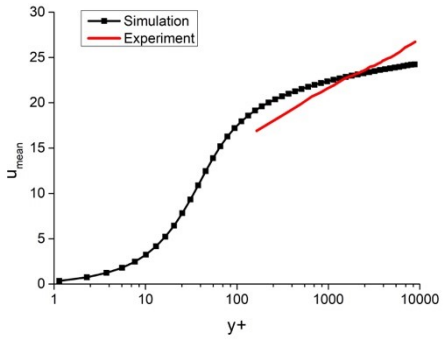

(a) Mean velocity in main direction

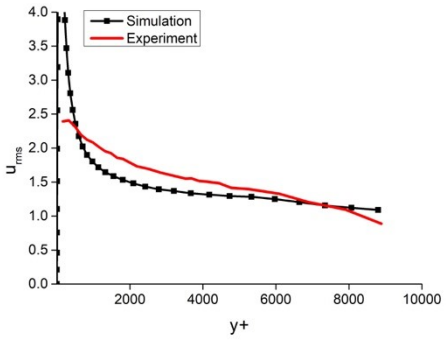

(b) Root mean square of velocity in main direction

Figure 8.14 - Comparison of flow velocity results obtained by free channel flow without the sign structure, which are used as inlet boundary conditions representing incoming turbulence

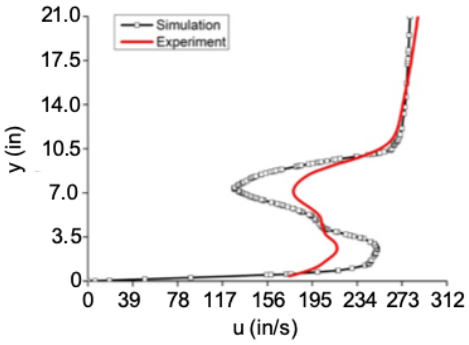

(a) Mean x-velocity in main direction (x=2H)

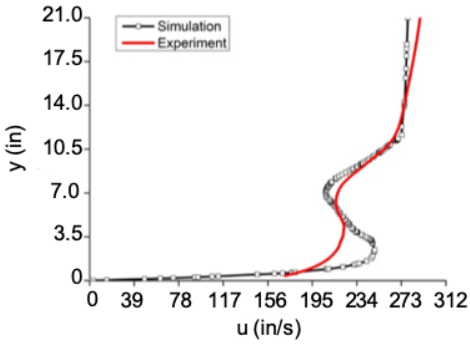

(b) Mean x-velocity in main direction (x=4H)

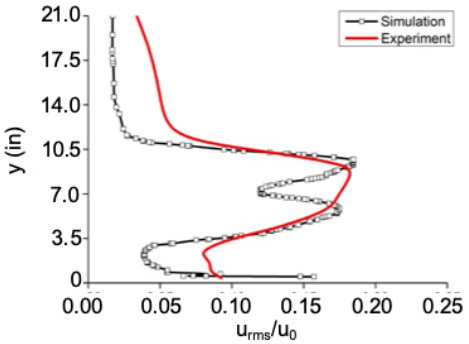

(c) Root mean square of x-velocity (x=2H)

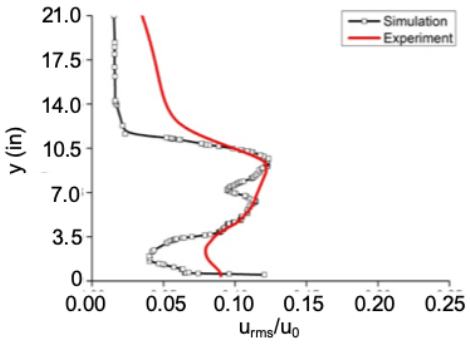

(d) Root mean square of x-velocity (x=4H)

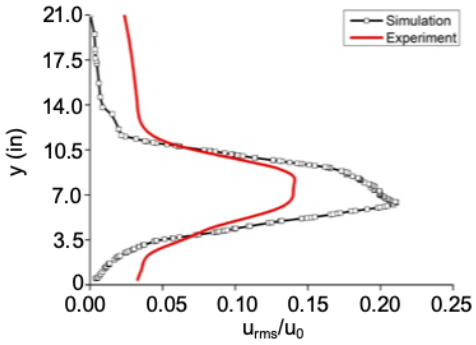

(e) Root mean square of y-velocity (x=2H)

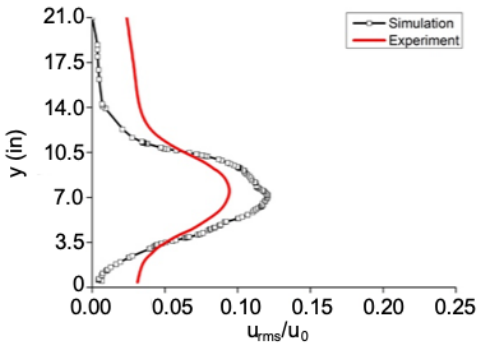

(f) Root mean square of y-velocity (x=4H)

Figure 8.15 - Comparison of mean and root mean-square velocity distributions between wind tunnel experiment and CFD simulation

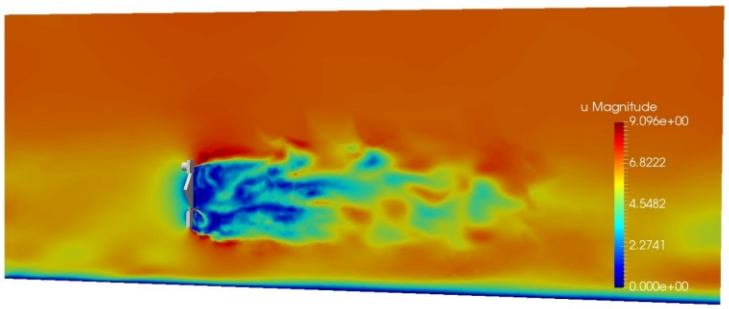

(a) Instantaneous velocity magnitude plotted on the central plane.

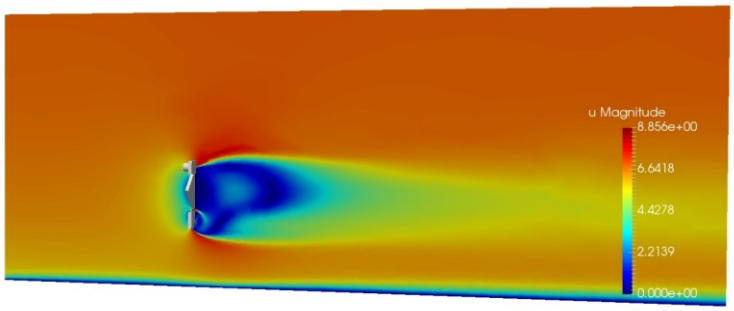

(b) Mean velocity magnitude plotted on the central plane.

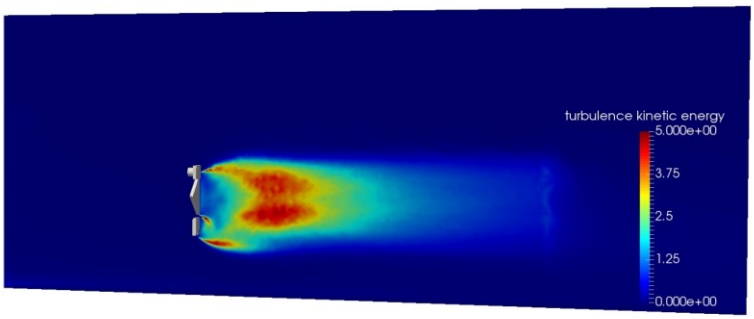

(c) Turbulence kinetic energy plotted on the central plan.

Figure 8.16 - Plots of representative instantaneous and averaged solution fields.

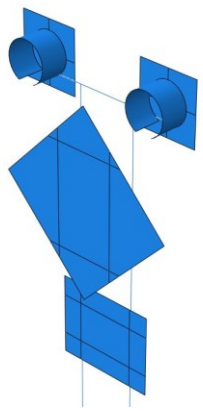

(a) Model with top panels

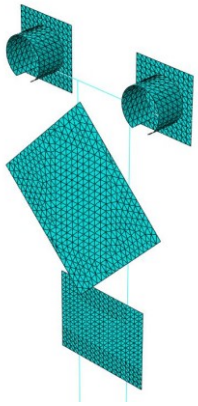

(b) Mesh of model with top panels

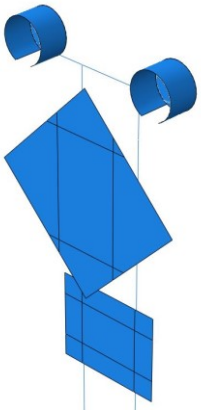

(c) Model without top panels

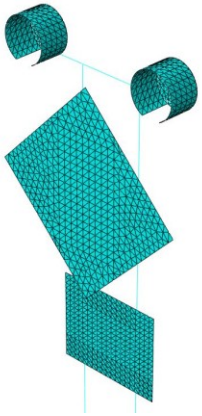

(d) Mesh of model without top panels

Figure 8.17 - The Abaqus models of the original and modified RICWS configurations.

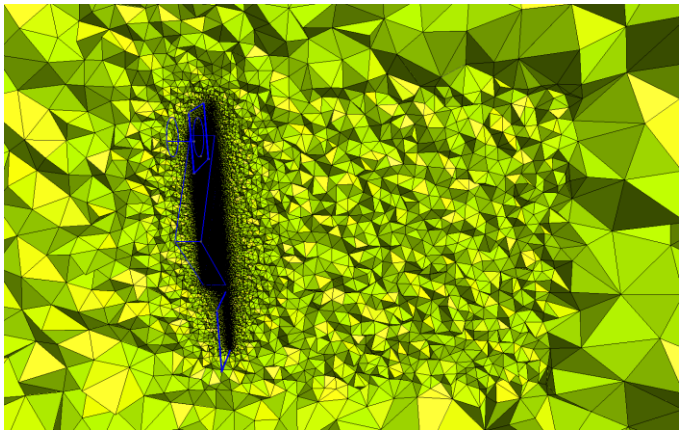

Figure 8.18 - Graded mesh around the RICWS structure (with panels around the lights)

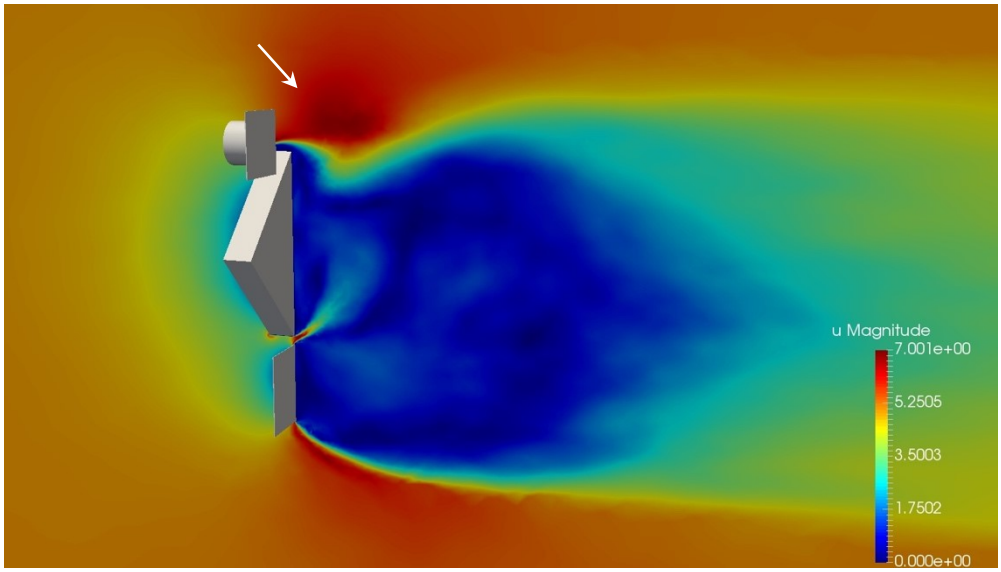

(a) Mean velocity magnitude with top panels

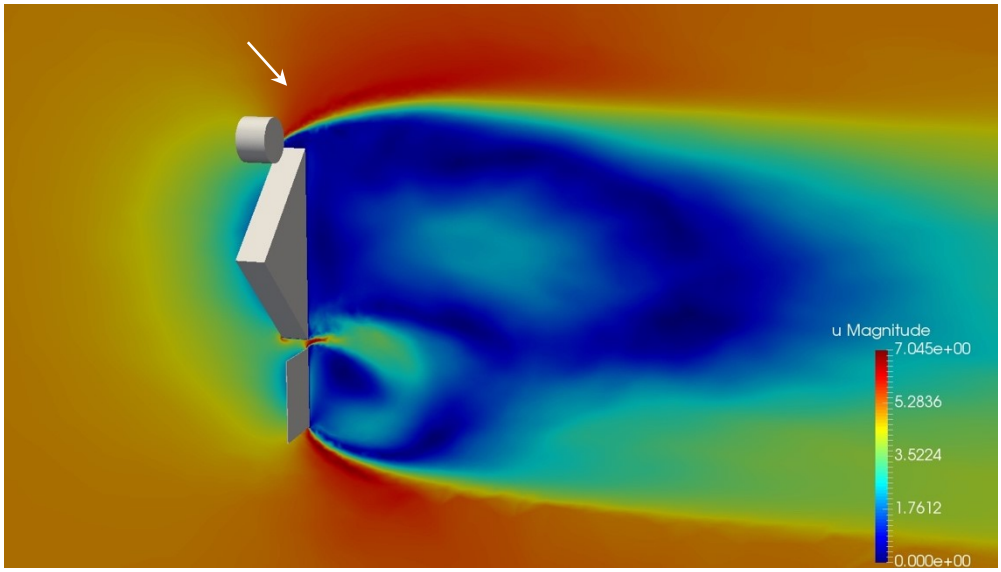

(b) Mean velocity magnitude w/o top panels

Figure 8.19 - Mean velocity magnitude plotted at central contour plane.

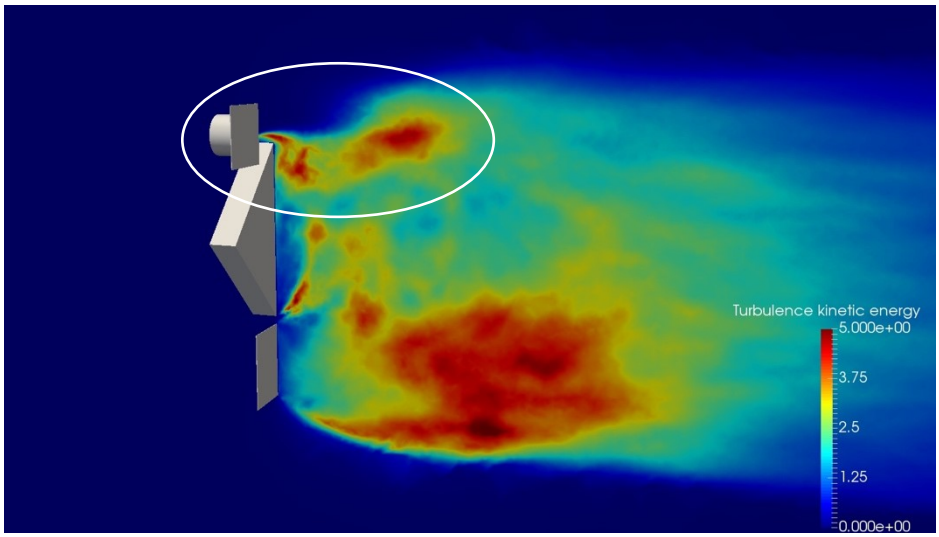

(a) Turbulence kinetic energy with top panels

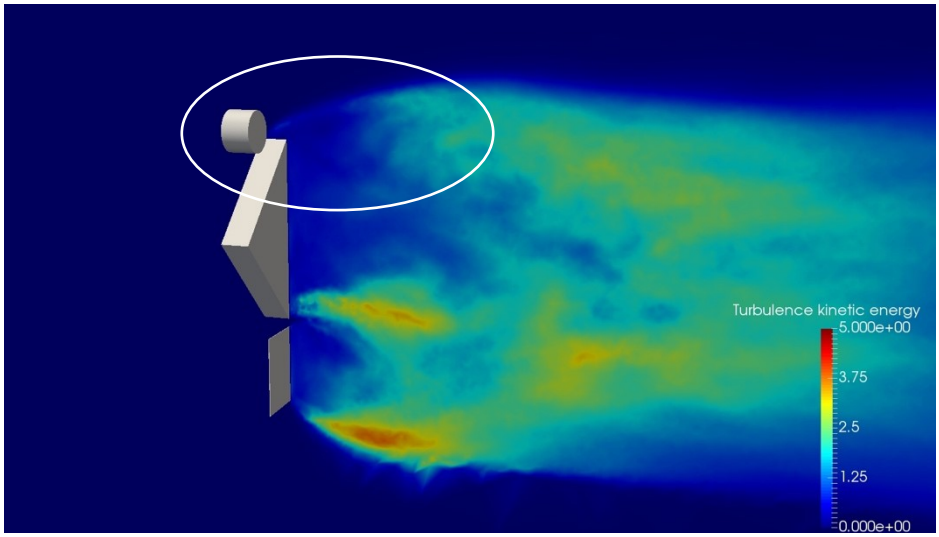

(b) Turbulence kinetic energy w/o top panels

Figure 8.20 – Turbulence kinetic energy plotted at central contour plane.

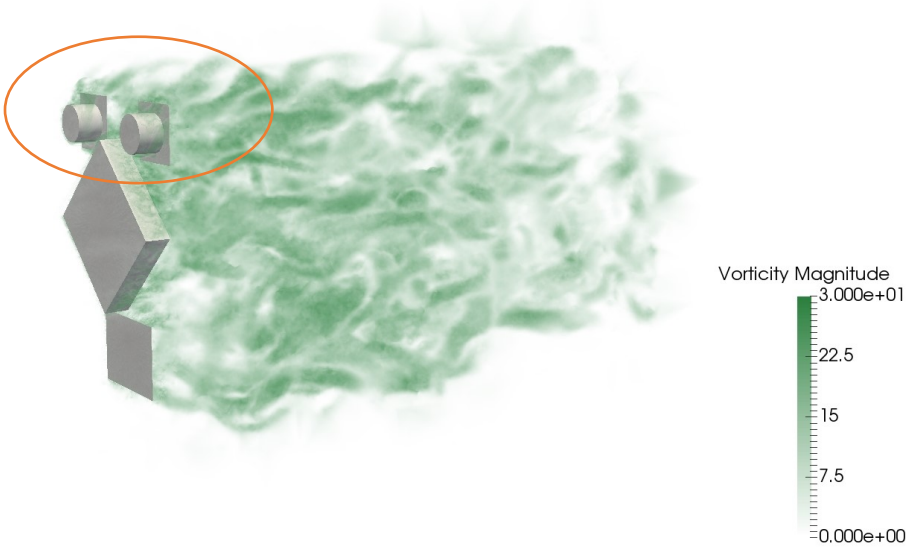

(a) Vorticity structures with top panels

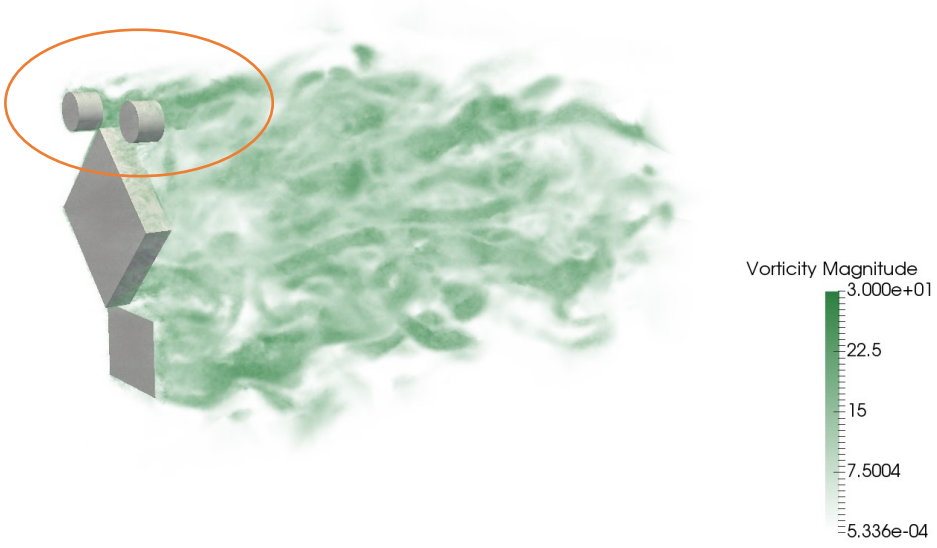

(b) Vorticity structures without top panels

Figure 8.21 - Comparison of instantaneous vorticity.

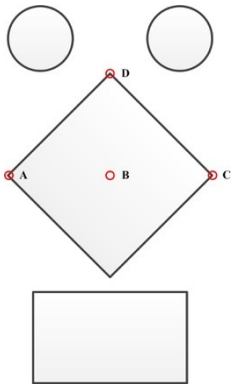

Figure 8.22 - Position of the four points monitored in the transient analysis.

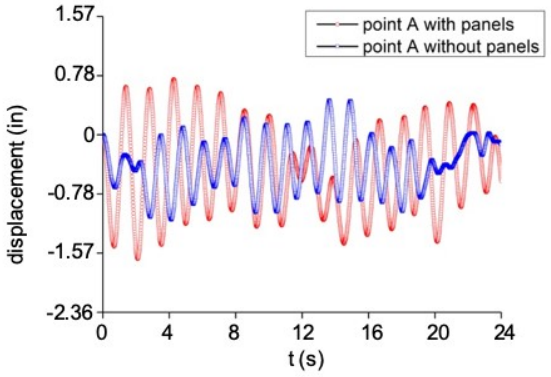

(a) Out-of-plane displacement at point A

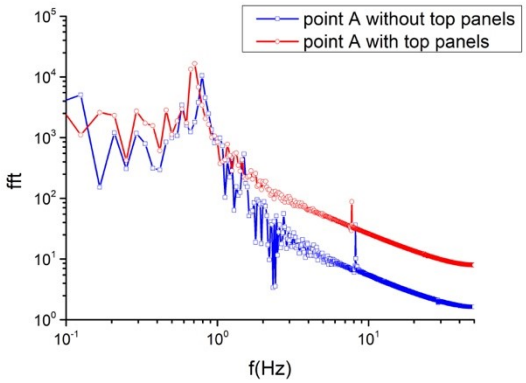

(e) Amplitudes of FFT analysis at point A.

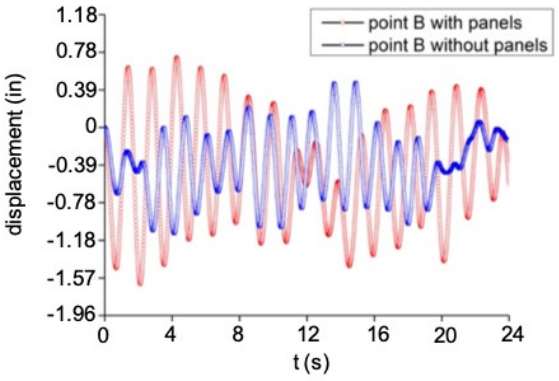

(b) Out-of-plane displacement at point B

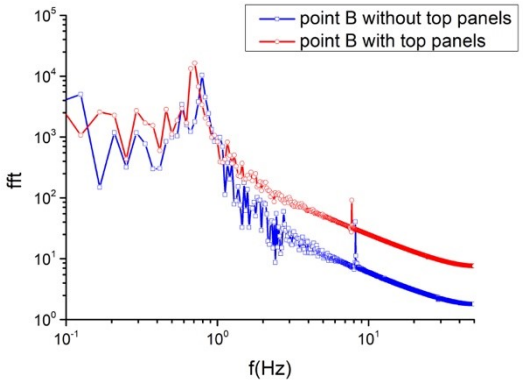

(f) Amplitudes of FFT analysis at point B.

Figure 8.23 - Vibration results of the RICWS structure from the transient Abaqus analysis.

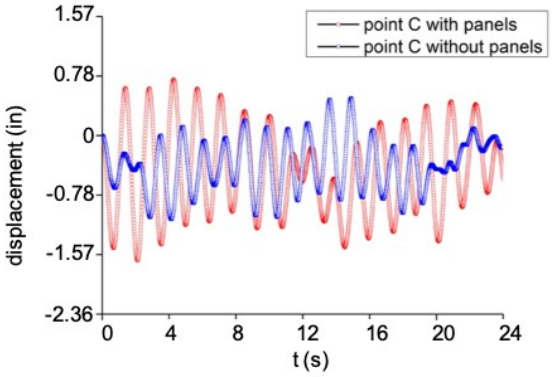

(c) Out-of-plane displacement at point C.

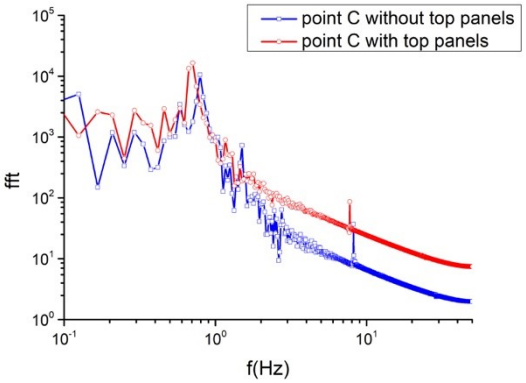

(g) Amplitudes of FFT analysis at point C.

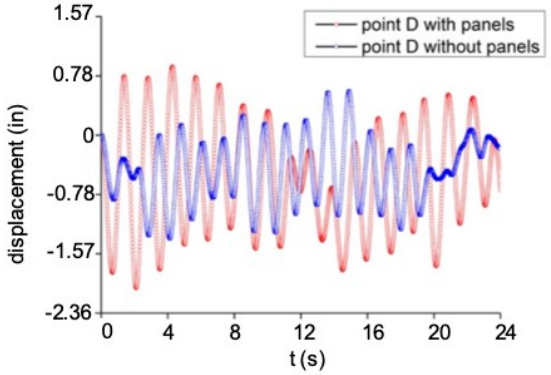

(d) Out-of-plane displacement at point D.

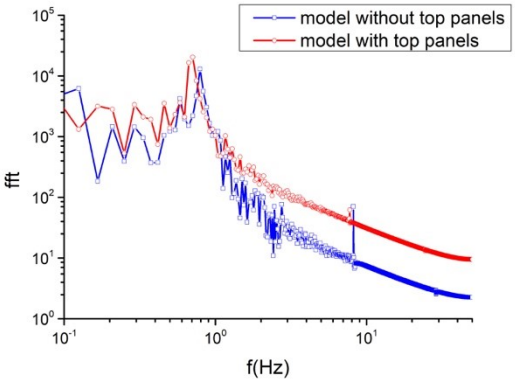

(h) Amplitudes of FFT analysis at point D.

Figure 8.23 cont. - Vibration results of the RICWS structure from the transient Abaqus analysis.

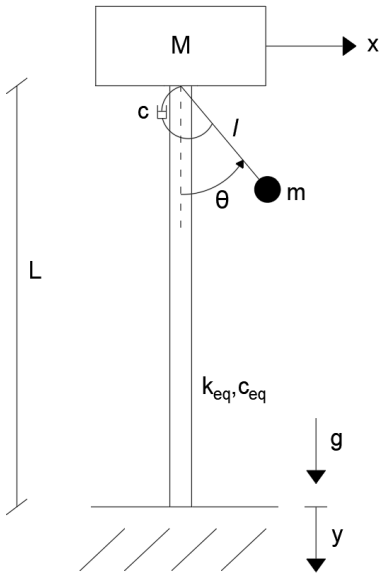

M – mass of sign
x – lateral displacement of sign
L – post height
l – TMD pendulum length
c – pendulum damping coefficient
m – TMD mass
θ – TMD rotation
k_{eq} – equivalent stiffness of post
c_{eq} – equivalent damping coefficient of post

Figure 8.24 - Representation of RICWS sign structure simplified model for TMD analysis and design

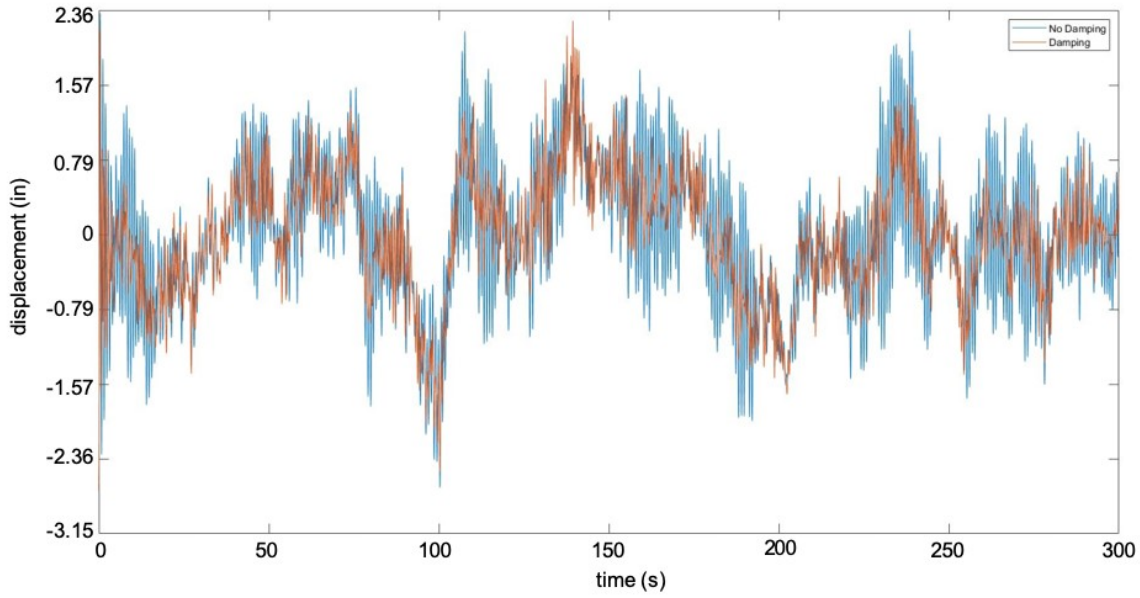

Figure 8.25 - Displacement of Sign Versus Time (With (red) and Without (blue) TMD)

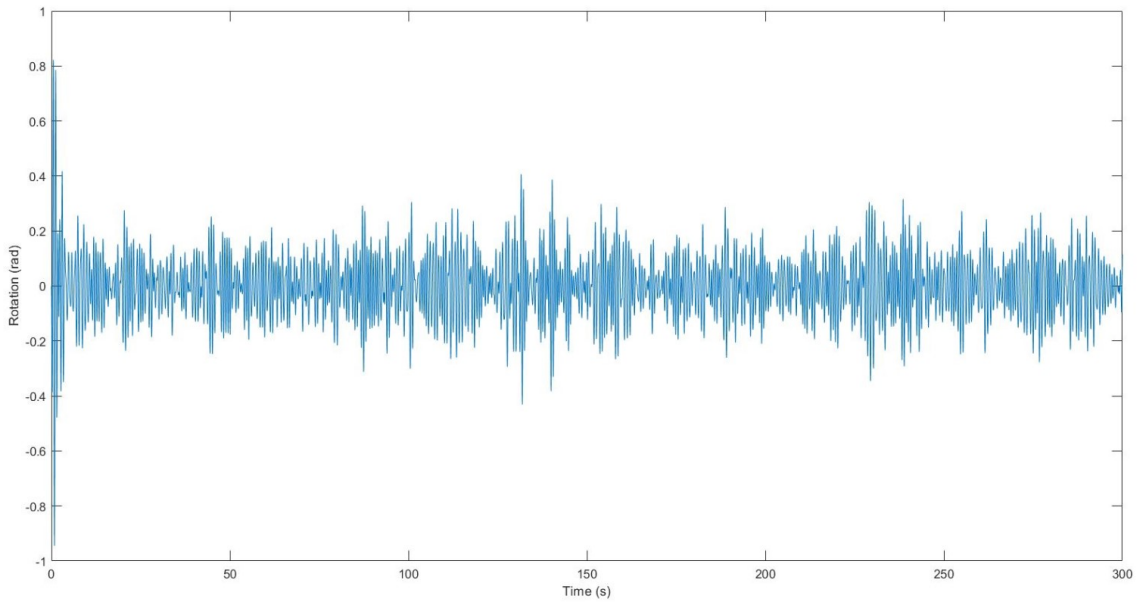

Figure 8.26 - Rotation angle of TMD versus time

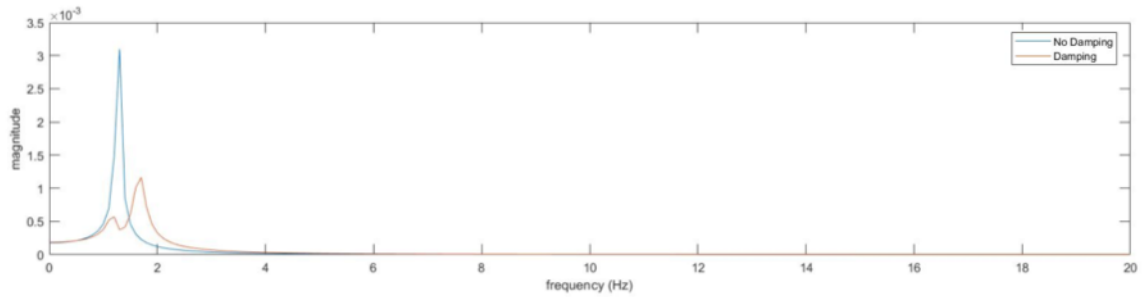

Figure 8.27 - Magnitude of the displacement of the sign (at mass center) in the frequency domain (blue – no TMD, red – with TMD)

Figure 8.28 - RICWS breakaway slip-base post connection with shim inserted.

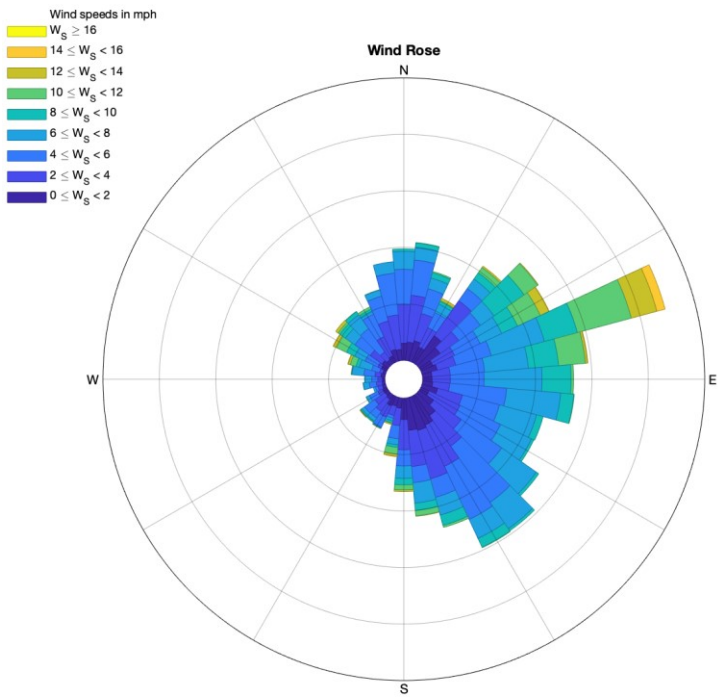

Figure 8.29 - Wind speed and direction during monitoring duration.

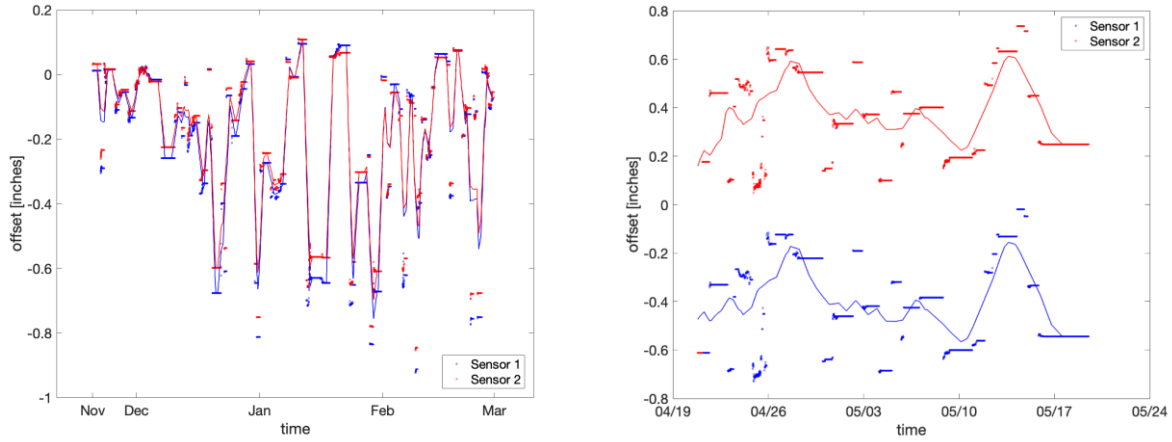

(a) (b)

Figure 8.30 - Displacement offset at low wind speeds and the corresponding moving average for (a) no modification (11/2017-3/2018) and (b) with modification.

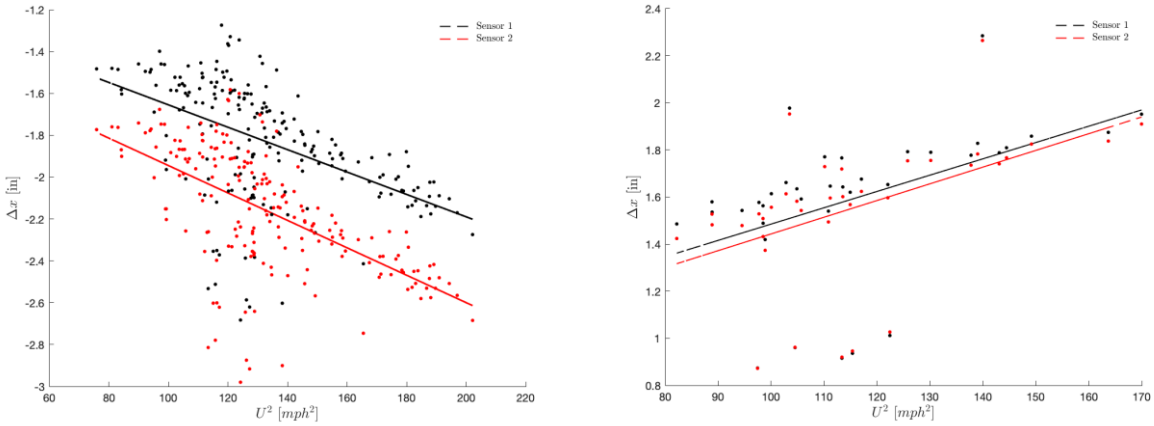

(a) (b)

Figure 8.31 - (a) Scattered data and linear fits for northerly wind events, (b) scattered data and linearly fits for southerly wind events.

CHAPTER 9: CONCLUSIONS AND FUTURE RESEARCH

This research aimed to address concerns associated with wind-induced vibrations in the DMS and RICWS structures. Both signs are much larger and heavier than signs traditionally supported on their specific support structures. The heavier signs were believed to undergo wind-induced vibrations not normally seen in typical roadside signs. The current AASHTO LRFD Specification for SLTS does not address vibration design for these nontraditional roadside signs.

The DMS Type A support system, specifically the friction fuse connection, is susceptible to the formation of stress concentrations and potential fatigue issues. This research assessed the fatigue life of the Type A support system with the current DMS design. Large amplitude oscillations under wind loading have already been observed in the RICWS. Research was done to explore the wind-induced dynamic behavior of the RICWS and to explore suitable modifications to the RICWS support system for reducing the amplitude of the wind-induced oscillations.

9.1 SUMMARY OF KEY CONCLUSIONS

1. Analysis of the DMS required the use of a dynamic FEM model. This implied that the mass of the structure had a significant impact on the response of the structure.

2. The fatigue life of the DMS was evaluated which required: (1) identification of the fatigue critical detail category of the fuse plate, which was considered the fatigue critical detail of the support system, (2) the limit-state wind loading, and (3) knowledge of the potential number of cycles the DMS would undergo at the critical stress range. The fuse plate was classified as Fatigue Category D based on research done by Brown et al. (2007). The fatigue category dictated the CAFT and number of cycles the detail could undergo for a given stress range. The fatigue limit-state wind loading was defined to be the mean hourly wind speed with 0.01 percent exceedance based on previous research presented in NCHRP 412 (1998) and NCHRP 469 (2002).

3. Dynamic loading functions were developed for use with the FEM model using the Davenport spectrum, which was found to fit well with the wind data recorded in the field.

4. Based on the analysis using the equivalent static pressure equation for natural wind gusts prescribed by the AASHTO LRFD Specification for SLTS, the specific DMS and Type A support system instrumented in the field met the requirements for infinite fatigue life if the behavior of the structure subjected to tangential loading resembled a fixed-free (Model 1) or fixed-side sway (Model 2) condition. If the behavior under tangential loading resembled a pinned-side sway (Model 3) condition, then the fatigue stress demand exceeded the CAFT. The fatigue stress demand when using Model 3 was 7.2 ksi, which just exceeded the CAFT of 7.0 ksi.

5. The specific DMS and Type A support system instrumented in the field did not meet the requirements for infinite fatigue life based on the dynamic analysis performed with the FEM model and appropriate dynamic loading functions. Fatigue stresses within the fuse plate reached 9.27 ksi, which exceeded the recommended CAFT of 7.0 ksi. A service life of 23.8 years

was conservatively estimated for the field DMS based on the number of cycles the DMS was estimated to undergo in its lifetime and the number of cycles allowed for a fatigue Category D detail and the critical stress range of approximately 10 ksi.

6. Other DMS in service may also be subjected to fatigue stresses beyond the recommended CAFT depending on the size of the sign panel, height of the posts, sign location, and the relative location of the friction fuse connection. For example, the two large DMS considered numerically resulted in fatigue stress limits above the CAFT and the instrumented DMS.

7. Analysis of the RICWS field data suggests vortex shedding has a significant role in the dynamic behavior of the RICWS under wind loading. Alignment between the natural frequency at which the sign was observed to oscillate and the range of shedding frequency experienced by the sign, suggest that lock-in is possible.

8. Because vortex shedding is such a prominent behavior, altering the dynamic characteristics may be a reliable method for reducing the amplitude of the oscillations observed in the RICWS. It seems crucial to increase the stiffness of the sign to space apart the natural and vortex shedding frequency. This could be done by increasing the stiffness of the sign (varying mass, base connection, or height of the sign).

9. Two other modifications are proposed to mitigate the oscillation of the RICWS structure: reducing the drag force on the sign and potential source of vortex generation, employing a tuned mass damper. Removal of the background shields around the lights of the RICWS reduces the form drag and corresponding vibration amplitudes. The validated FEM and CFD models were leveraged to implement and evaluate this proposed modification. A small-scale tuned mass damper (TMD) can limit the average displacement response of the RICWS; however, the TMD may not be sufficient by itself to prevent large displacements during extreme wind events. A combination of these modifications (e.g., TMD and removal of the background shields) could offer sufficient reduction of the dynamic response.

10. Of the proposed modifications, a simple modification of inserting a shim into the slip-base connection was implemented in the field to increase the stiffness while maintaining the breakaway sign support. However, analysis of the field data revealed that the stiffness did not appreciably change due to this simple modification. A different base connection design is recommended to improve the fixity and increase the stiffness.

9.2 RECOMMENDED FUTURE RESEARCH

The research presented here on the DMS was very specific to the structure and region of the DMS instrumented in the field. The key features of the Type A support system and DMS panel that affect the fatigue stress demand in the friction fuse connection should continue to be explored. Dynamic pressure functions should also be developed for other regions of the state where DMS are located but the characteristics of the wind loading may be different.

The results of the dynamic analysis performed with the experimentally validated FEM model differed significantly from the analysis with the equivalent static pressure equation for natural wind gusts prescribed in the AASHTO LRFD Specification for SLTS. Results of the dynamic analysis controlled, with a peak stress of 9.27 ksi compared to a peak stress of 7.2 ksi in the static analysis although both analyses used the same drag coefficient and equivalent limit-state wind loading. Reasons for the disagreement between the two analysis methods should continue to be explored. One possible source of disagreement could be from the assumptions made in the static analysis for normal wind loading, which did not account for the difference in deformation of the two different post lengths and associated load distribution. Other disagreement could stem from assumptions embedded in the original structures, generally cantilever structures, used in previous research (Kaczinski, Dexter, & Van Dien, 1998; Dexter & Ricker, 2002) to develop the equivalent static pressure equation for natural wind gusts (6.25), which features a constant of 5.2. It is likely that these original structures did not contain some of the key characteristics of the DMS, such as the breakaway connections, and there may be a need to revisit the derivation of these equations for roadside signs like the DMS that feature this unique support system where a constant value of 5.2 may not be appropriate.

The dynamic response of the DMS due to vortex shedding is not explored in detail in the research presented here. The FEM model utilized as the primary tool for the evaluation of the fatigue life of the structure does not consider vortex shedding. The phenomena of vortex shedding, and more specifically lock-in, is plausible for wind loading tangential to the sign. Further research is needed to determine the impact of vortex shedding on the response of the DMS. Experimental work at SAFL is recommended. It is also recommended that the dynamic behavior of the FEM model of the DMS under primarily tangential loading be improved, specifically in the friction fuse connection where adequate field data for comparison was not available.

The analysis of the RICWS is specific to this structure and sign layout. However, as smaller signs, such as the RICWS panels, get heavier, vortex shedding, and more specifically lock-in, is likely for the wind speeds commonly seen by these structures. A broader investigation of these newer sign types should consider the impact of vortex shedding on the structural design. In addition, aerodynamic modifications of the sign panels, similar to rear fairings, may be an effective approach to limit the dynamic response to normal wind loading, but the impact on the tangential wind response is not clear.

REFERENCES

AASHTO. (2012). LRFD Bridge Design Sepcifications, Customary U.S. Units, 6th Ed. Washington DC: American Association of State Highway and Transportation Officials (interim Revisions 2012 and 2013).

AASHTO. (2015). Standard Specifications for Sructural Supports for Highway Signs, Luminaires, and Traffic Signals. Washington DC: American Association of State Highway and Transportation Officials (Interim Revisions 2017).

ABAQUS (version 6.13) [Computer Software]. Providence, RI. Dassault Systèmes Simulia Corp.

Ahearn, E., & Puckett, J. (2010). *Reductionof Wind-Induced Vibrations in High-Mast Light Poles.* Laramie, WY: University of Wyoming.

Alegre, J., Aragon, A., & Gutierrez-Solana, F. (2004). A Finite Element Simulation Methodlology of the Fatigue Behavior of Punched and Drilled Plate Components. *Engineering Failure Analysis*, *11*(5), 737-750.

AWS Truepower. (2010). *Minnesota - Annual Average Wind Speed at 80 m.* WIND Exchange U.S. Department of Energy. Retrieved from https://windexchange.energy.gov/maps-data/63

Bazilevs, Y., Calo, V.M., Cottrell, J.A., Hughes, T.J.R., Reali, A. & Scovazzi, G. (2007). Variational multiscale residual-based turbulence modeling for large eddy simulation of incompressible flows. *Computer Methods in Applied Mechanics and Engineering, 197*(1), 173-201.

Beaupuits, J., Otarola, A., Rantakyro, F., Rivera, R., Radford, S., & Nyman, L.-A. (2004). Analysis of Wind Data Gathered at Chajnnantor (*ALMA Memo No. 497*) Tucson, Arizona: National Radio Astronomy Observatory.

Bec, J. (2010). Influence of Wind Spectrum Formula Choice on Footbridge Response. *Fifth International Symposium on Computational Wind Engineering*, Chapel Hill, NC, USA, May 23-27.

Brown, J. D., Lubitz, D. J., Cekov, Y. C., Frank, K. H., & Keating, P. B. (2007). *Evaluation of Influence of Hole Making Upon the Performance of Structural Steel Plates and Connections.* Austin, TX: University of Texas at Austin.

CH2MHill. (2015). *MnDOT RICWS Safety.* Mendota Heights: CH2MHill.

Davenport, A. G. (1961). The Spectrum of Horizontal Gustiness Near the Ground in High Winds. *Quarterly Journal of the Royal Meteorological Society*, *87*(372) ,194-211.

Dexter, R. J., & Ricker, M. J. (2002). *NCHRP Report 469: Fatigue-Resistant Design of Cantilevered Signal, Sign, and Light Supports.* Washington, DC: NCHRP.

Fisher, J., Nussbaumer, A., Keating, P., & Yen, B. (1993). *Resistance of Welded Details Under Variable Amplitude Long-Life Fatigue Loading* (NCHRP Report 354). Washington, DC: National Academy Press.

Garlich, M., & Thorkildsen, E. (2005). *Guidelines for th Installation, Inspection, Maintenance and Repair of Structural Suports for Highway Signs, Luminaires, and Traffic Signals.* Chicago: FHWA.

Gawronski, W. (2002). *Three Models of Wind-Gust Distrubances for the Analysis of Antenna Pointing Accuracy.* Pasadena, CA: Jet Propulsion Laboratory, California Institue of Tehcnology.

Geuzaine, C., & Remacle, J. F. (2009). Gmsh: A three-dimensional finite element mesh generator wit built-in-pre- and post-processing facilities. *International Journal for Numerical Methods in Engineering, 79*(11), 1309-1331.

Gutierrez-Solana, F., Pesquera, D., & Sanchez, L. (2004). Fatigue Behavior of Punched Structural Plates. *Engineering Failure Analysis*, 751-764.

Hughes, T.J.R., Mazzei, L., & Jansen, K.E. (2000). Large-eddy simulation and the variational multiscale method. *Computing and Visualization in Science 3*, 47-59.

Kaczinski, M. R., Dexter, R. J., & Van Dien, J. (1998). *Fatigue-Resistant Design of Cantilevered Signal, Sign and Light Supports* (NCHRP Report 412). Washington, DC: NCHRP.

Kimley Horn. (2015). Type A Sign Structure Detail. *Plan Set T.H. 94 DMS Moorhead to Alexandria*. St. Paul, MN: MnDOT.

Larsen, A., Esdahl, S., Andersen, J., & Vejrum, T. (2000). Storebaelt Suspension Bridge - Vortex Shedding Excitation and Mitigation by Guide Vanes. *Journal of Wind Engineering and Industrial Aerodynamics*, *88*(2-3), 283-296.

Liu, H. (1991). *Wind Engineering: A Handbook for Structural Engineers.* Englewood Cliffs, New Jersey: Prentice-Hall, Inc.

Logg, A., Mardal, K.A. & Wells, G. (2012). *Automated solution of differential equations by the finite* element *method: The FEniCS book.* Berlin: Springer.

Martinez, M. J. (2015). Minnesota Department of Transportation Construction Plan for Signing and Guardrail. *State Project No. 7005-105 (TH169)*. St. Paul, MN: MnDOT.

MathWorks. (2018). *Band-Limited White Noise*. Retrieved from https://www.mathworks.com/help/simulink/slref/bandlimitedwhitenoise.html

McGee, H. W. (2010). *Maintenance of Signs and Sign Supports: A Guide for Local Highway and Street Maintenance Personnel.* Washington, DC: FHWA.

MnDOT. (2000). Guidelines for Changeable Message Sign (CMS) Use. St. Paul, MN: Office of Traffic Engineering, MnDOT.

MnDOT. (2008). Construction Plan for Permanent L.E.D. Dynamic Message Signs. *State Project No. 8826-43 (TH35).* St. Paul, MN: MnDOT.

MnDOT (Director). (2015). *RICWS System Video* [Motion Picture]. St. Paul, MN: MnDOT.

MnDOT. (2016, July). *Improved Structural Design of Rural Intersection Conflict Warning Signs (RICWS)* (Research Need Statement). St. Paul, MN: MnDOT.

Stoter, S.K.F. (2017). Residual-based variational multiscale modeling in a discontinuous Galerkin framework. *Master Thesis*, Delft University of Technology, Delft, Netherlands.

Stoter, S.K.F., Turteltaub, S.R., Hulshoff, S.J., & Schillinger, D. (2018). A discontinuous Galerkin residual-based variational multiscale method for modeling subgrid-scale behavior of the viscous Burgers equation. *International Journal for Numerical Methods in Fluids, 88*(5), 217-238.

Tezduyar, T.E. & Osawa, Y. (2000), Finite element stabilization parameters computed from element matrices and vectors. *Computer Methods in Applied Mechanics and Engineering 190(3)*, 411-430.

Rassati, G., Swanson, J., & Yuan, Q. (2004). *Investigation of Hole Making Practices in the Fabrication of Structural Steel.* Chicago: American Institue of Steel Construction .

Valtinat, G., & Huhn, H. (2004). Bolted Connections with Hot Dip Galvanized Steel Members wtih Punched Holes. *Proc. ECCS/AISC Workshop, Connections in Steel Structures V: Innovative Steel Connections,* Amsterdam, June 3-5, 297-309.

Williamson, C. H., & Govardhan, R. (2004). Vortex-Induced Vibrations. *Annual Review of Fluid Mechanics*, *36,* 413-455.

APPENDIX A: DMS FIELD MONITORING SUPPLEMENTAL INFORMATION

Supplemental information for the DMS field deployment and data collection procedures are provided in this appendix. Details for the sensors used in the DMS instrumentation are provided in Table A.1 and Table A.2. A log of all major modifications to the DMS data collection system is provided in Table A.3.

The temperature compensation curve provided by the gage manufacturer is reproduced in Figure A.1. Detailed gage locations are provided in Figure A.2 through Figure A.8. The dimensions in Figure A.2 through Figure A.6 are taken from the dashed line referencing the edge of the section to the center of each gage. In Figure A.7 and Figure A.8 the dimensions are taken from the edge of the plate to the center of the gage. In Figure A.8 the gages shown with a red 'X' through them were not installed because conduit was covering this portion of the plate. Gage groups are illustrated in Figure A.9 through Figure A.11. In Figure A.9 through Figure A.11 a red box signifies that all gages outlined by the box are connected to the logger. A yellow box signifies that not all gages outlined by the yellow box are connected to the logger. The annotation to the right of the yellow box stipulates which gages outlined within the yellow box are connected to the logger for that group.

The program used for the data collection is provided in Section A.1. The program is from the most recent update, completed October 31, 2017. Between August 28, 2017 and October 31, 2017 there was an error in the data logger processing system that resulted in a drift in the clock used to designate the time stamp for the data sampled at 1 Hz (wind speed, wind direction, and air temperature). As a result, there was an offset between the time stamp of the 1 Hz data (wind speed, wind direction, and air temperature) and the 200 Hz data (strain and acceleration). The data sampled during the time the error existed could still be processed by applying the initial offset between the time stamp of the 1 Hz data and the time stamp of the 200 Hz data for a wind event to all the 1 Hz data entries in the wind event. Wind events were most easily recognized by large gaps in time between the time stamp indicating a wind event had concluded and another wind event had been triggered.

Table A.1 – Sensor details

Count	Sensor	Manufacture	Model	Sensor Parameters
6	0.118 in (3 mm) uniaxial strain gage	OMEGA	KFH-3-350-C1-11L3M3R	See Table A.2 for gage factor. Input voltage of 2.5V
36	0.236 in (6 mm) uniaxial strain gage	OMEGA	KFH-6-350-C1-11L3M3R	See Table A.2 for gage factor. Input voltage of 2.5V
10	Rectangular rosette with 0.118 in (3mm) gages	OMEGA	KFH-3-350-D17-11L3M3S	See Table A.2 for gage factor. Input voltage of 2.5V
2	Anemometer	Campbell Scientific	03002-L50 RM Young Wind Sentry Set	Speed: $\pm 1.1\ mph\ \left(\pm 0.5 \frac{m}{s}\right)$ Vane: $\pm 5°$
1	Temperature probe and shield	Campbell Scientific	107-17-PT Temperature Probe 41303-5A RM Young 6-Plate Solar Radiation Shield	$\pm 0.2℃$
2	Accelerometer	PCB Piezotronics	3711B1210G Single Axis DC Accelerometer	$200\ mV/g$

- All gages were attached to the CR9000X using a 350 ohm, 4-wire full-bridge terminal input module (4WFBS350) from Campbell Scientific

Table A.2 – Gage factor (GF) for all strain gages

Gage	GF
1	2.04
2	2.04
3	2.04
4	2.04
5	2.04
6	2.04
7	2.01
8	2.00
9	2.01
10	2.01
11	2.00
12	2.01
13	2.04
14	2.04
15	2.04
16	2.04
17	2.04
18	2.04
19	2.01
20	2.00
21	2.01
22	2.01
23	2.00
24	2.01
25	2.04
26	2.04
27	2.04
28	2.04
29	2.04
30	2.04
31	2.01
32	2.00
33	2.01
34	2.01
35	2.00
36	2.01
37	2.04
38	2.04

Gage	GF
39	2.04
40	2.04
41	2.04
42	2.04
43	2.01
44	2.00
45	2.01
46	2.01
47	2.00
48	2.01
49	2.01
50	2.00
51	2.01
52	2.01
53	2.00
54	2.01
55	2.04
56	2.04
57	2.04
58	2.04
59	2.04
60	2.04
61	2.00
62	2.00
63	2.00
64	2.04
65	2.04
66	2.04
67	2.04
68	2.04
69	2.04
70	2.04
71	2.00
72	2.00
73	2.00
74	2.04
Coupon(s)	2.04

Table A.3 – Log of major modifications to DMS data collection system

Date	Modification to Data Collection System
08/17/2017	DMS data collection begins Gages connected in Group 1 Threshold at 13.4 mph (6 m/s)
08/23/2017	Gages connected in Group 2 Added single coupon located on the ground, centered between support posts
08/28/2017	Updated program, updates caused error in time stamp between data sampled at 200 Hz (strain and acceleration) and data sampled at 1 Hz (wind speed, wind direction, air temperature)
09/01/2017	Threshold at 22.4 mph (10 m/s)
09/15/2017	DMS data logger died and restarted within same day
09/19/2017	Accelerometers glued directly to the support posts
09/20/2017	DMS data logger died and restarted
09/21/2017	Threshold at 26.8 mph (12 m/s)
09/22/2017	DMS data logger died and restarted within same day
09/29/2017	Accelerometer 1 moved to web Gages connected in Group 3 Coupon added, so that now one coupon on ground at base of each support post
09/30/2017	DMS data logger died and did not restart
10/14/2017	Replaced DMS data logger batteries and charger
10/31/2017	Replaced extension cord powering DMS New DMS program to correct time stamp error Removed Anemometer 2 for use with RICWS Threshold at 22.4 mph (10 m/s)
11/29/2017	Threshold at 31.3 mph (14 m/s) Refreshed DMS program
12/09/2017	Moved Accelerometer 1 from the web to the flange of the support post
01/20/2018	Site visit to refresh DMS modem

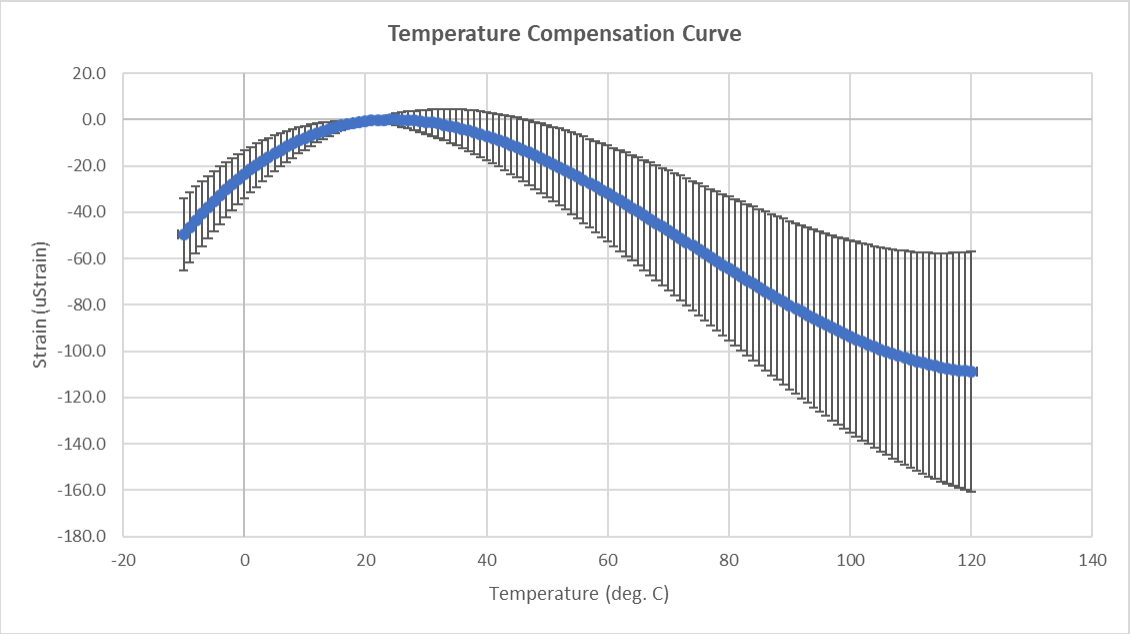

Figure A.1 – Temperature compensation curve provided for all strain gages

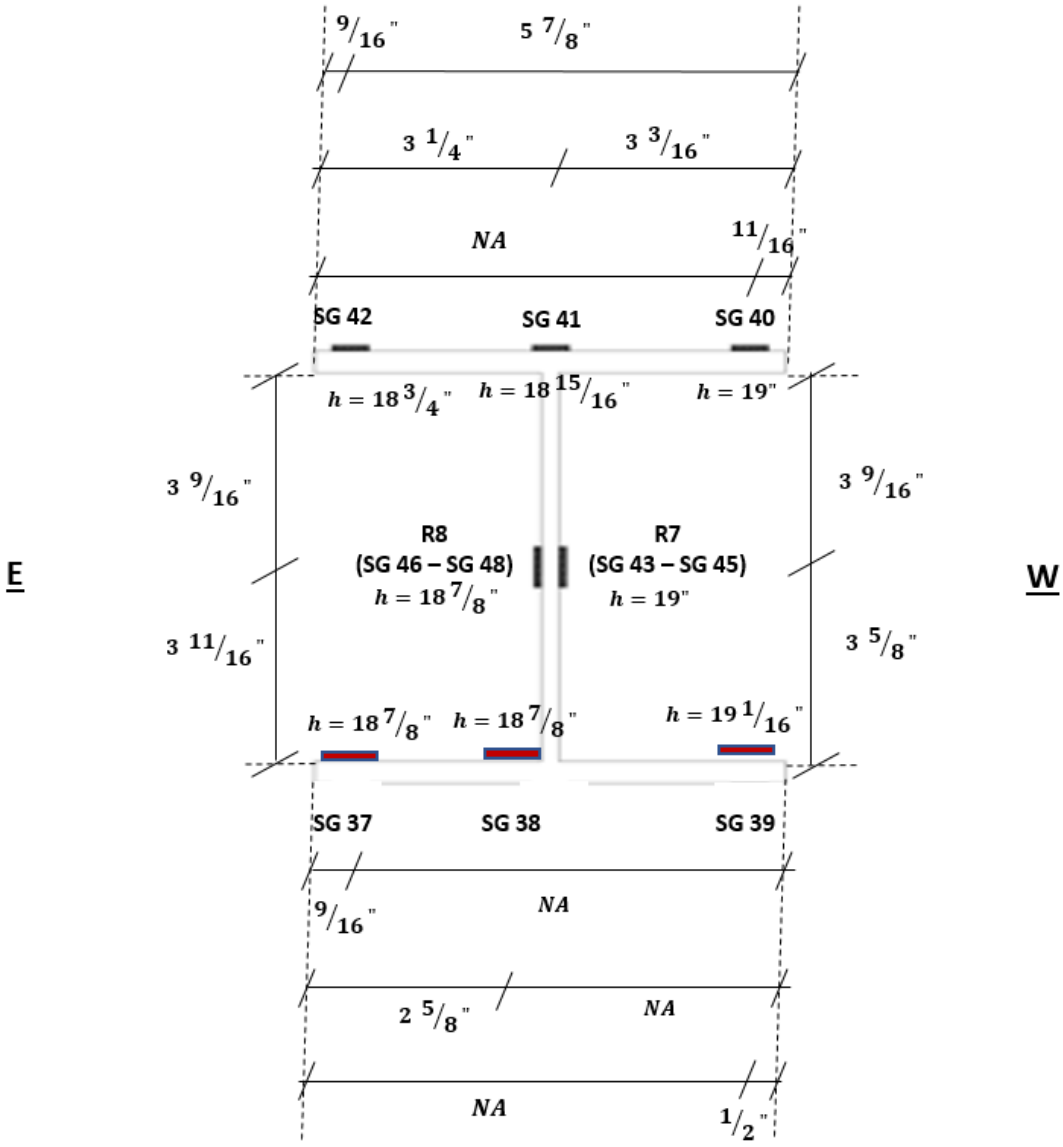

Figure A.2 – Location of strain gages at base of east post

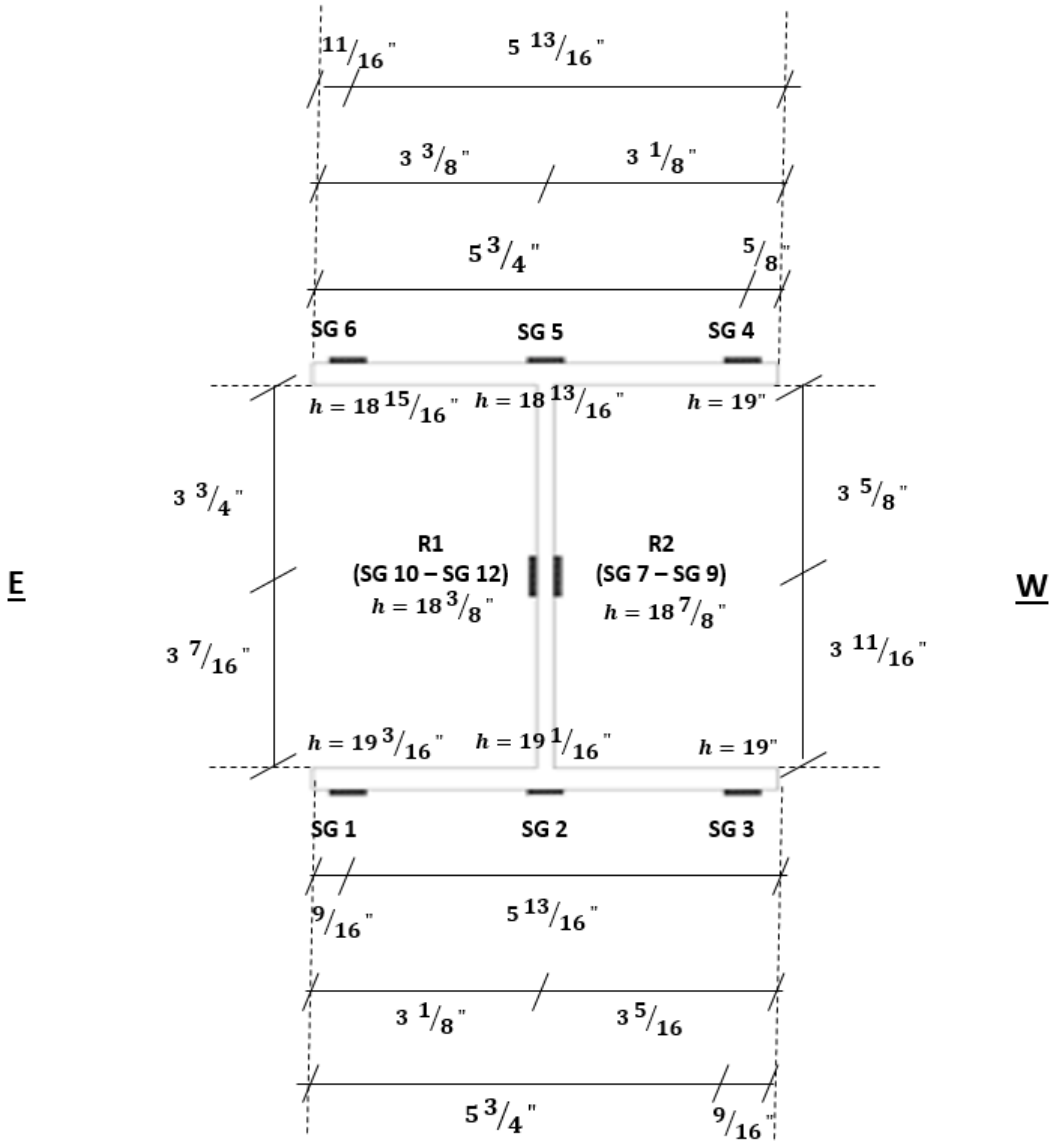

Figure A.3 –Location of strain gages at base of west post

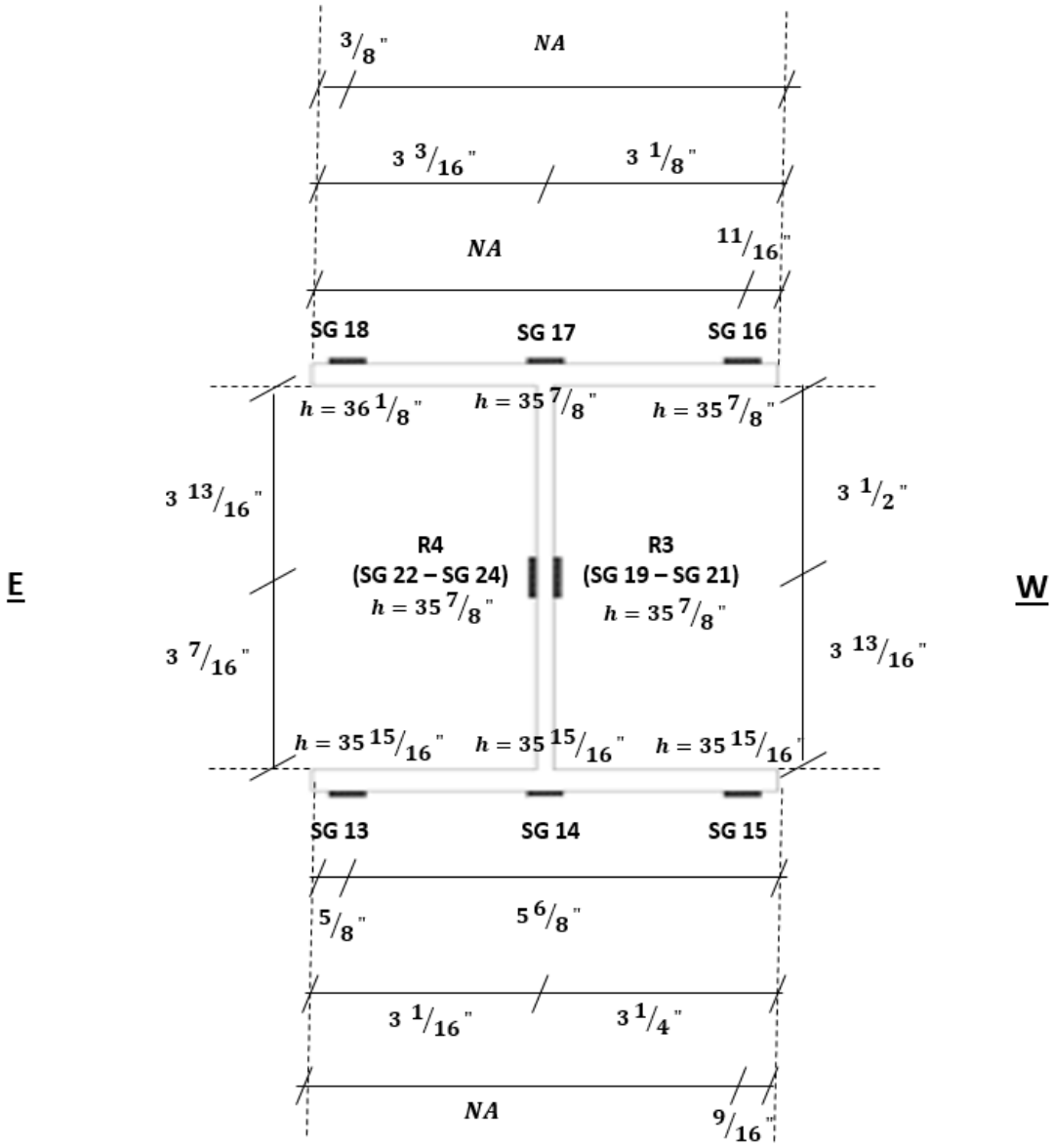

Figure A.4 – Location of strain gages 3 ft. from base of west post

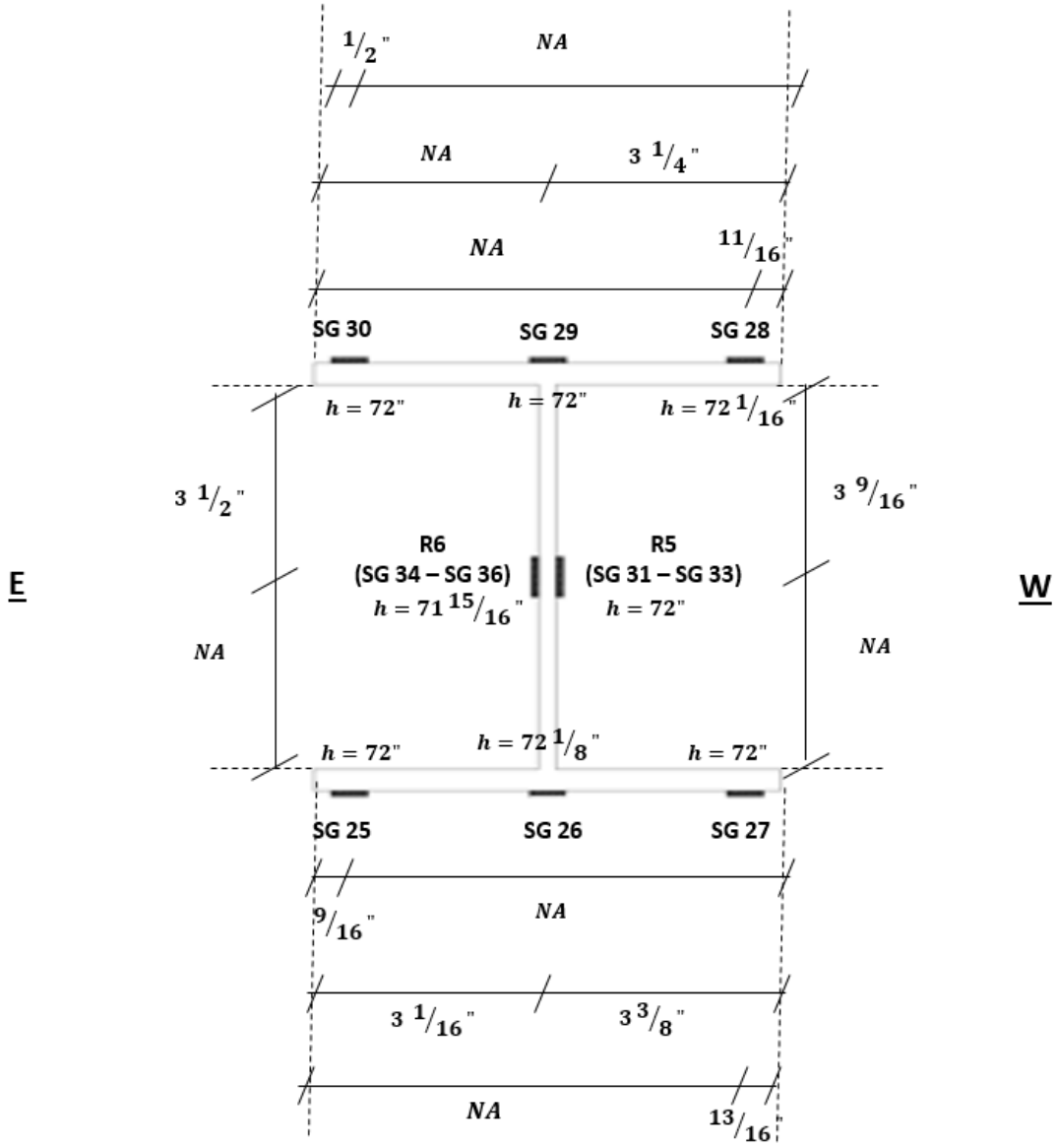

Figure A.5 – Location of strain gages 6 ft. from base of west post

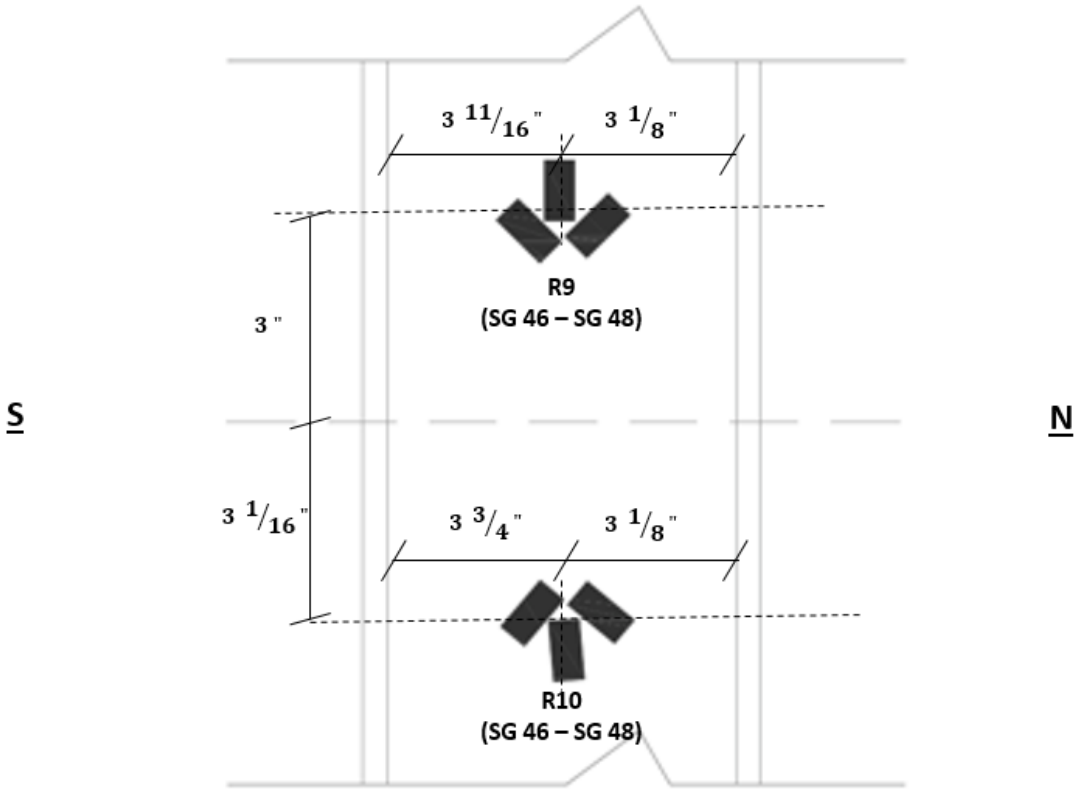

Figure A.6 – Location of strain gages at splice of west post

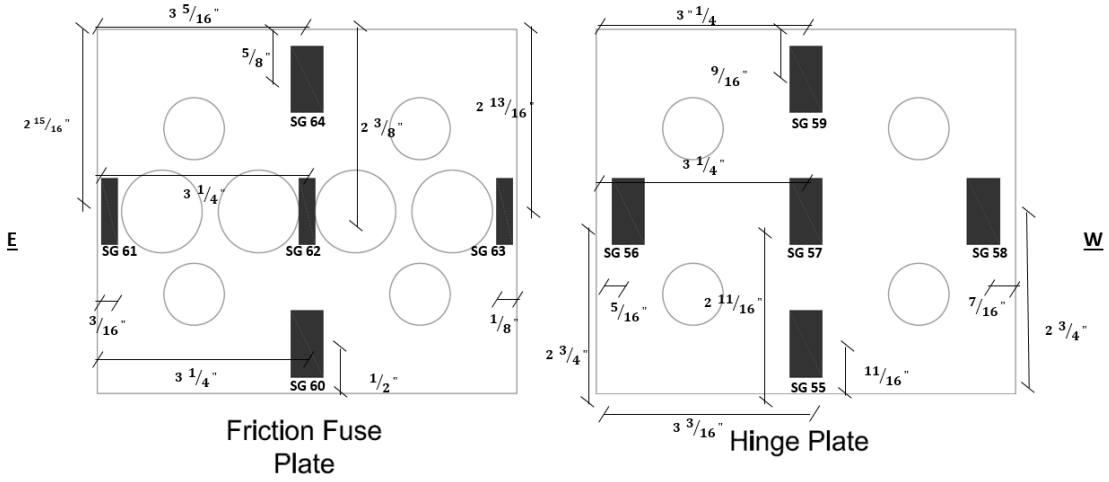

Figure A.7 – Location of strain gages on west friction fuse connection

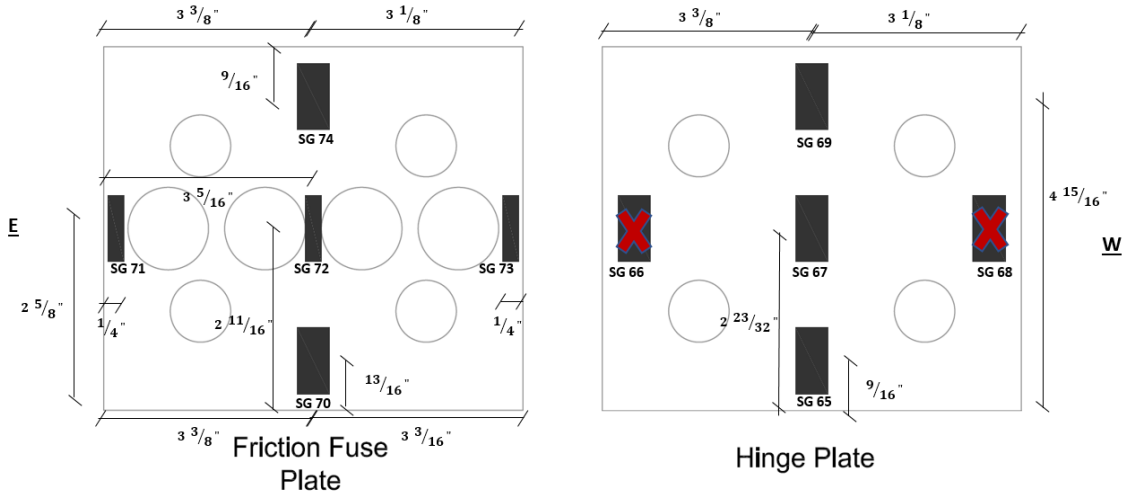

Figure A.8 – Location of strain gages on east friction fuse connection

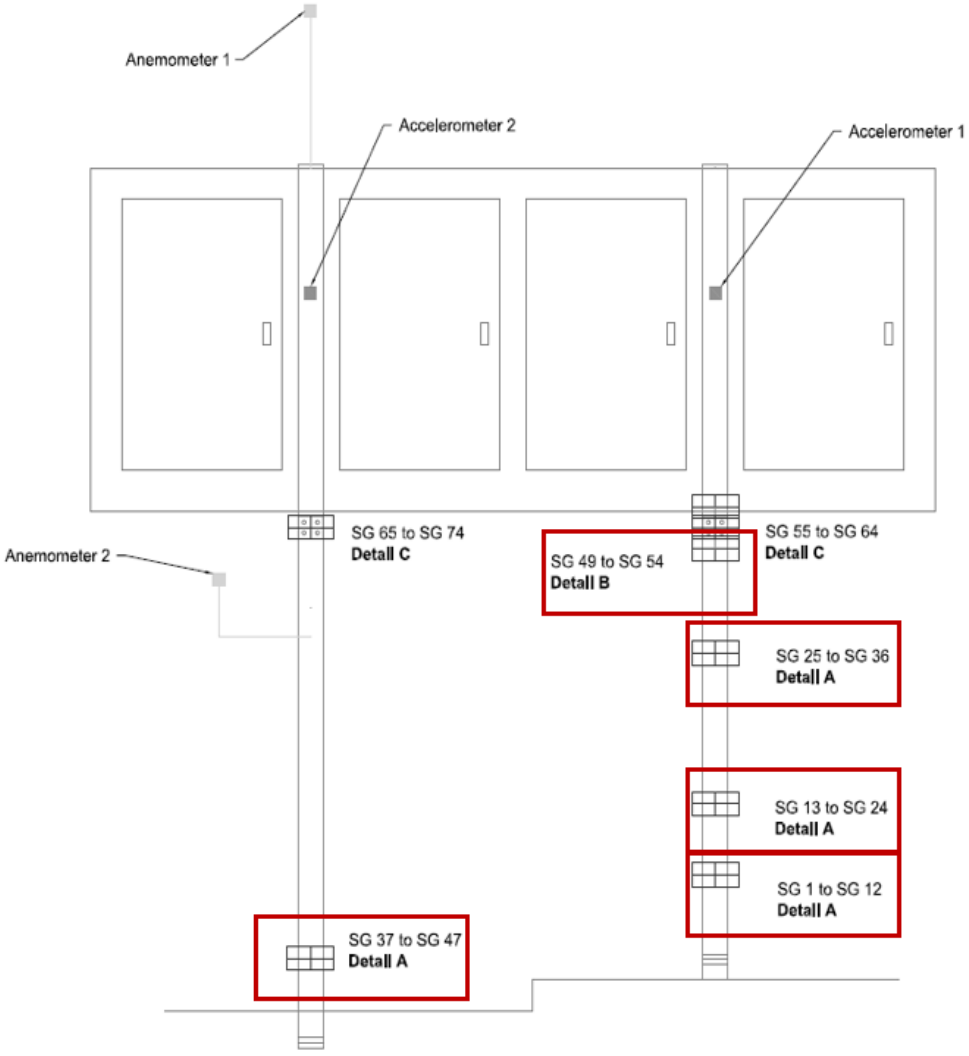

Figure A.9 – Strain gage Group 1

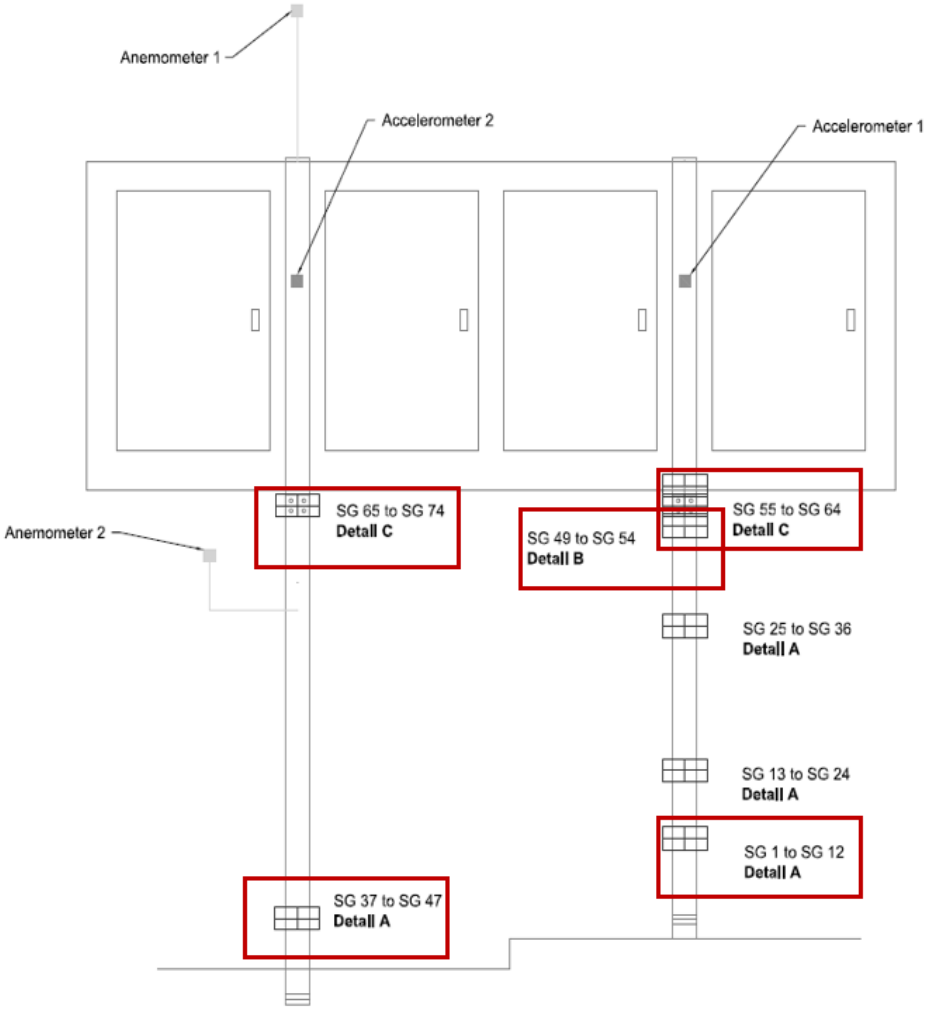

Figure A.10 – Strain gage Group 2

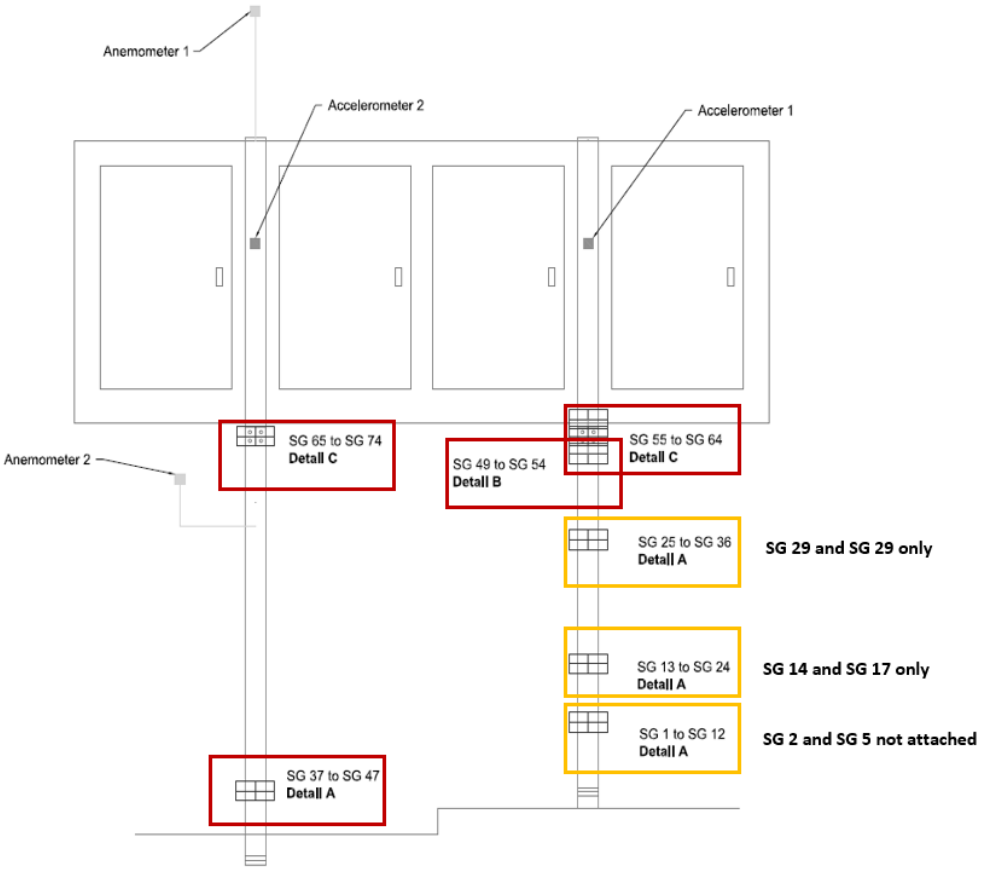

Figure A.11 – Strain gage Group 3

A.1 DMS DATA COLLECTION CODE

The following program was written by Chris Ellis of SAFL for the CR9000X used with the DMS data collection system. The code was last updated on October 31, 2017.

```
'CR9000X Series Datalogger


SlotConfigure(9050,9050,9050,9050,9060,9060,9060,9060,9071)


'\\\\\\\\\\\\\\\\\\\\  DECLARE VARIABLES  ////////////////////////////


'Constants

Const MainScanPeriod_mS = 5  'milliseconds

Const MeasIntegTime_uS = 60'microseconds

Const GageCount = 54

Const BrConfig = -1 'Block1 gage code for quater bridge strain using 4WFBS350
module

'Const PoissonRatio = 0.303  (Poisson Ratio not needed for 1/4 bridge gage
configuration)

Const SaveFastDataTimer = 1


'------------------Strain Variables-------------------------

Public GF(GageCount)  'Gage Factor - update with actual from gage package

Public Strain_mVperV(GageCount)

Units Strain_mVperV = mV/V

Public Strain(GageCount)

Units Strain = uStrain

Public Zero_MvperV(GageCount)

Units Zero_MvperV = mV/V

Public Zero_Strain(GageCount)

Units Zero_Strain = uStrain
```

```
Public MaxStrain(2)

Alias MaxStrain(1) = MaxStrainValue

Units MaxStrainValue = uStrain

Alias MaxStrain(2) = MaxStrainLoc

Public MaxStrain_1S

Units MaxStrain_1S = uStrain

Public SaveStrainThreshold = 100

Units SaveStrainThreshold = uStrain

'Variables in the Strain Zeroing Function

Public StrainCalMode  '0 for not calibrated, 2 for calibration in progress, 6
for calibration complete

Public ZeroStrains As Boolean = False


'_____________________Accelerometer Variables _____________________

Const AccelCount = 2

Public Accel(AccelCount)

Units Accel = g

Public AccelSlope(AccelCount) = {1/195.8,1/196.4}  'Order:  SN10392,SN10901

Public AccelOffset(AccelCount) = {-7.0/195.8,-3.0/196.4}  'Offsets updated
during in situ zeroing

Public AccelKnownOffset(AccelCount) = {0,0}

Alias Accel(1) = Accel_1  'Accel_1 >> SN10392

Alias Accel(2) = Accel_2  'Accel_2 >> SN10901

Public MaxAccel(2)

Alias MaxAccel(1) = MaxAccelValue

Units MaxAccelValue = g

Alias MaxAccel(2) = MaxAccelLoc

Public MaxAccel_1S

Units MaxAccel_1S = g
```

```
Public SaveAccelThreshold = 1

Units SaveAccelThreshold = g

'Variables in the Accel Zeroing Function

Public AccelCalMode  '0 for not calibrated, 2 for calibration in progress, 6
for calibration complete

Public ZeroAccels As Boolean = False


'-----------------Wind and Air Temperature Variables------------------

Public WindSpeed(2)

Alias WindSpeed(1) = WindSpeedUp

Alias WindSpeed(2) = WindSpeedDown

Units WindSpeed = m/s

Public MaxWindSpd(2)

Alias MaxWindSpd(1) = MaxWindSpdValue

Units MaxWindSpdValue = g

Alias MaxWindSpd(2) = MaxWindSpdLoc

Units MaxWindSpd = m/s

Public SaveWindSpdThreshold = 10

Units SaveWindSpdThreshold = m/s

Public WindDir(2)  'only 1 wind direction sensor populating both array
elements

Units WindDir = deg

Public AirTemp_mVperV

Units AirTemp_mVperV = mV/V

Public Rs

Units Rs = ohms

Public AirTemp

Units AirTemp = degC

Public LoggerTemp
```

```
Units LoggerTemp = degC
'Coefficients for 107 temp probe temp calculation
Const A = 8.271111E-4
Const B = 2.088020E-4
Const C = 8.059200E-8

'------------------General Variables-----------------------
Dim I
Public CalFileLoaded As Boolean
Public Batt_V
Units Batt_V = volts
Public Batt_mA
Units Batt_mA = mA
'Variables for both Strain and Accel Zeroing and Fast Saving
Public ZeroingTime_S = 10
Public ZeroingScans
Public SaveFastData As Boolean = False
Public SaveFastDataDuration_S = 300  'seconds
Public SaveFastDataOverride As Boolean = True



'---------------------------- Tables-----------------------------

DataTable(Raw,SaveFastData,-1)  'Trigger, auto size
  CardOut(0,-1)
  'DataInterval(0,MainScanPeriod_mS,mSec,100)
  Sample(GageCount,Strain(),FP2)
  Sample(AccelCount,Accel(),FP2)
```

```
EndTable


DataTable(_1Sec,SaveFastData,-1)  'Trigger, auto size
  CardOut(0,-1)
  DataInterval(0,1,Sec,100)
  Sample(2,WindSpeed(),FP2)  'these are 1 sec. running averages of wind
speeds measured in the Main Scan
  Sample(1,WindDir,FP2)
  Sample(1,AirTemp,FP2)
EndTable


DataTable(_5Min,True,1440)  '5 days of records
  CardOut(0,-1)
  DataInterval(0,5,Min,100)
  Average(GageCount,Strain(),FP2,False)
  StdDev(GageCount,Strain(),FP2,False)
  Maximum(GageCount,Strain(),FP2,False,False)
  Minimum(GageCount,Strain(),FP2,False,False)
  Average(AccelCount,Accel(),FP2,False)
  StdDev(AccelCount,Accel(),FP2,False)
  Maximum(AccelCount,Accel(),FP2,False,False)
  Minimum(AccelCount,Accel(),FP2,False,False)
  WindVector(1,WindSpeedUp,WindDir(1),FP2,False,0,0,0)
  WindVector(1,WindSpeedDown,WindDir(2),FP2,False,0,0,0)
  Maximum(2,WindSpeed(),FP2,False,False)
  Average(1,AirTemp,FP2,False)
  Average(1,Batt_V,FP2,False)
  Minimum(1,Batt_V,FP2,False,False)
  Average(1,Batt_mA,FP2,False)
```

```
  Maximum(1,Batt_mA,FP2,False,False)
  Sample(1,MainScanPeriod_mS,FP2)
  FieldNames( "MainScanPeriod_mS" )
  Sample(1,MeasIntegTime_uS,FP2)
  FieldNames( "MeasIntegTime_uS" )
EndTable

DataTable(CalHist,NewFieldCal,50)
  SampleFieldCal
EndTable



'\\\\\\\\\\\\\\\\\\\\\\\\\\\\ PROGRAM ////////////////////////////

BeginProg
  'For I = 1 To 19: GF(I) = 2
  'Next I
  'For I = 20 To GageCount: GF(I) = 2
  'Next I

  GF(1)=2.04 : GF(2)=2.04 : GF(3)=2.04 : GF(4)=2.04 : GF(5)=2.04 : GF(6)=2.04
: GF(7)=2.01 : GF(8)=2.0 : GF(9)=2.01 : GF(10)=2.01 : GF(11)=2.0 :
GF(12)=2.01
  GF(13)=2.04 : GF(14)=2.04 : GF(15)=2.04 : GF(16)=2.04 : GF(17)=2.04 :
GF(18)=2.04 : GF(19)=2.0 : GF(20)=2.0 : GF(21)=2.0 : GF(22)=2.04
  GF(23)=2.04 : GF(24)=2.04 : GF(25)=2.04 : GF(26)=2.04 : GF(27)=2.04 :
GF(28)=2.04 : GF(29)=2.0 : GF(30)=2.0 : GF(31)=2.0 : GF(32)=2.04
  GF(33)=2.04 : GF(34)=2.04 : GF(35) = 2.04 : GF(36) = 2.04
  GF(37)=2.04 : GF(38)=2.04 : GF(39)=2.04 : GF(40)=2.04 : GF(41)=2.04 :
GF(42)=2.04 : GF(43)=2.01 : GF(44)=2.0 : GF(45)=2.01 : GF(46)=2.01 :
GF(47)=2.0 : GF(48)=2.01
```

```
  GF(49)=2.01 : GF(50)=2.0 : GF(51)=2.01 : GF(52)=2.01 : GF(53)=2.0 :
GF(54)=2.01



  CalFileLoaded = LoadFieldCal(0)  '  If a calibration has been done,  will
load the zero from the Calibration file


  Scan(MainScanPeriod_mS,mSec,100,0)


    '_____________________________Strain
Gages_____________________________________

    'Nicole changed the excitation voltage to 2500. This is desired as we do
not want to exceed the maximum excitation voltage for the gages


BrFull(Strain_mVperV(1),14,mV50,4,1,8,1,3,2500,False,False,0,MeasIntegTime_uS
,1,0)


BrFull(Strain_mVperV(15),14,mV50,5,1,9,1,3,2500,False,False,0,MeasIntegTime_u
S,1,0)


BrFull(Strain_mVperV(29),14,mV50,6,1,10,1,3,2500,False,False,0,MeasIntegTime_
uS,1,0)


BrFull(Strain_mVperV(43),12,mV50,7,1,11,1,3,2500,False,False,0,MeasIntegTime_
uS,1,0)



StrainCalc(Strain(),GageCount,Strain_mVperV(),Zero_MvperV(),BrConfig,GF(),0)
'Strain calculation (Poisson Ratio not needed for 1/4 bridge gage
configuration)


    MaxSpa(MaxStrain(),GageCount,ABS(Strain()))

    If MaxStrainValue > MaxStrain_1S Then MaxStrain_1S = MaxStrain
```

```
    If ZeroStrains AND NOT (StrainCalMode = 2) Then StrainCalMode = 1'Set the
Mode for the zero function to 1 to start the zero process


'FieldCalStrain(Zeroing,Mvar,reps,GF_adj,Zeromv_V,ModeVar,KnownVar,index,Numa
vg,GF_Raw)


FieldCalStrain(10,Strain_mVperV(),GageCount,0,Zero_MvperV(),StrainCalMode,0,1
,ZeroingScans,0,Zero_Strain())

    If ZeroStrains AND NOT (StrainCalMode = 2) Then ZeroStrains = False



    '_________________________________Wind Speed_____________________________

    PulseCount(WindSpeed(),2,12,1,1,1000,0.75,0.2)  '03002 or 03101 RM Young
Wind Sentry Wind Speed Sensor measurement - 1 second running average

    If WindSpeed(1)<0.21 Then WindSpeed(1)=0

    If WindSpeed(2)<0.21 Then WindSpeed(2)=0

    MaxSpa(MaxWindSpd,2,WindSpeed())



'_________________________________Accelerometers_____________________________



VoltSe(Accel(),2,mV5000,7,25,0,MeasIntegTime_uS,AccelSlope(),AccelOffset())



    MaxSpa(MaxAccel(),AccelCount,ABS(Accel()))

    If MaxAccelValue > MaxAccel_1S Then MaxAccel_1S = MaxAccel



    If ZeroAccels AND NOT (AccelCalMode = 2) Then AccelCalMode = 1'Set the
Mode for the zero function to 1 to start the zero process

    FieldCal
(0,Accel(),AccelCount,0,AccelOffset(),AccelCalMode,AccelKnownOffset(),1,Zeroi
ngScans)

    If ZeroAccels AND NOT (AccelCalMode = 2) Then ZeroAccels = False
```

```
    '_________________Call Output Tables_____________________________

    CallTable Raw

    CallTable _5Min

    CallTable CalHist

    CallTable _1Sec

  Next Scan


  SlowSequence

  Scan(1,sec,10,0)

    ZeroingScans = ZeroingTime_S * 1000 / MainScanPeriod_mS


    If NOT SaveFastDataOverride Then

      If((MaxAccel_1S>SaveAccelThreshold) OR
(MaxWindSpdValue>SaveWindSpdThreshold)) AND NOT SaveFastData Then    'DELETED
MAX STRAIN THRESHOLD

        SaveFastData = True

        Timer(SaveFastDataTimer,Sec,2)

      EndIf

      If SaveFastData AND (Timer(SaveFastDataTimer,Sec,4) >
SaveFastDataDuration_S) Then SaveFastData = False

    EndIf

    MaxStrain_1S  = 0

    MaxAccel_1S  = 0

    '03002 or 03301 RM Young Wind Sentry Wind Direction Sensor measurement -
WindDir:


BrHalf(WindDir(1),1,mV5000,7,27,8,14,1,5000,False,0,MeasIntegTime_uS,352,0)

    If WindDir(1)>=360 OR WindDir(1)<0 Then WindDir(1)=0

    WindDir(2) = WindDir(1)

    '107 temperature probe (from manual)
```

```
BrHalf(AirTemp_mVperV,1,mV50,7,28,8,16,1,5000,False,0,MeasIntegTime_uS,1,0)

    Rs = 1000/AirTemp_mVperV - 250000

    AirTemp = (1/(A+B*LN(Rs)+C*(LN(Rs))^3))-273.15

    ModuleTemp(LoggerTemp,1,4,_60Hz)

    Battery(Batt_V,0)

    Battery(Batt_mA,1)

    BiasComp : Calibrate '<-- MGWm1+: compensate CR9041 ADC for temperature
changes occurring since program start.

  NextScan

  EndSequence

EndProg
```

APPENDIX B: RICWS FIELD MONITORING SUPPLEMENTAL INFORMATION

Supplemental information for the RICWS field deployment and data collection procedures are provided in this appendix. Details for the sensors used in the RICWS instrumentation are provided in Table B.1. A log of all major modifications to the RICWS data collection system is provided in Table B.2.
The program used for the data collection is provided in Section B.1 corresponding to the November 6, 2017 update.

Table B.1 – Sensor details

Count	Sensor	Manufacture	Model	Sensor Parameters
2	String Potentiometer	UniMeasure	JX-P510-15-N11-10S-N15	Pot 1 = 0.0015112 inches/mV Pot 2 = 0.0015086 inches/mV
1	Anemometer	Campbell Scientific	03002-L50 RM Young Wind Sentry Set	Speed: $\pm 1.1\ mph\ \left(\pm 0.5\ \frac{m}{s}\right)$ Vane: $\pm 5°$
1	Temperature probe and shield	Campbell Scientific	107-17-PT Temperature Probe 41303-5A RM Young 6-Plate Solar Radiation Shield	$\pm 0.2℃$
2	Accelerometer	PCB Piezotronics	3711B1210G Single Axis DC Accelerometer	$201\ mV/g$

Table B.2 – Log of major modifications to RICWS data collection system

Date	Modification to Data Collection System
11/17/2017	RICWS data collection begins Threshold at 15.7 mph (7 m/s)
11/21/2017	Threshold at 22.4 mph (10 m/s)
11/29/2017	Threshold at 31.3 mph (14 m/s)
01/12/2018	Threshold at 26.8 mph (12 m/s)
01/15/2018	Threshold at 22.4 mph (10 m/s)
01/19/2018	Threshold at 20.1 mph (9 m/s)
01/24/2018	Threshold at 31.3 mph (14 m/s)
02/02/2018	Threshold at 26.8 mph (12 m/s)
04/15/2018	Threshold at 40.3 mph (18 m/s)
04/29/2018	Accelerometer 1 detached from sign
05/08/2018	String potentiometer 2 piano wire replaced, Accelerometer 1 reinstalled
05/09/2018	Threshold at 26.8 mph (12 m/s)
08/15/2018	String potentiometer piano wires replaced, Accelerometer 1 repaired
01/22/2020	Shim modification applied, String potentiometer piano wires replaced
04/22/2020	Anemometer cleaned

B.1 RICWS DATA COLLECTION CODE

The following program was written by Chris Ellis of SAFL for the CR1000 used with the RICWS data collection system. The code was last updated on November 6, 2017.

```
'CR1000 Series Datalogger

'date:

'program author:

PipeLineMode
```

```
PreserveVariables


'Declare Constants

Const MainScanPeriod_mS = 10

Const MeasIntegTime_uS = 250

Const SaveFastDataTimer = 1


'Declare Public Variables

'-----------------Wind and Air Temperature Variables------------------

Public WindSpeed

Units WindSpeed = m/s

Public WindDir

Units WindDir = deg

Public SaveWindSpdThreshold = 7

Units SaveWindSpdThreshold = m/s

Public AirTemp

Units AirTemp = degC

'_____________________Accelerometer Variables _____________________

Const AccelCount = 2

Public Accel(AccelCount)

Units Accel = g

Public AccelSlope(AccelCount) = {1/198.7,1/198.2}  'Order:  SN11195,SN11196

Public AccelOffset(AccelCount) = {6/198.7,.5/198.2}  'Offsets updated during
in situ zeroing

Public AccelKnownOffset(AccelCount) = {0,0}

Alias Accel(1) = Accel_1  'Accel_1 >> SN11195

Alias Accel(2) = Accel_2  'Accel_2 >> SN11196

'Variables in the Accel Zeroing Function
```

```
Public AccelCalMode  '0 for not calibrated, 2 for calibration in progress, 6
for calibration complete

Public ZeroAccels As Boolean = False

'_____________________String Pot Variables _____________________

Const PotCount = 2

Public Pot(PotCount)

Units Pot = ???

'Pot(1) slope: 15"/(4928mV-(-4998mV))=.0015112 inches/mV

'Pot(2) slope:  15"/(4978mV-(-4965mV))=.0015086 inches/mV

Public PotSlope(PotCount) = {.0015112,.0015086}  'Order:
SN47100612,SN47100613

Public PotOffset(PotCount) = {7.5,7.5}'inches  'Offsets updated during in
situ zeroing

Public PotKnownOffset(PotCount) = {0,0}

Alias Pot(1) = Pot_1  'Pot_1 >> SN47100612

Alias Pot(2) = Pot_2  'Pot_2 >> SN47100613

'Variables in the Pot Zeroing Function

Public PotCalMode  '0 for not calibrated, 2 for calibration in progress, 6
for calibration complete

Public ZeroPots As Boolean = False

'_____________________Other Variables _____________________

Public CalFileLoaded As Boolean

Public batt_volt

Public SaveFastData As Boolean = False

Public SaveFastDataOverride As Boolean = True

Public SaveFastDataDuration_S = 60

Public ZeroingTime_S = 10

Public ZeroingScans

Public AllowRestart As Boolean = True
```

```
'Define Data Tables.

DataTable (Raw,True,-1) 'Set table size to # of records, or -1 to
autoallocate.

  'DataInterval (0,MainScanInterval_mS,mSec,10)

  Sample(2,Accel(),FP2)

  Sample(2,Pot(),FP2)

EndTable


DataTable(_1Sec,True,-1)

  'DataInterval(0,1,Sec,10)

  Sample(1,WindSpeed,FP2)

  Sample(1,WindDir,FP2)

  Sample(1,AirTemp,FP2)

EndTable


DataTable(_5Min,True,1440)  '5 days of records

  DataInterval(0,5,Min,100)

  Average(2,Accel(),FP2,False)

  StdDev(2,Accel(),FP2,False)

  Maximum(2,Accel(),FP2,False,False)

  Minimum(2,Accel(),FP2,False,False)

  Average(2,Pot(),FP2,False)

  StdDev(2,Pot(),FP2,False)

  Maximum(2,Pot(),FP2,False,False)

  Minimum(2,Pot(),FP2,False,False)

  WindVector(1,WindSpeed,WindDir,FP2,False,0,0,0)

  Maximum(1,WindSpeed,FP2,False,False)

  Average(1,AirTemp,FP2,False)

  Average(1,batt_volt,FP2,False)
```

```
  Minimum(1,batt_volt,FP2,False,False)
  Sample(1,MainScanPeriod_mS,FP2)
  FieldNames( "MainScanPeriod_mS" )
  Sample(1,MeasIntegTime_uS,FP2)
  FieldNames( "MeasIntegTime_uS" )
  Maximum(1,Status.SkippedScan,fp2,False,False)
  Maximum(1,Status.SkippedSlowScan,fp2,False,False)
  Sample(1,Status.MaxBuffDepth,fp2)
EndTable

DataTable(CalHist,NewFieldCal,50)
  SampleFieldCal
EndTable

'Main Program
BeginProg
  CalFileLoaded = LoadFieldCal(0)  '  If a calibration has been done,  will
load the zero from the Calibration file
  Scan (MainScanPeriod_mS,mSec,500,0)
    '_________________________________Wind Speed_____________________________
    PulseCount(WindSpeed,1,1,1,1000,0.75,0.2)  '03002 or 03101 RM Young Wind
Sentry Wind Speed Sensor measurement
    If WindSpeed<0.21 Then WindSpeed=0

'_________________________________Accelerometers_____________________________

VoltSe(Accel(),2,mV5000,9,False,0,MeasIntegTime_uS,AccelSlope(),AccelOffset()
)
    If ZeroAccels Then
      If NOT (AccelCalMode = 2) Then AccelCalMode = 1'Set the Mode for the
zero function to 1 to start the zero process
```

```
      FieldCal
(0,Accel(),AccelCount,0,AccelOffset(),AccelCalMode,AccelKnownOffset(),1,Zeroi
ngScans)

      If NOT (AccelCalMode = 2) Then ZeroAccels = False

    EndIf

    '_____________________________String Pots_____________________________

    VoltSe
(Pot(),2,mv5000,11,False,0,MeasIntegTime_uS,PotSlope(),PotOffset())

    If ZeroPots Then

      If NOT (PotCalMode = 2) Then PotCalMode = 1'Set the Mode for the zero
function to 1 to start the zero process

      FieldCal
(0,Pot(),PotCount,0,PotOffset(),PotCalMode,PotKnownOffset(),1,ZeroingScans)

      If NOT (PotCalMode = 2) Then ZeroPots = False

    EndIf



    If SaveFastData Then CallTable Raw

  NextScan



  SlowSequence

  Scan(1,sec,10,0)

    If NOT SaveFastDataOverride Then

      If WindSpeed > SaveWindSpdThreshold AND NOT SaveFastData Then

        SaveFastData = True

        Timer(SaveFastDataTimer,Sec,2)

      EndIf

      If SaveFastData AND (Timer(SaveFastDataTimer,Sec,4) >
SaveFastDataDuration_S) Then SaveFastData = False

    EndIf

    '---------Air Temp----------

    Therm107 (AirTemp,1,13,Vx2,0,250,1.0,0)
```

```
    '-----------03002 or 03301 RM Young Wind Sentry Wind Direction Sensor
measurement - WindDir:

    BrHalf(WindDir,1,mV2500,14,Vx3,1,2500,False,0,MeasIntegTime_uS,352,0)

    If WindDir>=360 OR WindDir<0 Then WindDir=0

    Battery (batt_volt)

    'Following added as only way to allow periodic logger calibration in
Pipeline Mode

    If IfTime(1,60,Min) AND NOT SaveFastData AND AllowRestart Then Restart

    ZeroingScans = ZeroingTime_S * 1000 / MainScanPeriod_mS

    If SaveFastData Then CallTable _1Sec

    CallTable _5Min

    CallTable CalHist

  NextScan

EndProg
```